Novel Modelling Techniques for Charged Many-Body Systems with Quantum and Relativistic Effects

Pontus Svensson

Worcester College

University of Oxford

A thesis submitted for the degree of

Doctor of Philosophy

Michaelmas 2024

Abstract

High energy density science is central for astrophysical and human-made fusion applications but is characterised by non-ideal plasma behaviour due to strong particle interactions, quantum effects, and relativistic corrections. In this thesis, two *molecular dynamics* (MD) formulations are presented along with their implementation, which address quantum and relativistic effects, respectively. First, an extension to wave packet molecular dynamics using anisotropic Gaussian states is presented, which is designed to model electron dynamics over ionic time scales in warm dense matter. Long-range interactions are treated with a generalised Ewald summation, and exchange effects are treated within a pairwise approximation. The MD formulation has been used to investigate electron *dynamic structure factors* (DSFs) and x-ray Thomson scattering, where electron and ion time scale features are extracted from a single computation. A semi-classical form for the DSF, that corrects for known quantum constraints, is provided. This method has been tested against explicit computations of the density response function in MD. The DSF is further discussed within a two-fluid model, parameterised by the equation of state and transport properties. By comparison with MD results – facilitated by Bayesian inference – the electron transport properties for a test system of warm dense hydrogen are extracted.

Second, relativistic corrections are investigated both due to kinematics and interactions. The velocity-dependent inertia of relativistic particles is seen to reduce diffusive transport for one-component plasmas, in line with analytical results. However, long-range electromagnetic interactions are modified due to the finite speed of light. This is accounted for in the MD model by time-evolving the long-range fields while the highly fluctuating short-range fields are approximated in a field-less description using either the electrostatic or Darwin approximation.

Keywords: Molecular dynamics, Warm dense matter, Wave packet molecular dynamics, Dynamic structure factors, X-ray Thomson scattering, Electron transport properties, Relativistic molecular dynamics

Acknowledgements

The work presented in this thesis is the result of many delightful discussions and collaborations, and I am the utmost grateful for all of them. First and foremost, I would like to thank my supervisors Gianluca Gregori and Sam Vinko, without whom none of this would have been possible. Your guidance and experience have been invaluable when exploring new ideas, and working in your research groups has exposed me to a broad range of physics. I want to acknowledge the support by Scott Richardson, Patrick Hollebon, Amy Skelt, and Yusuf Aziz for not only the funding that has allowed me to carry out this project, but also for all the interesting discussions and help with computational resources. I wish to thank Frank Graziani for our semi-regular bi-weekly meetings, they have certainly taught me a lot and introduced me to many new ideas. Thanks to all my co-authors for your valued input, and Hannah Poole, Daniel Plummer, Thomas Gawne, and Alessandro Forte for spending their time reading parts of the thesis.

This thesis is an outcome of countless hours in the Simon room, and I appreciate the discussions – and walks around University Park – with all who have shared the "Simon room experience" with me. Tom, Hannah, Charlie, Alessandro, Tom and Oliver, you welcomed me from the very beginning – despite the ongoing pandemic – and my time in Oxford would truly not have been the same without you all. Daniel and Charlie, our lunchtime walks and the accompanying discussions, physics-related or otherwise, have always been one of the highlights of my day.

Last but not least, I would like to thank my family for their enduring and loving support over the years. Especially Alice, who tolerates my endless monologues and always brightens up my day. Thanks!

Pontus Svensson, Stockholm, December 2024

List of Publications

Part of the work presented in this thesis has been published in the following publications, presented in order of appearance in the thesis and with a statement of contribution.

(A) **P. Svensson**, T. Campbell, F. Graziani, Z. Moldabekov, N. Lyu, V. S. Batista, S. Richardson, S. M. Vinko and G. Gregori, "Development of a new quantum trajectory molecular dynamics framework", Philosophical Transactions of the Royal Society A, **381**:20220325, (2023)
Contribution: Developed and implemented the extension of the wave-packet model, performed the numerical computations and wrote the original manuscript.

(B) M. Bonitz, J. Vorberger, M. Bethkenhagen, M. Böhme, D. Ceperley, A. Filinov, T. Gawne, F. Graziani, G. Gregori, P. Hamann, S. Hansen, M. Holzmann, S.X. Hu, H. Kählert, V. Karasiev, U. Kleinschmidt, L. Kordts, C. Makait, B. Militzer, Z. Moldabekov, C. Pierleoni, M. Preising, K. Ramakrishna, R. Redmer, S. Schwalbe, **P. Svensson** and T. Dornheim, "Toward first principles-based simulations of dense hydrogen", Physics of Plasmas **31** 110501 (2024)
Contribution: Wrote the wave packet section.

(C) **P. Svensson**, Y. Aziz, T. Dornheim, S. Azadi, P. Hollebon, A. Skelt, S. M. Vinko and G. Gregori, "Modeling of warm dense hydrogen via explicit real time electron dynamics: Dynamic structure factors", Physical Review E, **110**, 055205 (2024)
Contribution: Developed the theory, performed the wave packet simulations, analysed the results and wrote the original draft.

(D) **P. Svensson**, P. Hollebon, D. Plummer, S. M. Vinko and G. Gregori, "Modelling of warm dense hydrogen via explicit real time electron dynamics: Electron transport properties", Physical Review E, **111**, 045208 (2025)
Contribution: Developed the fluid theory and its linear response properties, performed the simulations and MCMC analysis. Prepered the origional manuscript.

(E) D. M. Testa, **P. Svensson**, J. Jackson, T. Campbell and G. Gregori, "Self-diffusion of a relativistic Lennard-Jones gas via semi-relativistic molecular dynamics", Physical Review E, **107**, 054138 (2023).
Contribution: Supervised the implementation of the model in `LAMMPS`, the post processing of the data and the editing of the manuscript.

(F) D. Plummer, **P. Svensson**, D. O. Gericke, P. Hollebon, S. M. Vinko and G. Gregori, "Ionization calculations using classical molecular dynamics", Physical Review E, **111**, 015204 (2025)
Contribution: Conceptualisation and aided in both the theoretical and numerical developments.

(G) T. Campbell, **P. Svensson**, B. Larder, D. Plummer, S. M. Vinko and G. Gregori, "A molecular dynamics framework coupled with smoothed particle hydrodynamics for quantum plasma simulations", arXiv:2408.03693 (2024)
Contribution: Aided in the practical developments of the molecular dynamics model.

List of Symbols

k_{B}	Boltzmann constant.
ε_0	Dielectric constant or vacuum permittivity.
μ_0	Magnetic constant or vacuum permeability.
c	Speed of light, $c^{-2} = \mu_0 \varepsilon_0$.
m_e	Electron mass.
q_e	Electron charge (defined negative).
m_p	Proton mass.
a_i	Wigner-Seitz radius, see Section 1.2.1.
Γ	Coulomb coupling constant, see Section 1.2.1.
λ_s	Screening length, see Sections 1.2.1 & 1.2.2.
ω_p	Plasma frequncy, see Section 1.2.1.
$\hbar$	Reduced planck constant.
E_{F}	Electron Fermi energy, see Section 1.1.
μ	Chemical potential, see Sections 1.2.2 & 1.2.4.
Λ_{th}	Thermal de Broglie wavelength, see section 1.2.2.
θ	Degeneracy parameter, see Section 1.2.2.
r_s	Brueckner coupeling parameter, see Section 1.2.2.
ξ	Spin-polarisation, see Section 2.4.2.
ε	Relativistic parameter, see Section 1.2.4.
$\gamma(\boldsymbol{v})$	Lorentz (gamma) factor, see Sections 1.2.4 & 6.2.
σ_{SB}	Stefan–Boltzmann constant.
$\phi(\boldsymbol{x})$	Electromagnetic scalar potential.
$\boldsymbol{A}(\boldsymbol{x})$	Electromagnetic vector potential, see Sections 4.1 & 6.3.
$\boldsymbol{E}(\boldsymbol{x})$	Electric field, see section 6.3.
$\boldsymbol{B}(\boldsymbol{x})$	Magnetic field, see Section 6.3.
$n(\boldsymbol{x})$	Charge density, see Section 6.3.
$\boldsymbol{j}(\boldsymbol{x})$	Current density, see Section 6.3.
$\mathcal{L}$	Lagrangian function, see Sections 2.3.1, 3.2 & 6.3.
$\mathcal{H}$	Hamiltonian function, see Sections 2.3.1, 3.2 & 6.2.
$\hat{H}$	Hamiltonian operator, see Section 3.2.
$g_{\alpha\beta}(r)$	Radial distribution function, see Section 2.3.2.
$S_{\alpha\beta}(\boldsymbol{k})$	Static structure factor, see Section 2.3.2.
$S_{\alpha\beta}(\boldsymbol{k}, \omega)$	Dynamic structure factor, see Sections 2.3.3 & 4.6.
$F_{\alpha\beta}(\boldsymbol{k}, t)$	Intermediate scattering function, see Section 2.3.3.
$\chi_{\alpha\beta}(\boldsymbol{k}, -\boldsymbol{k}, \omega)$	Density response function, see Sections 2.3.3 & 4.7.
$G_{\alpha\beta}(\boldsymbol{k}, \omega)$	Dynamic local field correction, see Section 2.3.3.
$\sigma_\mu(\omega)$	Electrical conductivity, see Sections 3.4.3 & 5.2.4.
$c_{s,\mu}$	Adiabatic sound speed, see Section 5.2.
η_μ, ζ_μ and $\nu_{L,\mu}$	Shear, bulk and longitudinal viscosity, see Section 5.2.
κ_μ	Thermal conductivity, see Section 5.2.
χ_μ	Thermal diffusivity, see Section 5.2.2.
γ_μ	Adiabatic index, see Section 5.2.

List of Figures

List of Tables

Table of Contents

Chapter 1
High Energy Density Physics and Non-ideal Plasmas

Abstract: The field of high-energy-density physics is discussed in terms of astrophysical and technical applications. These plasmas are commonly non-ideal, and their characterisation in terms of dimensionless parameters is introduced. The creation of high energy density states in the laboratory and some open questions within the field are discussed.

1.1 High energy density physics

The traditional definition of *high-energy-density physics* (HEDP) is systems where the energy density exceeds $10^{11}\,\mathrm{J/m^3}$, or equivalently, pressures above 1 Mbar (100 GPa) [1]. This energy density is comparable to the bulk moduli of solid materials [2] and chemical bonds with binding energies on the order of 1 eV and a bound length of a few Bohr radii (a_B):

$$\text{Energy density} \sim \frac{1\,\mathrm{eV}}{(2\,a_\mathrm{B})^3} \approx 1\,\mathrm{Mbar}. \tag{1.1}$$

As the pressure becomes comparable to the internal energy of chemical systems, the characteristic behaviour changes. Ions and electrons move separately rather than in chemical units. However, these ionisation processes start at pressures as low as 0.1 Mbar and the original definition could arguably be revisited [3]. The ionisation equilibrium is described by the *Saha equation* [4] and yields substantial ionisation fractions at energy densities below those of atoms and molecules. This effect is only enhanced in dense systems, where electrostatic interactions reduce the binding energy through a process called ionisation potential depression [5–8].

To roughly define the high-energy-density region of phase space, consider the (ideal) pressure relation [9]

$$P = P_\mathrm{ion} + P_\mathrm{ele} + P_\mathrm{rad}, \tag{1.2}$$

with contributions from ions (P_{ion}), electrons (P_{ele}) and radiation (P_{rad}). In the high-temperature and low-density regime, the radiation pressure [3]

$$P_{\text{rad}} = \frac{4\sigma_{\text{SB}}}{3c} T^4 \tag{1.3}$$

dominates. In the above, σ_{SB} is the Stefan–Boltzmann constant, c is the speed of light, and T is the temperature. A pressure of 1 Mbar is reached at $k_{\text{B}}T \approx 400\,\text{eV}$, where the convention of measuring temperature in energy units is used and k_{B} is the Boltzmann constant.

Comparatively, in the low-temperature and high-density regime, the dominant pressure contribution is the electron degeneracy pressure [10]

$$P_{\text{ele}} \approx \frac{2}{5} E_{\text{F}} n_e, \tag{1.4}$$

where n_e is the electron density, $E_{\text{F}} = \hbar^2 \left(3\pi^2 n_e\right)^{2/3} / (2m_e)$ is the Fermi energy, $\hbar$ is the reduced Planck constant and m_e is the electron mass. The degeneracy pressure exceeds 1 Mbar at a density of $n_e \approx 10^{23}\,\text{cm}^{-3}$, which is comparable to the free-electron density in many metals [11].

In between these two limits, at intermediate temperatures and densities, both the electrons and ions are to first approximation an ideal gas with the pressure:

$$P_{\text{ion}} + P_{\text{ele}} \approx (n_i + n_e)\, k_{\text{B}} T, \tag{1.5}$$

where n_i is the ion density. For fully ionised hydrogen, the gas pressure is the dominant contribution at $P = 1\,\text{Mbar}$ for densities and temperatures above $8 \times 10^{20}\,\text{cm}^{-3}$ and 2 eV, respectively. A summary of the HEDP region for a hydrogen plasma is shown in Figure 1.1.

High energy density physics covers conditions between condensed matter and classical plasma physics, requiring consideration of strong electrostatic interactions, quantum effects, collective dynamics, and an interplay with electromagnetic fields. As a relatively new field – particularly in the context of generating HED states in the laboratory [3] – it presents many open questions (see Section 1.4), especially when the physics from the different regimes interact.

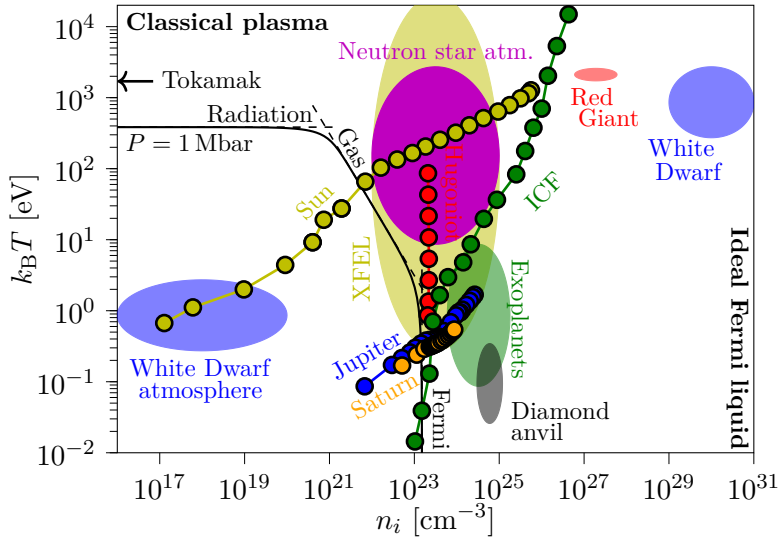

Figure 1.1: The high energy density region for hydrogen. The solid line shows the $P = 1\,\mathrm{Mbar}$ condition based on the model in equation (1.2) where the ideal electron pressure has been computed via Fermi-Dirac integrals. The regions where radiation, gas and Fermi pressure dominate are marked. Additionally, typical conditions for astrophysical and experimental methods are shown: Red giant, Exoplanets and Diamond anvil [12]; White dwarf, White dwarf atm., and Neutron star atm. [13]; ICF [14]; XFEL [15]; Jupiter (adiabat) [16]; Saturn (adiabat) [17]; Sun [18]; and Hugoniot [19]. Note that most experimental techniques and astrophysical motivations are not pure hydrogen plasmas, and the marked regions are rather typical ranges of conditions.

However, HEDP science is not only interesting in its own right, but has many astrophysical and technical applications, as illustrated in Figure 1.1.

Large gas giants can sustain high pressures and HED conditions in their interiors [16, 20–26] as the pressure is balanced by gravitational attraction in a hydrostatic equilibrium [27]. Notable examples in our solar system are Jupiter [16] and Saturn [17]. However, with the rapid increase in exoplanet discoveries in the last decade [28] the need for more accurate interior structure models has only increased [20, 29–31]. During the initial gravitational contraction of objects with masses below 10% of the solar mass [32, 33], the Fermi degeneracy pressure can balance the gravitational forces, and the core does not reach the temperatures required for fusion. This results in the formation of a brown dwarf[1], which is almost in its entirety HED matter [32–34].

[1]Whether the object is called a brown dwarf or giant planet depends on how it forms [33].

In larger stars, hydrogen fuses in the core and the constant flow of energy to the surface – where radiation is emitted – results in comparatively hot stellar objects (see Figure 1.1) that sustain their structure primarily by "classical" thermodynamic pressure [32], but the temperature gradient leads to a non-trivial transport behaviour [18, 35, 36]. Our Sun is a prime example, where the *equation of state* (EOS) models must account for electrostatic interactions, quantum and relativistic effects [18], models which were first tested by *helioseismology* [37]. Toward the end of the stellar evolution of stars with masses roughly less than twice the mass of the Sun, a non-fusing degenerate helium core is surrounded by a burning hydrogen envelope [38], and a red giant star is formed before helium fusion ignites. For larger stars with masses below eight solar masses, helium fusion commences in a non-degenerate core, and instead, a Fermi-degenerate carbon and oxygen core is created [38]. Both star types shed their envelope, resulting in white dwarf stars [38], which are almost in their entirety Fermi-degenerate [39], and relativistic [32] and interaction effects [32, 40, 41] are crucial for understanding their structure.

In stars with masses above the Chandrasekhar mass [42], the fully degenerate and relativistic electron pressure cannot prevent a gravitational collapse [32] and even more exotic objects like neutron stars can be formed, the atmospheres of which sustain the conditions discussed in this thesis [43–45]. This highlights the need to account for not only electron degeneracy but also relativistic and interaction effects, even for a cursory understanding of stellar evolution. However, these effects may also impact the stability of lower-density self-gravitating objects and the initial part of star formation [46].

In addition to astrophysical motivations, a major driver of HEDP science has been the quest for controlled thermonuclear fusion as an energy source, in particular *inertial confinement fusion* (ICF) [47–49]. The Lawson criteria [50] set a lower bound for the product of density and energy confinement time for the net energy production from a fusion plasma. Human-made devices typically aim to increase one of the two factors. *Magnetic confinement fusion* (MCF) confines the plasma using magnetic fields, while ICF instead reaches high-density states by compression of a fuel capsule using lasers. Recently, ground-breaking ICF experiments have

exceeded the Lawson criteria [51], a result of more than a decade of incremental improvements to both lasers and capsules, and a better understanding of HED physics.

The original (direct drive) ICF concept [47] was to compress a spherical fuel capsule by focusing lasers on the surface, from which the ejection of high-velocity particles acts as a rocket and propels the fuel inward [48, 49]. If the central region of the deuterium-tritium fuel, often termed the 'hot-spot', reaches a temperature of 4.3 keV, the heating from fusion processes[2] exceeds the bremsstrahlung losses [49]. At this threshold, the plasma is deemed 'ignited' and a burn wave propagates to the surrounding dense shell [52], where the plasma may be Fermi degenerate. Hydrodynamic instabilities – particularly Rayleigh-Taylor [53, 54] and Richtmyer-Meshov [55, 56] instabilities – can result in cold material mixing into the hot-spot and hampering ignition [49]. Attempts to address the ignition issue include, for example, *indirect drive ICF*, where the laser light is converted to a more uniform x-ray driver which reduces the seed for the instability [48, 49], and *fast ignition* [57] and *shock ignition* [58], where ignition is triggered by either heating from fast particles or launching a spherical shock wave into the hot-spot.

1.2 Parameters of non-ideal plasmas

Both in the astrophysical and technical applications discussed above, the plasma behaviour is non-ideal where the long-range electrostatic interaction, quantum non-locality and degeneracy, and relativistic effects are crucial for a detailed description of the plasma behaviour. The current uncertainties in the microscopic properties of non-ideal plasmas, such as EOS [59] and transport properties [60, 61], limit, for example, our understanding of the Jovian interior [62] and the modelling of ICF implosions [63]. The dimensionless parameters characterising these effects are discussed in the following, along with the regions of parameter space where their consideration is warranted.

[2]Only the energy of the charged α-particles can be reasonably captured in the plasma. Charge neutral neutrons will escape but should be captured in the surrounding structure for energy production in a power plant.

1.2.1 Electrostatic interactions

Consider a classical system of classical point particles with charge q_i and mass m_i, at a density n_i and temperature $k_\mathrm{B}T$. The system is immersed in a homogeneous neutralising background, which makes the system charge neutral and electrostatically stable. The typical Coulomb interaction energy per particle is on the order $q_i^2/(4\pi\varepsilon_0 a_i)$, where

$$a_i = \left(\frac{3}{4\pi n_i}\right)^{1/3} \tag{1.6}$$

is the *Wigner-Seitz radius* or *ion-sphere radius* which measures a typical distance between particles. The ratio of potential to kinetic energy[3] defines the *Coulomb coupling constant* [64–66]:

$$\Gamma_{ii} = \frac{q_i^2}{4\pi\varepsilon_0 a_i\, k_\mathrm{B}T}. \tag{1.7}$$

If $\Gamma_{ii} \ll 1$ the system is considered ideal and interaction effects can be seen as perturbations or individual collisions. However, due to the long-range nature of the Coulomb interaction – the interaction does not decay exponentially but rather algebraically with a low exponent [67] – plasmas have a collective nature dominated by large-scale electrostatic fields [68]. This is the realm of classical plasma physics. For $\Gamma_{ii} > 0.1$ interactions substantially alter the fundamental properties of the plasma [65] and systems with coupling constants above unity are called *strongly coupled*. In the large coupling limit, $\Gamma_{ii} \gg 1$, the system instead crystalises into a bcc lattice [69], the so-called Wigner crystal, at a critical $\Gamma_{ii} = 172 - 174$ [70, 71]. In more complete descriptions of materials, including quantum effects, the high-pressure regime is commonly not characterised by simple lattice structures, and exotic materials such as incommensurate structures [72], electrides [73, 74] and potentially even superconductive states [75, 76] are formed.

In the ideal-plasma regime, the particles act to screen each other and exponentially

[3]The average kinetic energy is $3k_\mathrm{B}T/2$, but this pre-factor is not included in the classical definition of Γ_{ii} and only constitute an order of unity change.

suppress the electric field on the length scale of the *Debye length* [68, 77]:

$$\lambda_{D,i} = \sqrt{\frac{\varepsilon_0 k_\mathrm{B} T}{q_i^2 n_i}} = \frac{a_i}{\sqrt{3\Gamma_{ii}}}. \tag{1.8}$$

These collective effects dominate if the number number of particles within the Debye-sphere is large, which is characterised by a large *plasma parameter* $\Lambda_i = 4\pi n_i \lambda_{D,i}^3 \gg 1$ [68][4]. However, as $\Lambda_i = \Gamma_{ii}^{-3/2}/\sqrt{3}$, the same condition is satisfied by $\Gamma_{ii} \ll 1$. For non-negligible Γ_{ii}, Stanton and Murillo [78] suggested a modified screening length

$$\lambda_{s,i} = \sqrt{1+3\Gamma_{ii}}\lambda_{D,i} \longrightarrow \begin{cases} \lambda_{D,i} & \text{if } \Gamma_{ii} \ll 1 \\ a_i & \text{if } \Gamma_{ii} \gg 1, \end{cases} \tag{1.9}$$

which suggests a transition in the screening behaviour at finite coupling, also seen in other models [79, 80]. However, the change in length scale is more fundamental, as the appropriate length scale to describe correlations in a plasma changes from $\lambda_{D,i}$ to a_i as Γ_{ii} increases. This is illustrated in Figure 1.2 where the correlations between the particles and the resulting electrostatic fields are shown. The above-mentioned transition of the correlation length scale is the most apparent in the screening behaviour, and for $\Gamma_{ii} > 1$, complex structures are formed on the length scale of a_i.

One of the characteristic time scales in a system of charged particles is given by the plasma frequency [68]

$$\omega_{p,i} = \sqrt{\frac{n_i q_i^2}{m_i \varepsilon_0}} = \sqrt{3\Gamma_{ii}}\sqrt{\frac{k_\mathrm{B} T}{m_i a_i^2}}, \tag{1.10}$$

the inverse of which $\omega_{p,i}^{-1}$ is the characteristic time scale for long length-scale density fluctuations. For non-ideal systems, a second important time scale is the inverse collision frequency ν_{ii}^{-1} [81]:

$$\nu_{ii} = \frac{q_i^4 n_i}{12\pi\varepsilon_0^2\sqrt{3m_i(k_\mathrm{B}T)^3}} = \Gamma_{ii}^2 \frac{\ln\Lambda_{ii}}{\sqrt{3}}\sqrt{\frac{k_\mathrm{B}T}{m_i a_i^2}}. \tag{1.11}$$

This is the characteristic time for collisions to markedly change the momentum of a particle

[4]Note that the exact pre-factor varies in the literature.

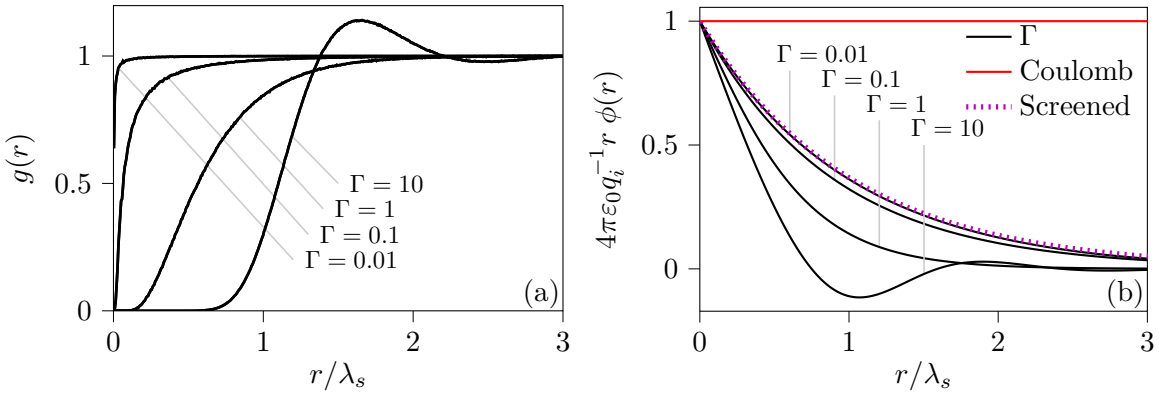

Figure 1.2: (a) The relative density of particles at a distance r from another particle at different coupling constants in a system with a single charge species. This measure of particle correlations is commonly referred to as the radial distribution function $g(r)$, see Section 2.3.2. At large coupling, features in $g(r)$ show strong inter-particle correlations. (b) Average electrostatic potential centred at an ion. The potential has been normalised with the contribution of an isolated charge to highlight screening. The traditional screening model $\exp(-r/\lambda_s)$ (screened) is also shown.

and depend on the *Coulomb logarithm* $\ln \Lambda_{ii}$ which represents the cumulative effect of many small deflections [82, 83]. However, as the coupling increases, collisions are not independent [64] and the concept of a Coulomb logarithm breaks down. Many authors have attempted to generalise the concept of the Coulomb logarithm by interpreting corrections to the classical results of, for example, electrical conductivity [84, 85], thermal conductivity [85] and temperature relaxation [80, 86] from strong coupling and quantum theories in terms of a modified $\ln \Lambda_{ii}$. Although the generalised Coulomb logarithm now depends on the specific property investigated [78, 85, 87].

Until now, only equal-sign charges with a repulsive interaction have been considered. However, in most naturally occurring systems both ions and electrons are present with an attractive interaction. The above discussion generally applies to both classical electrons and ions, with some modification to the screening length and characteristic density perturbations due to the large ion-electron mass ratio, as discussed further in Section 1.2.3. If q_i is the ion charge and q_e is the electron charge, the electron-ion interaction is characterised by the

coupling constant [88]

$$\Gamma_{ei}(r) = \frac{|q_i q_e|}{4\pi\varepsilon_0 k_\mathrm{B} T}\frac{1}{r} = \frac{\Gamma_{ii}}{Z}\frac{a_i}{r}, \tag{1.12}$$

where $Z = |q_i/q_e|$. Note the dependence on the typical distance r, as the attractive interaction can result in small separations between opposite signed charges and not necessarily characteristic separations of $r \approx a_e$. Non-linear interactions therefore enter at short distances, where the quantum uncertainty principle becomes important [89]. The introduction of quantum effects will alter the typical kinetic energies and will revise the coupling constant in equation (1.12).

1.2.2 Quantum plasmas

For dense plasmas, quantum effects enter in two main ways, (i) via the uncertainty principle that results in quantum diffraction and (ii) the symmetry effects of indistinguishable particles [89]. At the conditions investigated in this thesis, electrons typically need to be treated as fermions, but the heavier mass of the ions means that they tend to behave like classical particles.

The uncertainty principle requires the charge to be distributed in space, which prevents the singularity in equation (1.12) and avoids the *Coulomb collapse* which makes the classical model unstable. In semi-classical descriptions, the charge is smeared over the thermal de Broglie wavelength

$$\Lambda_{th} = \sqrt{\frac{2\pi\hbar^2}{m_e k_\mathrm{B} T}}, \tag{1.13}$$

an effect incorporated into the short-range interactions [89–94] or more formally a two-body scattering problem is solved to the same effect [95–98]. This type of potential is commonly referred to as a *quantum statistical potential* or QSP. The diffraction is intrinsically connected to the kinetic energy, as the curvature in the density distribution is associated with a shape-kinetic energy [99]. This is most clearly seen in Bohm's formulation of quantum mechanics [100] or *quantum hydrodynamics* [13, 101–103], where this additional kinetic energy enters as a separate potential.

Furthermore, the Pauli principle prevents two electrons from being in the same state and requires the wave function to be anti-symmetric under particle exchange [104]. These types of

considerations will be referred to as exchange, symmetry or Pauli effects/interactions. The symmetry requires an ideal Fermi gas in thermal equilibrium to populate states with energy ε according to the Fermi-Dirac distribution [10, 104]

$$f_{\mathrm{FD}}(\varepsilon) = \frac{1}{1 + e^{\beta(\varepsilon - \mu)}}, \tag{1.14}$$

but the distribution can be modified by interactions [105, 106]. In the above, $\beta^{-1} = k_{\mathrm{B}}T$ and μ is the chemical potential that is set to acquire the correct density [104]. As $T \to 0$ for free electrons, $\mu \to E_{\mathrm{F}}$ and yields a non-vanishing lower limit of the kinetic energy, in contrast to classical mechanics. For finite temperature, μ decreases and eventually becomes negative in the classical regime.

Three parameters are commonly used to characterise quantum effects. First, the ratio between the thermal energy and the Fermi energy [13, 65, 66],

$$\theta = \frac{k_{\mathrm{B}}T}{E_{\mathrm{F}}}, \tag{1.15}$$

where $\theta \gg 1$ and $\theta \ll 1$ represent the classical and quantum regimes, respectively. Second, the number of particles inside a cube with side length Λ_{th}, $\chi = n_e\Lambda_{th}^3$ [13, 65, 66]. However, χ is related to θ by $\chi = 8\theta^{-3/2}/(3\sqrt{\pi}) \approx 1.5\,\theta^{-3/2}$. Lastly, $\beta\mu$, the sign of which has a direct interpretation in terms of the distribution function. The crossing point $\beta\mu = 0$ occurs at $\theta \approx 0.989$ for an ideal system and therefore all three measures are effectively equivalent. In Figure 1.3, the regions are shown in phase space for fully ionised hydrogen, along with Γ_{ii}. A particularly challenging region to model due to both strong interactions and quantum effects is the region in parameter space where θ and Γ_{ii} are order unity, called *warm dense matter* (WDM).

Incorporating the modified kinetic energy from the Fermi-Dirac distribution into the

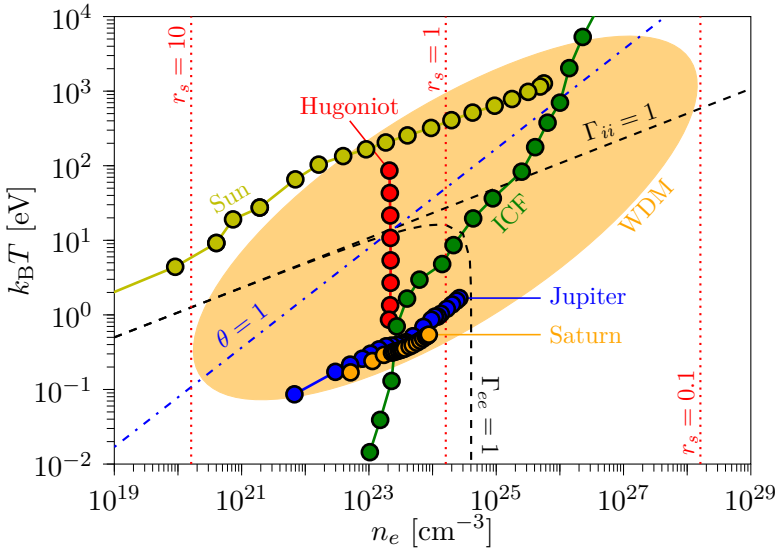

Figure 1.3: The warm dense matter region is shown alongside the coupling parameters. The extent of the WDM region is roughly taken from Dornheim *et al.* [15]. Astrophysical and laboratory conditions as defined in Figure 1.1.

definition of the coupling constants yields [66]

$$\Gamma_{ee} = \frac{q_e^2}{4\pi\varepsilon_0 a_e k_\mathrm{B} T} \left(\frac{F_{3/2}(\beta\mu)}{F_{1/2}(\beta\mu)} \right)^{-1} \longrightarrow \frac{q_e^2}{4\pi\varepsilon_0 a_e} \begin{cases} (k_\mathrm{B}T)^{-1} & \text{if } \theta \gg 1 \\ \frac{5}{2} E_\mathrm{F}^{-1} & \text{if } \theta \ll 1, \end{cases} \tag{1.16}$$

where $F_\nu(x)$ is the (complete) Fermi-Dirac integral [104]. Likewise, electron-ion coupling may be defined as $\Gamma_{ei}(r) = Z\Gamma_{ee} a_e / r$. In the low-temperature limit equation (1.16) yields $\Gamma_{ee} = 5(4\pi^{-1}/9)^{2/3}\, r_s \approx 1.4\, r_s$ where $r_s = a_e / a_\mathrm{B}$ is the *Brueckner coupling parameter*. Note that in the classical regime the coupling constant increases with density and decreases with temperature $\Gamma_{ee} \propto n_e^{1/3} T^{-1}$, yet for degenerate systems the coupling is independent of temperature and rather decreases with density $\Gamma_{ee} \propto n_e^{-1/3}$. Despite increasing interactions at higher densities, the kinetic energy of the degenerate Fermi-Dirac distribution grows more rapidly. This is only true when $\theta \ll 1$, which requires lower temperatures as r_s increases, but means that Γ_{ee} never grows too large in the WDM regime, see Figure 1.3.

The inclusion of Fermi-Dirac statistics also modifies the electron screening length λ_e

according to [104, 107]

$$\lambda_e^{-2} = \frac{q_e^2 n}{\varepsilon_0 k_\mathrm{B} T} \frac{F_{-1/2}(\beta\mu)}{F_{1/2}\ (\beta\mu)}, \tag{1.17}$$

which interpolates between Debye and Thomas-Fermi screening in their respective limit.

1.2.3 Separation of dynamical time scales

Although not strictly a coupling constant, the small electron-to-ion mass ratio has fundamental consequences for the systems under investigation. Even for the lightest ion – a single proton – the mass ratio is

$$\frac{m_p}{m_e} \approx 1836.15. \tag{1.18}$$

This mass difference is the reason for the classical treatment of ions, as θ for protons is m_p/m_e times larger than for electrons.

The classical Coulomb coupling Γ_{ii} is a purely statistical property and therefore independent of mass. However, even on the classical level, the mass difference results in substantially different time scales for the electron and ion motion, and thus resolving both in explicit numerical simulations is a challenge. In many scenarios, the electron population more or less has time to find a quasi-equilibrium for a given ionic configuration, which is the basis for the *Born–Oppenheimer* (BO) approximation. In the BO approximation, the ions are treated as an external potential in which the electron problem is solved. However, these schemes do not fully account for the energy transfer between species, which is particularly central in thermalisation processes. The simplest model that employs this time-scale argument to model ion dynamics is the Yukawa one-component plasma model (see Section 2.4.3), where ion-ion interactions are implicitly screened by electrons on the length scale of λ_e. A second approximation originating from the mass difference is the *Chihara decomposition* [108, 109] for the interpretation of scattering data, which will be discussed extensively in Chapter 4.

The different time scales for the electron and ion motion influence the dominant density perturbations and waves in each species. On the characteristic time scale of electron motion, the ions do not have time to respond and to first approximation are considered to be a

rigid background. This is akin to the traditional derivation of the plasma frequency [68], and the electron oscillations indeed have this behaviour for long wavelengths. On ion-time scales, electrons have time to screen the ions, resulting in an exponentially suppressed effective interaction between ions. On large length scales compared to the screening length, the ions therefore behave more like neutral particles and primarily show acoustic modes [110]. An analogous situation occurs for screening, where for electron time scale phenomena λ_e is the relevant screening length, but for ion time scale phenomena a combined screening length is formed $\lambda_{\text{eff}}^{-2} = \lambda_e^{-2} + \lambda_{s,i}^{-2}$ [87], as both species take part in the screening behaviour.

1.2.4 Relativistic corrections

The basic relativistic parameter for electrons is the ratio between the temperature and the rest-mass energy,

$$\varepsilon = \frac{k_{\text{B}}T}{m_e c^2}, \tag{1.19}$$

where c is the speed of light. If $\varepsilon \approx 0.01$, average velocities are approximately $0.1\,c$, and substantive corrections to the dynamics are expected. For relativistic conditions, the inertia of the particles becomes velocity dependent $m_e \to \gamma(\boldsymbol{v})m_e$ where $\gamma(\boldsymbol{v}) = \left(1 - \boldsymbol{v}^2/c^2\right)^{-1/2}$ is the *Lorentz factor*, an effect that has been shown to change the plasma transport properties [111]. Furthermore, interactions are also altered due to the finite speed of light, where magnetic and retardation effects become substantial [112].

Electrons can simultaneously be relativistic and degenerate, crucial for the structure of red giants and white dwarf stars [32]. The interplay between these effects can be characterised by [32, 113]

$$x = \frac{p_{\text{F}}}{m_e c}, \tag{1.20}$$

where $p_{\text{F}} = \sqrt{2m_e E_F}$ is the (classical) Fermi momentum. The Pauli principle pushes electrons to higher momentum states, and for $x \gtrsim 0.1$ average velocities exceed $0.1\,c$ for all temperatures. The Fermi-Dirac distribution still describes the statistics of the ideal relativistic Fermi gas when the states are populated in (canonical) momentum space using relativistic energies [10, 32],

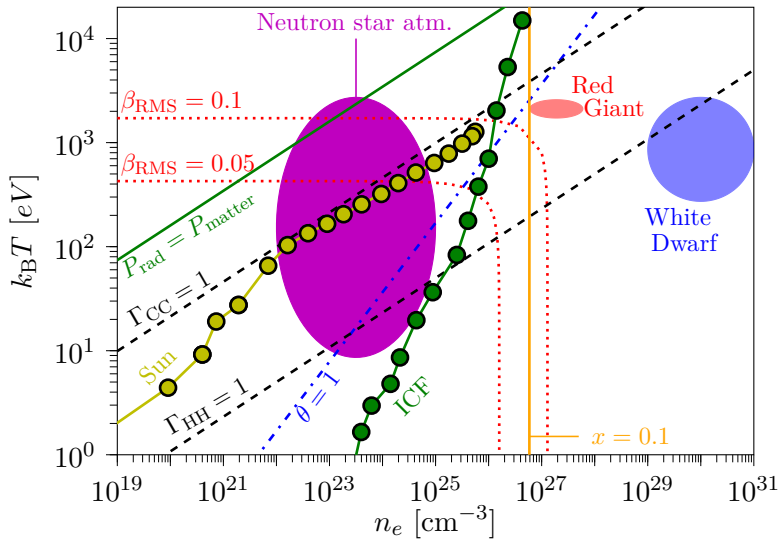

Figure 1.4: Phase space diagram for hydrogen illustrating regimes with relativistic corrections. Above and to the right of $\beta_{\rm RMS} = 0.05$ and $\beta_{\rm RMS} = 0.1$ moderate and substantive relativistic corrections are expected. At low temperatures, the relativistic corrections are characterised by $x = p_{\rm F}/(m_e c)$. The regime where radiation pressure dominates over matter pressure is shown above the $P_{\rm rad} = P_{\rm matter}$ line. The conditions for strongly coupled hydrogen $\Gamma_{\rm HH} = 1$ and carbon $\Gamma_{\rm CC} = 1$ plasmas are shown. Astrophysical and laboratory references are given in Figure 1.1.

and statistical properties can be described in terms of relativistic Fermi-Dirac integrals [113]. One form of *generalised Fermi-Dirac integrals* is

$$\tilde{F}_{i,j,k}(\eta,\varepsilon) = \frac{1}{\Gamma(1+i)} \int_0^\infty dt\, \frac{t^i (1+\varepsilon t)^j (1+\varepsilon t/2)^k}{1+\exp(t-\eta)}, \tag{1.21}$$

where $\Gamma(z)$ is the gamma-function. The average square velocity is $\langle \boldsymbol{v}^2/c^2 \rangle = 3\varepsilon \tilde{F}_{3/2,-1,3/2}(\beta\mu,\varepsilon) / \tilde{F}_{1/2,1,1/2}(\beta\mu,\varepsilon)$ and is shown in Figure 1.4 where multiple astrophysical objects are demonstrated to be relativistic in both the non-degenerate and degenerate regimes. The chemical potential μ is set by the density using $\Lambda_{th}^3 n_e/2 = \tilde{F}_{1/2,1,1/2}(\beta\mu,\varepsilon)$.

In the regime of relativistic electrons, the electron-electron coupling Γ_{ee} is typically not large, see Figure 1.3. However, ion coupling can be substantial for hydrogen and for slightly higher Z elements, such as carbon and oxygen, which are commonly found in the cores of late-stage stars [32]. The strong coupling regimes for pure hydrogen and carbon plasmas are marked in Figure 1.4.

At high temperatures, the radiation pressure in equation (1.3) dominates the pressure in *optically thick* plasmas [3]. In Figure 1.4 the point where the material pressure and the radiation pressure are equal is shown, above which the radiation will alter plasma properties such as the ion-acoustic speed [3, 114]. In particular, at ignition temperatures in ICF applications, radiative effects are instrumental in the description of the plasma [115]. If radiative effects or relativistic corrections become substantive first depends on density. At low density, plasmas become *optically thin*, such that for pressures below 1 Mbar the radiation might not establish an equilibrium with the matter before leaving the system, effectively reducing the radiation pressure and an ideal plasma behaviour is obtained [3].

1.3 Non-ideal plasmas in the laboratory

High energy density states are now routinely created in the laboratory using methods ranging from static compression, dynamic compression, and isochoric heating, all with different characteristics and capabilities of reaching complementary parts of the phase space. In the following, a summary of their characteristics will be given, but for a more complete account, see Falk [116].

Static compression achieves high pressures at relatively low temperatures by confining the sample between two surfaces. A *diamond anvil cell* (DAC) [117] can reach a few Mbar of pressure [116]. In combination with heating the sample [118, 119] both structural [120] and transport properties [119] have been measured under planetary conditions.

Dynamic compression on the other hand can reach higher pressure states, although these states are only short-lived. Historically, compression was achieved using gas guns [121] or explosives [122], however, since the advent of high-power laser facilities, lasers are commonly used to drive compression [116]. If a single shock wave is used to compress the material, a well-defined set of pressure states can be reached – the *principle Hugoniot* – given by the Rankine-Hugoniot relation and the initial conditions of the sample [123]. This type of shock compression is commonly used for EOS measurements [124, 125], reaching conditions relevant to astrophysics [126]. However, as seen in Figure 1.1 the *Hugoniot curve* is steep, reaching

hotter and less dense states, compared to many astrophysical objects. *Ramp compression* shapes the drive to avoid the creation of a shock, which limits entropy production and reaches lower temperature states [116], more similar to those in the interiors of gas giants [127, 128].

High-pressure states outside the principle Hugoniot can be explored by varying the initial conditions using DACs [129, 130], multiple shocks or ramp compression [127]. However, isochoric heating of thin samples – either by x-rays or particles – provides an additional method to reach a complementary part of the phase space with a well-constrained density [131]. X-rays for heating can be provided by conversion of laser light [132–134] or using a *free electron laser* (FEL) [135–138]. Particularly in the latter case, a single x-ray pulse is commonly used to create the plasma and perform the measurement. Thus, there is no time for hydrodynamic expansion and the result is an out-of-equilibrium electron-ion system. High-energy protons [139, 140], ions [131] and electrons [141] can also be used to heat the sample isochorically.

1.4 Open questions in high-energy density physics

High energy density science has applications for both astrophysical and energy applications, and can now be investigated in the laboratory. However, a variety of open questions remain. A selection of open problems related to the content of Chapters 3 – 6 is given below.

The modelling of the interior structure of gas giants is an active field of research, where the density and pressure profiles of the planets are constructed based on a hydrostatic equilibrium, balancing gravitational forces and pressure. However, an EOS is needed that introduces a dependence on the temperature profile, which in turn depends on the transport models [27]. Jupiter and Saturn have a special place within the planetary modelling community, as the space probes *Juno* [142] and *Cassini* [143] have visited them and provided additional constraints for the models. The detailed structure of Jupiter's gravitational field has been used to constrain its interior structure [23, 144, 145]. The low fraction of helium in Saturn's atmosphere [143] could be explained by the presence of "helium rain" [146]. However, the condition at which hydrogen and helium demixes is still discussed [17].

The uncertainties in the EOS [59] and transport coefficients [60, 61] for WDM also affect

the predictive capabilities of ICF modelling [63, 147, 148]. Furthermore, the influence of electron-ion collisions and non-adiabatic electron descriptions on transport properties is still being investigated [149–152]. To model burning ICF capsules, it is crucial to understand the heating by α-particles or stopping power in dense plasmas. Stopping power calculations are challenging as they combine non-equilibrium dynamics for both electrons and ions [87], and a variety of different techniques have been used to investigate the problem highlighting various aspects [103, 153, 154].

Many methods for modelling non-ideal plasmas rely on the Born-Oppenheimer approximation (e.g., DFT-MD) or assume a thermal ensemble (e.g., Monte Carlo methods), which is best suited for modelling equilibrium systems. However, many experimental realisations are often out-of-equilibrium, where energy is either deposited into the electrons (e.g., using short-pulse lasers [155]) or ions (e.g., via nuclear reactions [156] or shock waves [86, 157]). The so-called *correlation heating* [158] is an example of the intricate dynamics that can occur in moderately coupled plasmas when the electrons are heated and the ion screening is suddenly changed, which can result in a substantial increase in the temperature of the ions. As electrons and ions equilibrate between themselves, the *temperature relaxation time* between the species is enhanced by the mass ratio, and a temperature difference between the species can persist for a comparatively long time. Neither classical Landau-Spitzer relaxation [159] nor its generalisation to degenerate systems by Brysk [160] can satisfactorily describe the relaxation time seen in WDM experiments [140, 161–163], something which has invited the development of a large number of theoretical models, see, e.g., Refs. [80, 86, 87, 164, 165], and numerous numerical experiments [90, 94, 166, 167]. However, an overall accepted description remains elusive as a full description requires *non-adiabatic* electron dynamics over ionic time scales.

X-ray Thomson scattering is a commonly used diagnostic tool in WDM experiments, due to the ability of x-rays to penetrate dense plasmas [168]. Non-equilibrium contributions both from the particle distribution [169] as well as from spatial and temporal gradients [170, 171] will complicate the measurement interpretations. However, even in equilibrium, the scattering has contributions from both electronic and ionic time scales [108, 109], and the mass ratio

makes it demanding to model both within a single formulation. First principle computations still provide new formulations of the different contributions [172–174]. Uncertainties arise as different models are used to model the separate contributions [172], and there is still a need for models that treat electrons and ions on an "equal footing".

1.5 Structure of thesis and author contribution

The content of this thesis is based on derivations, implementations, and analysis that have been the sole work of the author, except where otherwise listed below. Some of the content has previously been published elsewhere as described in "List of Publications". The remainder of the thesis is structured as follows.

Chapter 2 discusses different modelling techniques for non-ideal plasmas focusing on atomistic modelling primarily using molecular dynamics and Monte Carlo methods. The different kinds of models and representations will be discussed. Next in Chapter 3, a derivation and implementation of an extension to the wave packet description for two-component plasmas is presented, appropriate for modelling systems with strong ion coupling and moderately degenerate electrons, utilising a pair-wise approximation for the exchange contribution. The `SOFT` computations in this chapter were provided by Ningyi Lyu. This chapter formed the basis of Paper (A) and the wave packet section of the review paper (B).

The model in Chapter 3 is employed in Chapters 4 and 5, where different aspects of the electron dynamic structure factor are investigated. Chapter 4 highlights both electron and ion features in x-ray scattering, considering a wide range of wavelengths. Special attention will be given to how quantum effects correct the high-frequency electron dynamics. The *path integral Monte Carlo* calculations (Section 4.3.3) and the *density functional theory molecular dynamics* (Section 4.3.4) in this chapter were carried out by Dr. Tobias Dornheim and Dr. Sam Azadi, respectively. Dr. Yusuf Aziz ran the impulse computations in Figure 4.7 and Appendix B.4, based on scripts provided by the author. Paper (C) is largely based on this chapter. Chapter 5 focuses purely on the long wavelength description, where a hydrodynamic model is developed and matched to the molecular dynamics data, allowing the extraction of electron transport

properties using *Bayesian inference* methods. The results were previously described in Paper (D).

Chapter 6 discusses an MD description of relativistic charged particles within a classical formulation. The effect of relativistic kinematics on mass diffusion is investigated for plasmas and Paper (E) which performed a similar investigation for neutral particles is the precursor for the initial part of Chapter 6. Furthermore, relativistic corrections to the interaction are discussed in terms of explicitly time-evolving the long-range electromagnetic fields. However, the highly fluctuating fields on small-length scales are treated at different levels with "field-less" approximations. An implementation of the model is presented that is used to study the thermalisation process of the electromagnetic fields and the microscopic structure of strongly coupled and relativistic plasmas.

Finally, a summary is given in Chapter 7 with an outlook on further development and use cases of the MD models developed in Chapters 3 and 6.

Chapter 2
Modelling of Non-ideal Plasmas

Abstract: The atomistic modelling of non-ideal plasmas is discussed, with a focus on molecular dynamics models. Typical observables and some technical aspects of molecular dynamics are highlighted before a summary of commonly used atomistic WDM models is provided.

2.1 Atomistic modelling of non-ideal plasmas

Atomistic modelling takes a first-principles microscopic view of a system, where the motion of individual particles is resolved. This is in contrast to continuum modelling, where coarse-grained governing equations are used to describe a system, examples of which are kinetic equations in classical plasma physics and hydrodynamic equations in fluid descriptions. In the process of coarse-graining, information is inherently lost, but in many scenarios this is necessary to describe a system. A single mole of atoms represented using double precision floating point numbers would require ~ 30000 Zettabytes of storage, which is on the order of a few hundred times the total digital storage in the world currently[1]. Nevertheless, first-principles modelling is needed to describe microscopic observables and benchmark continuum models on small scales.

When interactions are weak, approximate descriptions can be obtained by expanding around the case of no interactions, with interactions as additive perturbations [82, 83]. A prime example of this would be the classical Debye screening [68]. The first step to go beyond weak-coupling approximations is a self-consistent formulation, such as the *hypernetted chain* (HNC) approximation [175] or *Singwi-Tosi-Land-Sjölander* (STLS) approximation [176], but these models rely on approximate closures. In the opposite limit of strong coupling, matter commonly forms a lattice and the dynamics can be described as vibrations around lattice sites, essentially an expansion in $\Gamma_{ii}^{-1} \propto k_\mathrm{B}T$. An example would be the Debye-Waller factor in scattering theory [177].

[1]Estimates vary in the ballpark of a few tenths to hundred Zettabytes in 2024.

Table 2.1: Summary of common ensembles and the equivalent MD formulations. The set of fixed macroscopic quantities in each case is a subset of the number of particles N, volume V, total energy E, chemical potential μ, pressure p and temperature T. The probability is described by the energy of each microscopic realisation $\mathcal{H}$. The ensembles are given in Chapter 6 of Landau and Binder [178].

Ensemble	MD equivalent	Constant	Probability
Microcanonical	NVE	N, V, E	$P \propto \begin{cases} 1 & \text{if } \mathcal{H} = E \\ 0 & \text{else} \end{cases}$
Canonical	NVT	N, V, T	$P \propto e^{-\beta\mathcal{H}}$
Grand canonical		μ, V, T	$P \propto e^{-\beta(\mathcal{H}-\mu N)}$
Isothermal–isobaric	NpT	N, p, T	$P \propto e^{-\beta(\mathcal{H}+pV)}$

At intermediate coupling, neither of the two approaches described above is suitable, as the system behaves like a liquid, i.e., with correlations but freely moving. Two computational methods which can treat all levels of coupling are *Monte Carlo* (MC) and *Molecular dynamics* (MD) as they model interactions explicitly in many-body systems. Here, the focus will be on MD as this is the method employed in Chapters 3 – 6, but first a brief discussion of MC is given.

2.2 Monte Carlo

Monte Carlo methods are based on a statistical formulation where the thermal average $\langle f \rangle_T$ of a quantity f in an N particle system are evaluated as [10]

$$\langle f \rangle_T = \int \left(\prod_{i=1}^{N} d^3\boldsymbol{r}_i \, d^3\boldsymbol{p}_i \right) f(\boldsymbol{r}_1, \ldots, \boldsymbol{r}_N, \boldsymbol{p}_1, \ldots, \boldsymbol{p}_N) \times P(\boldsymbol{r}_1, \ldots, \boldsymbol{r}_N, \boldsymbol{p}_1, \ldots, \boldsymbol{p}_N), \qquad (2.1)$$

where $\boldsymbol{r}_i$ and $\boldsymbol{p}_i$ is the position and (canonical) momentum of particle i and $P(\cdots)$ is the probability of a given configuration. The probability can be evaluated in different statistical ensembles, where different macroscopic properties have been fixed. The main ensembles are summarised in Table 2.1, where the configurations are populated according to the total energy, the *Hamiltonian* $\mathcal{H}$.

The evaluation of equation (2.1) depends on the computation of a $6N$-dimensional integral.

The computational complexity of grid-based integration grows exponentially with N, as the number of function evaluations scales as

$$\mathcal{O}\left(\left(\frac{L}{\Delta x}\right)^{3N}\left(\frac{V}{\Delta v}\right)^{3N}\right), \tag{2.2}$$

where L (V) is the extent spatially (in velocity space) and Δx (Δv) the corresponding required resolution. Instead Monte Carlo integration considers equation (2.1) as an average and estimates the result as

$$\langle f \rangle \approx \frac{1}{M}\sum_{n=1}^{M} f(\boldsymbol{r}_1^n, \ldots, \boldsymbol{r}_N^n, \boldsymbol{p}_1^n, \ldots, \boldsymbol{p}_N^n), \tag{2.3}$$

typically a much more efficient way of evaluating high dimensional integrals if samples $(\boldsymbol{r}_i^n, \boldsymbol{p}_i^n)$ of $P(\cdots)$ can be generated [179].

This strategy requires "drawing" samples from $P(\cdots)$, for which a variant of the *Metropolis-Hastings algorithm* [180, 181] is commonly employed. The algorithms are based on modifying the state of the system – commonly a local move that changes the properties of a single particle [178] – and the move is accepted or rejected based on the change in energy. Multiple variants of this algorithm now exist, such as the affine-invariant sampler by Goodman and Weare [182] used in Chapter 5.

2.3 Molecular dynamics

Molecular dynamics is widely used in many fields of research, such as fluid theory [175], material physics [183] and biochemistry [184]. In its simplest form, MD solves Newton's equations of motion [185],

$$\frac{d\boldsymbol{r}_i}{dt} = \frac{\boldsymbol{p}_i}{m_i} \tag{2.4a}$$

$$\frac{d\boldsymbol{p}_i}{dt} = -\frac{\partial}{\partial \boldsymbol{r}_i}\mathcal{V}(\boldsymbol{r}_1, \ldots, \boldsymbol{r}_N), \tag{2.4b}$$

for a large number of particles $i = 1, \ldots, N$ with positions $\boldsymbol{r}_i$, momentums $\boldsymbol{p}_i$, and masses m_i. The motions of the particles are coupled via the potential energy $\mathcal{V}(\cdots)$ and it follows from equation (2.4) that the total energy of the system

$$E = \sum_{i=1}^{N} \frac{\boldsymbol{p}_i^2}{2m_i} + \mathcal{V}(\boldsymbol{r}_1, \ldots, \boldsymbol{r}_N) \tag{2.5}$$

is conserved. MD is commonly labelled by the conserved quantities during time evolution. Therefore, the time evolution described by equation (2.4) for a fixed number of particles N in a fixed volume V is referred to as NVE.

According to the *ergodic hypothesis* – first introduced by Boltzmann in 1898 [186] – the trajectories will, over long times, occupy all allowed states with equal probability, forming an equivalence between the time average in NVE and the microcanonical ensemble in Table 2.1 [10, 187]. Ensembles where conjugate macroscopic properties are instead fixed are modelled with MD using modified equations of motion, see Section 2.3.7. Ergodicity is distinctly a property of many-body systems and may be violated in systems with too few bodies [10]. In some cases, even many-body systems can exhibit non-ergodicity, e.g., *path integral molecular dynamics* (PIMD) [188] where the ergodic behaviour often must be imposed [189].

In many applications, the interaction is pairwise and symmetric between particles, $\mathcal{V} = \sum_{i<j} u(|\boldsymbol{r}_i - \boldsymbol{r}_j|)$, where $u(r)$ is the pair potential. In simulations with periodic boundary conditions, the system therefore also conserves the total momentum[2] $\boldsymbol{M} = \sum_i \boldsymbol{p}_i$ and a Galilean boosts invariance $\boldsymbol{G}$, and the MD is technically in some $NVE\boldsymbol{M}$ or $NVE\boldsymbol{MG}$ ensemble [190]. Each constraint fixes one degree of freedom and the difference in intensive properties between NVE and the MD ensembles is $\mathcal{O}\left(N^{-1}\right)$, negligible for large enough systems [190, 191].

2.3.1 Lagrangian and Hamiltonian mechanics

The molecular dynamics method is generally applicable to any system with a *Lagrangian* $\mathcal{L}$ or action integral

$$\mathcal{S} = \int_{-\infty}^{\infty} dt\, \mathcal{L}(\boldsymbol{q}, \dot{\boldsymbol{q}}, t), \tag{2.6}$$

[2]The total angular momentum is not conserved in a periodic simulation [190].

described in terms of generalised coordinates $\boldsymbol{q}$ and associated velocities $\dot{\boldsymbol{q}}$. *Hamilton's principle of stationary action*, $\delta\mathcal{S} = 0$, yields the Euler-Lagrange equations [185]:

$$\frac{d}{dt}\frac{\partial\mathcal{L}}{\partial\dot{\boldsymbol{q}}} - \frac{\partial\mathcal{L}}{\partial\boldsymbol{q}} = 0. \tag{2.7}$$

This type of generalised description allows the incorporation of constraints [185], quantum dynamics [192] and particle-field dynamics [193, 194] in MD. The latter two examples will be explored in Chapters 3 and 6, respectively.

The equivalent Hamiltonian formulation can be obtained based on the *canonical momentum* $\boldsymbol{p} = \partial\mathcal{L}/\partial\dot{\boldsymbol{q}}$ and the *Hamiltonian* $\mathcal{H}(\boldsymbol{q},\boldsymbol{p}) = \boldsymbol{p}\cdot\dot{\boldsymbol{q}} - \mathcal{L}$. The equations of motion are [187]

$$\frac{d\boldsymbol{q}}{dt} = \frac{\partial\mathcal{H}}{\partial\boldsymbol{p}} \tag{2.8a}$$

$$\frac{d\boldsymbol{p}}{dt} = -\frac{\partial\mathcal{H}}{\partial\boldsymbol{q}} \tag{2.8b}$$

and have a *symplectic* structure. Under a symplectic flow, phase-space volumes are preserved and respecting such properties when discretising the problem can markedly improve numerical performance [187], see the discussion in Section 2.3.4.

2.3.2 Observables: Static correlations

The primary output of an MD simulation is the particle trajectories, that is, the position $\boldsymbol{r}_i(t)$ and the momentum $\boldsymbol{p}_i(t)$ for all particles $i = 1,\ldots,N$ resolved over time t. Statistical properties such as the equation of state and (static) correlations between particles are now obtained by time averages.

The first measure of structure is the *pair correlation functions* $n^{\alpha\beta}(\boldsymbol{r},\boldsymbol{r}')$ between particles of species α and β. In terms of the local densities $n^{\alpha}(\boldsymbol{r})$ and $n^{\beta}(\boldsymbol{r}')$ of respective species, the pair correlation function is [175]

$$n^{\alpha\beta}(\boldsymbol{r}',\boldsymbol{r}'') = \left\langle n^{\alpha}(\boldsymbol{r}')n^{\beta}(\boldsymbol{r}'')\right\rangle_{T}, \tag{2.9}$$

where $\langle\cdot\rangle_T$ is the thermal average as described in equation (2.1). For spherical and isotropic systems, the pair correlation function is commonly normalised by the mean density and averaged such that only the dependence on $r = |\boldsymbol{r}' - \boldsymbol{r}''|$ remains [175, 185],

$$\begin{aligned} g_{\alpha\beta}(r) &= \frac{1}{N_\alpha n_\beta} \int n^{\alpha\beta}(\boldsymbol{r}', \boldsymbol{r} + \boldsymbol{r}') d^3\boldsymbol{r}' - \frac{\delta_{\alpha\beta}}{\sqrt{n_\alpha n_\beta}} \delta^{(3)}(\boldsymbol{r}) \\ &= \frac{1}{N_\alpha n_\beta} \left\langle \sum_{i,j} \delta^3(\boldsymbol{r} - \boldsymbol{r}_{ij}) \right\rangle_T - \frac{\delta_{\alpha\beta}}{\sqrt{n_\alpha n_\beta}} \delta^{(3)}(\boldsymbol{r}), \end{aligned} \tag{2.10}$$

where $\boldsymbol{r}_{ij}$ is the separation between particle i and j, and the index i (j) runs over all N_α (N_β) particles of type α (β). This is the *radial distribution function* (RDF), an example of which is shown in Figure 1.2(a). The RDF measures the density of particles of type β at a distance r from a particle of type α, normalised such that $g_{\alpha\beta}(r) = 1$ is the uncorrelated state. As $r \to \infty$ correlations decay in systems without long-range order and $g_{\alpha\beta}(r) \to 1$. In a system with repulsive interactions, regions with $g_{\alpha\beta}(r) < 1$ are seen due to the energetic penalty of close approaches. However, in systems with stronger coupling, interactions can produce both under and over-dense regions, as exemplified for $\Gamma_{ii} = 10$ in Figure 1.2(a).

The corresponding quantity to $g_{\alpha\beta}(r)$ in Fourier space is the *static structure factor*, $S_{\alpha\beta}(\boldsymbol{k})$, which based on the Fourier transformed densities,

$$n^\alpha_{\boldsymbol{k}} = \int d^3\boldsymbol{r}\; n^\alpha(\boldsymbol{r}) e^{-i\boldsymbol{k}\cdot\boldsymbol{r}}, \tag{2.11}$$

is defined as [64, 185, 195]

$$\begin{aligned} S_{\alpha\beta}(\boldsymbol{k}) &= \frac{1}{\sqrt{N_\alpha N_\beta}} \left\langle n^\alpha_{\boldsymbol{k}} n^\beta_{-\boldsymbol{k}} \right\rangle_T - \sqrt{N_\alpha N_\beta}\delta_{\boldsymbol{k},0} \\ &= \delta_{\alpha\beta} + \sqrt{n_\alpha n_\beta} \int d^3\boldsymbol{r}\; \left[g_{\alpha\beta}(\boldsymbol{r}) - 1\right] e^{-i\boldsymbol{k}\cdot\boldsymbol{r}}. \end{aligned} \tag{2.12}$$

In the small $\boldsymbol{k}$ limit, $S_{\alpha\beta}(\boldsymbol{k})$ describes the macroscopic properties of the system [64, 175], while $\boldsymbol{k} \to \infty$ describes the single particle behaviour and $S_{\alpha\beta}(\boldsymbol{k}) \to \delta_{\alpha\beta}$. The corresponding $S_{\alpha\beta}(\boldsymbol{k})$ for the RDFs in Figure 1.2 are shown in Figure 2.1.

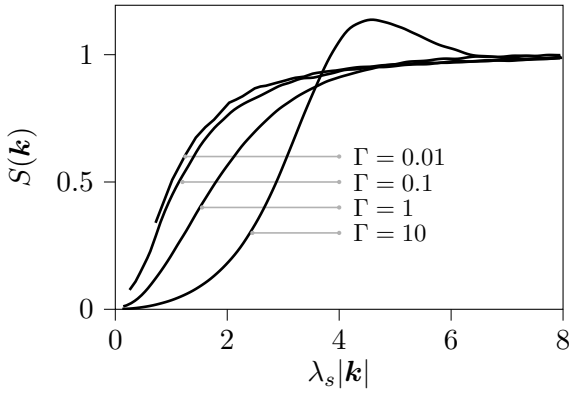

Figure 2.1: The static structure factor shows the correlations in Fourier space, corresponding to the data in Figure 1.2(a) for a system with only one type of charge species.

2.3.3 Observables: Dynamic correlations

Molecular dynamics simulations, in contrast to statistical methods, evolve the systems with a concept of physical time. Whereas the static correlations relate to the equation of state, the dynamic correlations relate to transport properties. An analogous type of structure will also appear between total and inelastic Thomson scattering, which is discussed in Chapter 4.

Transport properties describe the transport of mass, momentum, energy, charge, etc., in the presence of gradients and appear as closures in fluid theories [68, 196, 197]. Non-equilibrium scenarios with gradients can be set up in MD and full non-linear transport can be measured, for example, see Donkó and Hartmann for thermal conductivity [198] and shear viscosity [199]. However, initialisation and finite size effects must be considered. To linear order, transport can be measured from equilibrium simulations. As an initial example, consider mass diffusion described by Fick's law

$$\frac{\partial \rho}{\partial t} = \boldsymbol{\nabla} \cdot (D \boldsymbol{\nabla} \rho) \,, \tag{2.13}$$

where ρ is the density and D is the diffusion coefficient. The solution of equation (2.13) shows that the characteristic width of the density fluctuation spreads as $\sqrt{2tD}$ in each dimension. The diffusion coefficient, in terms of particle positions $\boldsymbol{r}_i(t)$ and velocities $\boldsymbol{v}_i(t)$, is therefore [200]:

$$D = \lim_{t\to\infty} \frac{\left\langle |\boldsymbol{r}_i(t) - \boldsymbol{r}_i(0)|^2 \right\rangle_T}{6t} = \frac{1}{3} \int_0^\infty dt \ \left\langle \boldsymbol{v}_i(t) \cdot \boldsymbol{v}_i(0) \right\rangle_T \,, \tag{2.14}$$

where vanishing velocity correlation at large time separations was assumed. The integrand in equation (2.14) is the *velocity autocorrelation function* (VACF) and shows how time correlations in microscopic variables can be related to a macroscopic transport property. This type of integral relation is a type of Green-Kubo relation and may be adapted for different transport properties depending on the underlying hydrodynamic model.

Generally, dynamic density correlation can be investigated with the *intermediate scattering function*

$$F_{\alpha\beta}(\boldsymbol{k},t) = \frac{1}{\sqrt{N_\alpha N_\beta}} \left\langle n^\alpha_{\boldsymbol{k}}(t) n^\beta_{-\boldsymbol{k}}(0) \right\rangle_T , \tag{2.15}$$

which correlates the spatially Fourier-transformed densities separated by a time t. However, commonly the correlations are studied in frequency space, where the generalisation of $S_{\alpha\beta}(\boldsymbol{k})$ is the *dynamic structure factor* (DSF)

$$S_{\alpha\beta}(\boldsymbol{k},\omega) = \frac{1}{2\pi}\int_{-\infty}^{\infty} dt\; F_{\alpha\beta}(\boldsymbol{k},t) e^{i\omega t} = \frac{1}{2\pi}\int_{-\infty}^{\infty} dt\; \frac{\left\langle n^\alpha_{\boldsymbol{k}}(t) n^\beta_{-\boldsymbol{k}}(0) \right\rangle_T}{\sqrt{N_\alpha N_\beta}} e^{i\omega t}, \tag{2.16}$$

which for $\boldsymbol{k} \neq 0$ is related to its static counterpart by

$$S_{\alpha\beta}(\boldsymbol{k}) = F_{\alpha\beta}(\boldsymbol{k},0) = \int_{-\infty}^{\infty} d\omega\; S_{\alpha\beta}(\boldsymbol{k},\omega). \tag{2.17}$$

The dynamic structure factor describes a rich set of physics, including hydrodynamic transport ($\boldsymbol{k} \to 0$) and the single particle behaviour ($\boldsymbol{k} \to \infty$). First, the long wavelength limit of a classical fluid – here most applicable to the description of the ions – is obtained by linearising the fluid equations and yields [196, 201]:

$$\frac{S_{\alpha\alpha}(\boldsymbol{k},\omega)}{S_{\alpha\alpha}(\boldsymbol{k})} = \frac{1-A}{\pi}\frac{\chi\boldsymbol{k}^2}{\left(\chi\boldsymbol{k}^2\right)^2+\omega^2} + \frac{A}{2\pi}\frac{\gamma_{\boldsymbol{k}}}{\gamma_{\boldsymbol{k}}^2+\left(\omega-\omega_{\boldsymbol{k}}\right)^2} + \frac{A}{2\pi}\frac{\gamma_{\boldsymbol{k}}}{\gamma_{\boldsymbol{k}}^2+\left(\omega+\omega_{\boldsymbol{k}}\right)^2}. \tag{2.18}$$

The width of the mode at $\omega = 0$, the *entropy mode*, is set by the *thermal diffusivity* χ and is related to heat conduction. The *acoustic modes* are characterised by a linear dispersion relation, that is, $\omega_{\boldsymbol{k}} = c_s|\boldsymbol{k}|$, with modes propagating at the *adiabatic sound speed* c_s. The width of the acoustic modes, $\gamma_{\boldsymbol{k}}$, is set by the thermal diffusivity and the *viscosity* [196]. The

adiabatic index γ sets the ratio of features, given that $A = \gamma^{-1}$. The corresponding features in the time domain are given by an exponential decay, and the sound mode has an oscillating behaviour on top of this behaviour. Fitting the above functional form to MD data is a common method to extract ion transport properties [110, 202, 203], which is largely interchangeable with the Green-Kubo relations [204]. When considering electrons, $\omega_{\boldsymbol{k}}$ will instead approach the plasma frequency ω_p (see Section 1.2.1) for long wavelengths, but a more complete description of this limit for electron-ion plasmas will be given in Chapter 5 and Appendix C, where the effect of collisions and screening will be explicitly considered.

In the opposite limit, only the single particle properties will be present in the spectrum, such as the particle mass m_α and the temperature T. For classical dynamics, thermal motion results in Gaussian profiles both in time [201]

$$F_{\alpha\alpha}(\boldsymbol{k}, t) = e^{-\frac{k_\mathrm{B}T}{2m_\alpha}t^2} \tag{2.19a}$$

and frequency space [201]

$$S_{\alpha\alpha}(\boldsymbol{k}, \omega) = \sqrt{\frac{m_\alpha}{2\pi k_\mathrm{B} T \boldsymbol{k}^2}} e^{-\frac{m_\alpha}{2k_\mathrm{B}T\boldsymbol{k}^2}\omega^2}. \tag{2.19b}$$

For all systems and length scales, the structure factor must adhere to the sum rules, relating the nth moments of $S_{\alpha\beta}(\boldsymbol{k}, \omega)$, $\langle\omega^n\rangle_{S_{\alpha\beta}}$, to the short-time behaviour of $F_{\alpha\beta}(\boldsymbol{k}, t)$. The first three moments for a classical single component system are [201]:

$$\left\langle\omega^0\right\rangle_{S_{\alpha\alpha}} \equiv \int_{-\infty}^{\infty} d\omega \quad S_{\alpha\alpha}(\boldsymbol{k}, \omega) = F_{\alpha\alpha}(\boldsymbol{k}, 0) \qquad = S_{\alpha\alpha}(\boldsymbol{k}), \tag{2.20a}$$

$$\left\langle\omega^1\right\rangle_{S_{\alpha\alpha}} \equiv \int_{-\infty}^{\infty} d\omega\, \omega^1 S_{\alpha\alpha}(\boldsymbol{k}, \omega) = \frac{\partial F_{\alpha\alpha}(\boldsymbol{k}, t)}{\partial t}\Big|_{t=0} = 0, \tag{2.20b}$$

$$\left\langle\omega^2\right\rangle_{S_{\alpha\alpha}} \equiv \int_{-\infty}^{\infty} d\omega\, \omega^2 S_{\alpha\alpha}(\boldsymbol{k}, \omega) = \frac{\partial^2 F_{\alpha\alpha}(\boldsymbol{k}, t)}{\partial t^2}\Big|_{t=0} = \frac{k_\mathrm{B}T}{m_\alpha}\boldsymbol{k}^2. \tag{2.20c}$$

All odd moments vanish in classical theory, as $F_{\alpha\alpha}(\boldsymbol{k}, t)$ is even in time due to time translation invariance. Higher-order even moments depend on the interaction in the system.

A related property is the density response function $\chi_{\alpha\beta}$, which is defined via the density

response δn_α of species α at $(\boldsymbol{r}, t)$ from an external potential V_β^{ext} acting on species β, given by [195]

$$\delta n_\alpha(\boldsymbol{r}, t) = \sum_\beta \int_{-\infty}^{t} dt' \int d^3\boldsymbol{r}' \; \chi_{\alpha\beta}(\boldsymbol{r}, \boldsymbol{r}', t - t') V_\beta^{\text{ext}}(\boldsymbol{r}', t'). \tag{2.21}$$

The density response function is a central object for modelling interactions [88, 205], or the response to external stimulus, e.g., scattering of light. To linear order in V_β^{ext} the (classical) fluctuation-dissipation theorem relates $\chi_{\alpha\beta}$ to $S_{\alpha\beta}(\boldsymbol{k}, \omega)$ via [195]

$$S_{\alpha\beta}(\boldsymbol{k}, \omega) = -\frac{k_\text{B} T}{\pi\omega} \frac{\text{Im}\left\{\chi_{\alpha\beta}(\boldsymbol{k}, -\boldsymbol{k}, \omega)\right\}}{\sqrt{N_\alpha N_\beta}}, \tag{2.22}$$

where the Fourier transform has been performed as

$$\chi_{\alpha\beta}(\boldsymbol{k}, -\boldsymbol{k}, \omega) = \int dt \int d^3\boldsymbol{r} \, d^3\boldsymbol{r}' \; e^{i\omega t - i\boldsymbol{k}\cdot(\boldsymbol{r} - \boldsymbol{r}')} \chi_{\alpha\beta}(\boldsymbol{r}, \boldsymbol{r}', t). \tag{2.23}$$

Causality – the system cannot react before the external potential has acted – requires $\chi_{\alpha\beta}(\boldsymbol{r}, \boldsymbol{r}', t) = 0$ for $t < 0$. It follows that $\text{Im}\{\chi_{\alpha\beta}(\omega)\}$ and $\text{Re}\{\chi_{\alpha\beta}(\omega)\}$ are odd and even, respectively, and adhere to the Kramers-Kronig relations [206]:

$$\text{Re}\left\{\chi_{\alpha\beta}(\boldsymbol{k}, -\boldsymbol{k}, \omega)\right\} = \frac{1}{\pi} P \int_{-\infty}^{\infty} d\omega' \; \frac{\text{Im}\left\{\chi_{\alpha\beta}(\boldsymbol{k}, -\boldsymbol{k}, \omega')\right\}}{\omega' - \omega}, \tag{2.24a}$$

$$\text{Im}\left\{\chi_{\alpha\beta}(\boldsymbol{k}, -\boldsymbol{k}, \omega)\right\} = \frac{1}{\pi} P \int_{-\infty}^{\infty} d\omega' \; \frac{\text{Re}\left\{\chi_{\alpha\beta}(\boldsymbol{k}, -\boldsymbol{k}, \omega')\right\}}{\omega - \omega'}, \tag{2.24b}$$

where P represents the principle value integration. Thus, both the real and imaginary parts of $\chi_{\alpha\beta}(\boldsymbol{k}, -\boldsymbol{k}, \omega)$ can be recovered from $S_{\alpha\beta}(\boldsymbol{k}, \omega)$. Combining equations (2.22) and (2.24a) results in the classical relation

$$S_{\alpha\beta}(\boldsymbol{k}) = -\frac{k_\text{B} T}{\sqrt{N_\alpha N_\beta}} \chi_{\alpha\beta}(\boldsymbol{k}, -\boldsymbol{k}, \omega = 0), \tag{2.25}$$

where the static structure factor is directly related to the static response function.

Being a central object in many models, the density response is commonly parameterised in terms of *local field corrections* (LFCs), $G_{\alpha\beta}(\boldsymbol{k}, \omega)$, where the non-ideal response has been

isolated. Concretely, for a single component system, the LFC is defined as [207]

$$\chi_{\alpha\alpha} = \frac{\chi_\alpha^{(0)}(\boldsymbol{k},\omega)}{1 - \tilde{u}_{\alpha\alpha}(\boldsymbol{k})\left[1 - G_{\alpha\alpha}(\boldsymbol{k},\omega)\right]\chi_\alpha^{(0)}(\boldsymbol{k},\omega)}, \tag{2.26}$$

where $\chi_\alpha^{(0)}$ is the response function for species α in a non-interacting system. The limit of $G_{\alpha\beta}(\boldsymbol{k},\omega) = 0$ is the *random phase approximation* (RPA) that treats the mean field self-consistently but not higher-order interaction effects [206, 208]. For a two-component system, Ichimaru *et al.* [195] write the response functions as

$$\chi_{\alpha\alpha}(\boldsymbol{k},\omega) = \chi_\alpha^{(0)}(\boldsymbol{k},\omega)\left[1 - \tilde{u}_{\beta\beta}\chi_\beta^{(0)}(\boldsymbol{k},\omega)\left(1 - G_{\beta\beta}(\boldsymbol{k},\omega)\right)\right]/D(\boldsymbol{k},\omega), \tag{2.27a}$$

$$\chi_{\alpha\beta}(\boldsymbol{k},\omega) = \tilde{u}_{\alpha\beta}\chi_\alpha^{(0)}(\boldsymbol{k},\omega)\chi_\beta^{(0)}(\boldsymbol{k},\omega)\left(1 - G_{\alpha\beta}(\boldsymbol{k},\omega)\right)/D(\boldsymbol{k},\omega), \tag{2.27b}$$

where $\beta \neq \alpha$ and the denominator is

$$\begin{aligned} D(\boldsymbol{k},\omega) = &\left(1 - \tilde{u}_{\alpha\alpha}\left[1 - G_{\alpha\alpha}\right]\chi_\alpha^{(0)}\right)\left(1 - \tilde{u}_{\beta\beta}\left[1 - G_{\beta\beta}\right]\chi_\beta^{(0)}\right) \\ &- \tilde{u}_{\alpha\beta}^2\left[1 - G_{\alpha\beta}\right]\left[1 - G_{\beta\alpha}\right]\chi_\alpha^{(0)}\chi_\beta^{(0)}. \end{aligned} \tag{2.28}$$

The response of the system therefore involves both interactions within and between species, highlighted by the presence of $G_{\alpha\alpha}$ and $G_{\alpha\beta}$, respectively. Local field corrections have been isolated both from approximate theories [64, 176, 209–211] and many-body calculations [207], which can be used to evaluate the non-ideal response.

Within this section, all quantum effects have been neglected and the $\hbar \to 0$ limit has been carried out when appropriate. The discussion of the quantum generalisation has been delayed to Chapter 4.

2.3.4 Numerics: Time integration

To numerically evaluate the MD trajectories, equations (2.4), (2.7) or (2.8) must be discretised in time. The numerical integrators in MD tend to be some of the simplest there are, as the emphasis is on the conserved and average properties of the system and not the accuracy of a

single trajectory [185, 187]. The rapidly varying potential commonly employed in MD results in a high sensitivity to the initial conditions, and accurate trajectories after many collisions are unfeasible for any integrator [185]. Furthermore, in MD the initial condition is commonly unknown – only the initial statistical properties are given – and highly accurate trajectories lose their purpose.

One of the most prevalent integrators is the *Strømer-Verlet integrator* – although Delambre used it already in 1791 [212] – which performs the time stepping based on the positions of the two most recent time steps and has a global integration error of $\mathcal{O}\left(\Delta t^2\right)$, where Δt is the time discretisation [185]. The *velocity-Verlet integrator* instead operates on the most recent positions and velocities, by introducing a half-time step. If $\boldsymbol{r}_i^n$ and $\boldsymbol{p}_i^n$ are the position and momentum at time step n, the time stepping proceeds as [187]:

$$\boldsymbol{p}_i^{n+1/2} = \boldsymbol{p}_i^n - \frac{\Delta t}{2}\frac{\partial}{\partial \boldsymbol{r}_i}\mathcal{V}(\boldsymbol{r}_1, \ldots, \boldsymbol{r}_N)\Big|_{\boldsymbol{r}_i=\boldsymbol{r}_i^n}, \tag{2.29a}$$

$$\boldsymbol{r}_i^{n+1} = \boldsymbol{r}_i^n + \Delta t\frac{\boldsymbol{p}_i^{n+1/2}}{m_i}, \tag{2.29b}$$

$$\boldsymbol{p}_i^{n+1} = \boldsymbol{p}_i^{n+1/2} - \frac{\Delta t}{2}\frac{\partial}{\partial \boldsymbol{r}_i}\mathcal{V}(\boldsymbol{r}_1, \ldots, \boldsymbol{r}_N)\Big|_{\boldsymbol{r}_i=\boldsymbol{r}_i^{n+1}}. \tag{2.29c}$$

This is an example of a time-stepping algorithm for a *separable Hamiltonian* where the Hamiltonian can be written as a sum of two terms, each only depending on the positions and momenta, i.e., $\mathcal{H}(\boldsymbol{q}, \boldsymbol{p}) = \mathcal{T}(\boldsymbol{q}) + \mathcal{V}(\boldsymbol{p})$. For any separable Hamiltonian, a second-order correct time propagator can be constructed as [187]

$$\boldsymbol{\Phi}_{\Delta t,\mathcal{H}} = \boldsymbol{\Phi}_{\Delta t/2,\mathcal{V}} \circ \boldsymbol{\Phi}_{\Delta t,\mathcal{T}} \circ \boldsymbol{\Phi}_{\Delta t/2,\mathcal{V}} + \mathcal{O}\left(\Delta t^3\right), \tag{2.30}$$

where $\boldsymbol{\Phi}_{\Delta t,\mathcal{K}}$ propagates the system for a time Δt assuming the Hamiltonian $\mathcal{K}$. For a separable Hamiltonian, the component propagators in equation (2.30) can be evaluated exactly, and readily yields equation (2.29) for a classical system. If each of the maps in equation (2.30) is symplectic, the combined map is as well, and preserving this property has been seen to greatly improve energy conservation in simulations. This is because the discretised formulation now

Table 2.2: Example of a Butcher tableau which shows the coefficients used for a Runge-Kutta integrator. For explicit integrators, the tableau has a lower triangular structure.

c_1	a_{11}	a_{12}	$\dots$	a_{1s}
c_2	a_{21}	a_{22}	$\dots$	a_{2s}
$\vdots$	$\vdots$	$\vdots$	$\ddots$	$\vdots$
c_s	a_{s1}	a_{s2}	$\dots$	$a_{s,s}$
	b_1	b_2	$\dots$	b_s

solves a related Hamiltonian problem within an exponentially small error, and the difference between the Hamiltonians is $\mathcal{O}\left(\Delta t^2\right)$ [187]. The close connections between the Hamiltonians limit the energy drift.

In scenarios where the above construction methods cannot readily be applied, the general Runge-Kutta methods [213, 214] may be used. Runge-Kutta methods solve arbitrary systems of first-order *ordinary differential equations* (ODEs). Consider the ODE

$$\frac{\partial}{\partial t}\boldsymbol{y} = f(t, \boldsymbol{y}), \tag{2.31}$$

where $\boldsymbol{y}$ is a vector of all the model parameters and f is some function. The s stage Runge-Kutta integrator is then given by

$$\boldsymbol{y}(t + \Delta t) = \boldsymbol{y}(t) + \Delta t \sum_{i=1}^{s} b_i \boldsymbol{k}_i, \tag{2.32}$$

where

$$\boldsymbol{k}_i = f\left(t + c_i \Delta t,\ \boldsymbol{y}(t) + \Delta t \sum_{j=1}^{s} a_{ij} \boldsymbol{k}_j\right). \tag{2.33}$$

The coefficients a_{ij}, b_i and c_i are specific to the method used. Finding the appropriate coefficients is a separate task [215] and a variety of suggestions exist in the literature. The coefficients are commonly represented in a *Butcher tableau* [216] as shown in Table 2.2. Generally, equation (2.33) is an implicit equation for $\boldsymbol{k}_i$ and highly non-linear for a general f. However, if the Butcher tableau has a lower triangular structure, i.e. $a_{ij} = 0$ if $i \leq j$, the method is called explicit and equation (2.33) is readily evaluated.

Unfortunately, only implicit Runge-Kutta solvers can be symplectic [187] and therefore, in general, some iterative scheme is needed to solve equation (2.33) in each time step to retain

the desirable properties of symplectic integrators [187]. Tao proposed [217] a general explicit and symplectic integration scheme for non-separable Hamiltonians in an extended phase space. Otherwise, explicit symplectic integrators for non-separable Hamiltonians have only been found in some instances, e.g., for Vlasov system with static [187, 218] and dynamic [219] external fields.

2.3.5 Numerics: Short-range interactions

While the time-stepping algorithm is crucial for good long-time stability in MD, the majority of the computational time is spent evaluating energies and forces. This is why implicit integration schemes are punishing as multiple force evaluations are needed for each time step.

The naive *all pairs* algorithm for a system of N pair-interacting particles would require looping over all $N(N-1)/2$ pairs of particles when evaluating the interactions, which quickly becomes unfeasible even with modern computational resources. Fortunately, for interactions where beyond some cut-off radius r_c the interaction can be neglected, the computational effort may be reduced to $\mathcal{O}(N)$. A schematic of three different algorithms is shown in Figure 2.2 based on the description by Rapaport [185].

Assume that the computational domain is subdivided into rectangular cuboid cells, where the linear dimension of each cell is larger than r_c. For interactions with particle i, only particles in the cell in which particle i is located and neighbouring cells must be considered [185], see Figure 2.2(b). In general, this reduces the number of pairs considered to be $\mathcal{O}(N)$. The *cell subdivision* algorithm can be seen to be inefficient based on purely geometric grounds, where if the particles are uniformly distributed and the cell edges are of length r_c, only $\frac{4\pi}{3}r_c^3/(3r_c)^3 \approx 16\%$ of the pairs tested are actually within the cut-off distance [185]. Alternatively, each particle can have an associated list of all particles within a distance $r_c + r_s$ form itself, and only particles in this *neighbour list* must be considered for interactions, see Figure 2.2(c). This greatly reduced the number of pairs considered and the *skin distance* r_s makes the list valid until some particle has moved more than $r_s/2$. The construction of the neighbour list is commonly performed with a cell subdivision to make this operation $\mathcal{O}(N)$.

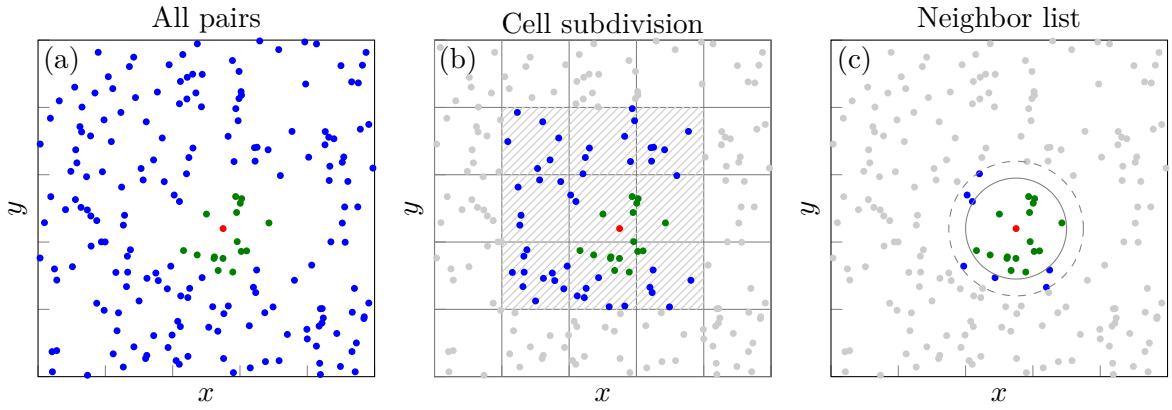

Figure 2.2: Schematic of different algorithms for computing short-range interactions. The central highlighted particle interacts with all green particles, while the algorithm must also test for an interaction with all blue points. Grey points are not considered for interactions in this time step. (a) Naive $\mathcal{O}(N^2)$ algorithm where all particles are tested. (b) Subdivide the simulation box into cells such that particles in only a few cells must be cheeked. (c) Neighbour list algorithm where each particle keeps track of particles within the cut-off radius r_c (circle) plus some skin r_s (dashed circle). A state is shown where the neighbour list has newly been updated.

The choice of r_s is a balance between reducing the number of pairs considered in each time step, and the number of time steps that a single neighbour list can be kept before needing to be updated [185]. The MD implementations within this thesis build on the open-source MD code *Large-scale Atomic/Molecular Massively Parallel Simulator* (`LAMMPS`) [220], which utilises the neighbour list technique for pair interactions.

2.3.6 Numerics: Long-range interactions

The methods described above to accelerate pair interaction evaluations can only be applied if the interaction can be faithfully neglected beyond some distance. This is a common scenario when neutral particles interact, but the Coulomb interaction between charged particles typically decays too slowly with distance for this to be practical. Further considerations are also warranted when modelling systems with periodic boundary conditions, where a lattice of simulation boxes is formed. The total energy in a periodic system is, for some pair potential

$u_{\alpha\beta}(\boldsymbol{r})$, given by

$$\mathcal{V}(\boldsymbol{r}_1, \ldots, \boldsymbol{r}_N) = \frac{1}{2} \sum_{\boldsymbol{n} \in \mathbb{Z}^3}{}' \sum_{i,j} u_{\alpha\beta} \left(\boldsymbol{r}_i - \boldsymbol{r}_j + L\boldsymbol{n} \right). \tag{2.34}$$

The sum over $\boldsymbol{n}$ models interactions with offset cubic simulation boxes with length $L = \sqrt[3]{V}$ – the extension to rectangular boxes is trivial – and the prime denotes that the term $i = j$ is removed in the case of $\boldsymbol{n} = \boldsymbol{0}$. The labels α and β are chosen appropriately based on the type of particles i and j, respectively. The convergence properties of this lattice sum should be considered for Coulomb interactions [67].

In 1921, Ewald [221] considered how to treat the sum in equation (2.34) using a combination of real space and Fourier space evaluation, which is efficient for short-range and smooth interactions, respectively. The Ewald summation is based on smoothly separating the divergence and the tail in the Coulomb interaction between two particles with charges q_i and q_j [222],

$$\frac{q_i q_j}{4\pi\varepsilon_0 r} = \frac{q_i q_j}{4\pi\varepsilon_0 r} f(r) + \frac{q_i q_j}{4\pi\varepsilon_0 r} \left(1 - f(r) \right), \tag{2.35}$$

where the first term can be neglected beyond some distance and the Fourier transform of the second term decays quickly with wave number. The classical choice is

$$f(r) = \operatorname{erfc}(gr) \tag{2.36a}$$

and

$$1 - f(r) = \operatorname{erf}(gr), \tag{2.36b}$$

where g is the Ewald parameter. The Ewald parameter determines where the transition occurs between the terms in equation (2.35), as demonstrated in Figure 2.3.

The long-range contribution from the Coulomb potential, $\varphi^{(\ell)}_{\alpha\beta}(r) = \operatorname{erf}(gr)/(4\pi\varepsilon_0 r)$, in the Ewald sum, can be re-written in terms of interaction charge distributions,

$$\begin{aligned} \mathcal{V}^{(\ell)}(\boldsymbol{r}_1, \ldots, \boldsymbol{r}_N) = {} & \frac{1}{2} \int d^3\boldsymbol{x}_1 d^3\boldsymbol{x}_2 \, \varphi^{(\ell)}_{\alpha\beta}(|\boldsymbol{x}_1 - \boldsymbol{x}_2|) \rho_{uc}(\boldsymbol{x}_1) \rho_{tot}(\boldsymbol{x}_2) \\ & - \frac{1}{2} \sum_{i=1}^{N} \int d^3\boldsymbol{x}_1 d^3\boldsymbol{x}_2 \, \varphi^{(\ell)}_{\alpha\beta}(|\boldsymbol{x}_1 - \boldsymbol{x}_2|) \rho_i(\boldsymbol{x}_1) \rho_i(\boldsymbol{x}_2), \end{aligned} \tag{2.37}$$

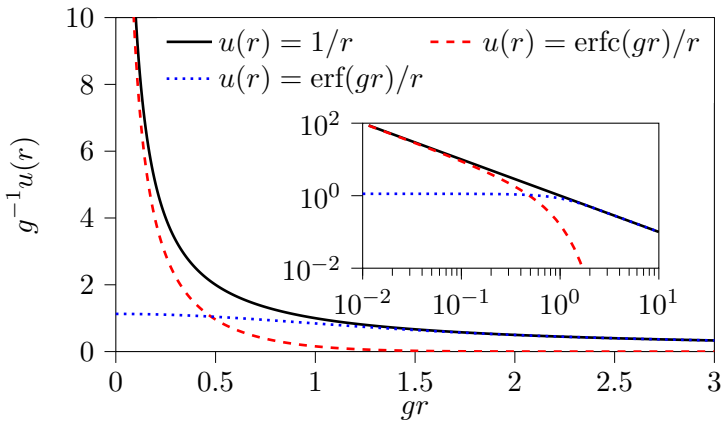

Figure 2.3: Potentials used in Ewald summation where Coulomb interaction (solid line) is smoothly separated into a short (dashed line) and long-range (dotted line) contribution. The inset shows the same data on a logarithmic scale.

where ρ_{uc} is the charge distribution in the box and ρ_{tot} is the total charge distribution including periodic images, i.e.,

$$\rho_{tot}(\boldsymbol{x}) = \sum_{\boldsymbol{n}\in\mathbb{Z}^3} \rho_{uc}(\boldsymbol{x} - L\boldsymbol{n}). \tag{2.38}$$

The second term in equation (2.34) removes the self-contribution, not included in the original sum, and ρ_i is the charge density of a single particle i. By repeated use of the Fourier convolution theorem and Plancherel's theorem, the total interaction energy for a system of point particles is [222]

$$\mathcal{V}(\boldsymbol{r}_1, \ldots, \boldsymbol{r}_N) = \mathcal{E}_r + \mathcal{E}_k + \mathcal{E}_s, \tag{2.39}$$

where

$$\mathcal{E}_r = \frac{1}{2} {\sum_{\boldsymbol{n}\in\mathbb{Z}^3}}' \sum_{i,j} \frac{q_i q_j}{4\pi\varepsilon_0} \frac{\mathrm{erfc}(g r_{ij}^{\boldsymbol{n}})}{r_{ij}^{\boldsymbol{n}}}, \tag{2.40a}$$

$$\mathcal{E}_k = \frac{1}{2L^3} \sum_{\boldsymbol{k}\neq\boldsymbol{0}} \frac{4\pi}{4\pi\varepsilon_0 \boldsymbol{k}^2} e^{-\boldsymbol{k}^2/(4g)} |\tilde{\rho}_{uc}(\boldsymbol{k})|^2, \tag{2.40b}$$

$$\mathcal{E}_s = -\frac{g}{\sqrt{\pi}} \sum_{i=1}^{N} \frac{q_i^2}{4\pi\varepsilon_0}. \tag{2.40c}$$

The above definitions use $\boldsymbol{k} = 2\pi\boldsymbol{n}/L$, the distance $r_{ij}^{\boldsymbol{n}} = |\boldsymbol{r}_i - \boldsymbol{r}_j - L\boldsymbol{n}|$, the Fourier transform

charge density

$$\tilde{\rho}_{uc}(\boldsymbol{k}) = \sum_{i=1}^{N} q_i e^{-i\boldsymbol{k}\cdot\boldsymbol{r}_i}, \tag{2.41}$$

and charge neutrality $\tilde{\rho}_{uc}(\mathbf{0}) = 0$ has been assumed. The exponential decay with $\boldsymbol{k}$ in equation (2.40b) results in a rapid convergence of the sum, and the specific number of $\boldsymbol{k}$-modes needed depends on the desired accuracy [223]. A generalisation of this construction will be given in Chapter 3. Instead of splitting the interaction kernel in equation (2.35), an equivalent construction can be made by adding and subtracting a charge cloud around each particle where the interaction naturally separated into the terms in equation (2.40) [224]. This second approach is more similar to the considerations in Chapter 6.

As the number of required $\boldsymbol{k}$-modes grows with the box size, the Ewald summation scales as $\mathcal{O}\left(N^{3/2}\right)$ [225]. To further improve computational efficiency, grid-based computations can be employed, where the *fast Fourier transform* (FFT) can be utilised and reduced computational complexity to $\mathcal{O}\left(N \log N\right)$ [222]. Particle-mesh methods are based on approximating the charge distribution on a grid on which the FFT algorithm can operate. A modified Poisson problem is solved in reciprocal space so that only the long-range contribution to the interaction is included, either by using the grid version of $\tilde{\rho}_{uc}(\boldsymbol{k})$ in equation (2.39) [226] or using optimised kernels for the modified Poisson equation [227]. The latter is commonly referred to as the `PPPM` method. These grid computations are computationally similar to algorithms used in *particle-in-cell* (PIC) methods [228], however, they differ in the interpretation of the particles as in MD a computational particle represents a single physical particle. Additional methods have been proposed to accelerate the classical Ewald sum to $\mathcal{O}\left(N\right)$ using *random batch sampling* [229, 230], where only a random subset of $\boldsymbol{k}$-modes are considered in each time step. However, this introduces additional stochasticity in the interaction and may require smaller time steps.

2.3.7 Ensembles and thermalisation

The preparation of the MD system should be discussed. For an ergodic system, the average properties are independent of the initial condition [10] and the system should be prepared to have the desired conserved properties. Sophisticated methods have been developed to

formally perform MD simulations in other ensembles than NVE, as listed in Table 2.1, via the introduction of additional global degrees of freedom that modify the equations of motion and conserved quantities. Notable examples are the Nosé-Hoover thermostat for the NVT [231, 232] and NpT [233] ensembles, commonly applied in chains to improve ergodicity [234]. These considerations have also been generalised to Fermi-Dirac distribution functions [235]. The Langevin thermostat [236] adds a drag linear in particle momentum and a stochastic force to the equations of motion which, on average, balances at the desired temperature.

In this thesis, computations have primarily been performed in NVE to remove any thermostat dependence on the dynamic properties. To achieve the correct temperature, a velocity re-scaling algorithm has been used. During the thermalisation phase, velocities are periodically re-scaled to achieve the desired temperature if the instantaneous temperature falls outside an acceptable window. This should only be seen as a method of adding an appropriate amount of energy to the system, because in NVE, $T = T(E)$. During thermalisation, no data used to derive physical observables were collected.

2.4 One-component Plasma Models

Having discussed MD models in general, consider now some specific examples. The models typically fall within one of two categories, one or two-component models. One-component models are simplifications in which only a single charge species is explicitly considered, treating the other as either a polarising or non-polarising background. Two-component models provide a more complete description of plasmas, treating electrons and ions explicitly. Two-component models can be challenging, as they typically exhibit two distinct time scales, see Section 1.2.3, and attractive Coulomb interaction results in strong interaction effects and potentially the Coulomb collapse.

2.4.1 One-component plasma (OCP)

The model commonly referred to as the *one-component plasma* or simply OCP, is a system of classical point charges of a single type in a neutralising background, parametrised by the

Coulomb coupling constant Γ_{ii}[3]. Computations which treat the long-range interactions in this system have been carried out since the 1960s [237], followed by extensive exploration by Hansen and co-workers in the 1970s and '80s, see, e.g., Refs. [69, 238–240], an effort which has continued to the present day [110, 241–245].

The OCP model is one of the primary benchmarks for strong coupling theory. As a complete model for physical systems, it most appropriately describes the ions at very high density, where the high electron Fermi energy makes electron screening negligible and $\Gamma_{ee} \to 0$ [205]. The OCP description of ions has some peculiarities, for example, its long wavelength description in terms of hydrodynamics is debated [110, 246] and the density perturbation has a plasmon dispersion rather than the acoustic modes expected for ions at most conditions (see Section 1.2.3).

2.4.2 Uniform electron gas (UEG)

In some aspects, models that employ a uniform rigid background provide a description more characteristic of the electrons than the ions. However, to treat the electrons, a quantum description is needed and the model is referred to as the *uniform electron gas* (UEG) or *Jellium* [15]. The quantum formulation introduces $\hbar$ as a dimensionful parameter in the OCP Hamiltonian, and two parameters are needed to describe the thermodynamic conditions of the system, commonly r_s and θ. For fermions, the *spin-polarisation* $\xi = |n^\uparrow - n^\downarrow|/(n^\uparrow + n^\downarrow)$ describing asymmetry in the density of spin-up $n^\uparrow$ and spin-down $n^\downarrow$ electrons enters as a third and final parameter [15].

The LFC of the UEG is often used to approximate electron properties in two-component systems [247, 248], for which both analytical models [249] and parameterisations from Monte Carlo have been used [207, 250]. Interaction effects in the UEG predict non-monotonic plasmon dispersion, the *roton feature*, at low temperature [173, 251], and altered electron screening of ions [88, 252], the latter of which is relevant to the last one-component plasma model which will be discussed.

[3]Seen using the appropriate unit system in Appendix D.1.

2.4.3 Yukawa one-component plasma (YOCP)

The pair potential between ions with charge q_α in the Yukawa model is

$$u_{\alpha\alpha}(r) = \frac{q_\alpha q_\alpha}{4\pi\varepsilon_0}\frac{e^{-\kappa r}}{r}, \tag{2.42}$$

where the electrons are assumed to instantaneously screen the ions. Compared to the OCP, an additional dimensionless parameter κa_i characterises the system, given by the electron screening length κ^{-1}. Screening can be seen to effectively reduce the coupling strength [253], and the crystalline phase at large Γ_{ii} transitions from bcc to fcc as κ increases [70]. The particular functional form for the interaction is motivated by the static limit $\omega \to 0$ of the RPA density response [107] and for small $\boldsymbol{k}$ this type of screening also appears in theories with a more complete description of interactions [88] (see also Appendix C.1).

The Yukawa model has been well studied with classical MD, see, e.g., Refs. [243, 254–257], and used as a reference model [258]. On large length scales compared to the screening length κ^{-1}, the behaviour of the Yukawa system is substantially different from the OCP and has characteristics more similar to those of a neutral fluid [110]. To go beyond a description with static screening using MD, an explicit two-component model is needed.

2.5 Two-component Plasma Models

Two-component models provide a more complete description of the physics in plasmas, where electron-ion screening and collisions are modelled explicitly, and quantum aspects regularise the short-length scale physics. Differing levels of the quantum treatment have resulted in a variety of different computational models, and a selection of commonly used models for WDM computations are discussed below. For a more complete overview and comparisons, see the review by Bonitz *et al.* [66].

2.5.1 Path integral Monte Carlo (PIMC)

Ab initio path integral Monte Carlo (PIMC) is based on Feynman's path integral formulation of quantum mechanics. For distinguishable particles, thermal averages of an observable $\hat{O}$ can be evaluated in coordinate representation $\boldsymbol{R} = [\boldsymbol{r}_1^\intercal, \dots \boldsymbol{r}_N^\intercal]^\intercal$ as

$$\begin{aligned}\left\langle \hat{O} \right\rangle_T &= Z^{-1} \int d^3\boldsymbol{R} d^3\boldsymbol{R}' \ \langle \boldsymbol{R}| \, e^{-\beta \hat{H}} \, |\boldsymbol{R}'\rangle \, \langle \boldsymbol{R}'| \, \hat{O} \, |\boldsymbol{R}\rangle \\ &= Z^{-1} \int d^3\boldsymbol{R}_0 \cdots d^3\boldsymbol{R}_M \, \langle \boldsymbol{R}_0| \, e^{-\tau \hat{H}} \, |\boldsymbol{R}_1\rangle \cdots \langle \boldsymbol{R}_{M-1}| \, e^{-\tau \hat{H}} \, |\boldsymbol{R}_M\rangle \, \langle \boldsymbol{R}_M| \, \hat{O} \, |\boldsymbol{R}_0\rangle \, ,\end{aligned} \tag{2.43}$$

where Z is the normalisation. The factors in the second line correspond to the thermal density matrix at an increased temperature $\tau^{-1} = M\beta^{-1} = Mk_\mathrm{B}T$ for which a high-temperature approximation may be used for sufficiently large M [259]. The above integral can be evaluated with the techniques discussed in Section 2.2 and is, in principle, capable of giving quasi-exact (i.e. exact within the given statistical error bars) results for a host of observables without the need for any external input.

For fermions, at warm dense matter conditions, the above formulation must be anti-symmetrised leading to the notorious fermion sign problem [260, 261], resulting in an exponential increase in the required compute time with respect to system size and towards low temperatures. To tame the sign problem, the *fixed-node approximation* [262] can be used at the cost of an approximation, or averaging over a large number of independent calculations is performed [263].

The quantum statistical average in equation (2.43) can formally be seen as the classical thermal average in a system of ring polymers, where the quantum non-locality is encoded into the spring forces between beads in the polymer [264]. This is the basis for *path integral molecular dynamics* [189], which uses MD techniques and ergodicity to evaluate equation (2.43), however, the dynamics cannot be used to study time correlations directly [265].

2.5.2 Density functional theory (DFT)

The most widely used method for modelling WDM systems nowadays is an adiabatic method working within the Born-Oppenheimer approximation where the electrons are treated within the framework of *density functional theory* (DFT) and the ions are treated as classical particles in MD, referred to as DFT-MD. In 1964, Hohenberg and Kohn [266] established the basis for DFT in ground state systems – later extended to finite temperature by Mermin [267] – which guarantees the existence of a universal density functional describing the energy of the system. The equilibrium density profile in any external potential (e.g., ion influence) is the profile that minimises this functional. However, the functional is unknown. The kinetic contribution to the functional can be approximated within Thomas-Fermi theory (orbital-free) or based on the non-interacting orbital formulation by Kohn and Sham [268]. Approximations for the remaining *exchange-correlation* contributions have been extensively investigated at zero [269] and finite temperatures [270], but the search for improved functionals continues [271].

Both orbital-free [272, 273] or Kohn-Sham [16, 17, 274, 275] DFT has been used to model WDM systems via DFT-MD, deriving both equations of state and transport properties. However, the DFT formulation does not capture electron-electron collisions [174, 276], especially important for conductivities at higher temperatures. The model is adiabatic because the electronic states are populated at a pre-defined temperature, resulting in the conserved energy being a combination of the free energy of the electrons and the energy of the ions [277]. Time-dependent formulations can also be constructed, however, they are restricted to electronic time scales. *Time-dependent DFT* (TD-DFT) can either be performed by explicitly evolving orbitals [278] or by linear response theory [174, 279, 280] where an adiabatic approximation for exchange and correlation effects is commonly used [281].

2.5.3 Kinetic theory molecular dynamics (KTMD)

Graziani *et al.* [282] proposed an MD scheme for the ions where the electrons are treated kinetically using a reduced distribution function formulation, termed *kinetic theory molecular dynamics* (KTMD). Some initial attempts to implement the model have been made [283].

However, no dynamic implementation of the electrons has been carried out and anti-symmetric closures [284, 285] should be investigated for the treatment of WDM.

2.5.4 Quantum statistical potentials (QSP)

Two influential semi-classical treatments for two-component plasmas and electron-ion interactions were provided by Kelbg *et al.* [95] and Deutsch *et al.* [96]. Short-range quantum behaviour and exchange effects are based on solutions of two-body systems and encoded in pair potentials. By construction, these potentials have an explicit temperature dependence and are restricted to regimes where exchange effects may be approximated on the pair-exchange level. Other interaction models based on Bohmian mechanics have also been put forward [235]. These types of models have a special niche as they allow for the modelling of electron dynamics over ionic time scales.

An alternative route to achieve an efficient dynamical description of electrons is based on the time-dependent variational principle, referred to as *wave packet molecular dynamics* (WPMD). In the WPMD formulation, the electron wave function is described by a parametrised functional form, allowing for a fast evaluation of the electron and ion time evolution. In the following chapter, such descriptions will be discussed and generalised for two-component plasmas. The wave-packet formulation addresses two concerns with the two-component models discussed above. First, the ability to model electron dynamics and not be restricted to equilibrium systems or the Born-Oppenheimer approximation. This opens the possibility to model non-equilibrium scenarios and describe simultaneously electron and ion-time scale dynamics and the potential interplay between these. Second, the ability to model systems with more than 10^3 particles gives the model access to long wave-length properties of WDM. These aspects will be investigated in Chapters 4 and 5, where electron scattering and transport properties are studied, respectively.

Chapter 3
Quantum Trajectory Molecular Dynamics

Abstract: The restricted functional form for the electron wave function in *wave packet molecular dynamics* (WPMD) is generalised to an elongated Gaussian state and adapted for warm dense matter simulations. Long-range Coulomb interactions are treated with a generalised Ewald summation, and exchange interactions are approximated on a pair exchange level, incorporating kinetic and interaction contributions. The model shows good parallel support and close to linear scaling with particle number. The model is compared to the traditional isotropic approximation in WPMD for ground state and thermal properties, where differences occur primarily in the electronic subsystem. The electrical conductivity differs by 15% between the wave packet models in a warm dense hydrogen test system.

3.1 Introduction

Warm dense matter (WDM) is characterised by ion correlations and electron degeneracy. Two-component modelling is often performed using DFT-MD [24, 272–275], or various Monte Carlo approaches [15, 19, 26], but also one-component models are used as proxies [64, 110, 202]. However, none of these models treats the ion dynamics and simultaneously evolves the electrons, evoking either the Born-Oppenheimer approximation or using statistical formulations. Direct access to electron dynamics would aid investigations of, e.g., x-ray scattering (see Chapter 4), electron transport (see Chapter 5) and more general non-equilibrium [103, 169] and relaxation phenomena [94].

The main hindrance for models with dynamic electrons is the electron-ion mass ratio, which requires a dynamical model to resolve two distinct time scales when both electron and ion processes are of interest. Some questions remain regarding the interplay between the two time scales and the effect on ion transport [149–152]. The need for a quantum treatment of electrons puts further requirements on the computational model. *Time-dependent DFT* can evolve electron states within the DFT approximation [172, 278, 286]. However,

this is not feasible on time scales relevant for ion dynamics due to the computational cost. Phenomenological hydrodynamics based on DFT functionals [102, 287] has been used to evolve both electron and ion degrees of freedom [103], but fluid models of electrons lack some kinetic aspects [288]. For a complete description of the ion dynamics, formulations using quantum statistical potentials (QSPs) have often been employed [95–98]. Alternatively, formulations based on Bohm's interpretation of quantum mechanics have been used to the same effect [235].

A family of methods that sits between semi-classical MD and time-dependent DFT in terms of computational cost is *wave packet molecular dynamics* (WPMD) [289, 290]. These methods work directly on the electron wave functions which are restricted to a parametrised functional form allowing for efficient time evolution. The choice of parametrisation is therefore central to the model and has historically been chosen such that interaction integrals can be evaluated analytically to speed up computation. In this chapter, an extended functional form will be introduced and compared to the traditional approximation. The model has been natively implemented in `LAMMPS` [220] including long-range electrostatic interactions and a pair-wise exchange approximation.

The remainder of this chapter is structured as follows. Sections 3.2 and 3.3 outline the theoretical and numerical development, respectively. In Section 3.4, the model is compared to other models for ground state and time-dependent properties. In particular, the electrical conductivity of a warm dense hydrogen test system is compared between the traditional and extended WPMD models.

3.2 Theoretical Description

Wave packet models were originally introduced in the 1970s by Heller, who recognised that a Gaussian wave packet remains Gaussian in a quadratic potential and the mass centre follows classical equations of motion [291], an idea extended to approximate solutions of Schrödinger's equation [291, 292]. A derivation of the wave packet formulation for arbitrary functional forms

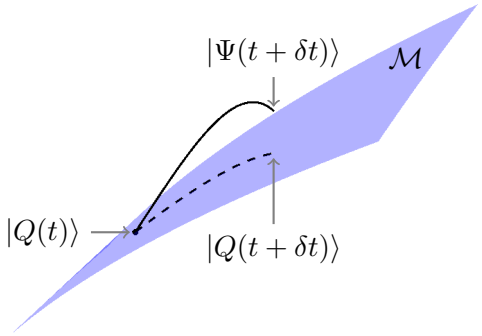

Figure 3.1: Schematic representation of dynamics in the Hilbert space starting from a state $|Q(t)\rangle$. The variational approximation $|Q(t+\delta t)\rangle$ is constrained to the sub-manifold $\mathcal{M}$ (surface) and for short times the difference between the true solution $|\Psi(t+\delta t)\rangle$ and $|Q(t+\delta t)\rangle$ is orthogonal to the tangent space of $\mathcal{M}$ at $|Q(t)\rangle$.

is obtained by varying the action

$$\mathcal{S} = \int dt\ \langle Q|\, i\hbar \frac{d}{dt} - \hat{H}\,|Q\rangle\,, \tag{3.1}$$

where $\hat{H}$ is the system Hamiltonian. The state $|Q\rangle = |Q(Q_\mu)\rangle$ is given by a parametrisation, and the action is varied with respect to its parameters Q_μ. This is the *time-dependent variational principle* (TDVP) [192] where the state is restricted to a sub-manifold $\mathcal{M}$ in Hilbert space. For unrestricted states, the TDVP yields Schrödinger's equation [289]. For the state $|Q\rangle$ to remain on $\mathcal{M}$, the time derivative $d\,|Q\rangle\,/dt$ must be in the tangent space of $\mathcal{M}$, $\mathcal{T}_{|Q\rangle}\mathcal{M}$, and thus the variational principle projects the true derivative onto $\mathcal{T}_{|Q\rangle}\mathcal{M}$ in some manner. The TDVP is therefore closely related to both the *Dirac-Frenkel* and *McLachlan* variational principles and all variational principles are equivalent if $\mathcal{T}_{|Q\rangle}\mathcal{M}$ is a complex linear subspace [293].

The resulting time evolution is schematically shown in Figure 3.1. For short times, δt, the approximation $|Q(t+\delta t)\rangle$ provides the best approximation on $\mathcal{M}$ to the true Schrödinger evolution $|\Psi(t+\delta t)\rangle$ given $|\Psi(t)\rangle = |Q(t)\rangle$. Concretely, it can be shown that $\langle\Delta(t,\delta t)|\Delta(t,\delta t)\rangle$ is minimised to $\mathcal{O}(\delta t^3)$, where $|\Delta(t,\delta t)\rangle = |\Psi(t+\delta t)\rangle - |Q(t+\delta t)\rangle$ is the discrepancy between the true and approximate evolution [289]. This guarantees good approximations for short times, but over longer times $|Q(t+\delta t)\rangle$ and $|\Psi(t+\delta t)\rangle$ may drift apart. The long-time evolution is

instead constrained by appropriate conservation laws, most notably energy conservation [294]. The method can therefore, as with classical MD, be characterised by conserved properties.

Following the procedure in Feldmeier and Schnack [289], an unphysical global phase may be removed, resulting in the Lagrangian

$$\mathcal{L} = \frac{i\hbar}{2} \sum_{\mu} \left(\dot{Q}_{\mu} \frac{\partial}{\partial Q_{\mu}} \left\langle Q(Q_{\mu}^{*}) \middle| Q(Q_{\mu}) \right\rangle + \dot{Q}_{\mu}^{*} \frac{\partial}{\partial Q_{\mu}^{*}} \left\langle Q(Q_{\mu}^{*}) \middle| Q(Q_{\mu}) \right\rangle \right) - \mathcal{H}, \tag{3.2}$$

where $\mathcal{H} = \langle Q | \hat{H} | Q \rangle$ is the Hamiltonian function and the states are assumed to be normalised, i.e. $\langle Q | Q \rangle = 1$. The equations of motion now follow from the Euler-Lagrange equations (2.7) and in general take the quasi-Hamiltonian form [289]

$$i\hbar \sum_{\nu} \mathcal{C}_{\mu\nu} \frac{dQ_{\nu}}{dt} = \frac{\partial \mathcal{H}}{\partial Q_{\mu}^{*}}, \tag{3.3}$$

where

$$\mathcal{H} = \frac{\langle Q | \hat{H} | Q \rangle}{\langle Q | Q \rangle} \equiv \langle \hat{H} \rangle, \tag{3.4a}$$

and

$$\mathcal{C}_{\mu\nu} = \frac{\partial^2}{\partial Q_{\mu}^{*} \partial Q_{\nu}} \ln \left(\left\langle Q(Q_{\mu}^{*}) \middle| Q(Q_{\nu}) \right\rangle \right). \tag{3.4b}$$

Further development requires a specific form for $|Q\rangle$. When modelling electrons and fermions more generally, the state should adhere to the Pauli principle. Knaup *et al.* [295] and Jakob *et al.* [296, 297] considered anti-symmetric states in the form of a Slater-determinant

$$|Q\rangle = \frac{1}{N!} \sum_{P \in S_N} (-1)^P \left| q_{P(1)} \right\rangle \otimes \left| q_{P(2)} \right\rangle \otimes \cdots \otimes \left| q_{P(N)} \right\rangle, \tag{3.5}$$

where $|q_i\rangle$ is a single-particle orbital and P runs over all the permutations in the symmetric group S_N of N items. However, this approach scales unfavourably with particle number N, so here a product state

$$|Q\rangle = |q_1\rangle \otimes |q_2\rangle \otimes \cdots \otimes |q_N\rangle \tag{3.6}$$

has been utilised instead and exchange effects are approximated by Pauli potentials of the

type first introduced by Klakow *et al.* [298, 299]. The product state simplifies the evaluation of $\mathcal{H}$, which scales as $\mathcal{O}\left(N^4\right)$ for a Slater-determinant without truncation [289], but also the structure of $\mathcal{C}_{\mu\nu}$ which becomes diagonal in particle blocks. Equation (3.3) may therefore be inverted sequentially per particle instead of simultaneously for the whole system (formally non-local), and the orbitals $|q_i\rangle$ only couple to each other via the energy $\mathcal{H}$.

Before considering the specific $|q_i\rangle$ and the evaluation of $\mathcal{H}$, some consequences of the approximation (3.6) can immediately be seen. The Pauli principle and the resulting Fermi-Dirac statistics, equation (1.14), is valid for any Hamiltonian $\hat{H}$ and specifically for vanishing interactions. Therefore, the right-hand side of equation (3.3) is not the source of these effects. Rather $\mathcal{C}_{\mu\nu}$ should act as a metric on $\mathcal{M}$ which prevents access to forbidden states. The Pauli potentials act to suppress states where $|q_i\rangle = |q_j\rangle$, but only with a finite energy penalty and do not formally forbid them. Therefore, this approximation method should only be used for moderately degenerate systems.

3.2.1 Wave Packets

The shape of the wave packet $|q_i\rangle$ dictates the states that the model can describe. The choice is generally free and based on intuition – for self-similar wave packets additional constraints can be imposed between amplitude and phase [300] – but most commonly motivated by computational ease and efficiency. The traditional form is an isotropic Gaussian [298, 299],

$$\langle \boldsymbol{x}|q_i\rangle = \left(2\pi\sigma_i^2\right)^{-3/4} \times \exp\left[-\left(\frac{1}{4\sigma_i^2} - \frac{i\pi_i}{\hbar}\right)|\boldsymbol{x}-\boldsymbol{r}_i|^2 + \frac{i}{\hbar}\boldsymbol{p}_i^\intercal(\boldsymbol{x}-\boldsymbol{r}_i)\right], \tag{3.7}$$

parametrised by the centre of mass position $\boldsymbol{r}_i$ and momentum $\boldsymbol{p}_i$, and a width σ_i with an associated momentum variable π_i[1]. In this formulation, the width is a dynamical degree of freedom, free to adjust based on the local environment of the electron. However, other variants exist as described by Grabowski [290]:

- Lenglet and Maynard [301] studied strong field interactions and individual collisions

[1]Formally, π_i is the conjugate momentum variable to σ_i^2 and the presented form therefore slightly differs from e.g., Grabowski [290], but chosen for consistency below.

using Hermite-Gauss functions.

- Morozov and Valuev [302]; Grabowski *et al.* [303]; and Angermeier and White [304] used split wave packets, i.e., a sum of isotropic Gaussians, for their description when investigating ground state and collisional dynamics.
- Jakob *et al.* [296, 297] included a Bloch wave on top of an isotropic Gaussian to formally treat the lattice of computational boxes in simulations with periodic boundary conditions.
- Ebeling and Militzer [305] used a combination of isotropic Gaussians and (static) 1s-states, in their ionisation model.
- Ebeling *et al.* [306] used a harmonic constraint in the functional form to regularise the width, see also the discussion in Section 3.2.4.

However, one generalisation of equation (3.7) to non-isotropic states is

$$\langle \boldsymbol{x} | q_i \rangle = \left((2\pi)^3 \det\left(\boldsymbol{\Sigma}_i\right) \right)^{-1/4} \times \exp\left[-(\boldsymbol{x} - \boldsymbol{r}_i)^\intercal \left(\frac{1}{4} \boldsymbol{\Sigma}_i^{-1} - \frac{i}{\hbar} \boldsymbol{\Pi}_i \right) (\boldsymbol{x} - \boldsymbol{r}_i) + \frac{i}{\hbar} \boldsymbol{p}_i^\intercal (\boldsymbol{x} - \boldsymbol{r}_i) \right]. \tag{3.8}$$

This functional form is considered here to better account for local gradients on the length scale of the wave packet. A similar form was used by Ono and Ando [307] when describing molecular systems. Their formulation will be extended including long-range interactions, exchange effects, and many-particle dynamics, all needed to describe WDM plasmas. The wave packet in equation (3.8) is parameterised by 18 degrees of freedom: the position $\boldsymbol{r}_i$, the momentum $\boldsymbol{p}_i$ and two symmetrical 3×3 matrices, $\boldsymbol{\Sigma}_i$ – describing the elongation and orientation – and $\boldsymbol{\Pi}_i$ the associated momentum to $\boldsymbol{\Sigma}_i$.

The equations of motion for the anisotropic wave packet follow from the Lagrangian (3.2) and have a classical structure. Namely, for the centre of mass degrees of freedom [307]:

$$\frac{d\boldsymbol{r}_i}{dt} = \frac{\partial \mathcal{H}}{\partial \boldsymbol{p}_i}, \qquad \frac{d\boldsymbol{p}_i}{dt} = -\frac{\partial \mathcal{H}}{\partial \boldsymbol{r}_i}, \tag{3.9a}$$

and for internal degrees of freedom:

$$\frac{d}{dt}\Sigma_{i\alpha\beta} = \tau_{\alpha\beta} \frac{\partial \mathcal{H}}{\partial \Pi_{i\alpha\beta}}, \qquad \frac{d}{dt}\Pi_{i\alpha\beta} = -\tau_{\alpha\beta} \frac{\partial \mathcal{H}}{\partial \Sigma_{i\alpha\beta}}. \tag{3.9b}$$

Above, $\Sigma_{i\alpha\beta} = (\boldsymbol{\Sigma}_i)_{\alpha\beta}$ and $\Pi_{i\alpha\beta} = (\boldsymbol{\Pi}_i)_{\alpha\beta}$ are the components of the symmetric matrices. The factor $\tau_{\alpha\beta}$ is unity if $\alpha = \beta$ and a half otherwise, accounting for the symmetric structure of $\boldsymbol{\Sigma}_i$ and $\boldsymbol{\Pi}_i$, where the off-diagonal components in symmetrical positions are treated as symbolically the same.

For plasma modelling, a system of classical ions and electron wave packets is considered. Ions are defined by their position $\boldsymbol{R}_I$, momentum $\boldsymbol{P}_I$, charge q_I, and mass M_I. The electrons with charge q_e and mass m_e are treated quantum mechanically with position $\hat{\boldsymbol{x}}_i$ and momentum $\hat{\boldsymbol{p}}_i$ operators. The Hamiltonian is

$$\begin{aligned}\hat{H} =& \sum_I \frac{\boldsymbol{P}_I^2}{2M_I} + \frac{1}{4\pi\varepsilon_0}\sum_{I<J}\frac{q_I q_J}{|\boldsymbol{R}_I - \boldsymbol{R}_J|} \\ &+ \sum_i \frac{\hat{\boldsymbol{p}}_i^2}{2m_e} + \frac{q_e^2}{4\pi\varepsilon_0}\sum_{i<j}\frac{1}{|\hat{\boldsymbol{x}}_i - \hat{\boldsymbol{x}}_j|} + \frac{q_e}{4\pi\varepsilon_0}\sum_i\sum_I \frac{q_I}{|\hat{\boldsymbol{x}}_i - \boldsymbol{R}_I|}.\end{aligned} \tag{3.10}$$

To perform the time evolution, the state average of the Hamiltonian ought to be evaluated. The kinetic contribution can be evaluated explicitly as

$$\left\langle \frac{\hat{\boldsymbol{p}}_i^2}{2m_e} \right\rangle = \frac{\boldsymbol{p}_i^2}{2m_e} + \frac{2}{m_e}\operatorname{Tr}\left\{\boldsymbol{\Pi}_i\boldsymbol{\Sigma}_i\boldsymbol{\Pi}_i\right\} + \frac{\hbar^2}{8m_e}\operatorname{Tr}\left\{\boldsymbol{\Sigma}_i^{-1}\right\}, \tag{3.11}$$

which includes a classical contribution and two terms from internal degrees of freedom. The second term in equation (3.11) is the kinetic energy associated with the changing shape of the wave packet, while the last term is the shape-kinetic energy [99], with the same origin as the Bohm potential in Section 1.2.2. The shape kinetic energy keeps $\boldsymbol{\Sigma}_i$ positive definite and the wave packet well defined during the time evolution.

For the state average of the interaction terms in the Hamiltonian (3.10), no explicit formulation convenient for an MD implementation has been found. The remainder of this section is dedicated to the efficient *on-the-fly* evaluation of these terms and the introduction of the exchange approximation.

3.2.2 Generalised Ewald summation

To perform efficient and scalable N-body computations with electrostatic forces, part of the interaction is evaluated in real space (truncated at some distance) and in part in Fourier space (truncated Fourier representation), as discussed in Sections 2.3.5 and 2.3.6. Performing the separation described in equations (2.35) and (2.36) in the wave packet description requires the evaluation of state averages on the form

$$\left\langle \frac{1}{|\hat{\boldsymbol{x}}_i - \hat{\boldsymbol{x}}_j|} \right\rangle = \left\langle \frac{\operatorname{erfc}\left(g|\hat{\boldsymbol{x}}_i - \hat{\boldsymbol{x}}_j|\right)}{|\hat{\boldsymbol{x}}_i - \hat{\boldsymbol{x}}_j|} \right\rangle + \left\langle \frac{\operatorname{erf}\left(g|\hat{\boldsymbol{x}}_i - \hat{\boldsymbol{x}}_j|\right)}{|\hat{\boldsymbol{x}}_i - \hat{\boldsymbol{x}}_j|} \right\rangle. \tag{3.12}$$

The Ewald parameter g will be determined by scanning different g and optimising for performance, where the cut-off radius and the number of $\boldsymbol{k}$-modes [223] are selected to achieve the needed accuracy. Below, self-consistent treatments of both terms in equation (3.12) are presented. To the author's knowledge, the $\boldsymbol{k}$-space evaluation has only been mentioned once for isotropic wave packets [308] and is commonly neglected in wave packet formulations.

Short-range forces

The force evaluation is the most performance-critical part of an MD simulation. Therefore, explicit formulations for the interactions are crucial. State averages similar to those needed have previously been approached by Taylor expansion [307] or direct numerical evaluation of the integral [309]. However, these approaches do not retain a strict notion of energy conservation, either due to truncation errors or numerical noise. Instead, an approximation will be made on the functional form of the integrand in equation (3.12), an approximation which can be successively improved by including more terms. With an appropriate approximation, efficient evaluation of the interaction can be obtained while simultaneously retaining good energy conservation properties, because the potential is approximated and not the computation of the state average.

The state averages of Gaussian interaction kernels, i.e. $\langle \exp(-\alpha|\hat{\boldsymbol{x}}_i - \hat{\boldsymbol{x}}_j|)\rangle$ for some α, can be performed analytically [310, 311]. Therefore, if the interaction kernel is approximated

as a sum of Gaussian modes – a Gaussian decomposition – the state average can promptly be evaluated. Therefore, assume

$$V^{(\beta)}(r) \simeq \sum_{p=1}^{N_p^{(\beta)}} c_p^{(\beta)} e^{-\alpha_p^{(\beta)} r^2}, \tag{3.13}$$

where $V^{(s)}(r) = \mathrm{erfc}(gr)/r$ and $V^{(\ell)}(r) = \mathrm{erf}(gr)/r$, and the coefficients $c_p^{(\beta)}$ and $\alpha_p^{(\beta)}$ are fitting parameters for each mode p. The coefficients are found as the solution to a minimisation problem and pre-computed for each g.

The state averages of the interaction kernel $V^{\beta}(r)$ is a volume integration weighted by some Gaussian profile, and a reasonable definition for the error in the Gaussian mode decomposition is

$$\delta\mathcal{L} = \int_0^{r_{\max}} dr\, r^2 \left| V^{(\beta)}(r) - \sum_{p=1}^{N_p^{(\beta)}} c_p^{(\beta)} e^{-\alpha_p^{(\beta)} r^2} \right|^2 = \boldsymbol{c}^{\intercal}\mathbf{S}\boldsymbol{c} - 2\boldsymbol{c}^{\intercal}\boldsymbol{A} + \delta\mathcal{L}_0, \tag{3.14}$$

where $\boldsymbol{c}^{\intercal} = [c_1^{(\beta)}, \ldots, c_{N_p^{(\beta)}}^{(\beta)}]$,

$$\delta\mathcal{L}_0 = \int_0^{r_{\max}} dr\, r^2 |V^{(\beta)}(r)|^2, \tag{3.15a}$$

$$(\boldsymbol{A})_p = \int_0^{r_{\max}} dr\, r^2 V^{(\beta)}(r) e^{-\alpha_p^{(\beta)} r^2}, \tag{3.15b}$$

and

$$(\mathbf{S})_{pq} = \int_0^{r_{\max}} dr\, r^2 e^{-(\alpha_p^{(\beta)} + \alpha_q^{(\beta)}) r^2}. \tag{3.15c}$$

No small r cut off is needed for the potentials investigated, as all integrals are convergent. For the short-range interaction, $\beta = s$, the integrals are convergent, and $r_{\max} = \infty$ was chosen. Depending on the Ewald parameter, the decomposition required $N_p^{(s)} = 5 - 15$ modes. The decomposition of the long-range term, $\beta = \ell$, will also be necessary for Sections 3.2.2 and 3.2.3 when treating self and exchange-terms, but not for the standard electrostatic contribution. The exchange contribution is exponentially suppressed by the overlap $|\langle q_i | q_j \rangle|^2$ for large distances, and therefore the introduction of finite $r_{\max}$ does not constitute a significant limitation. In

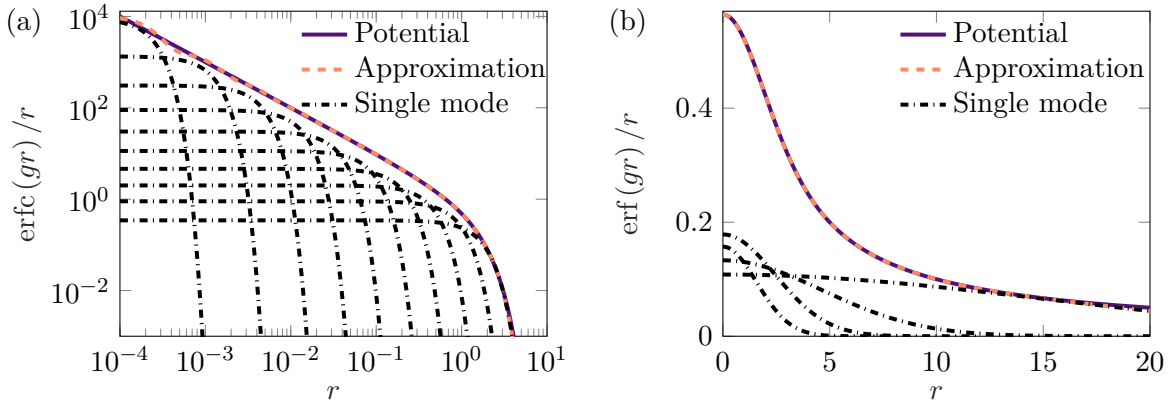

Figure 3.2: The Gaussian mode decomposition of the short-range interaction (a) and the long-range interaction (b) with an Ewald parameter $g = 0.5$.

particular, $r_{\max} = 15\, a_{\mathrm{B}}$ was used in this case and $N_p^{(\ell)} \leq 5$ was typically needed.

There is a need for a robust minimisation of $\delta\mathcal{L}$ to find $c_p^{(\beta)}$ and $\alpha_p^{(\beta)}$. For a fixed set of $\alpha_p^{(\beta)}$, the minimisation is solved by inversion of the linear system of equations $\partial\mathcal{L}/\partial c_p = 0$, i.e.,

$$\mathbf{S}\boldsymbol{c} = \boldsymbol{A}, \tag{3.16}$$

and the optimal linear coefficients $c_p^{(\beta)}$ are given as a function of the set of $\alpha_p^{(\beta)}$. Instead of using a particular set of $\alpha_p^{(\beta)}$ [311], a general minimisation algorithm [312] was used to find the optimal set of $\alpha_p^{(\beta)}$ given optimal coefficients $c_p^{(\beta)}$. For a stable decomposition, the search was limited to $\alpha_p^{(s)} > 0$ and $r_{\max}^{-2}/2 < \alpha_p^{(\ell)} < g^2$.

Figure 3.2 demonstrates the final decomposition resulting from this procedure, typical of the ones used for MD simulations. The singular nature of the short-range interaction is approximated by a series of modes with successively larger amplitude and shorter range. The exponential decay of the Gaussian modes does not make it suitable for treating the Coulomb tail, and the decomposition is not used for treating the long-range interactions discussed next.

Long-range forces

To limit surface effects in a finite-size simulation box, the simulation is periodically repeated and results in a lattice sum for the interaction, see equation (2.34). Analogous to the case of

point particles, the Ewald sum is written as a sum with a main and a self-contribution $\mathcal{E}_k + \mathcal{E}_s$. The treatment of the main contribution proceeds as described in Section 2.3.6 if the extent of the wave packet is accounted for in the charge distribution,

$$\rho_{\text{uc}}(\boldsymbol{x}) = \sum_I q_I \delta^{(3)}(\boldsymbol{x} - \boldsymbol{R}_I) + q_e \sum_i |\langle \boldsymbol{x}|q_i\rangle|^2, \tag{3.17}$$

but ions are still treated as points. Making explicit use of the functional form of the wave packet, equation (3.8), the Fourie transformed charge distribution is

$$\tilde{\rho}_{\text{uc}}(\boldsymbol{k}) = \sum_I q_I e^{-i\boldsymbol{k}\cdot\boldsymbol{r}_i} + q_e \sum_i e^{-i\boldsymbol{k}\cdot\boldsymbol{r}_i} e^{-\frac{1}{2}\boldsymbol{k}^\intercal \boldsymbol{\Sigma}_i \boldsymbol{k}}. \tag{3.18}$$

An additional factor appears for electrons, suppressing the electron contribution for large $\boldsymbol{k}$. This charge distribution is used in equation (2.40b) for the Ewald summation and used for force evaluation.

In any given computation, only a finite number of $\boldsymbol{k}$-vectors may be used, and the associated truncation error for classical point particles was described by Kolafa and Perram [223]. It can be shown that the resulting force from the Ewald summation for distributed particles is suppressed by factors $\exp(-0.5\boldsymbol{k}^\intercal\boldsymbol{\Sigma}_i\boldsymbol{k}) \times \exp(-0.5\boldsymbol{k}^\intercal\boldsymbol{\Sigma}_j\boldsymbol{k})$ for each $\boldsymbol{k}$-vector and the Ewald sum converges more rapidly, an effect of the smoother electron density profile which requires fewer $\boldsymbol{k}$-vectors to describe. The classical error bound is therefore used as an upper bound for the error.

The self-energy contribution $\mathcal{E}_s$ is modified when finite extent particles are introduced. Incorporating the functional form of the wave packets into the argument in Section 2.3.6 yields:

$$\begin{aligned} 4\pi\varepsilon_0\mathcal{E}_s &= -\frac{g}{\sqrt{\pi}}\sum_I q_I^2 - \sum_i q_e^2 \int d^3\boldsymbol{x}_1 |\langle \boldsymbol{x}_1|q_i\rangle|^2 \int d^3\boldsymbol{x}_2 \frac{\operatorname{erf}(g|\boldsymbol{x}_1 - \boldsymbol{x}_2|)}{2|\boldsymbol{x}_1 - \boldsymbol{x}_2|} |\langle \boldsymbol{x}_2|q_i\rangle|^2 \\ &\approx -\frac{g}{\sqrt{\pi}}\sum_I q_I^2 - \frac{1}{2}\sum_i q_e^2 \sum_{p=1}^{N_p^{(\ell)}} \frac{c_p^{(\ell)}}{\sqrt{\det\left(\mathbf{I} + 4\alpha_p^{(\ell)}\boldsymbol{\Sigma}_i\right)}}. \end{aligned} \tag{3.19}$$

The integral is exponentially small if $\boldsymbol{x}_1 \not\approx \boldsymbol{x}_2$ and the Gaussian decomposition of the long-range

interaction kernel has been utilised. The correct point-particle limit $\boldsymbol{\Sigma}_i \to 0$ is obtained if $\sum_p c_p^{(\ell)} = 2g/\sqrt{\pi}$, the case if the decomposition retains the correct value at $r = 0$.

The self-energy term, $\mathcal{E}_s$, concerns an added interaction in $\mathcal{E}_k$ between a particle and itself. It is therefore translation invariant and independent of $\boldsymbol{r}_i$. The self-term does not directly influence the equations of motion for the mass centre, but the dependence on $\boldsymbol{\Sigma}_i$ impacts the dynamics of internal degrees of freedom, which in turn couples to $\boldsymbol{r}_i$. For classical particles or static envelopes, $\mathcal{E}_s$ is a constant energy shift that does not influence the dynamics.

3.2.3 Pauli interactions

The lack of a properly anti-symmetrised state must be compensated for with an additional repulsion between electrons. In the wave packet description, the difference in kinetic energy between a pair-wise anti-symmetrised state and the product state has been used as the source of this repulsion. Klakow *et al.* [298, 299] argued for the kinetic contribution to dominate, although the exchange contribution to the Coulomb interaction can be significant [304]. The electron force field model (eFF) uses the kinetic energy difference but introduces fitting parameters in the Pauli interaction, which were tuned to achieve stable bounds for elements with $Z \leq 6$ [313]. The eFF model – with only minor modifications – is the most extensively used wave packet model in recent years [150, 151, 166, 314–318]. Angermeier and White [304] considered a correlation potential based on spatially symmetric states between electrons with opposite spin. However, the model introduces a free parameter which scales this contribution. This treatment of the Pauli interaction is adapted here to the anisotropic Gaussian state and is extended to account for the interaction with all surrounding participles.

The Pauli potential is formulated by considering two particles, i and j, with the two-particle Hamiltonian

$$\hat{H}_2 = \frac{\hat{\boldsymbol{p}}_i^2 + \hat{\boldsymbol{p}}_j^2}{2m_e} + \frac{q_e^2}{4\pi\varepsilon_0}\frac{1}{|\hat{\boldsymbol{x}}_i - \hat{\boldsymbol{x}}_j|} + V_{\mathrm{bg}}\left(\hat{\boldsymbol{x}}_i, t\right) + V_{\mathrm{bg}}\left(\hat{\boldsymbol{x}}_j, t\right), \tag{3.20a}$$

where $V_{\mathrm{bg}}(\hat{\boldsymbol{x}}_i, t)$ is the electrostatic interaction from all other particles acting on particle i.

Explicitly, the background is

$$V_{\mathrm{bg}}(\boldsymbol{x},t) = \sum_{k\neq i,j} \frac{q_e^2}{4\pi\varepsilon_0} \int d^3\boldsymbol{x}_k \frac{|\langle \boldsymbol{x}_k|q_k\rangle|^2}{|\boldsymbol{x}-\boldsymbol{x}_k|} + \sum_I \frac{1}{4\pi\varepsilon_0}\frac{q_I q_e}{|\boldsymbol{x}-\boldsymbol{R}_I|}, \tag{3.20b}$$

where k (I) runs over all other electrons (ions) in the system. For a two-electron system, the spin and spatial degrees of freedom factorise and the wave function may be characterised as a singlet or triplet state, with spatially symmetric

$$\left|q_i q_j^+\right\rangle = \frac{1}{\sqrt{2}}\left(|q_i\rangle \otimes |q_j\rangle + |q_j\rangle \otimes |q_i\rangle\right) \tag{3.21}$$

or anti-symmetric

$$\left|q_i q_j^-\right\rangle = \frac{1}{\sqrt{2}}\left(|q_i\rangle \otimes |q_j\rangle - |q_j\rangle \otimes |q_i\rangle\right) \tag{3.22}$$

states, respectively. The names refer to the multiplicity in spin degrees of freedom for each spatial structure.

In the wave packet treatment, individual electrons are assigned either as spin up ($|\uparrow\rangle$) or spin down ($|\downarrow\rangle$). The Pauli interaction is the difference between the state average of $\hat{H}_2$ for either $\left|q_i q_j^-\right\rangle$ ($\mathcal{V}_{ij}^P$) or $\left|q_i q_j^+\right\rangle$ ($\mathcal{V}_{ij}^C$) and the product state $|q_i\rangle \otimes |q_j\rangle$. The contribution from the latter is accounted for by equation (3.11) and the standard electrostatic interaction. In terms of state averages, the Pauli interaction is

$$\begin{aligned}\mathcal{V}_{ij}^{P/C} &= \frac{\left\langle q_i q_j^{\mp}\right| \hat{H}_2 \left|q_i q_j^{\mp}\right\rangle}{\left\langle q_i q_j^{\mp}\middle| q_i q_j^{\mp}\right\rangle} - \langle q_i q_j|\, \hat{H}_2\, |q_i q_j\rangle \\ &= \mp \frac{\langle q_i q_j|\, \hat{H}_2\, |q_j q_i\rangle - \langle q_i q_j|\, \hat{H}_2\, |q_i q_j\rangle\, |\langle q_i|q_j\rangle|^2}{1 \mp |\langle q_i|q_j\rangle|^2},\end{aligned} \tag{3.23}$$

which for the localised Gaussian wave functions considered, scale as $|\langle q_i|q_j\rangle|^2$ for large separations between particles i and j. Due to the exponential decay of the overlap with respect to the distance between the particles i and j, the Pauli interaction is short-range between these two particles. However, the background term introduces a long-range contribution in terms of the background particles, which should be accounted for by another Ewald summation.

Explicit evaluations for all terms in equation (3.23) are key to employing the model on a large scale. Analytical expressions for $\mathcal{V}_{ij}^{P/C}$ have been obtained using the Gaussian decomposition of the interaction term, the result of which is summarised in Appendix A.1.

Equal spin electrons must interact via $\mathcal{V}_{ij}^{P}$. The choice of $\mathcal{V}_{ij}^{P}$ or $\mathcal{V}_{ij}^{C}$ for a pair of opposite spin electrons has been considered in two ways. First, along the lines of Angermeier and White [304], where opposite spin interactions are modelled with $\mathcal{V}_{ij}^{C}$, scaled by a factor ρ, $\mathcal{V}_{ij}^{C} \to \rho\mathcal{V}_{ij}^{C}$. This method will be used throughout this chapter. For ground-state helium or molecular hydrogen, the electronic structure is well described by a singlet state and $\rho = 1$. However, for a free electron gas, this overestimates the correlation effects as the appropriate two-particle state is not simply the singlet state and $\rho < 1$ is more suitable [304]. The appropriate value for ρ – most likely temperature and density-dependent $\rho = \rho(n, T)$ – is *a priori* unknown. Second, motivated by the multiplicity of the different spin configurations, half of the opposite spin interactions are modelled via $\mathcal{V}_{ij}^{P}$ and the other half by $\mathcal{V}_{ij}^{C}$, in keeping with the spin-dependent QSP interactions, see, e.g., Filinov *et al.* [98]. To this end, each electron species was divided into two sub-groups. The latter method is employed in Chapters 4 and 5.

The Pauli potential $\mathcal{V}_{ij}^{P}$ seems divergent as $|q_j\rangle \to |q_i\rangle$ and the overlap tends to unity. However, the numerator vanishes as well and results in a finite energy barrier. This is a particular example of the more general remark at the end of Section 3.2, which limits this type of construction of Pauli interactions to moderately degenerate systems.

Long-range Pauli interaction

The electrostatic interactions, which are the basis for the background term V_{bg}, are long-range with respect to the particles in the background. Performing the same kind of separation into short and long-range contributions as discussed in equation (3.12) results in

$$\mathcal{V}_{p,\mathrm{bg}} = \mathcal{E}_{\mathrm{bg},r} + \mathcal{E}_{\mathrm{bg},k} + \mathcal{E}_{\mathrm{bg},s}. \tag{3.24}$$

The real-space evaluation $\mathcal{E}_{\mathrm{bg},r}$ takes the form of a three-body term which may be efficiently truncated in the background particle due to the short-range interaction kernel. The $\boldsymbol{k}$-space

term

$$\mathcal{E}_{\mathrm{bg},k} = \frac{1}{4\pi\varepsilon_0} \int d^3\boldsymbol{x}_1 d^3\boldsymbol{x}_2 \frac{\operatorname{erf}(g|\boldsymbol{x}_1 - \boldsymbol{x}_2|)}{2|\boldsymbol{x}_1 - \boldsymbol{x}_2|} \mu(\boldsymbol{x}_1)\rho_{\mathrm{tot}}(\boldsymbol{x}_2) \tag{3.25}$$

can once more be written as an interaction between two density fields, i.e., the total charge ρ_{tot} and a density related to the overlaps

$$\begin{aligned}\mu(\boldsymbol{x}) = -\sum_{i<j} \frac{(\pm\rho)\, q_e}{1 \mp |\langle q_i|q_j\rangle|^2} \Big[2\,\mathrm{Re}\left\{\langle q_j|\boldsymbol{x}\rangle \langle \boldsymbol{x}|q_j\rangle \langle q_j|q_j\rangle\right\} \\ - \left(|\langle \boldsymbol{x}|q_i\rangle|^2 + |\langle \boldsymbol{x}|q_j\rangle|^2 \right) |\langle q_i|q_j\rangle|^2 \Big].\end{aligned} \tag{3.26}$$

The upper and lower sign is chosen for Pauli interactions ($\pm\rho = +1$) and correlation interactions ($\pm\rho = -\rho$), respectively. This contribution can be evaluated in $\boldsymbol{k}$-space as described in Appendix A.1.

The corresponding self-energy contribution $\mathcal{E}_{\mathrm{bg},s}$ now takes the form of a pair interaction term

$$\begin{aligned}\mathcal{E}_{\mathrm{bg},s} = \sum_{i<j} \int d^3\boldsymbol{x}_1 d^3\boldsymbol{x}_2 \frac{\operatorname{erf}(g|\boldsymbol{x}_1 - \boldsymbol{x}_2|)}{2|\boldsymbol{x}_1 - \boldsymbol{x}_2|} \frac{(\pm\rho)\, q_e^2/(4\pi\varepsilon_0)}{1 \mp |\langle q_i|q_j\rangle|^2} \left(|\langle \boldsymbol{x}|q_i\rangle|^2 + |\langle \boldsymbol{x}|q_j\rangle|^2 \right) \\ \times \left[2\,\mathrm{Re}\left\{\langle q_j|\boldsymbol{x}\rangle \langle \boldsymbol{x}|q_j\rangle \langle q_j|q_j\rangle\right\} - \left(|\langle \boldsymbol{x}|q_i\rangle|^2 + |\langle \boldsymbol{x}|q_j\rangle|^2 \right) |\langle q_i|q_j\rangle|^2 \right]\end{aligned} \tag{3.27}$$

and needs to be included to remove the anomalous contribution in equation (3.25). This completes the current description of exchange contributions.

3.2.4 Confining potentials

Many authors have observed an indefinite expansion of the wave packets at sufficiently high temperatures [150, 295, 306, 308, 319, 320], resulting in a packet that extends over multiple ions without the ability to localise at multiple sites [303]. If the wave packet spreads too large, no electron density perturbations can form, and interaction between particles effectively ceases. This is seen as a flaw of the limited functional form, and multiple proposals have been presented to counteract this expansion [166, 306, 321]. Currently, an additional confinement

potential is added,

$$\mathcal{V}_\Sigma = \frac{A_w}{2} \sum_i \sum_{\alpha=1}^{3} \left(\sigma_{i,\alpha} - l_w\right)^2 \theta\left(\sigma_{i,\alpha}^2 - l_w^2\right), \tag{3.28}$$

where $\sigma_{i,\alpha}^2$ is the αth eigenvalue of $\mathbf{\Sigma}_i$ and $\theta(x)$ is the Heaviside step function. The parameters l_w and A_w set the width of a free particle $\sigma_{\text{free}}(l_w, A_w) > l_w$ by balancing the shape-kinetic energy. This potential is rotationally invariant and acts only on wave packets with a width larger than l_w. In the limit of $l_w = 0$, the potential reduces to

$$\mathcal{V}_\Sigma = \frac{A_w}{2} \sum_i \mathrm{Tr}\left\{\mathbf{\Sigma}_i\right\} = \frac{A_w}{2} \sum_i \left\langle \left(\hat{\boldsymbol{x}}_i - \langle \hat{\boldsymbol{x}}_i \rangle\right)^2 \right\rangle, \tag{3.29}$$

and represent a harmonic potential centred at the particle position. In this specific limit, the confinement potential has also been used to address the heat capacity in the classical limit [305].

3.2.5 Temperature measurements

Equipartition defines the system temperature T, in terms of any degree of freedom Q_μ as

$$\left\langle Q_\mu \frac{\partial \mathcal{H}}{\partial Q_\nu} \right\rangle_T = \delta_{\mu\nu} k_\mathrm{B} T, \tag{3.30}$$

where $\langle \cdot \rangle_T$ represent the thermal average in the microcanonical ensemble or NVE. Using either the centre of mass momentum $Q_\mu = Q_\nu = \boldsymbol{p}_i$,

$$\left\langle \frac{\boldsymbol{p}_i^2}{m} + \boldsymbol{p}_i^\intercal \frac{\partial \mathcal{V}}{\partial \boldsymbol{p}_i} \right\rangle_T = 3 k_\mathrm{B} T, \tag{3.31}$$

or the momentum related to the packet dynamics,

$$\left\langle \frac{4}{m} \mathrm{Tr}\left\{\mathbf{\Pi}_i \mathbf{\Sigma}_i \mathbf{\Pi}_i\right\} + \sum_{\alpha\beta} \Pi_{i\alpha\beta} \tau_{\beta\alpha} \frac{\partial \mathcal{V}}{\partial \Pi_{i\beta\alpha}} \right\rangle_T = 6 k_\mathrm{B} T, \tag{3.32}$$

two independent measures of temperature are derived. However, the two formulations result in the same temperature after thermal averaging. Previously, Ma *et al.* [166] considered the

width kinetic energy contribution to the temperature measurement for isotropic wave packets. In the above, $\mathcal{V}$ is the state average interaction, which in the case of Pauli interactions is momentum dependent. When $\partial\mathcal{V}/\partial\Pi_{i\beta\alpha} = 0$, equation (3.32) describes the average thermal energy of wave packet deformation.

3.3 Numerical Realisation

The above-described model has in its entirety been implemented in `LAMMPS` [220], which is an open-source MD implementation in `C++` utilising `MPI` to distribute the computation. In particular, the `OpenMPI` implementation [322] of the MPI standard has been used. `LAMMPS` is structured around *domain decomposition*, where the spatial domain is divided into regions treated by separate MPI processes. Each process is responsible for evolving all particles in its domain. Information regarding particles close to the edge of the regions is communicated as needed for interactions, and $\boldsymbol{k}$-vector resolve properties are scattered to all processes. This structure parallelises the computational load and scales to a large number of processors, but the structure also improves data locality and cache performance compared to multithreading on shared memory machines.

The Pauli potentials introduced in Section 3.2.3 result in non-separable Hamiltonians, and the standard velocity-Verlet integrator [323] cannot be used along the description in Section 2.3.4. Instead, explicit second and fourth-order Runge-Kutta methods [213, 214] have been applied. A variety of Butcher tableaus were tested, all with similar numerical performance. Therefore, the classical RK4 algorithm was selected as the default choice and used for the computations in this chapter and in Chapters 4 and 5. The Butcher tableau of the RK4 algorithm is shown in Table 3.1.

Table 3.1: The Butcher tableau for the classical RK4 integrator used for the time evolution of the electron and ion degrees of freedom.

0				
1/2	1/2			
1/2	0	1/2		
1	0	0	1	
	1/6	1/3	1/3	1/6

3.3.1 Numerical performance

The numerical performance of the implementation is shown in Figure 3.3 with a varying number of particles and number of processors used. In Figure 3.3(a), the scaling with particle number is shown at the fixed density $r_s = 2$. Close to linear scaling in particle number is demonstrated, showing the feasibility of employing this model to large system sizes. The exact exponent varies in the range of $1.1 - 1.3$, depending on the degree of parallelisation, caused by different limiting factors in the computation. This should be contrasted with DFT-based methods, which commonly scale as $\mathcal{O}\left(N^3\right)$.

Figure 3.3(b) shows the speed-up as the computation is distributed over multiple cores for a fixed system of 2000 protons and 2000 electrons (*strong scaling*). The optimal scaling is proportional to 1/(#MPI) as a fixed amount of work is divided between the processes assuming that there is no incurred cost of parallelisation. The short-range interaction (Pair) and $\boldsymbol{k}$-space evaluation (Ewald) involve little or no communication between processes and therefore scale preferably up to rather few particles per processor. The communication cost (Comm.) increases with parallelisation, but is small in comparison.

The limiting factor is the synchronisation time (Sync), which is the time different processes need to wait for each other due to an unbalanced load. This unbalance is due to a fluctuating number of particles per processor, an effect that grows as fewer particles on average are allocated to each core. Eventually, this plateaus the speed-up. In the above example, the synchronisation time becomes significant when, on average, somewhere between 30 and 60 protons are assigned to each region. Note that this plateau moves further out in terms of processor counts as a larger number of particles are considered. Dynamic load balancing or

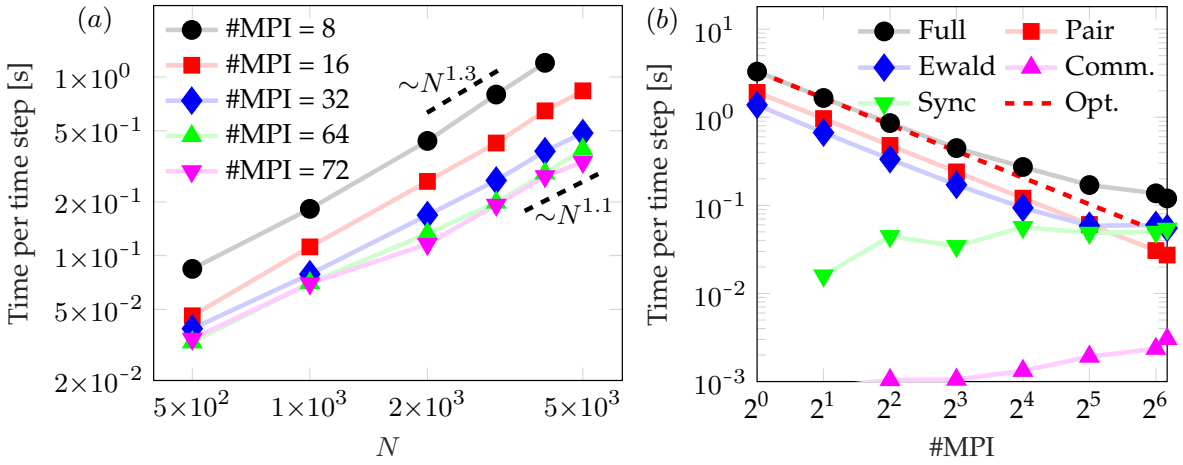

Figure 3.3: Scaling of computational cost for a quasi-neutral system with N protons. The density is $r_s = 2$ and the temperature equals the Fermi temperature. (a) Scaling with particle number for different levels of parallelisation, in the range between $N^{1.1}$ and $N^{1.3}$. The Ewald parameter g was optimised to within $\pm 0.5 a_B^{-1}$ for each case. (b) MPI parallelisation of the computation for a system of $N = 2000$ ions with a fixed Ewald parameter. Showing the full computation (Full), pair interaction (Pair), Ewald summation (Ewald), communication between MPI processes (Comm.), and the synchronisation time different processors need to wait for each other due to an unbalanced load (Sync). The result is compared to the optimal scaling based on the single thread performance (Opt.).

multithreading inside the domain decomposition could address this issue.

3.4 Test Systems

3.4.1 Ground state properties

The properties of the extended wave packet formulation and comparisons with the traditional isotropic model will be explored below in a set of test problems. First, the ground state energy of diatomic hydrogen (H_2) is investigated. The molecular state of hydrogen is considered as the ability of the wave packet to stretch is believed to improve the description of molecular binding [290], and the system naturally breaks rotational symmetry and "activates" the additional degrees of freedom in the elongated wave packets. Ground state properties are obtained by evolving an initially random electron state with the inclusion of friction in the equations of motion which guarantees monotonic energy loss, see Appendix A.2.

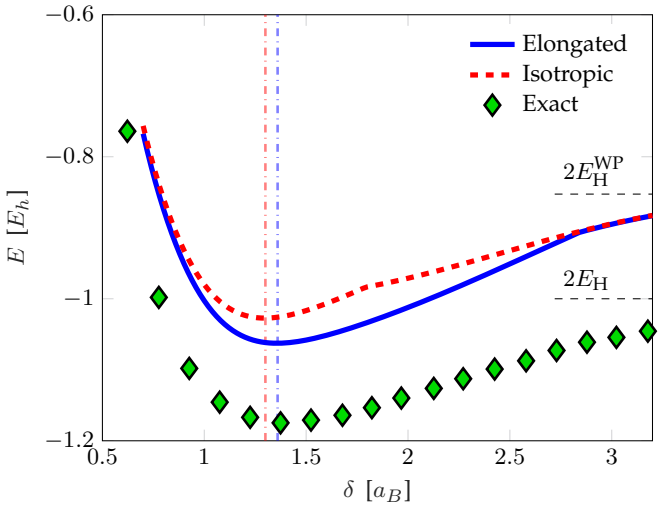

Figure 3.4: Ground state energy of H_2-molecule, E, as a function of nuclear separation δ, computed for the full wave packet model (Elongated), the isotropic wave packets (Isotropic) and the virtually exact result from Angermeier and White [304] (Exact). The ground state is modelled as a triplet state in the wave packet computations, with $\rho = 1$ in the correlation potential $\mathcal{V}_{ij}^{C}$. The equilibrium displacement is marked for the two wave packet models (vertical lines) and the energy of two isolated hydrogen atoms is marked (horizontal lines).

The ground state energy of H_2 within the wave packet model for both elongated and isotropic Gaussian states are shown in Figure 3.4 for a varying nuclear separation δ. The virtually exact results for the energy scales considered here are also provided for reference [304]. The achieved ground state has either the electron wave packets centred between the two nuclei or close to each nucleus (atomic configuration). The configuration that minimises energy depends on the separation δ, and there is a transition from the centred electron density to the atomistic configuration as δ increases. The transition between the two configurations occurs at larger separations $\delta \approx 2.8\,a_{\mathrm{B}}$ for the elongated packets compared to the isotropic one $\delta \approx 1.8\,a_{\mathrm{B}}$. The elongated wave packets are seen to improve the description of the molecular state when $\delta < 2.8\,a_{\mathrm{B}}$. However, an offset is observed to the exact result. In the atomic limit, this offset is caused by the limited functional form of the Gaussian wave packet, which cannot reproduce the cusp at the nuclear positions or the comparatively long tail of the density profile in the true ground state. This energy offset is close to independent of nuclear separations for δ larger than the equilibrium separation. Suggesting that these effects are the main missing features also in the molecular regime, and further improvements of the functional form should

first focus on the description of these aspects in isotropic states.

3.4.2 Binary collisions

As a second test problem, binary collisions between electrons and ions are considered. A full numerical solution of the Schrödinger equation computed by the `SOFT` code [324–326] is used as a benchmark. The centre of mass trajectories for impact parameters in the range $b = 0.6 - 3.0\,a_\mathrm{B}$ is shown in Figure 3.5, alongside a measure of the extent of the electron state orthogonal to the collision direction. The centre of mass trajectories agree well between the two wave packet models and `SOFT`. A qualitatively different behaviour between the wave packet and the full numerical solution is the ability of the electron to fragment. In the full numerical solution, part of the electron density remains bound to the ion, which is not permitted by the wave packet functional form.

The two wave packet models differ in their internal descriptions. For larger impact parameters, the elongated model reproduces the extent of the electron state in the `SOFT` computation better compared to the isotropic formulation where all directions are averaged and a too slow expansion is observed in the direction perpendicular to the collision. In the case of smaller impact parameters, the full numerical solution is close to isotropic but has a non-Gaussian structure during the close approach between the electron and the ion. Neither of the wave packet models represents this intermediate state well, impacting the subsequent evolution to an equal degree.

One of the central quantities in the description of dynamic correlations and relaxation processes is the energy transfer in collisions. Figure 3.6 shows the energy transfer between an electron and an ion in a binary collision. The energy transfer is calculated by time evolving the initially stationary proton, kept fixed in Figure 3.5. Primarily, differences are observed between the two wave packet models for intermediate impact parameters, as in either limit the configuration is close to symmetric or approaches the classical limit. Furthermore, the differences are the most pronounced for smaller wave packets, where the gradients on the length scale of the packet are more pronounced. The result suggests that there might be an

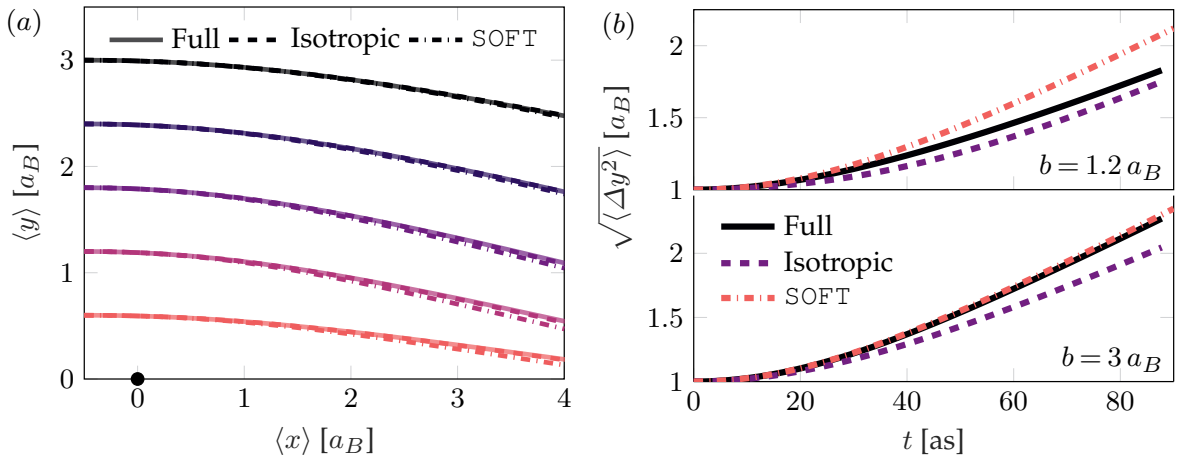

Figure 3.5: Electron scattering of a fixed proton with different impact parameters b computed using an elongated wave packet (Full), an isotropic wave packet (Isotropic) and `SOFT`. (a) The centre of mass trajectories where $\langle x \rangle$ and $\langle y \rangle$ are the state-averaged positions in the x and y directions. (b) Extent of the electron wave function along the y-direction, $\sqrt{\langle y^2 \rangle - \langle y \rangle^2}$, for two impact parameters. The initial wave function was isotropic Gaussians with a width of $1\,a_B$ and a classical momentum such that the total classical energy of each trajectory was $\frac{3}{2}k_\mathrm{B}T$ and $k_\mathrm{B}T = 10\,\mathrm{eV}$.

appreciable difference in the dynamical properties of the two models.

3.4.3 Transport properties

The two previous tests treated few-body systems, but the strength of the wave packet formulation is the ability to model large collections of particles. In the last example of this chapter, this is demonstrated by modelling a partially degenerate and spin un-polarised ($\xi = 0$) hydrogen plasma, with temperature $\theta = 1$ and density $r_s = 2$. Accordingly, a system of 10^3 protons and 500 spin up and down electron wave packets were evolved for 225 fs in NVE after an initial thermalisation phase of 75 fs with velocity re-scaling (Section 2.3.7) based on the temperature description in Section 3.2.5. The simulation was repeated five times with different initial particle configurations for each wave packet model. The treatment of opposite spin interactions by Angermeier and White [304] with $\rho = 1$ was used. The parameters of the regularising confinement potential were $A_w = 3\,E_h/a_\mathrm{B}^2$ and $l_w = 1\,a_\mathrm{B}$.

The radial distribution functions are shown in Figure 3.7(a), computed classically without regard for the extent of the wave packets or the effect of exchange. Exchange contributions –

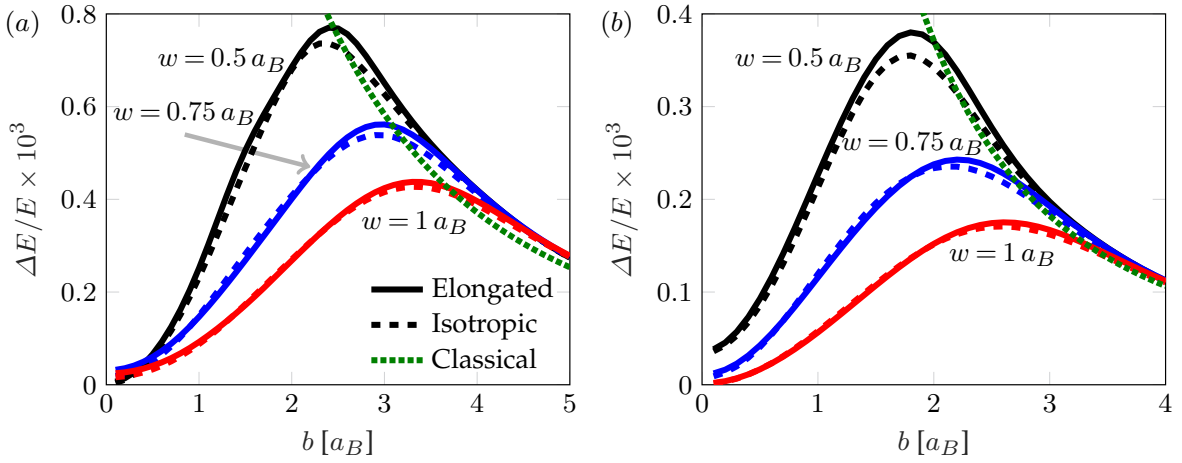

Figure 3.6: Transfer of (classical) kinetic energy $\Delta E/E$ from the electron to the ion in a single electron-ion scattering event as a function of impact parameter b. Initial velocity is set as described in Figure 3.5 with a temperature (*a*) $k_\mathrm{B}T = 5\,\mathrm{eV}$ and (*b*) $k_\mathrm{B}T = 10\,\mathrm{eV}$. The result is shown for different free particle widths w set by the confining potential in equation (3.28) by varying l_w with $A_w = 3\,E_h/a_B^2$.

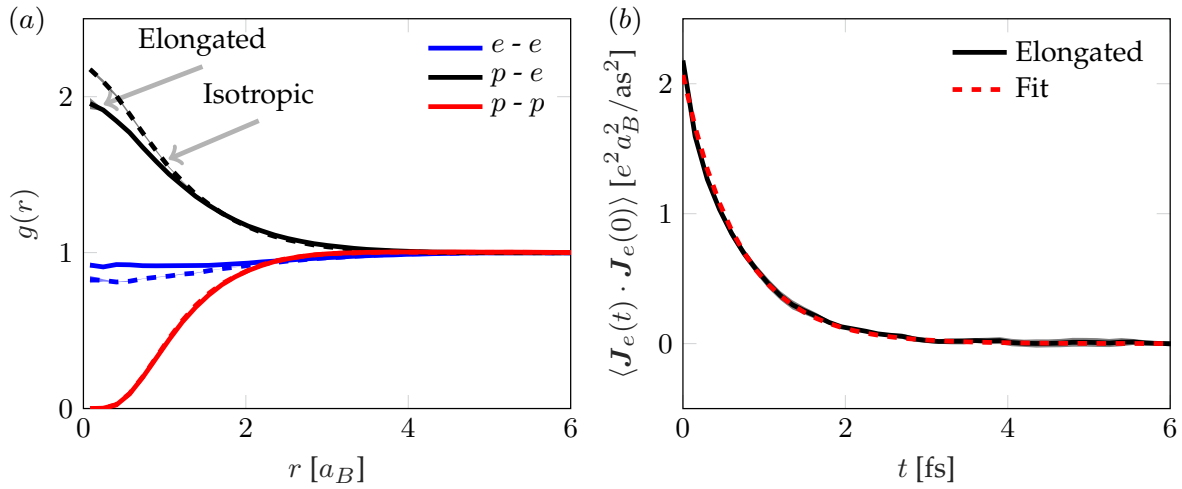

Figure 3.7: (a) Classical radial distribution function for proton-proton (*p*-*p*), electron-electron (*e*-*e*) and proton-electron (*p*-*e*) in both wave packet models, elongated (solid) and isotropic (dashed). Qualitatively similar structures are seen between the two models, where a stronger electron-electron and ion-electron interaction is observed for isotropic packets. The typical errors – estimated from the distinct runs – are shown in the shaded area and only noticeable at small r. (b) The electron current autocorrelation function for the wave packet model (Elongated) is well described by an exponential decay (fit). The thermodynamic conditions are described in Section 3.4.3.

for the RDF calculation itself – set the $r = 0$ limit for equal spin electrons, and not accounting for this explains the lack of a decrease in $g(r)$ for small r. The ion structure is similar between the models and the primary differences are seen in the electron structure. The isotropic packets are seen to interact more strongly both with the ions and between themselves, suggesting a more localised packet in the isotropic case, as expected from Figure 3.5.

Electrical conductivity is one of the fundamental transport properties strongly influenced by inter-species interactions – see discussion in Chapter 5 – and is of major interest in the WDM regime. For atomistic simulations, the Green-Kubo relation for conductivity is [327]

$$\sigma(\omega) = \frac{1}{3k_{\mathrm{B}}T\,V}\int_0^\infty \langle \boldsymbol{J}(t)\cdot\boldsymbol{J}(0)\rangle_T\, e^{i\omega t}\,dt, \tag{3.33}$$

where $\boldsymbol{J}$ is the total electrical current in the simulation. The current is dominated by the contribution from the N_e electrons

$$\boldsymbol{J} \approx \boldsymbol{J}_e = \frac{q_e}{m_e}\sum_{i=1}^{N_e}\langle\hat{\boldsymbol{p}}_i\rangle\,. \tag{3.34}$$

The current-current autocorrelation function is well approximated by an exponential fit, see Figure 3.7(b), a fit which has been used to evaluate equation (3.33) and limit the influence of numerical noise [204]. An exponential current-current autocorrelation function results in a Drude-like conductivity model

$$\sigma(\omega) = \frac{\sigma_0}{1+(\omega/\lambda)^2} + i\,\frac{\sigma_0\omega/\lambda}{1+(\omega/\lambda)^2}, \tag{3.35}$$

where σ_0 and λ are related to the amplitude and time constant of the decaying correlation function. Physically, σ_0 is the DC conductivity while λ corresponds to the inverse of the mean free scattering time. A roughly 15% difference is observed in the predictions of both σ_0 and λ between the models. For elongated wave packets $\sigma_0^{\mathrm{elo}} = (34\,300 \pm 1\,900)\ \Omega^{-1}\mathrm{cm}^{-1}$ and $\lambda^{\mathrm{elo}} = (1.48 \pm 0.06)\ \mathrm{fs}^{-1}$, while for the isotropic model $\sigma_0^{\mathrm{iso}} = (29\,800 \pm 1\,200)\ \Omega^{-1}\mathrm{cm}^{-1}$ and $\lambda^{\mathrm{iso}} = (1.73 \pm 0.06)\ \mathrm{fs}^{-1}$. It is no coincidence that the fractional changes in σ_0 and λ are equal in size but opposite in sign between the models, as for a Drude-like conductivity model

the product of the parameters is constrained by a sum rule [200]. This method for computing conductivity directly from the time dynamics of the current is of considerable interest, as the commonly used Kubo-Greenwood formulation used in DFT-MD does not account for electron-electron scattering [276].

3.5 Conclusion

In this chapter, an extended ansatz for the functional form of the wave packets in wave packet molecular dynamics is presented, which allowed for an MD description – treating partially degenerate electrons and ionic correlations – which bridge the gap in time scale between electron and ion dynamics. The extended functional form allows the wave packet to respond to local gradients on the length scale of the packet itself. The new form has been incorporated self-consistently into `LAMMPS` with good parallel support, treating long-range Coulomb interactions via an Ewald summation and purpose-built Pauli interactions to approximate spin interactions on a pair-exchange level. The computational strategies for an explicit and efficient evaluation of all interaction terms have been discussed. Together with close to a linear scaling with particle number, this formulation is an efficient tool for treating systems of many particles in the WDM regime.

The added flexibility in the wave packet shape improves the description of ground-state hydrogen molecules and binary electron-ion collisions compared to the traditional wave packet shape when tested against exact results. Furthermore, differences are seen for the energy transfer in binary collisions between wave packet models, and the DC electrical conductivity is seen to increase by 15% for a warm dense hydrogen system as the functional form is extended. The properties of this new wave packet model will be further explored in Chapters 4 and 5.

Chapter 4

Dynamic Structure Factors via Explicit Real Time Electron Dynamics

Abstract: The electron dynamic structure factor (DSF) for warm dense hydrogen is investigated on the basis of explicit real-time electron dynamics both for electron and ion time scales, without invoking either the Born-Oppenheimer approximation or the Chihara decomposition. Two descriptions of the electron DSF are presented based on the wave packet model in Chapter 3. The first of these is a semi-classical method in which the classical formulation is corrected based on known quantum constraints. The second is a formulation where the density-response function is evaluated in molecular dynamics and related to the DSF via the fluctuation-dissipation theorem. The static and low-frequency ion behaviour is compared to PIMC and DFT-MD, while the high-frequency behaviour is compared to models for x-ray Thomson scattering. The inelastic scattering signal acquires the correct limits for small and large momentum transfer, and a characteristic flattening of the plasmon dispersion due to interactions is observed in line with analytical models. The models treat electrons and ions on an equal footing, self-consistently describing screening and collisions.

4.1 Introduction

Many of the primary diagnostics for many-body systems are based on light scattering, where the change in photon energy and momentum carries information regarding the energy and momentum states within the sample [206, 328, 329]. The (non-relativistic) interaction Hamiltonian between charged particles and an electromagnetic field is

$$\hat{H}_{\text{int}} = -\sum_i \frac{q_i}{m_i}\hat{\boldsymbol{p}}_i \cdot \boldsymbol{A}(\boldsymbol{r}_j) + \sum_i \frac{q_i^2}{2m_i}\boldsymbol{A}^2(\boldsymbol{r}_i), \tag{4.1}$$

where $\boldsymbol{A}(\boldsymbol{x})$ is the vector potential of the electromagnetic field. The charge and mass of the particle are q_i and m_i, respectively. To first order, the $\boldsymbol{p} \cdot \boldsymbol{A}$ term in equation (4.1) describes

absorption and emission processes, while (non-resonant) scattering is described by the $\boldsymbol{A}^2$ term [328, 330]. The scattering is dominated by the electron contribution – due to the mass ratio – but the ions influence the electron dynamics, and the ion motion can directly be seen in the scattering of the electrons. The scattering probability is described by *Fermi's golden rule* [331], resulting in a differential cross-section proportional to the electron dynamic structure factor $S_{ee}(\boldsymbol{k},\omega)$ [206],

$$\frac{d^2\sigma}{d\Omega d\omega} \propto S_{ee}(\boldsymbol{k},\omega), \tag{4.2}$$

for an energy and momentum change of $\hbar\omega$ and $\hbar\boldsymbol{k}$, respectively. The quantum formulation of the dynamic structure factor in equation (2.16) is acquired through the use of *Heisenberg operators* for the spatially Fourier-transformed density $\hat{n}^\alpha_{\boldsymbol{k}}(t)$. The dynamic structure factor is [206]

$$S_{\alpha\beta}(\boldsymbol{k},\omega) = \frac{1}{2\pi}\int_{-\infty}^{\infty} d\tau\, \frac{e^{i\omega\tau}}{\sqrt{N_\alpha N_\beta}} \left\langle \hat{n}^\alpha_{\boldsymbol{k}}(\tau)\hat{n}^\beta_{-\boldsymbol{k}}(0)\right\rangle_T, \tag{4.3}$$

where the subscripts/superscripts α and β denote the group of particles considered and $\langle\cdot\rangle_T$ is the thermal average. The scattering is therefore related to density fluctuations on the length and time scales of $|\boldsymbol{k}|^{-1}$ and ω^{-1}, respectively.

In this chapter, the focus is on x-ray Thomson scattering (XRTS), a common diagnostic for WDM systems, as the high photon energy can penetrate high-density plasmas [168]. The plasma temperature can be extracted from the scattering spectrum in a model-independent way via detailed balance [133, 332–335]. However, comparisons with synthetic spectra are commonly used for analysis [133, 336–338]. On the other hand, the DSF includes a detailed description of plasma dynamics and can be used to test theoretical models. Therefore, the need to model x-ray scattering – or equivalently dynamic structure factors – goes both ways, furthering diagnostic techniques as well as benchmarking theoretical models.

Most XRTS analyses rely on the Chihara decomposition or the Born-Oppenheimer approximation [116, 168]. The wave packet model presented in the previous chapter can access dynamical properties without resorting to either of these approximations. However, some of the quantum aspects of the scattering need to be expanded on. The extraction and interpretation

of DSF from the wave packet formulation is thus the subject of this chapter, where particular attention is given to a test system of warm dense hydrogen. The remainder of this chapter is structured as follows. Section 4.2 discusses commonly used models and approximations for XRTS. In Section 4.3, the test system is introduced along with computational models for benchmarking, comparisons of which are shown for statics and ion dynamics in Section 4.4. The classical and quantum aspects of the DSF are discussed in Sections 4.5 and 4.6, respectively. A semi-classical formulation of the DSF is reached. Instead, a formulation based on the linear response formulation is discussed in Section 4.7. The results of both models are compared to the standard models of XRTS in Section 4.8.

4.2 Modelling of XRTS spectrum

4.2.1 Chihara decomposition

The density response for a two-component system – electrons (e) and protons (p) – in equation (2.27b) can be rewritten as

$$\chi_{ee} = \left(\frac{\chi_{ep}}{\chi_{pp}}\right)\left(\frac{\chi_{pe}}{\chi_{pp}}\right)\chi_{pp} + \frac{\chi_e^{(0)}}{1 - \tilde{u}_{ee}(\boldsymbol{k})[1 - G_{ee}]\chi_e^{(0)}}, \tag{4.4}$$

where the functional arguments have been omitted for brevity. The first term represents the proton response scaled by the cross-species response (commonly described symmetric with respect to the species index [108]), relating to both screening and bound state dynamics. The second term has the same form as in the UEG, but the *local field correction* (LFC) G_{ee} in the single-component case has been replaced by G_{ee} evaluated in the presence of ions [108, 109]. Via the fluctuation-dissipation theorem – see equations (2.22) and (4.19) for classical and quantum versions, respectively – the density response is directly related to the DSF and highlights contributions both on the ionic and electronic time scales.

The Chihara decomposition relies on a chemical picture where Z_B and Z electrons per ion are labelled as bound and free, respectively. Neglecting correlations between ion motion and

internal bound state dynamics, Chihara gives the total electronic structure factor as [108, 109]:

$$S_{ee}(\boldsymbol{k},\omega) = |f(\boldsymbol{k}) + n(\boldsymbol{k})|^2 S_{ii}(\boldsymbol{k},\omega) + Z S^0_{ee}(\boldsymbol{k},\omega) + Z_B S_{bf}(\boldsymbol{k},\omega). \tag{4.5}$$

Each term has a distinct physical interpretation. The ion-ion structure factor $S_{ii}(\boldsymbol{k},\omega)$ is scaled by the form factors of the bound $f(\boldsymbol{k})$ and screening $n(\boldsymbol{k})$ electron clouds representing the adiabatic electron motion following the ions. The free-electron structure factor S^0_{ee} describes the density correlations in the free-electron population and is commonly modelled by the second term in equation (4.4). Last, the bound-free contribution S_{bf} represents fluctuations in the bound state population. Due to the different time scales and physics related to each term, separate models are often employed for each term in equation (4.5), which may result in a less constrained model overall [172]. Furthermore, the separation of the electron population into bound and free states can be problematic in WDM systems [339].

4.2.2 XRTS models

The *hypernetted chain* (HNC) approximation is commonly used to treat the ion-ion correlations in XRTS analysis [168, 175, 340], which due to its analytical nature allows for exploration of phase space. Explicit many-body calculations either based on *Monte Carlo* (MC) or *molecular dynamics* (MD) on the other hand, do not rely on any closures and are applicable at arbitrary large coupling strengths. However, computational cost limits the number of spectra that can be generated compared to analytical models. Within the particle methods, models range from one-component models (see Section 2.4) to quantum two-component treatments (see Section 2.5) where the effective interactions are based on, e.g. DFT [272, 274] and PIMC [341, 342]. From MD trajectories, $S_{ii}(\boldsymbol{k},\omega)$ may be directly extracted, while MC computations require a type of analytical continuation to access dynamical properties [343, 344]. However, for many applications, the ion dynamics occur in a narrow frequency range and

$$S_{ii}(\boldsymbol{k},\omega) = S_{ii}(\boldsymbol{k})\delta(\omega) \tag{4.6}$$

is a common approximation when the ion dynamics are not directly investigated. For particle methods which explicitly solve for the electron density, the screening cloud $n(\boldsymbol{k})$ can be computed self-consistently [345].

The random phase approximation (RPA) [208] is the base model for the free-electron contribution S^0_{ee}. The RPA qualitatively describes both the single-particle ($\boldsymbol{k} \to \infty$) and collective ($\boldsymbol{k} \to 0$) regimes, but electron-ion collisions and electron correlations can shift and broaden features in the spectrum. Mermin's formulation of the dielectric functions is commonly used to incorporate the effect of inter-species collisions [89, 346–349], while approximations or parametrisations of LFCs G_{ee} can be used to model electron correlations [247, 248]. For atomistic models of $S^0_{ee}(\boldsymbol{k}, \omega)$, an explicit treatment of the electron dynamics is needed [350] and, particularly, the time dependence is required for the ω-dependence. *Time-dependent DFT* (TD-DFT) evolve electronic properties and may access $S^0_{ee}(\boldsymbol{k}, \omega)$ [172, 286], although the restricted time scales considered do not permit simultaneous evaluation of $S_{ii}(\boldsymbol{k}, \omega)$. Alternatively, *linear response TD-DFT* may be utilised for linear response properties, avoiding explicit time evolution [174, 279, 280]. DFT formulations are commonly performed in the adiabatic approximation [281]. Statistical methods, such as PIMC, do not rely on the Born-Oppenheimer approximation [263], but as in the case of ions, the ω-dependence cannot be directly accessed. Instead, reconstructions based on LFCs have been suggested for the warm dense electron gas [251, 351, 352].

The properties of bound states, $f(\boldsymbol{k})$ and $S_{bf}(\boldsymbol{k}, \omega)$, are commonly taken from atomic data and computations [168, 353], as the requirements for modelling these states are substantially different from the free-electrons. The bound-free term, $S_{bf}(\boldsymbol{k}, \omega)$, typically contributes at a larger ω and can overlap with the free-electron feature [168, 353–355].

A combined treatment of S^0_{ee} and S_{ii} within a single MD model requires not only resolving electron density perturbation over ionic time-scales but also the treatment of large enough systems to access the collective behaviour. Semi-classical QSP models [89, 91–93, 356, 357] and wave packet descriptions [358] have previously been used to model the plasmon resonances for WDM. This chapter extends these discussions by simultaneously resolving the ion features

and focusing on intrinsically quantum aspects of the scattering.

4.3 Simulation models

4.3.1 System parameters

The discussion will focus on a particular test system of warm dense hydrogen, for which the description in terms of the wave packet model in Chapter 3 is appropriate. In particular, a density of $r_s = 2$ or approximately $n_i = n_e \approx 2 \times 10^{23}\,\mathrm{cm}^{-3}$, and temperature $T = 250\,\mathrm{kK} \approx 21.5\,\mathrm{eV}$, result in moderately coupled protons $\Gamma_{pp} \approx 0.63$ and partially degenerate electrons $\theta \approx 1.72$. This level of degeneracy results in substantial quantum corrections to the spectrum, while the pair-exchange approximation is still satisfactory.

The Saha equation with Debye-Hückel or ion-sphere ionisation potential depression models [6] predict full ionisation under these conditions and therefore all electrons are treated as free, i.e. $f(\boldsymbol{k}) = 0$, $Z = 1$ and $Z_B = 0$. The coupling is far below the Wigner crystallisation point [70, 71], and the system is homogeneous and isotropic. The computational result is therefore averaged over equivalent directions and depends only on the magnitude of the wave vector $k = |\boldsymbol{k}|$. The Chihara decomposition then simplifies to

$$S_{ee}(k,\omega) = |n(k)|^2 S_{ii}(k,\omega) + S^0_{ee}(k,\omega). \tag{4.7}$$

The screening length, equation (1.17), and plasma frequency, equation (1.10), for the condition is $\lambda_s \approx 1.54\,a_\mathrm{B} \approx 0.81\,\text{Å}$ and $\hbar\omega_p \approx 16.7\,\mathrm{eV}$, respectively.

4.3.2 Wave packet simulations

For the wave packet computations, the model in Chapter 3 is employed with $N_p = 2048$ protons and an equal number of electrons. The system was initially thermalised using velocity re-scaling after which data collection occurred in NVE. The presented data have been averaged over 70 simulations of length 40 fs, interleaved with short thermalisation phases. With a time step of 4×10^{-5} fs, the energy drift was below one percent of the ion thermal energy for the

complete run. The computational details for the impulse computations in Section 4.7 are discussed separately in Appendix B.4.

For the simulations, Pauli interactions of the second type discussed in Section 3.2.3 were used and each spin species was subdivided such that a quarter of all electron pairs interacted through $\mathcal{V}_{ij}^{C}$. The confinement potential did not have a flat bottom, i.e. $l_w = 0$, and a confinement strength of $A_w = 3\,\mathrm{Ha}/a_\mathrm{B}^2$ was used. A full exploration of the dependence on this regularisation has not been carried out, but in Appendix B.1 an additional confinement strength is tested. It is established that the ion structure is insensitive to the choice of A_w and only a minor dependence is seen for the electrons.

4.3.3 PIMC simulations

A comparison for the static structure is provided by PIMC simulations, see Section 2.5.1, where the Fermion sign problem is tackled directly by averaging over independent simulations [263]. This comes with a substantial computational cost and the system size investigated was therefore limited to $N_p = 32$ protons. However, the results are, in principle, exact within the statistical errors and for the given size system.

4.3.4 DFT-MD simulations

The ion dynamics were tested against DFT-MD. Specifically, the DFT was performed using the `CP2K` package [359] with a mixed Gaussian and plane basis set. The Kohn-Sham orbitals were expanded in contracted Gaussians, whereas the electronic charge density was represented using plane waves. The former used an accurate triple basis set with additional sets of polarisation functions TZV2PX [360], while for the latter a cutoff of 500 Ha was employed. The exchange-correlation functional was approximated within the local density approximation (LDA) with a norm-conserving pseudopotential [361]. For the Brillouin zone integration, only the Γ-point was used.

The MD was carried out with $N_p = 128$ protons and an ionic time step of 0.0725 fs was seen to conserve energy appropriately. Thermalisation was performed using a Nosé-Hoover

thermostat with a time constant of 100 fs, after which data was collected in NVE for 1700 fs.

4.4 Static and ionic properties

The PIMC simulations have full access to static properties, while the DFT-MD simulations model ion structure and dynamics along with electron screening. These properties are used to benchmark the wave packet model. The static structure factor is the zero time separation of the intermediate scattering function, i.e. $S_{\alpha\beta}(\boldsymbol{k}) = F_{\alpha\beta}(\boldsymbol{k}, 0)$. The classical intermediate scattering function computed based on mass centres $\boldsymbol{r}_i(t)$ ($\boldsymbol{r}_j(t)$) of particles of type α (β) is

$$F_{\alpha\beta}(\boldsymbol{k}, \tau) = \frac{1}{\sqrt{N_\alpha N_\beta}} \sum_{i,j} \left\langle e^{-i\boldsymbol{k}\cdot(\boldsymbol{r}_i(t+\tau) - \boldsymbol{r}_j(t))} \right\rangle_t , \tag{4.8}$$

which is evaluated by a time average $\langle\cdot\rangle_t$ from the MD trajectories. The static structure factor for the WPMD and PIMC models is shown in Figure 4.1(a) where the wave packet model is seen to mostly agree with Monte Carlo results, except for a reduced electron structure at shorter wavelengths, a consequence of the limited functional form of the wave packets. The finite extent wave packet softens short-range interactions and does not allow for density fluctuations below the typical packet size. These effects are especially noticeable for wavelengths below the average packet sizes.

However, the ion structure factor shows more structure at intermediate $\boldsymbol{k}$-values suggestive of suppressed electron-ion screening in WPMD compared to PIMC. This interpretation is supported by Figure 4.1(b) which shows the average form factors of the electron screening clouds around the ions in the simulation. The screening cloud is isolated from the cross-species structure factors, $|n(\boldsymbol{k})| = |S_{ie}(\boldsymbol{k})/S_{ii}(\boldsymbol{k})|$, similar to how it has previously been defined in real-space for DFT applications [345]. A suppressed form factor $|n(\boldsymbol{k})|$ at large $\boldsymbol{k}$ is seen in the WPMD model, likely due to the functional form not allowing a highly localised electron density close to the ion core. The ion structure is insensitive to the choice of confinement potential (see Appendix B.1) and the average packet size, but the restricted form still influences the screening at intermediate $\boldsymbol{k}$. The ion structure factor from the DFT-MD agrees well with the

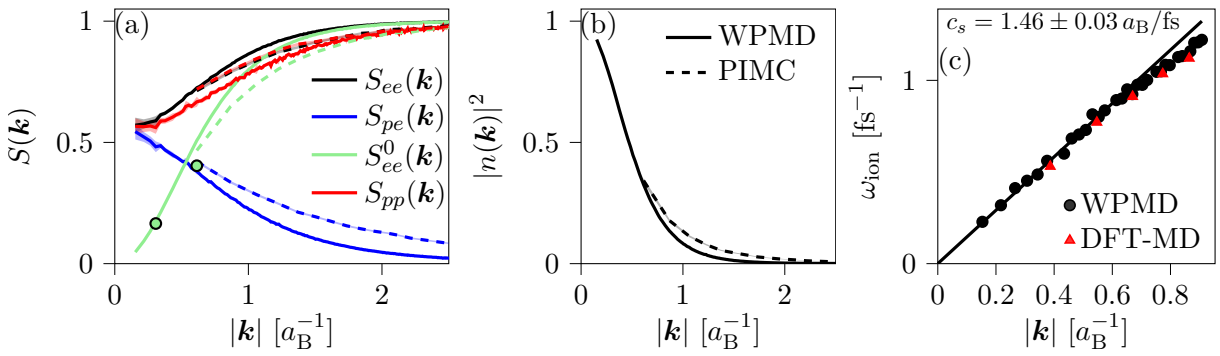

Figure 4.1: Comparisons of static structure and ion dynamics. Shaded regions correspond to 95% confidence intervals estimated from simulations with different initial conditions. (a) Static structure factors for electron-electron $S_{ee}(\boldsymbol{k})$, proton-proton $S_{pp}(\boldsymbol{k})$, proton-electron $S_{pe}(\boldsymbol{k})$ and free electron-electron $S^0_{ee}(\boldsymbol{k}) = S_{ee}(\boldsymbol{k}) - |n(\boldsymbol{k})|^2 S_{pp}(\boldsymbol{k})$ compared between WPMD (solid) and PIMC (dashed). Dots show the static structure computed within the impulse response formulation, see Section 4.7. (b) The screening form factors $n(\boldsymbol{k})$ with the WPMD (solid) and PIMC (dashed) simulations. Statistical errors are estimated from the independent runs and shown by the shaded areas which are comparable to the line width. (c) Ion acoustic dispersion within WPMD (circles) and DFT-MD (triangles) is based on a constrained GCM-fit to the intermediate scattering function [203, 362]. Ion sound speed, c_s, in the wave packet model is based on a linear fit $\omega_{\mathrm{ion}}(\boldsymbol{k}) = c_s|\boldsymbol{k}|$ for $|\boldsymbol{k}| \leq 0.5\, a_B^{-1}$.

PIMC results.

The free-electron contribution to the static structure factor can be extracted from WPMD and PIMC, but this extraction is not directly possible in models that treat the electrons adiabatically [350]. The free-electron contribution is shown in Figure 4.1(a) and tends to agree between the models for wavelengths large compared to the packets. The access to free-electron dynamics allows for the investigation of electron time scale features in Sections 4.5 – 4.8 using the WPMD model. However, the low-frequency ion dynamics is considered first.

The WPMD and DFT-MD methods can evolve a sufficient number of ions for a time long enough to model ion acoustic modes, although the required time steps are substantially different. The wave packet model considers thermal electron motion, whereas the adiabatic electron treatment in DFT-MD only requires the ion dynamics to be temporally resolved. The ion-acoustic resonance is obtained by fitting a generalised collective mode (GCM) [203, 362] constrained by the first three classical sum rules, equation (2.20), to the intermediate scattering function for protons ($\alpha = \beta = p$). In the GCM, one diffusive and two oscillating features

were included, such that three parameters were fitted for each $\boldsymbol{k}$, namely, the oscillation frequency ω_{ion}, and the decay times of the oscillating and diffusive mode. The ω_{ion} for the two computational models is seen to agree in Figure 4.1(c), both in the regions of linear dispersion and as the dispersion flattens. The linear regime is indicative of an acoustic mode and the slope is related to the ion sound speed [110, 175, 202, 203]. A fit to the wave packet data suggests an ion sound speed of $c_s = 1.46\,a_{\text{B}}/\text{fs} \approx 77.3\,\text{km/s}$, while no prediction is made for the DFT model due to the limited data for the linear dispersion.

4.5 Classical dynamic structure factors

The classical formulation of time correlations in equation (4.8) has been applied to electrons previously for semi-classical MD [89, 93, 356, 357] and WPMD [358]. However, the classical formulation neglects inherently quantum aspects, some of which will be discussed in Section 4.6. Nevertheless, the classical treatment can demonstrate the interplay between electron and ion dynamics.

The electron density correlations over time are shown in Figure 4.2(a), which reveals two distinct time scales. The longer time scale features represent the correlations between adiabatic screening clouds around the ions. This is explicitly demonstrated by subtracting the screening contribution,

$$F^0_{ee}(\boldsymbol{k},\tau) = F_{ee}(\boldsymbol{k},\tau) - |n(\boldsymbol{k})|^2 F_{pp}(\boldsymbol{k},\tau), \tag{4.9}$$

which is seen to isolate the high-frequency signal to a high degree. This is observed computationally before $F_{pp}(\boldsymbol{k},\tau)$ has converged if all contributions in equation (4.9) are taken from the same simulation, as the electrons will quasi-instantaneous equilibrate to a specific ion configuration.

The free-electron contribution S^0_{ee} in the Chihara decomposition, is described by the high-frequency signal $F^0_{ee}(\boldsymbol{k},\tau)$. Figure 4.2(b) shows the free-electron term resolved in frequency space, where a clear plasmon resonance close to the plasma frequency ω_p is demonstrated.

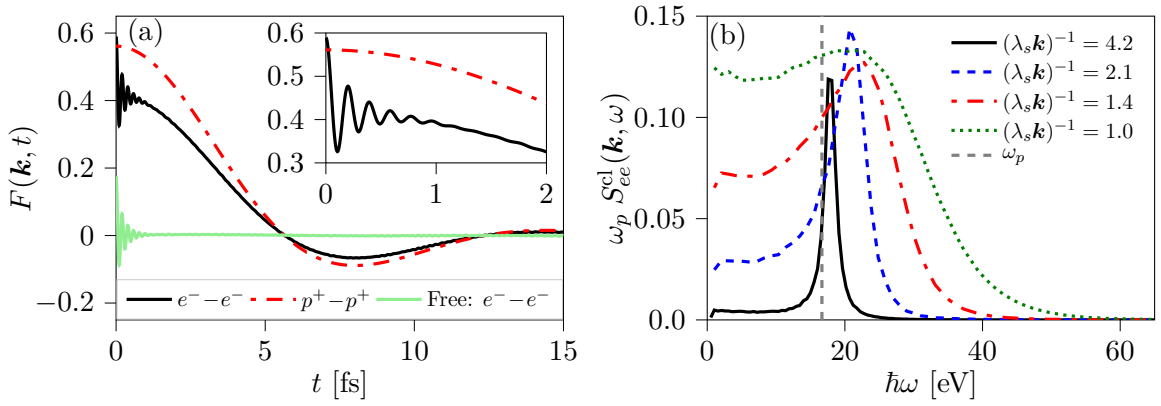

Figure 4.2: (a) Classical intermediate scattering functions $F(\boldsymbol{k}, t)$ at $k = 0.31\, a_{\mathrm{B}}^{-1}$ for electrons $(e^- - e^-)$, protons $(p^+ - p^+)$ and the isolated free-electron contribution (Free: $e^- - e^-$). The ion screening and the plasma oscillations are shown. (b) The dynamic structure factor for free-electrons with a clear plasmon feature in the collective regime ($(\lambda_s \boldsymbol{k})^{-1} \gg 1$) which is broadened as the non-collective regime is approached.

On length scales large compared to the screening length, $(\lambda_s \boldsymbol{k})^{-1} \gg 1$, collective dynamics dominate and a narrow feature is seen, only broadened by collisional interactions. On smaller length scales, the plasmon feature is widened and a single particle mode appears at $\omega = 0$ within the classical formulation. Being a particle method, WPMD treats both the collective and single particle regimes, where collisions and screening are self-consistently accounted for.

The use of the Chihara decomposition above has only been to interpret and isolate different physical processes. The WPMD formulation does not rely on the Chihara decomposition as electron and ion dynamics are treated on an equal footing. A combined spectrum showing both ion-acoustic and plasmon modes is demonstrated in Figure 4.8 after quantum corrections have been applied.

4.6 Quantum aspects of dynamic structure factors

Up to this point, the discussion has been classical and the explicit time dependence of the Heisenberg operators in equation (4.3) has been neglected. The classical treatment does not adhere to known constraints such as the f-sum rule and detailed balance [177, 363, 364]. The f-sum rule refers specifically to the second sum rule. In a quantum treatment, the first three

sum rules in equation (2.20) are modified to [201]

$$\left\langle \omega^0 \right\rangle_{S_{ee}} = \int_{-\infty}^{\infty} d\omega \quad S_{ee}(\boldsymbol{k},\omega) = F_{ee}(\boldsymbol{k},0) \qquad = S_{ee}(\boldsymbol{k}), \tag{4.10a}$$

$$\left\langle \omega^1 \right\rangle_{S_{ee}} = \int_{-\infty}^{\infty} d\omega\ \omega^1 S_{ee}(\boldsymbol{k},\omega) = \frac{\partial F_{ee}(\boldsymbol{k},t)}{\partial t}\Big|_{t=0} = \frac{\hbar \boldsymbol{k}}{2m_e}, \tag{4.10b}$$

$$\left\langle \omega^2 \right\rangle_{S_{ee}} = \int_{-\infty}^{\infty} d\omega\ \omega^2 S_{ee}(\boldsymbol{k},\omega) = \frac{\partial^2 F_{ee}(\boldsymbol{k},t)}{\partial t^2}\Big|_{t=0} = \frac{k_\mathrm{B}T}{m_e}\boldsymbol{k}^2 + \mathcal{O}\left(\hbar^2\right), \tag{4.10c}$$

where an an asymmetry between positive and negative ω is needed. Another aspect of this asymmetry is detailed balance,

$$S(\boldsymbol{k},-\omega) = e^{-\beta\hbar\omega} S(-\boldsymbol{k},\omega), \tag{4.11}$$

which is required for any structure factor $S(\boldsymbol{k},\omega)$ and a consequence of the occupation of states in the statistical formulation [363, 364]. Classical formulations are time inversion symmetric, $F_{\alpha\beta}(\boldsymbol{k},\tau) = F_{\alpha\beta}(\boldsymbol{k},-\tau)$, in equilibrium and directly contradict detailed balance. However, accounting for the operator algebra only requires $F_{\alpha\beta}(\boldsymbol{k},\tau) = F^*_{\alpha\beta}(\boldsymbol{k},-\tau)$, and in quantum formulations, $F_{\alpha\beta}(\boldsymbol{k},\tau)$ is necessarily complex-valued.

For typical ion dynamics in the WDM regime, $\beta\hbar\omega \ll 1$, and the ions can largely be treated classically. The electrons on the other hand have plasma frequencies where $\beta\hbar\omega_p \gtrsim 1$ and $\mathcal{O}(\hbar)$ modifications are substantial. For the test system under consideration $\beta\hbar\omega_p \approx 0.8$.

Consider the intermediate scattering function in the Schrödinger picture

$$\begin{aligned} F_{\alpha\alpha}(\boldsymbol{k},\tau) &= \frac{1}{N_\alpha}\left\langle \langle \Psi(t+\tau)|\, \hat{n}^\alpha_{\boldsymbol{k}} e^{-i\hat{H}\tau/\hbar} \hat{n}^\alpha_{-\boldsymbol{k}}\, |\Psi(t)\rangle \right\rangle_t \\ &= \frac{1}{N_\alpha}\sum_{i,j}\left\langle \langle \Psi(t+\tau)|\, e^{-i\boldsymbol{k}\cdot\hat{\boldsymbol{r}}_i} e^{-i\hat{H}\tau/\hbar} e^{i\boldsymbol{k}\cdot\hat{\boldsymbol{r}}_j}\, |\Psi(t)\rangle \right\rangle_t, \end{aligned} \tag{4.12}$$

where $|\Psi(t)\rangle$ is the simulation state at some time t. Note the additional time propagator, not acting on the simulation state but rather the modified state

$$\left|\Psi'(t)\right\rangle = e^{i\boldsymbol{k}\cdot\hat{\boldsymbol{r}}_j}\left|\Psi(t)\right\rangle. \tag{4.13}$$

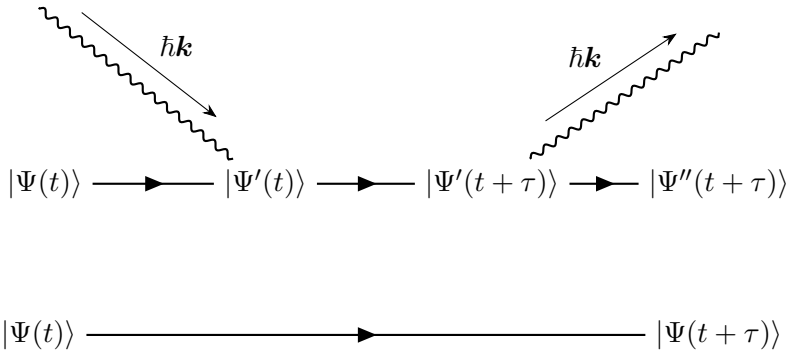

Figure 4.3: Schematic of the scattering mechanics which is implicit in the definition of the dynamic structure factor. Equation (4.12) is a sum over terms $\langle\Psi(\tau)|\Psi''(\tau)\rangle$ where the absorption and emission are performed by different orbitals.

The modified state has gained the momentum $\hbar\boldsymbol{k}$ compared to the thermal state. Methods which can represent and propagate $|\Psi'\rangle$ in time can evaluate equation (4.12) without additional assumptions – an idea which extends to two-time correlations more generally [365] – but equilibrium methods typically only treat the thermal state $|\Psi(t)\rangle$. Equation (4.12) can be interpreted as the overlap between unperturbed dynamics $|\Psi(t)\rangle$ and a state $|\Psi''(t+\tau)\rangle$ that experiences a type of scattering. The scattering in question is depicted in Figure 4.3, where the original state $|\Psi(t)\rangle$ absorbs some momentum $\hbar\boldsymbol{k}$ ($|\Psi'(t)\rangle$), is propagated for some time τ ($|\Psi'(t+\tau)\rangle$) and emits the same momentum ($|\Psi''(t+\tau)\rangle$). The particle that introduces the momentum $\hbar\boldsymbol{k}$ is arbitrary, as the DSF is related to multiple types of scattering [206], but can be thought of as a photon. The classical approximation therefore amounts to neglecting the influence of the momentum shift on the dynamics.

The effect of this momentum shift is clear in a non-interacting system, describing the large $\boldsymbol{k}$ limit in interacting systems. The dominant contribution to $F_{\alpha\alpha}(\boldsymbol{k},\tau)$ is the self-contribution, $i=j$, which if written in terms of plane waves $|\boldsymbol{p}\rangle$ is

$$\begin{aligned} F_{\alpha\alpha}(\boldsymbol{k},\tau) &= \sum_{\boldsymbol{p},\boldsymbol{p'}} \Big\langle \langle\boldsymbol{p}|\Psi(0)\rangle \langle\Psi(0)|\boldsymbol{p'}\rangle\, e^{i\omega_{\boldsymbol{p}}\tau} \times \langle\boldsymbol{p'}|\, e^{-i\boldsymbol{k}\cdot\hat{\boldsymbol{r}}} e^{-i\hat{H}\tau/\hbar} e^{i\boldsymbol{k}\cdot\hat{\boldsymbol{r}}}\, |\boldsymbol{p}\rangle \Big\rangle_T \\ &= \sum_{\boldsymbol{p}} \Big\langle |\langle\Psi(0)|\boldsymbol{p}\rangle|^2 \Big\rangle_T\; e^{-i\tau\left(\omega_{\boldsymbol{p}+\hbar\boldsymbol{k}}-\omega_{\boldsymbol{p}}\right)}, \end{aligned} \tag{4.14}$$

and $\hbar\omega_{\boldsymbol{p}} = \boldsymbol{p}^2/(2m_\alpha)$ is the energy of the plane-wave state $|\boldsymbol{p}\rangle$. The pre-factor represents the

probability of each plane wave state in the thermal ensemble, and the exponential describes a sort of interference between the unmodified and modified states. The exponent expands to $\omega_{\boldsymbol{p}+\hbar\boldsymbol{k}} - \omega_{\boldsymbol{p}} = (\boldsymbol{p}\cdot\boldsymbol{k})/m + \omega_R$. The $(\boldsymbol{p}\cdot\boldsymbol{k})/m_\alpha$ term is the translation of the unmodified state for non-interacting systems, an equivalent of which is found in the classical formulation. The second term is the recoil energy $\hbar\omega_R = \hbar^2\boldsymbol{k}^2/(2m_\alpha)$, which is the energy associated with the momentum kick $\hbar\boldsymbol{k}$. Assuming a classical thermal distribution of the momentum states $|\boldsymbol{p}\rangle$, the resulting dynamic structure factor is

$$S_{\alpha\alpha}(\boldsymbol{k},\omega) = \sqrt{\frac{m_\alpha\beta}{2\pi\boldsymbol{k}^2}}e^{-\frac{m_\alpha\beta}{2\boldsymbol{k}^2}(\omega-\omega_R)^2}. \tag{4.15}$$

This spectrum incorporates the *Compton shift*, satisfies the f-sum rule and detailed balance. The same result can be derived using operator notation and commutators; see, e.g., Scopigno *et al.* [201].

In quantum kinetic formulations, the quantum recoil is commonly added by shifting the resonance by ω_R [366]. Single particle modes are shifted as in equation (4.15), while collective plasma oscillations with frequency ω_0 are modified as [348, 367]

$$\omega_0^2 \to \omega_0^2 + \omega_R^2. \tag{4.16}$$

Traditional, classical results have been corrected to comply with detailed balance via [201, 368, 369]

$$S(\boldsymbol{k},\omega) = \frac{\beta\hbar\omega}{1-\exp\left(-\beta\hbar\omega\right)}S^{\mathrm{cl}}(\boldsymbol{k},\omega), \tag{4.17}$$

where the superscript "cl" has been added to denote the classical structure factor. Ortner *et al.* [356] motivated this correction by assuming that the MD simulation is described by the classical fluctuation-dissipation theorem, equation (2.22), and the dielectric response is adequately captured. However, the same corrections are found when considering the relaxation function formulation [370]. The above correction satisfies the f-sum rule if the classical result obeys the classical third sum rule as $\langle\omega\rangle_S = \beta\hbar\langle\omega^2\rangle_{S^{\mathrm{cl}}}/2$.

The traditional correction cannot be applied to the single particle limit as $S(\boldsymbol{k}) > S^{\mathrm{cl}}(\boldsymbol{k})$,

and $S(\boldsymbol{k}) \nrightarrow 1$ for $\boldsymbol{k} \to \infty$. Furthermore, expanding the single-particle limit in equation (4.15) gives

$$S(\boldsymbol{k}, \omega) = e^{\frac{\beta\hbar}{2}(\omega - \omega_R/2)} S^{\text{cl.}}(\boldsymbol{k}, \omega), \tag{4.18}$$

which is remarkably different from equation (4.17) for $\beta\hbar\omega \gtrsim 1$. Therefore, an interpolation between the two cases is proposed, whereby isolating the single-particle and collective modes, each contribution is corrected appropriately. The single particle mode is corrected according to equation (4.18) and the collective modes are shifted according to equation (4.16) and weighted according to equation (4.17). The different components of the spectrum are isolated by fitting a sum of a GCM (one diffusive and one collective mode) and a weighted single-particle spectrum to the classical results. The total functional form is constrained by three sum rules, equation (2.20). Further details are given in Appendix B.2.

Before proceeding to discuss alternative methods for computing $S_{ee}(\boldsymbol{k}, \omega)$ via the fluctuation-dissipation theorem, it is worth pointing out the benefit of deriving the electron dynamics from equations (4.12) and (4.13). The fluctuation-dissipation theorem relies on an equilibrium assumption, but in many experimental realisations gradients and non-thermal distribution functions may alter the XRTS signal [169–171, 371–373]. Equations (4.12) and (4.13) could add to this discussion of these effects. However, the wave-packet approximation and especially the confinement potential strongly influence the result in this case. As seen in the non-interacting case of equation (4.14) the confinement potential would add a suppression factor when the modified $\langle \Psi(\tau) | \, \hat{\boldsymbol{r}}_i \, | \Psi(\tau) \rangle$ and unmodified $\langle \Psi'(\tau) | \, \hat{\boldsymbol{r}}_i \, | \Psi'(\tau) \rangle$ trajectories have a separation comparable to the size of the wave packet. The wave packet formulation is thus not suited for this type of description.

4.7 Density response and dynamic structure factors

Time-dependent DFT methods have considered the *density response function* $\chi_{ee}(\boldsymbol{r}, \boldsymbol{r}', t - t')$ and its relation to $S_{ee}(\boldsymbol{k}, \omega)$ via the fluctuation-dissipation theorem [172], instead of directly treating the two-time correlation functions. For finite $\hbar$, the fluctuation-dissipation theorem

reads [195, 206]:

$$S_{ee}(\boldsymbol{k},\omega) = -\frac{\hbar}{1-\exp\left(-\beta\hbar\omega\right)}\frac{\mathrm{Im}\left\{\chi_{ee}(\boldsymbol{k},-\boldsymbol{k},\omega)\right\}}{\pi N_e}, \tag{4.19}$$

which satisfies detailed balance as $\mathrm{Im}\{\chi_{ee}\}$ is odd in ω. The relation between $S_{ee}(\boldsymbol{k},\omega)$ and $\mathrm{Im}\{\chi_{ee}\}$ imposes an equivalent f-sum rule for $\mathrm{Im}\{\chi_{ee}\}$, which is $\hbar$-independent and a consequence of mass conservation, see Giuliani and Vignale [363]. Therefore, even classical models satisfy this f-sum rule. In Appendix B.3 an equivalent of the f-sum rule for the wave packets is derived and some nuances are discussed when the wavelength of the external perturbation is comparable to the size of the wave packet.

For the computation of the density-response functions directly in MD, the methodology of Sakko *et al.* [374] was used. Accordingly, an impulse of strength I_0 acts as an external stimulus $V_\alpha^{\mathrm{ext}}(\boldsymbol{r},t) = I_0\delta(t)\exp\left(i\boldsymbol{k}\cdot\boldsymbol{r}\right)\delta_{\alpha e}$, giving the electrons a momentum kick with spatial structure. This particular structure of external perturbations relates the spatial Fourier transform of the density response to the response function via

$$\delta n_\alpha(\boldsymbol{k},t) = I_0\int d^3\boldsymbol{r}d^3\boldsymbol{r}'e^{-i\boldsymbol{k}\cdot(\boldsymbol{r}-\boldsymbol{r}')}\chi_{\alpha e}(\boldsymbol{r},\boldsymbol{r}',t), \tag{4.20}$$

and the Fourier transform in time yields the density response function in equation (4.19). In practice, real-valued impulses must be applied in the MD. The real and imaginary parts of the impulses are simulated separately, and the density perturbations are added appropriately within linear theory. The impulse is implemented as an instantaneous change in the momentum variables, as described in Appendix B.3.

The density response was averaged over multiple starting configurations taken from thermal simulations to account for statistical variations in ion configurations and the thermal electron population. Further details on the impulse computations are given in Appendix B.4. After proper thermal averaging, the response without an external potential must vanish, although for any given initial configuration some thermal fluctuations will be measured. Unperturbed trajectories were also recorded and the thermal fluctuation was subtracted from the response to accelerate convergence when performing parameter scans. However, this acceleration technique

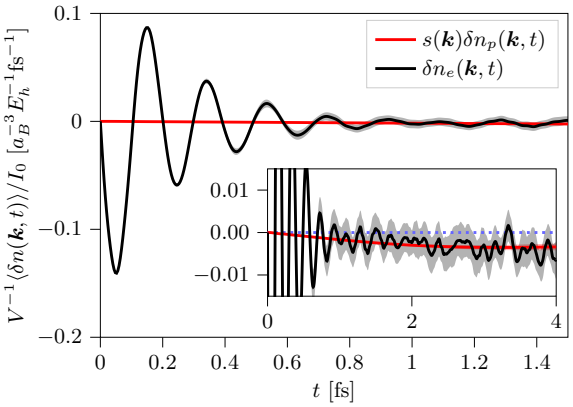

Figure 4.4: Fourier transform density response resolved in time for the electrons δn_e (perturbed species) and the protons δn_p at $\boldsymbol{k} = 0.31\,k_\mathrm{B}^{-1}$. The proton response is scaled with a screening factor $s(\boldsymbol{k})$ to match long-time electron response. The dominant signal is the high-frequency plasma oscillations on top of a smaller amplitude proton response over longer time scales (as shown in the inset). Subtraction of the scaled proton signal isolates the high-frequency dynamics analogously to Figure 4.2. Shaded areas are 95% confidence intervals, estimated from variations between impulse simulations.

was not used for the final density response seen in Figure 4.4.

After the external perturbation of the electron population, the electron density response in Figure 4.4 is a damped oscillation in time, representing a plasma oscillation damped by collisions. The inset of Figure 4.4 shows the density response of the ions related to the cross-species response function χ_{pe} and not χ_{pp} appearing in the Chihara decomposition. The ion response is weak but is proportional to the long-time signal for electrons, suggesting a screening relation between the two responses. This method for determining $S_{ee}(\boldsymbol{k},\omega)$ via χ_{ee} is primarily used to model the high-frequency electron dynamics – which limits the time window of χ_{ee} needed to be converged – and the screening contribution is subtracted analogously to Section 4.5. The classical thermal simulation data are then used to substitute the screening contribution.

4.7.1 Linear response

The magnitude of the density response is determined by I_0. A large density response is beneficial for improving the signal-to-noise ratio for measuring χ_{ee}, but the response must remain in the linear response regime for the fluctuation-dissipation theorem to be valid. Figure

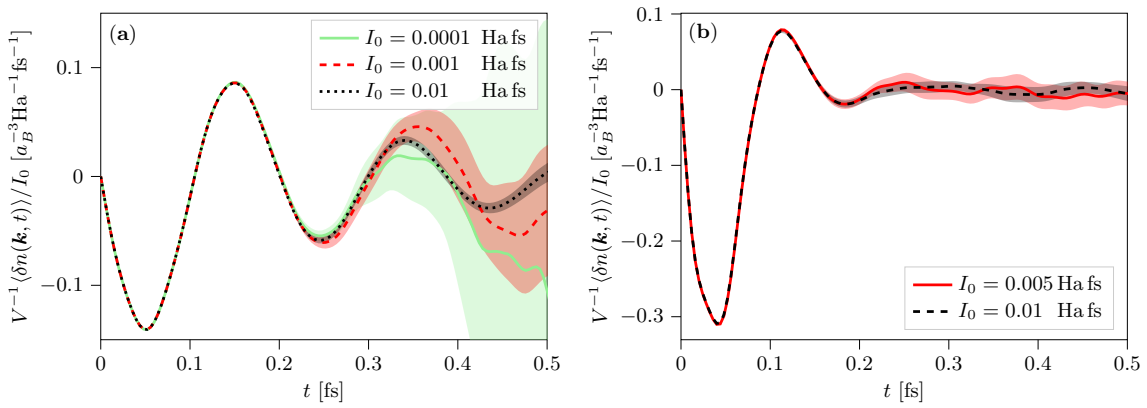

Figure 4.5: The linearity of the impulse response tested for $(\lambda_s \boldsymbol{k})^{-1} = 2.1$ (a) and $(\lambda_s \boldsymbol{k})^{-1} = 1.1$ (b) with respect to impulse strength I_0. Shaded areas represent an estimate of the 95% confidence interval assuming all the simulation results are Gaussian distributed around the response function. All simulations agree within the error estimates.

4.5 shows the density response normalised by I_0, which in the linear regime is independent of the impulse strength. The change in momentum for any particle due to the impulse is limited by

$$|\Delta \boldsymbol{p}_i| \leq I_0 |\boldsymbol{k}|, \tag{4.21}$$

as given by equation (B.10a) in Appendix B. A first estimate for the upper bound of the impulse strength is given by limiting the associated change in energy to 1% of $k_\mathrm{B}T$. In Figure 4.5 the response due at two different wavelengths is shown, for which the estimate for I_0 is $I_0 \lesssim 0.01$ Ha fs and $I_0 \lesssim 0.005$ Ha fs in the long and short wavelength case, respectively. The linearity of the density response around this level of impulse strength is seen when comparing substantially different impulses in Figure 4.5. All the results shown are within the 95% confidence interval from each other. The statistical uncertainty becomes more severe for longer time differences after the impulse as the signal decays, especially for weaker impulses. For the shorter wavelength case in Figure 4.5(a), non-linear effects were observed for $I_0 = 0.1$ Ha fs. In the following comparisons, the impulse strength is $I_0 = 0.01$ Ha fs.

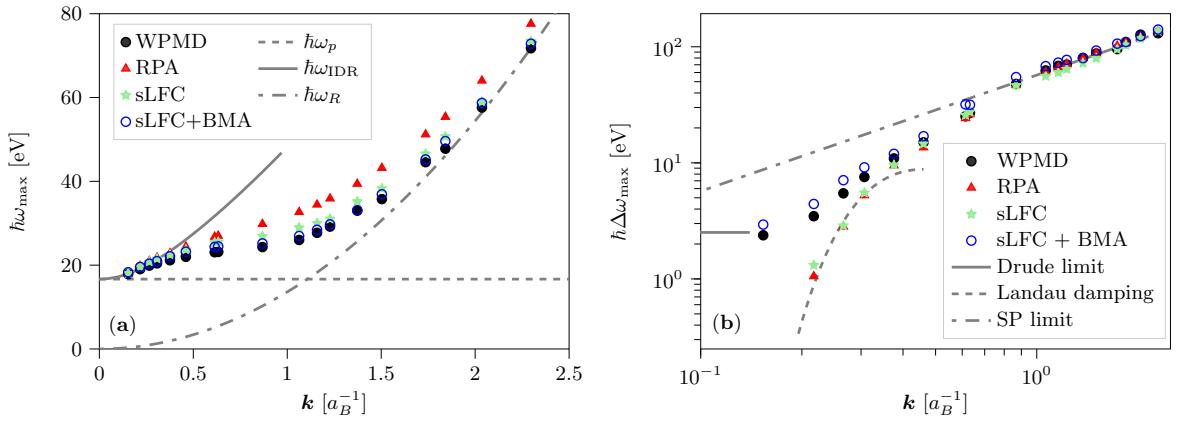

Figure 4.6: (a) Position and (b) width of the largest feature in the free-electron DSF. Widths are given as FWHM of a Gaussian fit to the feature. The models compared are the semi-classical formulation based on WPMD, the random phase approximation (RPA), with local field correction for UEG [207] (sLFC) and extended Mermin formulation (sLFC + BMA) [247, 248] with collision frequencies within the Born approximation [348] using ion structure from the wave packet simulation. The position of the features are compared to the analytical model by Thiele *et al.* [348] labelled ω_{IDR} and the recoil frequency ω_R in the small and large $\boldsymbol{k}$-limits, respectively. The long wavelength limit of the width is compared with the Drude limit of the Mermin formulation with collisions in the BMA model and to classical Landau damping rates [288]. For large $\boldsymbol{k}$-vectors the single-particle limit (SP limit) describes the width of the feature.

4.8 Dynamic structure factor: Comparison and predictions

The results of the two computational techniques for the electron DSF are compared to the commonly used models for XRTS analysis discussed in Section 4.2.2. The position and width of the largest feature in the free-electron structure factor are shown in Figures 4.6(a) and 4.6(b), respectively. The dominant feature in the collective regime is a plasmon resonance, whereas the Compton feature dominates in the single-particle limit. For $|\boldsymbol{k}| < 0.5a_{\mathrm{B}}^{-1}$, the position of the plasmon is well represented by the analytical model by Thiele *et al.* [348], however, for $\boldsymbol{k}$-vectors in the range $\lambda_s|\boldsymbol{k}| = 1 - 3$, the dispersion is flattened in both the wave packet model and the RPA. The flattening is especially pronounced for models which incorporate interaction effects. The plateau is shifted downwards as electron correlations and electron ion collisions are accounted for, using static LFC (sLFC) parameterised for the UEG by Dornheim *et al.* [207] and the first Born approximation [348] using the extended

Mermin formulation [247, 248] (sLFC+BMA), respectively. The downshift of the plasmon resonance due to electron correlations is arguably related to the *roton feature* discussed for hydrogen at lower temperatures [173, 251, 375] and the shift due to collisions is related to an imaginary component of the dynamic collision frequency [248]. The wave packet model and the sLFC+BMA model predict a similar dispersion, with a slightly larger downshift within the MD model. For non-collective dynamics, $|\boldsymbol{k}| > 3\lambda_s^{-1}$, all computational models converge to the Compton shift ω_R, but the RPA model does so substantially slower than the other models.

When comparing the widths of the plasmon features in Figure 4.6(b), two distinct groups of models appear. The WPMD and sLFC+BMA, and the RPA and sLFC models, characterised by either including electron-ion collisions or not. When collisions between the species are accounted for, the electron density wave can efficiently lose momentum, and a finite width of the plasmon feature is approached for long wavelengths. This behaviour is obtained by the Drude limit of the Born-Mermin ansatz [248]. The prediction of similar widths between the WPMD and sLFC+BMA models is therefore indicative of similar electron-ion coupling within the models. For electron only models, the dominant damping mechanism is Landau damping, as is demonstrated by comparison with the classical Landau damping rate [288] in Figure 4.6(b). For intermediate $\boldsymbol{k}$, models with and without cross-species collisions result in similar widths, suggesting that kinetic effects are dominant. All models agree in the single particle limit.

Two spectra are shown in Figure 4.7 where the impulse response computations are compared with the models in Figure 4.6. For the conditions under consideration, the effect of detailed balance is apparent in the spectrum. A high level of agreement is demonstrated between the semi-classical equilibrium formulation and the impulse response computations, suggesting that the corrections applied to the classical formulation are the dominant ones. Some differences in the integrals of the spectrum – the static structure factor – are shown in Figure 4.1(a), where a reduction is observed when $\boldsymbol{k}^{-1}$ is comparable to the size of the wave packet. This is once more attributed to the restricted functional form of the wave packet which does not allow the impulse to stimulate density perturbations smaller than the wave packet. Overall, the spectral

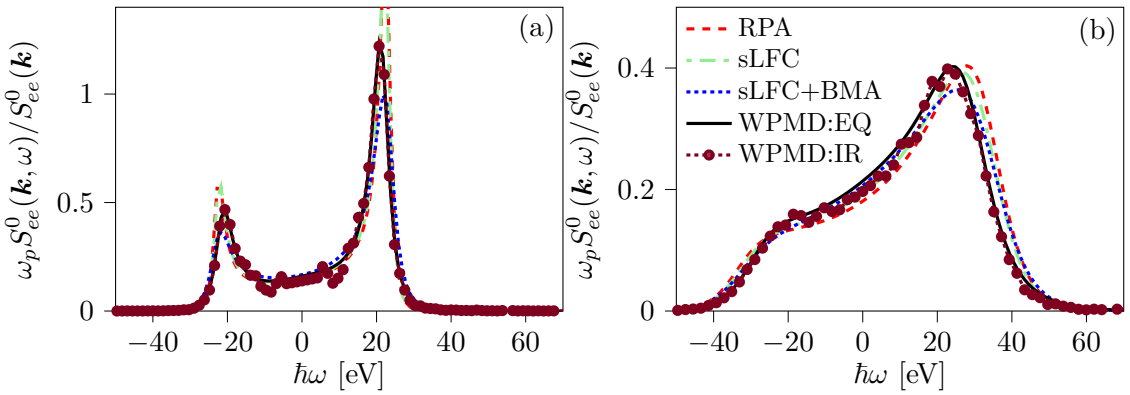

Figure 4.7: Comparisons of free-electron dynamic structure factors in the collective regime (a) $(\lambda_s \boldsymbol{k})^{-1} = 2.1$ and (b) $(\lambda_s \boldsymbol{k})^{-1} = 1.1$. The models are given in Figure 4.6 with the addition of the impulse response results (WPMD:IR) as described in Section 4.7. A fit of $\mathrm{Im}\{\chi_{ee}\}$ for small ω was used to regularise the effect of noise when applying the fluctuation-dissipation theorem. The impulse response computations agree well with the semi-classical corrections for the WPMD (WPMD:EQ).

shapes of all the models are very similar, where the primary differences are the shift of the peak and the peak width, the trends of which were described above.

Lastly, the ability of the WPMD model to incorporate both the electron and the ion time scale features is demonstrated in Figure 4.8. The complete electron structure factor shows the free-electron feature with a comparatively narrow and large amplitude ion feature around $\omega = 0$. When the ion feature is resolved, clear ion acoustic modes are observed. The ion spectrum also includes an entropy mode at $\omega = 0$, which is wide enough to meagre with the ion-acoustic modes which prevents a clear graphic separation. However, the entropy mode constitutes roughly 52% of the total integral of the ion feature. The ion feature is corrected based on equation (4.17), but the introduced asymmetry is minor due to the limited frequency range of the ion density perturbations.

4.9 Conclusion

The ability of x-rays to penetrate dense plasmas and the wealth of physical information encoded in the scattering spectrum have resulted in *x-ray Thomson scattering* (XRTS) being one of the primary diagnostics for warm dense matter experiments. In particular, the spectrum describes

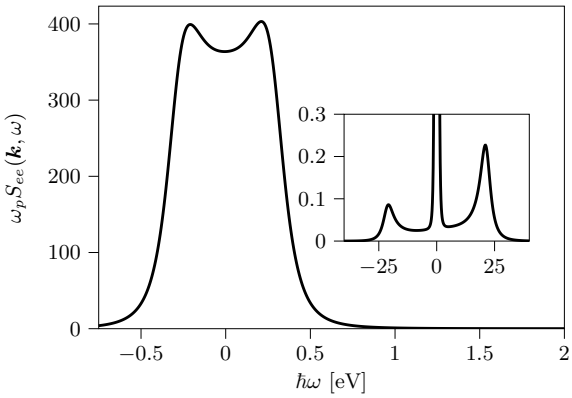

Figure 4.8: The complete electron structure factor at $\boldsymbol{k} = 0.31\, a_{\mathrm{B}}^{-1}$, incorporating the scaled ion dynamics and the plasmon feature. The ion time scale feature is extracted based on GCM fit (see Section 4.5) and scaled by the screening factor $|n(\boldsymbol{k})|^2$. A minor asymmetry is introduced in the ion component by the traditional detailed balance correction, equation (4.17). The electron feature – visible in the inset – is given by the semi-classical correction formulation.

both ion and electron time-scale phenomena, where a quantum treatment is needed for the inelastic scattering. In this chapter, the wave packet model was used to simultaneously describe both time scales without invoking either the Born-Oppenheimer or the Chihara decomposition. The static properties of the model have been benchmarked against PIMC, where some effects of the wave packet restriction are seen for length scales on the order of and below the typical wave packet size. Comparison of the ion dynamics with DFT-MD shows good agreement for the ion-acoustic dispersion over a wide range of length scales.

The quantum aspects of the scattering have been discussed from the perspective of real-time evolution. The classical formulations are seen as the limit where the effect of the quantum recoil on the dynamics is neglected. Ultimately, two approaches for computing dynamic structure factors within the wave packet formulation have been suggested. First, a semi-classical approach where the classical computations are corrected based on known quantum constraints, where the collective and single particle behaviour is treated separately. Second, via the fluctuation-dissipation theorem and explicit evaluation of the density response function in MD by introducing external impulse in the simulation. Both formulations agree well, validating the semi-classical approach and suggesting that the corrections applied account

for the dominant quantum effects.

Comparing the inelastic scattering with commonly used models for XRTS, the wave packet models show broadly the same spectral shapes as RPA-based models when approximate treatments of electron correlations and electron-ion collisions are incorporated. In particular, the characteristic flattening of the plasmon dispersion in interacting models is observed, and a similar level of collisional broadening of the plasma feature is seen as in the first Born approximation.

The equal treatment of the electron and ion degrees of freedom results in a combined spectrum of excitations, where a narrow ion feature close to $\omega = 0$ is seen on top of a broader electron feature. The only missing contribution to the XRTS spectrum in the wave packet model is now the contribution from bound states. Bound states are not appropriately modelled in the current wave packet model with the Gaussian functional form and the pairwise exchange approximation. In the following chapter, the long wavelength limit of the free-electron scattering is further considered and modelled within a hydrodynamic description.

Chapter 5

Electron Transport Properties via Explicit Real Time Electron Dynamics

Abstract: Electron transport properties are extracted from simulations of the atomistic two-component model presented in Chapter 3, by mapping the long wavelength behaviour of the dynamic structure factors to a two-fluid model. The mapping procedure is performed by fitting simultaneously in wavelength and frequency space, a process performed via Markov Chain Monte Carlo sampling. The free-electron dynamic structure factor and its properties within a hydrodynamic formulation are investigated, justifying its application to warm dense matter. Specifically, the model is applied to the test system in Chapter 4 and the inferred electron transport properties agree with various reference calculations. The exception is the electron viscosity, where a substantial decrease is observed compared to the classical models.

5.1 Introduction

The properties of dense and highly non-ideal plasmas remain uncertain [59], due to an interplay of complicating factors during experimental realisations using lasers [116, 128, 137, 376–378], for example, the transient nature of the state and a mixture of thermodynamic conditions present simultaneously within the sample. Transport properties are especially unconstrained, where two recent workshops [60, 61] have demonstrated discrepancies between models that range over orders of magnitude. These discrepancies are most noticeable when comparing first-principle models and analytical models commonly employed in hydrodynamic simulations, a discrepancy that influences the predictive capabilities of hydrodynamic simulations [63, 148, 379, 380].

Atomistic first-principle models based on MD or MC can fully account for interactions and correlations, but are limited to smaller system sizes as discussed in the introduction to Chapter 2. Extracting hydrodynamic constituent relations based on first-principle computations is an

efficient way to incorporate non-ideal effects when describing phenomena on longer length scales. Two prime examples are the widely used SESAME [381] and FPEOS [26] tables, parameterising the equation of state. In this chapter, the transport properties of the electrons within the two-component model are extracted by mapping the long wavelength behaviour of the dynamic structure factors from MD to a hydrodynamic model. The mapping is facilitated by Bayesian parameter estimation [382], allowing for validation of the hydrodynamic model in question, and estimation of uncertainty and correlations between the inferred properties. The methodology is general and may be applied to any modelling technique or even experimental data with access to the electron dynamic structure factor at sufficiently long wavelengths. In this chapter, the methodology is applied to the wave packet model described in Chapter 3.

The remainder of the chapter is structured as follows. Section 5.2 describes the two-fluid model used and derives the structure factor within this model. The requirements for appropriately comparing the hydrodynamic model with MD data are discussed in Section 5.3. The details of the Bayesian inference model are given in Section 5.4, followed by its application to MD data in Section 5.5.

5.2 Hydrodynamic model

Electron plasma waves are caused by electrostatic forces attempting to restore local charge neutrality, and a two-fluid model is the minimal theoretical description. The two-fluid model is valid for long enough wavelengths that kinetic effects are negligible. It was demonstrated in Chapter 4 that collisional interaction with the ions is the primary damping mechanism for electron plasma waves, at sufficiently long wavelengths. Schmidt *et al.* [383] considered a quantum hydrodynamic formulation for electrons in a single fluid treatment. However, their formulation lacks the correct limiting behaviour of the plasmon feature, as collisional exchange of momentum and energy between electrons and ions is neglected. Their formulation is extended in this section for a classical hydrodynamic model, a choice which is further motivated in Section 5.3.

Specifically, the fluid equations of interest are for electrons ($\mu = e$, $\bar{\mu} = i$) and ions ($\mu = i$,

$\bar{\mu} = e$), respectively:

$$\frac{D\rho_\mu}{Dt} + \rho_\mu \boldsymbol{\nabla} \cdot \boldsymbol{v}_\mu = 0, \tag{5.1a}$$

$$\rho_\mu \frac{D\boldsymbol{v}_\mu}{Dt} + \boldsymbol{\nabla} \cdot \mathbf{P}_\mu = -\frac{q_\mu}{m_\mu} \rho_\mu \boldsymbol{\nabla}\phi - \boldsymbol{R}_{\mu\bar{\mu}} \left(\rho_\mu, \boldsymbol{v}_\mu - \boldsymbol{v}_{\bar{\mu}}\right), \tag{5.1b}$$

$$\rho_\mu \frac{D\epsilon_\mu}{Dt} + \mathbf{P}_\mu \colon \boldsymbol{\nabla}\boldsymbol{v}_\mu + \boldsymbol{\nabla} \cdot \boldsymbol{q}_\mu = -\frac{q_\mu}{m_\mu} \rho_\mu \boldsymbol{v}_\mu \cdot \boldsymbol{\nabla}\phi - g \left(T_\mu - T_{\bar{\mu}}\right), \tag{5.1c}$$

which in convective form describe the conservation of mass, momentum, and energy. In the above, m_μ, q_μ, ρ_μ, $\boldsymbol{v}_\mu$, and ϵ_μ are the particle mass, particle charge, mass density, (fluid) velocity, and internal energy (per unit mass). Furthermore,

$$\frac{D}{Dt} \equiv \frac{\partial}{\partial t} + \boldsymbol{v}_\mu \cdot \boldsymbol{\nabla} \tag{5.2}$$

is the material derivative.

The constitutive relations for the pressure tensor $\mathbf{P}_\mu$ and the heat flux $\boldsymbol{q}_\mu$ are chosen as in classical hydrodynamics. The pressure tensor is described by the Navier–Stokes form [175, 196, 197],

$$\mathbf{P}_\mu = p_\mu \mathbf{I} - \left[\zeta_\mu - \frac{2\eta_\mu}{3}\right] (\boldsymbol{\nabla} \cdot \boldsymbol{v}_\mu)\, \mathbf{I} - \eta_\mu \Big[\boldsymbol{\nabla}\boldsymbol{v}_\mu + (\boldsymbol{\nabla}\boldsymbol{v}_\mu)^\intercal\Big], \tag{5.3}$$

where p_μ is the (thermodynamic) pressure, η_μ is the shear viscosity and ζ_μ is the bulk viscosity. The heat flux is described by Fourier's law [175, 196, 197]

$$\boldsymbol{q}_\mu = -\kappa_\mu \boldsymbol{\nabla} T_\mu, \tag{5.4}$$

where κ_μ is the thermal conductivity.

A memory function formulation is used to represent the momentum transfer between species,

$$\boldsymbol{R}_{\mu\bar{\mu}} \left(\rho_\mu, \Delta\boldsymbol{v}\right) = \int_{-\infty}^{\infty} d\tau\ \rho_\mu(\tau) r_{\mu\bar{\mu}}(\tau)\, \Delta\boldsymbol{v}(t-\tau), \tag{5.5}$$

where momentum conservation is satisfied if $\rho_e r_{ei} = \rho_i r_{ie}$. The Fourier transform of $r_{\mu\bar{\mu}}(\tau)$ is the dynamic collision frequency $\nu_{\mu\bar{\mu}}(\omega)$. The coupling $r_{\mu\bar{\mu}}$ has a causal structure and the

dynamic collision frequency must satisfy the Kramers–Kronig relations in equation (2.24). The motivation for this exact form will be apparent in Section 5.2.3. The energy exchange between electrons and ions is a slower process than the momentum transfer, and the corresponding collision frequency is typically suppressed by the mass ratio [165]. Energy exchange is therefore described by a relatively simple two-temperature model with a temperature relaxation rate of g [61, 94]. This type of energy transfer is commonly used in combination with Fourier heat flow [384–386] and is a special case of a more general heat transport model [387].

The fluid equations (5.1a) – (5.1c) are closed by Poisson's equation for the electrostatic potential ϕ:

$$\varepsilon_0 \boldsymbol{\nabla}^2 \phi = -\left(\frac{q_i}{m_i} \rho_i + \frac{q_e}{m_e} \rho_e \right). \tag{5.6}$$

The inclusion of electrostatic interactions on this form is well-motivated for collisional systems [246].

Using thermodynamic relations [196, 388], the energy conservation equation (5.1c) may be reformulated purely in terms of a local temperature T_μ:

$$\begin{aligned} \rho_\mu C_{V,\mu} \frac{DT_\mu}{Dt} = &- \boldsymbol{\nabla} \cdot \boldsymbol{q}_\mu + \left(\zeta_\mu - \frac{2\eta_\mu}{3} \right) (\boldsymbol{\nabla} \cdot \boldsymbol{v}_\mu)^2 + \eta_\mu \left[\boldsymbol{\nabla} \boldsymbol{v}_\mu + (\boldsymbol{\nabla} \boldsymbol{v}_\mu)^\intercal \right] : \boldsymbol{\nabla} \boldsymbol{v}_\mu \\ &- \rho_\mu C_{V,\mu} \frac{\gamma_\mu - 1}{\alpha_{T,\mu}} \boldsymbol{\nabla} \cdot \boldsymbol{v}_\mu - \frac{q_\mu}{m_\mu} \rho_\mu \boldsymbol{v}_\mu \cdot \boldsymbol{\nabla} \phi - g \left(T_\mu - T_{\bar{\mu}} \right), \end{aligned} \tag{5.7}$$

where $C_{V,\mu}$ is the specific heat a constant volume, γ_μ is the adiabatic index and $\alpha_{T,\mu}$ is the coefficient of thermal expansion. Furthermore, the pressure may be eliminated from the system through the application of [196, 388]:

$$\boldsymbol{\nabla} p_\mu = \frac{c_{s,\mu}^2}{\gamma_\mu} \left(\boldsymbol{\nabla} \rho_\mu + \rho_\mu \alpha_{T,\mu} \boldsymbol{\nabla} T_\mu \right), \tag{5.8}$$

which introduces $c_{s,\mu}^2 = (\partial p_\mu / \partial \rho_\mu)_{s_\mu}$, the adiabatic sound speed for classical fluids.

The hydrodynamic equations (5.1a), (5.1b), and (5.7) closed with equations (5.3), (5.4), (5.5), (5.6), and (5.8) form the bases for the hydrodynamic analysis in this chapter. The transport coefficients will be extracted from atomistic simulations in Section 5.5 and are for now unspecified. This results in a rather general formulation, although the hydrodynamic

description is limited to small wave numbers $\boldsymbol{k}$ and low frequencies ω. Theories that generalise to finite $\boldsymbol{k}$ and ω, the so-called viscoelastic theories [175, 196, 370], introduce additional *a priori* unknown coefficients to be inferred and the comparison with MD data is thus restricted to the hydrodynamic regime.

5.2.1 Linearised hydrodynamic equations

The density-density correlation spectrum from small amplitude fluctuations is investigated by linearising the hydrodynamic equations around a static and homogeneous equilibrium. Due to the large mass ratio between ions and electrons, dynamics develops on two well-separated time scales. The comparatively *slow* ion dynamics and the corresponding electron screening, and the *fast* plasma oscillations. Specifically, perturbations on the form

$$\begin{aligned} \rho_e &= \rho_{0,e} + \delta\bar{\rho}_e + \delta\rho_e, \quad & \rho_i &= \rho_{0,i} + \delta\bar{\rho}_{i,0}, \\ \boldsymbol{v}_e &= \delta\bar{\boldsymbol{v}}_e + \delta\boldsymbol{v}_e, & \boldsymbol{v}_i &= \delta\bar{\boldsymbol{v}}_i, \\ T_e &= T_{0,e} + \delta\bar{T}_e + \delta T_e, & T_i &= T_{0,i} + \delta\bar{T}_i, \end{aligned} \tag{5.9}$$

are considered. The index 0 and the "bar" represents the equilibrium and slow time scale perturbations, respectively. All remaining perturbations are fast. The heavy ions only exhibit slow perturbations. Charge neutrality requires $q_i\rho_{0,i}/m_i = -q_e\rho_{0,e}/m_e$, and temperature equilibrium is assumed $T_{0,i} = T_{0,e}$. The separation into slow and fast electron dynamics corresponds to the screening cloud and free electron term in the Chihara decomposition [108, 109], as explicitly shown in Section 4.5. In this chapter, only the free electron dynamics (fast perturbations) are considered, but for completeness the slow dynamics is described in Appendix C.1.

The slow dynamics are isolated by time averaging the electron equations over time scales long compared to both the inverse (electron) plasma frequency ω_p^{-1} and the time scale of thermal electron motion. In linear perturbation theory, fast fluctuations average to zero. Isolated equations for the fast perturbations are obtained by subtracting the time-averaged

equations from the original electron equations which, to linear order, yields

$$\frac{\partial \delta\rho_e}{\partial t} = -\rho_{0,e}\boldsymbol{\nabla}\cdot\delta\boldsymbol{v}_e, \tag{5.10a}$$

$$\rho_{0,e}\frac{\partial \delta\boldsymbol{v}_e}{\partial t} = -\frac{c_{s,e}^2}{\gamma_e}\left(\boldsymbol{\nabla}\delta\rho_e + \rho_{0,e}\alpha_{T,e}\boldsymbol{\nabla}\delta T_e\right) + \eta_e\boldsymbol{\nabla}^2\delta\boldsymbol{v}_e + \left(\zeta_e + \eta_e/3\right)\boldsymbol{\nabla}\boldsymbol{\nabla}\cdot\delta\boldsymbol{v}_e - \frac{q_e}{m_e}\rho_{0,e}\boldsymbol{\nabla}\delta\phi - \boldsymbol{R}_{ei}\left(\rho_{0,e},\delta\boldsymbol{v}_e\right), \tag{5.10b}$$

$$\rho_{0,e}C_{V,e}\frac{\partial \delta T_e}{\partial t} = -\rho_{0,e}C_{V,e}\frac{\gamma_e - 1}{\alpha_{T,e}}\boldsymbol{\nabla}\cdot\delta\boldsymbol{v}_e + \kappa_e\boldsymbol{\nabla}^2\delta T_e - g\delta T_e, \tag{5.10c}$$

$$\boldsymbol{\nabla}^2\delta\phi = -\frac{q_e}{m_e\varepsilon_0}\delta\rho_e, \tag{5.10d}$$

and the transport coefficients are constants to first order. In a higher order treatment – an equivalent of *Zakharov's equations* [389] – the slow and fast dynamics couple together, however, such treatment is beyond the current scope.

The density and temperature fields in equations (5.10a) and (5.10c), do not couple to the full velocity field perturbation $\delta\boldsymbol{v}_e$, but rather only with the divergence $\boldsymbol{\nabla}\cdot\delta\boldsymbol{v}_e$. Therefore, two velocity degrees of freedom – the shear modes – decouple from the density fluctuations [196] and three modes will appear in the spectrum of density correlations. In the following, these modes will be identified as one entropy and two plasmon modes.

5.2.2 Hydrodynamic fluctuations and dynamic structure factors

The spectrum of density-density correlations is examined through a spatial Fourier transform in combination with a temporal Laplace transform, following the well-established methodology in Refs. [175, 196, 239, 370, 383, 388, 390]. The notation

$$\delta\tilde{\boldsymbol{x}}_{\boldsymbol{k}}^{\mu}(s) = \int_0^\infty dt\, e^{-st}\int d^3\boldsymbol{r}\, e^{-i\boldsymbol{k}\cdot\boldsymbol{r}}\delta\boldsymbol{x}_\mu(\boldsymbol{r},t) \tag{5.11}$$

is used to describe the desired transform of any vector quantity $\delta\boldsymbol{x}_\mu$. The linearised system in equation (5.10) may be written as

$$\left[s\mathbf{I} + \mathbf{D}_e(\boldsymbol{k})\right]\,\delta\tilde{\boldsymbol{y}}_{\boldsymbol{k}}^e(s) = \delta\boldsymbol{y}_{\boldsymbol{k}}^e(0) \tag{5.12}$$

for the combined perturbation variable

$$\delta\tilde{\boldsymbol{y}}^{\mu}_{\boldsymbol{k}}(s) = \left[\delta\tilde{\rho}^{\mu}_{\boldsymbol{k}}(s),\, i\rho_{0,\mu}\boldsymbol{k}\cdot\delta\tilde{\boldsymbol{v}}^{\mu}_{\boldsymbol{k}}(s),\, \rho_{0,\mu}\delta\tilde{T}^{\mu}_{\boldsymbol{k}}(s)\right]^{\intercal}, \tag{5.13}$$

and initial condition

$$\delta\boldsymbol{y}^{\mu}_{\boldsymbol{k}}(0) = \left[\delta\rho^{\mu}_{\boldsymbol{k}}(0),\, i\rho_{0,\mu}\boldsymbol{k}\cdot\delta\boldsymbol{v}^{\mu}_{\boldsymbol{k}}(0) + i\boldsymbol{k}\cdot\boldsymbol{R}_{0,\boldsymbol{k}}/s,\, \rho_{0,\mu}\delta T^{\mu}_{\boldsymbol{k}}(0)\right]^{\intercal}. \tag{5.14}$$

Variables without a "tilde" are evaluated in the time domain and represent the initial condition at $t = 0$. $\boldsymbol{R}_{0,\boldsymbol{k}}$ describes the contribution to the momentum memory function from $t < 0$. The linearised dynamics are completely determined by the hydrodynamic matrix

$$\mathbf{D}_e(\boldsymbol{k}) = \begin{bmatrix} 0 & 1 & 0 \\ -\left(\omega_p^2 + \gamma_e^{-1}c_{s,e}^2\boldsymbol{k}^2\right) & \nu_{ei} + \nu_{L,e}\boldsymbol{k}^2 & -\alpha_{T,e}\gamma_e^{-1}c_{s,e}^2\boldsymbol{k}^2 \\ 0 & \alpha_{T,e}^{-1}\left(\gamma_e - 1\right) & \gamma_e\left(\mathfrak{g}_e + \chi_e\boldsymbol{k}^2\right) \end{bmatrix} \tag{5.15}$$

and the eigenvalues of $\mathbf{D}_e(\boldsymbol{k})$ describe the modes present in the system. The hydrodynamic matrix is defined in terms of the plasma frequency $\omega_p^2 = \rho_{0,e}q_e^2/(m_e^2\varepsilon_0)$, the longitudinal (kinematic) viscosity $\nu_{L,e} = \left(4\eta_e/3 + \zeta_e\right)/\rho_{0,e}$, the thermal diffusivity $\chi_e = \kappa_e/(\rho_{0,e}\gamma_e C_{V,e})$ and the normalised heat transfer $\mathfrak{g}_e = g_e/(\rho_{0,e}\gamma_e C_{V,e})$.

In terms of the perturbation variables, the (classical) electron DSF in equation (2.16) for a system of N_e electrons, is

$$S^0_{ee}(\boldsymbol{k},\omega) = \frac{1}{2\pi}\int_{-\infty}^{\infty} dt\, \frac{e^{i\omega t}}{N_e m_e^2}\left\langle\delta\rho^e_{\boldsymbol{k}}(t)\delta\rho^{e*}_{\boldsymbol{k}}(0)\right\rangle_T, \tag{5.16}$$

where $\langle\cdot\rangle_T$ is the thermal average. Using transformed variables, the DSF is evaluated as [175, 196]:

$$\frac{S^0_{ee}(\boldsymbol{k},\omega)}{S^0_{ee}(\boldsymbol{k})} = \frac{1}{\pi}\,\mathrm{Re}\left[\lim_{\varepsilon\to 0}\frac{\left\langle\delta\tilde{\rho}^e_{\boldsymbol{k}}(\varepsilon - i\omega)\delta\rho^{e*}_{\boldsymbol{k}}(0)\right\rangle_T}{\left\langle\delta\rho^e_{\boldsymbol{k}}(0)\delta\rho^{e*}_{\boldsymbol{k}}(0)\right\rangle_T}\right]. \tag{5.17}$$

The DSF is normalised by its integral – the static structure factor – relating to the initial density perturbations, as the hydrodynamic description evolves the perturbations but does

not specify their initial amplitudes, although the fluctuation-dissipation theorem can set the normalisation, see Section 5.2.4.

Thermally averaging equation (5.12) with the initial density perturbations yields

$$[s\mathbf{I} + \mathbf{D}_e(\boldsymbol{k})] \ \langle \delta\tilde{\boldsymbol{y}}^e_{\boldsymbol{k}}(s)\delta\rho^{e*}_{\boldsymbol{k}}(0)\rangle_T = \langle \delta\boldsymbol{y}^e_{\boldsymbol{k}}(0)\delta\rho^{e*}_{\boldsymbol{k}}(0)\rangle_T \,, \tag{5.18}$$

which under the common equilibrium assumption that initial perturbations in density, velocity and temperature are statistically independent [196, 370, 383, 388, 390] only one component on the right-hand side is non-vanishing and

$$\langle \delta\tilde{\rho}^e_{\boldsymbol{k}}(s)\delta\rho^{e*}_{\boldsymbol{k}}(0)\rangle_T = (s\mathbf{I} + \mathbf{D}_e(\boldsymbol{k}))^{-1}_{11} \ \langle \delta\rho^e_{\boldsymbol{k}}(0)\delta\rho^{e*}_{\boldsymbol{k}}(0)\rangle_T. \tag{5.19}$$

Evaluation of the inverse result in the final explicit expression for the dynamic structure factor

$$\frac{\pi S^0_{ee}(\boldsymbol{k},\omega)}{S^0_{ee}(\boldsymbol{k})} = \mathrm{Re}\left[\frac{s^2 + A(\boldsymbol{k})s + B(\boldsymbol{k})}{s^3 + A(\boldsymbol{k})s^2 + C(\boldsymbol{k})s + D(\boldsymbol{k})}\right]_{s=-i\omega}, \tag{5.20}$$

where

$$A(\boldsymbol{k}) = \mathfrak{v}_e(\boldsymbol{k},\omega) + \gamma_e\mathfrak{h}_e(\boldsymbol{k}), \tag{5.21a}$$

$$B(\boldsymbol{k}) = \frac{\gamma_e - 1}{\gamma_e}c^2_{s,e}\boldsymbol{k}^2 + \gamma_e\mathfrak{h}_e(\boldsymbol{k}) \ \mathfrak{v}_e(\boldsymbol{k},\omega), \tag{5.21b}$$

$$C(\boldsymbol{k}) = \omega_p^2 + c^2_{s,e}\boldsymbol{k}^2 + \gamma_e\mathfrak{h}_e(\boldsymbol{k}) \ \mathfrak{v}_e(\boldsymbol{k},\omega), \tag{5.21c}$$

$$D(\boldsymbol{k}) = \left(\gamma_e\omega_p^2 + c^2_{s,e}\boldsymbol{k}^2\right)\mathfrak{h}_e(\boldsymbol{k}), \tag{5.21d}$$

with $\mathfrak{v}_\mu(\boldsymbol{k},\omega) = \left[\nu_{\mu\bar{\mu}}(\omega) + \nu_{L,\mu}\boldsymbol{k}^2\right]$ and $\mathfrak{h}_\mu(\boldsymbol{k}) = \left[\mathfrak{g}_\mu + \chi_\mu\boldsymbol{k}^2\right]$. The structure factor is independent of the thermal expansion coefficient $\alpha_{T,e}$ which therefore cannot be inferred from the dynamic structure factor. Figure 5.1 shows schematically the dependence on the remaining coefficients $c_{s,e}$, $\mathfrak{h}_e$, and $\mathfrak{v}_e$. The position and width of the plasmon feature are determined mainly by $c_{s,e}$ and $\mathrm{Re}\{\mathfrak{v}_e\}$, respectively. The imaginary component of $\mathfrak{v}_e$ may also shift the position. The entropy feature at $\omega = 0$ is primarily determined by $\mathfrak{h}_e$, however, all coefficients

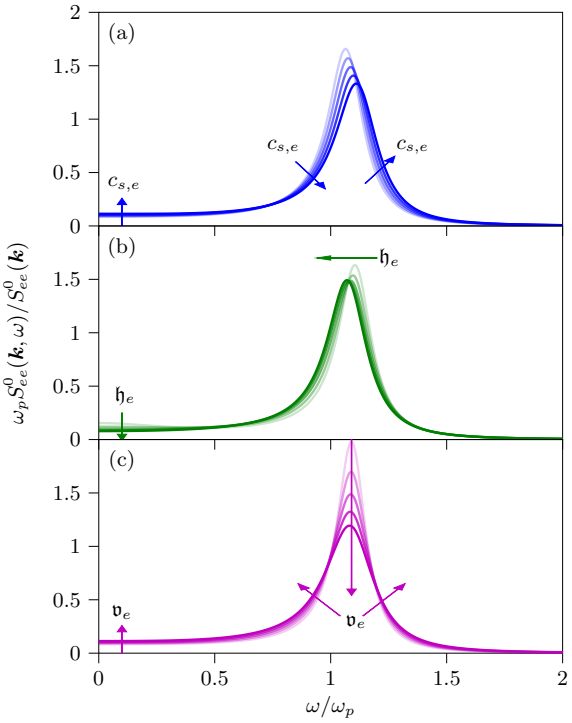

Figure 5.1: Schematic dependence on the coefficients (a) $c_{s,e}$, (b) $\mathfrak{h}_e$ and (c) $\mathrm{Re}\{\mathfrak{v}_e\}$ on the hydrodynamic dynamic structure factor in equation (5.20). Arrows indicate the change as each variable is increased.

modify multiple parts of the spectrum to some degree.

The functional form in equation (5.20) is not written in terms of three Lorentzians, which is common for hydrodynamic theories. These forms are obtained by an expansion in small $\boldsymbol{k}$ [391]. However, for non-zero ν_{ei} and $\mathfrak{g}_e$ the collisional terms are dominant for sufficiently long wavelengths, which prevents a straightforward analogous computation. The more general form in equation (5.20) will be used here.

5.2.3 Limiting behaviours of the hydrodynamic formulation

When dissipative effects via inter-species collisions, viscous drag and heat conduction are small, i.e., $\mathfrak{h}_e \ll \omega_p$ and $\mathfrak{v}_e \ll \omega_p$, the dispersion relation $|s\mathbf{I} + \mathbf{D}_e(\boldsymbol{k})| = 0$ can be evaluated analytically:

$$s_0 = -\left(\frac{\gamma_e\omega_p^2 + c_{s,e}^2\boldsymbol{k}^2}{\omega_Q^2}\right) \times \mathfrak{h}_e, \tag{5.22a}$$

$$s_{1,2} = \pm i\omega_Q - (\gamma_e - 1)\frac{c_{s,e}^2 \boldsymbol{k}^2}{2\omega_Q^2}\mathfrak{h}_e - \frac{\mathfrak{v}_e(\boldsymbol{k}, \mp\omega_Q)}{2}, \tag{5.22b}$$

where $s = -\gamma - i\omega$ describes the resonance frequency ω and the damping rate γ. Equations (5.22a) and (5.22b) show an entropy mode at $\omega = 0$ which is damped by heat transfer and two plasma modes at $\omega \approx \pm\omega_Q$ which follow Bohm-Gross dispersion

$$\omega_Q^2 = \omega_p^2 + c_{s,e}^2 \boldsymbol{k}^2. \tag{5.23}$$

The plasma modes are primarily damped by the momentum loss $\mathfrak{v}_e$ and not the energy loss $\mathfrak{h}_e$ because the plasma mode is fast $\omega_p \gg c_{s,e}\boldsymbol{k}$, as previously illustrated in Figure 5.1. This differs from standard hydrodynamics, where heat conduction dampens the acoustic mode [196]. This was previously noted by Vieillefosse and Hansen [239].

By comparing the generalised Bohm-Gross dispersion [392] and equation (5.23), one identifies the ideal dispersion relation as

$$c_{s,e}^2 \approx \langle \boldsymbol{v}_e^2 \rangle_T = \begin{cases} 3k_\mathrm{B}T_{0,e}/m_e & k_\mathrm{B}T \gg E_\mathrm{F} \\ \frac{3}{5}v_\mathrm{F}^2 & k_\mathrm{B}T \ll E_\mathrm{F} \end{cases}, \tag{5.24}$$

where $\langle \boldsymbol{v}_e^2 \rangle_T$ is the averaged square electron velocity, v_F is the Fermi-speed and E_F the Fermi-energy. In the absence of inter-species collisions, the damping rates are proportional to $\boldsymbol{k}^2$ and likewise the width of the resonance features in $S_{ee}^0(\boldsymbol{k}, \omega)$. This is the behaviour predicted by Schmidt *et al.* [383]. Therefore, inter-species collisions are needed for the appropriate long-wavelength behaviour for two-component systems, which typically have a finite width plasmon feature [133, 248, 393].

The effect of collisional momentum transfer between electrons and ions is isolated if $\boldsymbol{k} \to 0$ and $g = 0$. Equation (5.20) in this limit takes the form

$$\frac{\pi S_{ee}^0(\boldsymbol{k}, \omega)}{S_{ee}^0(\boldsymbol{k})} = \frac{\mathrm{Re}\{\nu_{ei}\}\,\omega_p^2}{\Big(\omega^2 - \omega_p^2 - \mathrm{Im}\{\nu_{ei}\}\omega\Big)^2 + \big(\mathrm{Re}\{\nu_{ei}\}\omega\big)^2}, \tag{5.25}$$

where the real value of the dynamic collision frequency $\mathrm{Re}\{\nu_{ei}\}$ primarily gives the width of the feature and the imaginary component $\mathrm{Im}\{\nu_{ei}\}$ shifts the resonance. This limit agrees with the Drude-like limit of Mermin's relaxation time approximation [248], motivating the choice of momentum coupling between the electron and ion fluids.

Lastly, one-component systems have been extensively studied through LFCs $G_{ee}(\boldsymbol{k},\omega)$ [207, 249, 250], which in turn can be related to the viscosity of the electron fluid [394, 395]. In the long wavelength limit G_{ee} approaches zero, specifically $G_{ee}(\boldsymbol{k},\omega) \propto \boldsymbol{k}^2$ [248]. Therefore, for the one-component case, the hydrodynamic limit of S^0_{ee} is the RPA [248]. This limit is reflected in the hydrodynamic model when $\mathfrak{v}_e \to 0$ and $\mathfrak{h}_e \to 0$.

5.2.4 Electron electrical conductivity

The electron electrical conductivity is a central property of the electron fluid which does not directly enter into the current hydrodynamic description. However, the conductivity relates to the system response under an external potential $\delta\phi_{\mathrm{ext}}$, which can be modelled. Introducing a small external potential through $\phi \to \phi + \delta\phi_{\mathrm{ext}}$, a driving term

$$\tilde{\boldsymbol{d}} = \left[0,\ \frac{q_e\rho_{e,0}}{m_e}\boldsymbol{k}^2\delta\tilde{\phi}^{\mathrm{ext}}_{\boldsymbol{k}},\ 0\right]^{\intercal} \tag{5.26}$$

is added to the right-hand side of equation (5.12). On thermal averaging of equation (5.12), the initial perturbations vanish and the response to the driving field is described by

$$\left[s\mathbf{I} + \mathbf{D}_e(\boldsymbol{k})\right]\ \langle\delta\tilde{\boldsymbol{y}}^e_{\boldsymbol{k}}(s)\rangle_T = \tilde{\boldsymbol{d}}, \tag{5.27}$$

which gives the density response function

$$\chi_{ee}(\boldsymbol{k},-\boldsymbol{k},\omega) = \frac{\rho_{0,e}}{m_e^2}\boldsymbol{k}^2\left(s\mathbf{I} + \mathbf{D}_e(\boldsymbol{k})\right)^{-1}_{12}\Big|_{s=-i\omega}. \tag{5.28}$$

The dielectric response relates to the off-diagonal component of the hydrodynamic matrix, as the density field (row 1) responds to a source in the momentum equation (column 2). The density response relates to the dielectric function $\varepsilon(\boldsymbol{k},\omega)$, where $\varepsilon(\boldsymbol{k},\omega)^{-1} =$

$1 + q_e^2/(\varepsilon_0 \boldsymbol{k}^2)\chi_{ee}(\boldsymbol{k}, -\boldsymbol{k}, \omega)$ [206], which in turn results in the macroscopic conductivity model $\sigma(\omega)$ [112]. Within the hydrodynamic formulation, the conductivity model has a Drude-like form,

$$\sigma(\omega) = \varepsilon_0 \lim_{\boldsymbol{k}\to 0} \omega \,\mathrm{Im}\left\{\varepsilon(\boldsymbol{k}, \omega)\right\} = \frac{\varepsilon_0 \,\mathrm{Re}\{\nu_{ei}\}\omega_p^2}{\mathrm{Re}\{\nu_{ei}\}^2 + \left(\omega - \mathrm{Im}\{\nu_{ei}\}\right)^2}, \tag{5.29}$$

with a DC value of $\sigma_{\mathrm{DC}} = \varepsilon_0 \omega_p^2 / \mathrm{Re}\{\nu_{ei}(\omega = 0)\}$. Electron-electron collisions do not appear explicitly as they adhere to the conservation relations in equation (5.1). However, electron-electron collisions can still alter the distribution function which affects conductivity [82, 83], and within a hydrodynamic formulation, these effects are accounted for in the effective momentum transfer between electrons and ions ν_{ei} [396].

Equation (5.28) constitutes a separate derivation of the dynamic structure factor given by the (classical) fluctuation-dissipation theorem in equation (2.22). This alternative derivation is consistent with equation (5.20) given the static structure factor

$$S_{ee}^0(\boldsymbol{k}) = \frac{k_{\mathrm{B}} T}{m_e \omega_p^2} \frac{\boldsymbol{k}^2}{1 + \lambda_e^2 \boldsymbol{k}^2} \tag{5.30}$$

and $\lambda_e^{-2} = \gamma_e \omega_p^2 / c_{s,e}^2$. This static structure agrees with the RPA approximation [195] for a general screening length λ_e and recovers the Debye and Thomas-Fermi screening lengths [107] in their corresponding limits, see Appendix C.3.1.

5.3 Test system and model requirements

The transport coefficients in the hydrodynamic model have remained unspecified up to this point and will be extracted by comparison with a molecular dynamics simulation which, due to its atomistic nature, does not require any closure in terms of transport coefficients. Specifically, the wave packet model in Chapter 3 is employed for a test system with the same thermodynamic conditions as in Chapter 4.

Before attempting to describe the MD data using the hydrodynamic description, an upper limit for $\boldsymbol{k}$ must be established, beyond which kinetic effects are substantial. Landau damping is one such purely kinetic effect acting to broaden the resonance. Figure 5.2 compares the

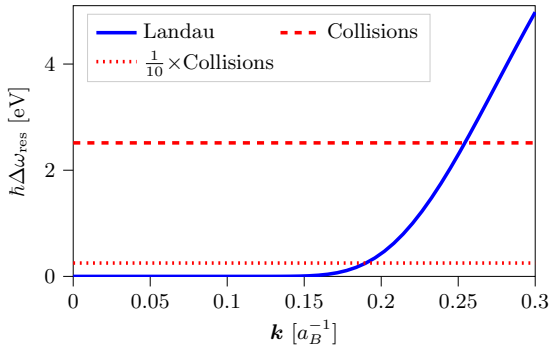

Figure 5.2: Width of the plasmon feature (FWHM) from classical Landau damping [288] and the $\boldsymbol{k} \to 0$ limit [248] of the Born-Mermin approximation [346]. The electron-ion collision frequency is given in the first Born approximation [348] using the ion structure from Figure 4.1(a). A tenth of the collisional width is shown for comparison.

classical Landau damping [288] with the expected broadening due to electron-ion collisions in the first Born approximation [348] and the Mermin relaxation-time approximation [346]. Requiring the collisional broadening to be an order of magnitude larger than Landau damping restricts the domain of validity to $\boldsymbol{k} \lesssim 0.19\, a_{\mathrm{B}}^{-1}$.

The required system size to model in the MD is set by the number of spectra needed within the regime of validity of the hydrodynamic model. MD simulations performed in a periodic cubic box with side length of length L can only represent a discrete set of $\boldsymbol{k}$-vectors given by:

$$\boldsymbol{k} = \frac{2\pi}{L}\boldsymbol{n}, \tag{5.31}$$

where $\boldsymbol{n} \in \mathbb{Z}^3$. Furthermore, for isotropic systems, only $\boldsymbol{k}$-vectors with different magnitudes will yield new information. Requiring access to at least three distinct spectra with $|\boldsymbol{k}| \leq 0.19\, a_{\mathrm{B}}^{-1}$, at least $N_p \approx 5600$ protons need to be simulated. In combination with the necessity to resolve the electron dynamics, a method like WPMD is therefore preferable compared to other *ab initio* approaches. In this chapter, simulations with $N_p = 5628$ are used.

Quantum hydrodynamics (QHD) is often put forward as a generalisation of classical hydrodynamics, where an additional Bohm-like contribution is added to the momentum [13, 102, 288, 397] and potentially higher order fluid equations [288, 383]. Classical hydrodynamic descriptions can still capture some quantum effects by modifying the equation of state and

transport coefficients, but they cannot capture the non-local Bohm contribution. Quantum hydrodynamics adds (in quadrature) a quantum recoil $\omega_R = \hbar \boldsymbol{k}^2/(2m_e)$ to the plasmon dispersion [288, 397]. Comparing the shift in the dispersion due to the quantum recoil and pressure contribution for the test system,

$$\frac{\omega_R^2}{c_{s,e}^2 \boldsymbol{k}^2} \approx 0.1 \times (a_\mathrm{B} \boldsymbol{k})^2 \,, \tag{5.32}$$

it is clear that for the $\boldsymbol{k}$-vectors considered here the recoil is negligible. The high-temperature approximation for $c_{s,e}^2$ was assumed in the above estimate. Care must be taken for the Bohm contribution to have the desired effect in many-body systems [287], partially amended by the introduction of an additional pre-factor for the Bohm potential [101] which might be time and length-scale dependent [102]. Furthermore, the Bohm pressure tensor is necessarily anisotropic in the presence of perturbations, preventing a straightforward isotropic second-order closure [288], i.e., closing the hydrodynamic hierarchy in terms of a single temperature as in Section 5.2 is not appropriate. This results in an erroneous recoil term if not properly accounted for [398]. Moreover, closing the equations on the level of the momentum equation would miss the entropy mode at $\omega = 0$ [196, 364].

5.4 Fitting model, degeneracy and error estimation

It has been common practice to fit hydrodynamic expressions to ion dynamic structure factors from MD to extract transport properties [110, 202, 203], closely mimicking how it can be done experimentally [399, 400]. The transport coefficients typically relate to the widths of features and multiple $\boldsymbol{k}$-vectors (angles) are commonly needed for a reliable extraction. What is proposed here is practically similar but for electrons instead.

A two-stage fitting procedure is commonly employed for ion transport properties [110, 202, 203]. A hydrodynamic functional form is first fitted to each spectra for each different $\boldsymbol{k}$ separately, followed by fitting the resulting parameters to the appropriate hydrodynamic scaling to obtain the transport coefficients. A similar procedure using equation (5.20) could also be

implemented. However, the limited number of $\boldsymbol{k}$-vectors compared to many one-component investigations incentivises a careful error estimation. It is therefore desirable to have a single combined fit where uncertainties are systematically propagated.

For this purpose, Bayesian inference was used [382], a technique which is now commonly applied to experimental scattering data from warm dense matter samples [338, 401–403]. The fitting model is based on *Bayes' theorem*

$$P\left(\boldsymbol{x}|\boldsymbol{y}\right) = \frac{P\left(\boldsymbol{y}|\boldsymbol{x}\right) P\left(\boldsymbol{x}\right)}{P\left(\boldsymbol{y}\right)} \tag{5.33}$$

for a set of parameters $\boldsymbol{x}$ and observables $\boldsymbol{y}$. The parameters are the transport coefficients and error parameters $\boldsymbol{x} = [c_{s,e}, \chi_e, \mathrm{Re}\{\nu_{ei}\}, \nu_{L,e}, b_{\boldsymbol{k}_1}, s_{\boldsymbol{k}_1}, \ldots, b_{\boldsymbol{k}_n}, s_{\boldsymbol{k}_n}]^\intercal$, while the "observations" are the normalised structure factors from MD

$$\boldsymbol{y} = [S(\boldsymbol{k}_1, \boldsymbol{\omega}_{\boldsymbol{k}_1})/S(\boldsymbol{k}_1), \ldots, S(\boldsymbol{k}_n, \boldsymbol{\omega}_{\boldsymbol{k}_n})/S(\boldsymbol{k})]^\intercal \equiv [y_1(\boldsymbol{\omega}_{\boldsymbol{k}_1}), \ldots, y_n(\boldsymbol{\omega}_{\boldsymbol{k}_n})]^\intercal\,, \tag{5.34}$$

where $S(\boldsymbol{k}, \omega) = S^0_{ee}(\boldsymbol{k}, \omega)$. The effect of the finite time window used for the FFT of the MD data was investigated in terms of window functions [404] and had a negligible effect. $P\left(\boldsymbol{x}|\boldsymbol{y}\right)$ is the resulting distribution of transport properties (and error parameters) given the data. The likelihood function $P\left(\boldsymbol{y}|\boldsymbol{x}\right)$ is a model choice constructed as follows. Spectra for different $\boldsymbol{k}$ were considered independent and each frequency point was modelled with a Gaussian error around the hydrodynamic model y_i^{HD}. Therefore, the likelihood function employed in the analysis was:

$$\ln P\left(\boldsymbol{y}|\boldsymbol{x}\right) = -\sum_{i=1}^{n} \sum_{\omega \in \boldsymbol{\omega}_{\boldsymbol{k}_i}} \left\{ \ln\left[2\pi\sigma_i^2(\omega; \boldsymbol{x})\right] + \frac{1}{2}\left[\frac{y_i(\omega) - y_i^{\mathrm{HD}}(\omega; \boldsymbol{x})}{\sigma_i(\omega; \boldsymbol{x})}\right]^2 \right\}. \tag{5.35}$$

The error was modelled as a floored relative error,

$$\sigma_i(\omega; \boldsymbol{x}) = \min\left[s_i, b_i y_i^{\mathrm{HD}}(\omega; \boldsymbol{x})\right], \tag{5.36}$$

where s_i and b_i were allowed to be different for each $\boldsymbol{k}$-vector and were inferred from the data.

The prior distribution $P(\boldsymbol{x})$ for transport properties is assumed to be constant for positive values, constituting the minimum reasonable assumption. For the scale parameters s_i and b_i, *Jefferys's prior* was adopted [382] which makes the problem invariant under scaling of s_i and b_i. The prior was evaluated using Fisher's information matrix of a multivariate Gaussian [405]. The likelihood for the observation $P(\boldsymbol{y})$ is not needed for parameter estimation [382]. The resulting distribution, $P(\boldsymbol{x}|\boldsymbol{y})$, will be sampled numerically in the following section, using a Markov Chain Monte Carlo (MCMC) algorithm [180, 181]. For this, the `emcee` implementation [406] of the affine-invariant ensemble sampler by Goodman and Weare [182] was employed.

The time scale for energy relaxation $\mathfrak{g}_e^{-1}$ is long compared to the damping of the plasma oscillation due to momentum dissipation. Typically $\mathfrak{g}_e/\nu_{ei} \approx m_e/m_i$ [165] and therefore the free-electron spectrum is not particularly sensitive to $\mathfrak{g}_e$ which was therefore omitted from the fitting. To further constrain the fitting procedure, the adiabatic index is assumed to be $\gamma_e = 3$ – common practice for fluid models of fast plasma oscillations [407] – and a parameterisation for the dynamic collision frequency was introduced:

$$\nu_{ei}(\omega) = \mathrm{Re}\{\nu_{ei}(\omega_p)\} \times \frac{\nu_{ei}^{\mathrm{BMA}}(\omega)}{\mathrm{Re}\{\nu_{ei}^{\mathrm{BMA}}(\omega_p)\}}, \tag{5.37}$$

where $\mathrm{Re}\{\nu_{ei}(\omega_p)\}$ was sampled and $\nu_{ei}^{\mathrm{BMA}}(\omega)$ is the collision frequency in the Born-Mermin approximation evaluated as described by Thiele *et al.* [348] using the ion structure from Figure 4.1(a).

The use of Green-Kubo relations [60, 61, 175, 196] provides an alternative route for the computation of transport properties. However, they are derived from solutions of equations similar to equation (5.12) and for ionic systems, good agreement has been found between the Green-Kubo and the hydrodynamic approach [204]. The methods are therefore largely interchangeable, but an advantage of the hydrodynamic method is the validation of the model via inspection of the fits and its direct applicability to experimental data.

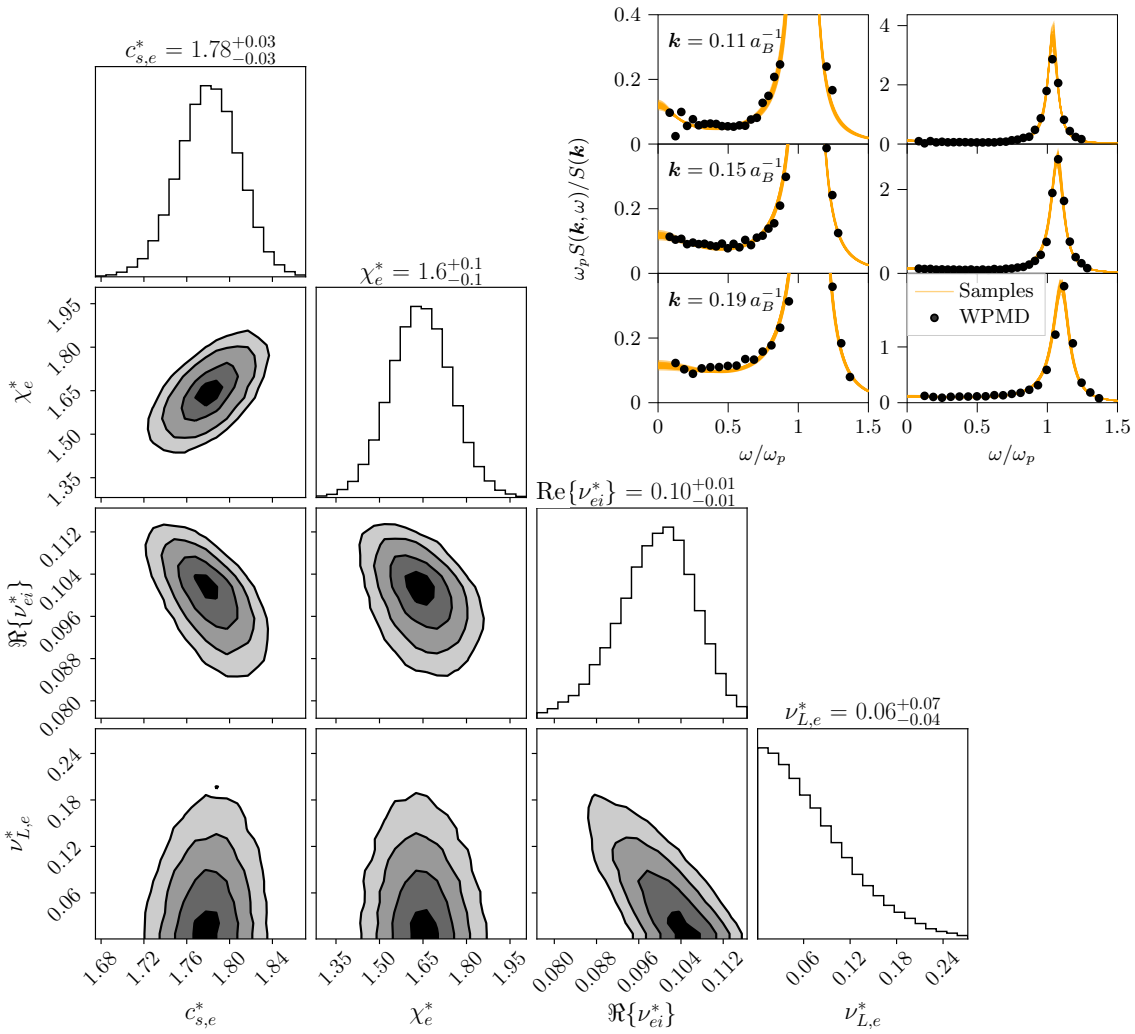

Figure 5.3: (Lower left) Marginalised posterior distributions of transport parameters as given by the MCMC sampling using the three smallest $\boldsymbol{k}$-modes in the WPMD simulations. The collision frequency is to be understood as evaluated at $\omega = \omega_p$. All parameters are given in dimensionless units, see equation (5.38), and the quoted numerical values are the median and the 16th and 84th percentiles. Figure generated using `corner.py` [408]. (Upper right) Sample fits (Samples) from the MCMC sampling along with the MD data (WPMD). Each row of figures corresponds to different $\boldsymbol{k}$-vectors as indicated. The right column shows the fitting of the plasma feature while the left columns focus on the entropy feature.

5.5 Inference: Transport properties

The Bayesian inference model was used to simultaneously sample $S^0_{ee}(\boldsymbol{k},\omega)$ for the three smallest $\boldsymbol{k}$-vectors in the MD simulation. The resulting posterior distributions for the transport parameters as well as sample fits are shown in Figure 5.3. Transport parameters are normalised according to:

$$\begin{aligned} c^*_{s,e} &= \sqrt{\frac{m_e}{k_\mathrm{B}T_{e,0}}}c_{e,s} \qquad & \nu^*_{ei} &= \sqrt{\frac{m_e a_e^2}{k_\mathrm{B}T_{e,0}}}\nu_{ei} \\ \chi^*_e &= \sqrt{\frac{m_e}{a_e^2 k_\mathrm{B}T_{e,0}}}\chi_e \qquad & \nu^*_{L,e} &= \sqrt{\frac{m_e}{a_e^2 k_\mathrm{B}T_{e,0}}}\nu_{L,e}, \end{aligned} \quad , \tag{5.38}$$

where $a_e = r_s a_\mathrm{B}$. The sample fits in Figure 5.3 demonstrate the ability of the hydrodynamic model to fit both the dominant plasmon feature and the weaker entropy feature at $\omega = 0$, for multiple $\boldsymbol{k}$-vectors simultaneously. This strengthens the confidence in the hydrodynamic description of the long wavelength electron DSF for frequencies up to the plasma frequency.

The inferred posterior distributions in Figure 5.3 show correlations between the inferred values of the transport coefficients. Particularly strong correlations are observed between the collision frequency $\mathrm{Re}\{\nu_{ei}(\omega_p)\}$ and the viscosity $\nu_{L,e}$, which is natural since both parameters relate to the width of the plasmon feature and are combined in $\mathfrak{v}_e(\boldsymbol{k},\omega)$. The momentum-dissipation mechanisms are distinguished from each other by considering multiple $\boldsymbol{k}$-vectors. However, the inferred distribution for the viscosity coefficient does not show a clear peak away from the boundary $\nu_{L,e} = 0$, and the viscosity dependence with its $\boldsymbol{k}^2$-scaling is challenging to measure for the small $\boldsymbol{k}$-vectors required for the validity of the hydrodynamic description. Other correlation functions rather than the density-density correlation function considered here, e.g., the transverse current auto-correlation function describing shear modes [204], might be preferable to further probe the viscosity. Furthermore, correlations between the estimated $c_{s,e}$ and ν_{ei} represent the uncertainty between the width of the plasmon feature and its exact position in the MD data resolved over a discrete set of frequency points. The position of the plasmon feature also couples to ν_{ei} via the imaginary part and equation (5.25). The correlations between the estimates of $c_{s,e}$ and χ_e demonstrate the sensitivity of the comparatively small

entropy feature to the "wings" of the plasmon feature.

Table 5.1 summarises the inferred electron transport coefficients and error estimates from Figure 5.3, along with an analogous sampling in which only the two spectra are fitted (not shown). Using a smaller number of spectra yields transport coefficients within the error bands of the original fits, although with larger uncertainty. This indicates that the MD simulations have reached a length scale well described by the hydrodynamic formulation. The incorporation of additional spectra is shown in Appendix C.2 and substantial changes in inferred parameters are seen if spectra with $\boldsymbol{k} \gtrsim 0.24\, a_{\mathrm{B}}^{-1}$ are included in the fit. A prominent feature is that plasmon broadening due to Landau damping is erroneously attributed to viscous damping at length scales consistent with the estimates presented in Section 5.3.

Along with the inferred values of the transport coefficients from the WPMD simulations in Table 5.1, the transport properties from a set of reference models are shown. The reference models vary in complexity, some are analytical and others are parameterisations of MD results. However, none of the models are a direct match to the WPMD description due to either neglecting quantum effects or the presence of ions to some extent. Further details of the reference calculations are provided in Appendix C.3. The estimated value of $c_{s,e}$ is approximately 3% higher than the ideal value given by equation (5.24). This discrepancy might be attributed to quantum corrections as no strong deviations due to Coulomb coupling are seen in the one-component plasma reference calculation. The dispersion based on the $\boldsymbol{k} \to 0$ limit of the RPA is in line with the inferred values, but based on the estimated errors the models cannot be conclusively distinguished.

Thermal diffusivity is the ratio between thermal conductivity and heat capacity. In comparison with classical kinetic models and MD data for a one-component plasma, the WPMD fit suggests a 35% lower thermal diffusivity. A quantum two-component calculation using DFT-MD instead suggests a 75% higher value than the WPMD fits, although this reference model uses an ideal heat capacity and the inclusion of interactions would reduce the thermal diffusivity. The collision frequency for momentum loss at the plasma frequency $\mathrm{Re}\{\nu_{ei}^{*}(\omega_p)\}$ is comparable to the values given by the first Born approximation, albeit slightly

Table 5.1: Extracted and reference transport properties for the electron fluid. Values are given in dimensionless form described by equations (5.38) and (5.39). The inferred values for the transport coefficients are based on the fitting procedure discussed in Section 5.4 for the two (not shown) and three (see Figure 5.3) smallest $\boldsymbol{k}$-vectors in the molecular dynamics simulation. Values are the median and the errors are computed from the 16th and 84th percentiles. Reference calculations are discussed in Appendix C.3.

Property	WPMD & MCMC $\#\boldsymbol{k}=2$	WPMD & MCMC $\#\boldsymbol{k}=3$	Reference calculations Value	Comment	Section
$c^*_{s,e}$	$1.74^{+0.04}_{-0.04}$	$1.78^{+0.03}_{-0.03}$	$\sqrt{3}$	Bohm-Gross dispersion in high temperature approximation, equation (5.24).	C.3.1
			1.69	Memory function and parameterisation of Monte Carlo simulations for the one component plasma.	C.3.3
			1.78	Modified Bohm-Gross dispersion based on the $\boldsymbol{k}\to 0$ limit of RPA for moderately degeneracy.	C.3.4
χ^*_e	$1.6^{+0.1}_{-0.1}$	$1.6^{+0.1}_{-0.1}$	2.3	Classical kinetic SMT model with effective Boltzmann formulation for collisions and ideal heat capacity.	C.3.2
			2.5	Parameterisation of (classical) MD and Monte Carlo simulations for one component plasma.	C.3.3
			2.8	Parameterisation of Coulomb log for thermal conductivity by DFT-MD and ideal heat capacity.	C.3.5
$\mathrm{Re}\{\nu^*_{ei}(\omega_p)\}$	$0.10^{+0.01}_{-0.01}$	$0.10^{+0.01}_{-0.01}$	0.16[1]	Dynamic collision frequency at $\omega=\omega_p$ in first Born approximation.	C.3.4
$\nu^*_{L,e}$	$0.07^{+0.09}_{-0.05}$	$0.06^{+0.07}_{-0.04}$	7.5	Classical kinetic SMT model with effective Boltzmann formulation for collisions.	C.3.2
			4.6	Parameterisation of (classical) MD simulations for one component plasma.	C.3.3
			8.7×10^{-3}	$T=0$ parametrisation for a homogeneous quantum Fermi liquid.	C.3.6
σ^*_{DC}	$16.1^{+1.6}_{-1.2}$	$16.7^{+1.4}_{-1.1}$	12.0	Classical kinetic SMT model with effective Boltzmann formulation for collisions.	C.3.2
			10.4[1]	Based on dynamic collision frequency at $\omega=0$ in first Born approximation and the conductivity model of Eq. (5.29).	C.3.4

[1]The collision frequency and conductivity are different representations of the same property within the hydrodynamic model, and therefore the same models are used for comparison evaluated at the appropriate ω.

lower. This is possibly related to the restricted form of the electron wave packets which, with its distributed nature, reduced the strength of collisions.

The previously discussed properties are largely in alignment with classical models. However, the inferred electron viscosity is markedly lower than that of its classical counterparts. All reference calculations for the longitudinal viscosity $\nu_{L,e}$ have neglected the contribution from the bulk viscosity ζ_e, which both in a quantum zero temperature [394, 395] and classical [239] one-component plasmas is negligible compared to the shear viscosity η_e. Due to the distribution of longitudinal viscosities in the MCMC sampling, a concrete estimate for $\nu_{L,e}$ cannot be given. Nevertheless, the inference suggests an order of magnitude reduction compared to the classical model. The predicted mean value is still above the $T = 0$ limit.

5.5.1 Electrical conductivity

Given the inference for $\mathrm{Re}\{\nu_{ei}(\omega_p)\}$ and the conductivity model in Section 5.2.4, the conductivity of the test system is evaluated in Figure 5.4. The conductivity is normalised by

$$\sigma^*(\omega) = \sqrt{\frac{m_e a_e^2}{k_\mathrm{B} T_{e,0} \varepsilon_0^2}} \sigma(\omega). \tag{5.39}$$

The Drude-like conductivity model has an additional suppression for large ω due to the frequency dependence of the collision frequency. The inferred collision frequency is sensitive to the spectrum close to $\omega \approx \omega_p$, and the high-frequency behaviour is extrapolated based on the model of dynamic collision frequencies. Similar extrapolation is performed for the DC conductivity – shown in the inset of Figure 5.4 – but in this case, the static and $\omega = \omega_p$ collision frequencies differ by 15%. Recently, Hentschel *et al.* [409] discussed the sensitivity of extrapolating a measurement of the dynamic collision frequency at $\omega \approx \omega_p$ to the DC conductivity, where the inference becomes uncertain as more free parameters are included in the model for the dynamic collision frequency. The comparison of DC conductivities in Table 5.1 supports the general conclusion for the collision frequency.

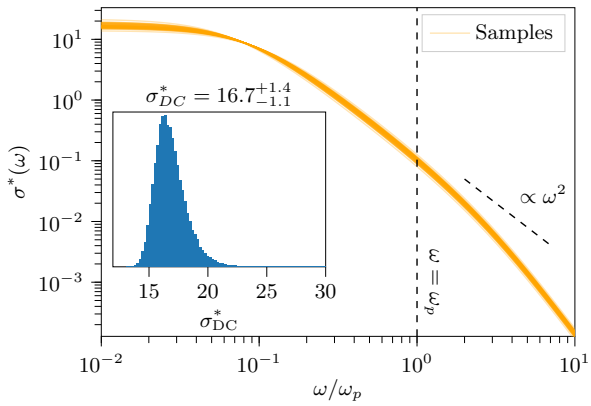

Figure 5.4: The conductivity model was evaluated based on samples of the transport coefficients from the MCMC. The model is seen with a Drude-like character where the high-frequency behaviour decays as ω^{-2}. In the insert, the distribution of DC conductivities, σ^*_{DC}, is shown. Quoted values are the median and the 16th and 84th percentiles.

5.6 Conclusion

The long-wavelength behaviour of the electron dynamic structure factor of atomistic two-component simulations within the warm dense regime was compared to a phenomenological two-fluid model. The two-fluid description couples the electron and ion fluids via (mean-field) electrostatic interactions and collisional terms, and describes the ion motion with the associated electron screening as well as the free electron oscillations. From the latter, a model for the free-electron dynamic structure factor was derived using linear perturbation theory. The model incorporates one entropy and two plasmon modes and agrees with the Born-Mermin approximation in the long-wavelength limit. It is therefore argued to be an appropriate description of electron dynamics on long-length scales.

The dynamic structure factor is parameterised using transport parameters and by mapping the structure factors to the results of atomistic simulations via Markov Chain Monte Carlo (MCMC) sampling, transport properties have been extracted. The sampling was performed over multiple spectra simultaneously, to consistently treat the error estimation. This methodology is general and can be applied to any simulation of two-component plasmas in which the electron dynamics is probed.

In this chapter, the methodology was applied to the test system in Chapter 4 and simulated

using the model in Chapter 3. Most of the inferred transport properties are in line with reference calculations, and the inferred errors are fractionally small. Discrepancies are within expectations because no reference calculation is a direct match to the WPMD system, either due to being limited to small coupling or because it neglects quantum effects and the presence of ions to some degree. The exception is the inferred value of the electron viscosity, which is predicted to be at least an order of magnitude smaller than classical models. This discrepancy is likely due to quantum effects in the electron-electron interaction or the presence of ions, which is not accounted for in the classical one-component reference calculations.

Chapter 6
Relativistic Molecular Dynamics

Abstract: Relativistic corrections to classical molecular dynamics of one-component plasmas are investigated through two effects. First, relativistic kinematics with velocity-dependent inertia is shown to yield the Maxwell-Jüttner velocity distribution and reduce mass diffusion compared to the classical limit. Second, corrections due to electromagnetic interaction are discussed and a formulation separating the short and long-range behaviour of the fields is presented. Large-scale fields are treated as dynamic variables and coupled to smooth source terms. The force on the particles from the highly fluctuating fields on small length scales is approximated by particle-particle pair interactions – either by an electrostatic or Darwin approximation – and these forces have a limited range, as they originate from screened source terms.

6.1 Introduction

Particles experience relativistic corrections when travelling at an appreciable fraction of the speed of light c, occurring in a variety of human-made applications, e.g., particle accelerators [410], the undulator of FELs [411], laser-plasma interactions [412] and magnetic confinement fusion [413], and astrophysics, e.g., jets [414] and cosmic rays [415]. Systems can also be *thermally relativistic*, where the thermal motion of particles experiences relativistic corrections. The existence of such conditions on a broad range of astrophysical objects was discussed in Section 1.2.4. A prominent example is the Sun, where relativistic corrections are needed to model the internal structure and interpret helioseismology measurements [18]. Thermally relativistic electrons are found in non-degenerate and degenerate systems, often along with moderately or strongly coupled ions [32]. A (classical) relativistic MD treatment which handles both relativistic effects as well as strong interactions is therefore sought after and developed in this chapter.

Relativistic MD is used in nuclear physics applications, where the *UrQMD* model [416]

is a prevalent example, similar in construction to the wave packet model in Chapter 3 using a relativistic Lagrangian. Nuclear physics models are commonly Lorentz invariant with pair interactions [417, 418], but do not treat electromagnetic fields explicitly. Additionally, to account for creation and annihilation processes, the nuclear physics models let the MD particles combine and decay based on supplied cross-sections [416, 419, 420]. However, here no nuclear reactions are considered and all particles will remain a single type.

In the relativistic regime, the electrostatic approximation commonly employed in MD breaks down. Magnetic interactions and the finite speed at which electromagnetic waves propagate become significant in this regime to describe interactions [112]. A microscopic formulation which treats electromagnetic fields and is scalable to a large number of particles would be well suited to benchmark collisional modules in *particle-in-cell* (PIC) simulations [421–423]. The effect of such collisions on instability growth is still discussed for conditions relevant to fast ignition [424]. Highly scalable MD – using 10^8 particles – has demonstrated turbulent behaviours [425] and Rayleigh-Taylor instability growth [426] from an atomistic formulation in the fluid regime. If similar simulations could be performed for plasmas where magnetic fields are modelled, they could see a glimpse of the *turbulent dynamo* [427].

Focusing on the development of a new relativistic molecular dynamics formulation, this chapter will consider classical one-component plasmas. The purely kinematic effect of relativistic inertia is studied in Section 6.2, where the velocity distribution and the diffusion coefficient are computed. Section 6.3 introduces a length scale separation in the treatment of the electromagnetic fields. The long-range interactions are treated with time-evolving fields, and a set of approximations for the short-range fields are discussed. The implementation of the model and an example of static structure are given in Sections 6.4 and 6.5, respectively.

6.2 Relativistic kinematics

In special relativity, the classical inertia m_i – the mass of particle i – is replaced with $\gamma(\boldsymbol{v}_i)m_i$, where γ is the Lorentz factor. The inertia is therefore velocity-dependent and grows with particle speed to reduce the acceleration. In the relativistic limit $|\boldsymbol{v}_i| \to c$, $\gamma(\boldsymbol{v}_i)$ diverges

and limits the speed of massive particles to below c. Furthermore, the relativistic expression for the kinetic energy alters the equilibrium distribution of velocities to a Maxwell-Jüttner distribution [428].

The relativistic Lagrangian for N particles with an instantaneous and pair-wise interaction $u_{\alpha\beta}$ is [112, 429]

$$\mathcal{L}_{\text{Rel.}} = -\sum_{i=1}^{N} m_i c^2 \sqrt{1 - \frac{\boldsymbol{v}_i^2}{c^2}} - \sum_{i<j} u_{\alpha\beta}(\boldsymbol{r}_{ij}), \tag{6.1}$$

where the label α (β) is chosen based on the type of particle i (j), and $\boldsymbol{r}_{ij} = \boldsymbol{r}_i - \boldsymbol{r}_j$ is the separation between particles. The corresponding canonical momentum is $\boldsymbol{p}_i = m_i \gamma_i \boldsymbol{v}_i$ and the Lorentz factor is $\gamma_i = \sqrt{1 + \boldsymbol{p}_i^2/(m_i c)^2}$. Therefore, the Hamiltonian of the system is

$$\mathcal{H}_{\text{Rel.}} = \sum_{i=1}^{N} m_i c^2 \sqrt{1 + \frac{\boldsymbol{p}_i^2}{(m_i c)^2}} + \sum_{i<j} u_{\alpha\beta}(\boldsymbol{r}_{ij}), \tag{6.2}$$

and the time evolution follows from equation (2.8). Similar models have previously been incorporated into MD [111, 430–432], as a first approximation to relativistic effects.

An OCP model in the form of equation (6.2) with Coulomb interactions will be investigated with MD below – henceforth referred to as the REL-OCP model – to characterise the influence of relativistic kinematics on velocity distribution and mass diffusion. In Appendix D.1, it is shown by using an appropriate unit system that the REL-OCP model is completely parametrised by Γ[1] and ε defined in equations (1.7) and (1.19), respectively. Systems with long-range Coulomb interactions most likely have substantial post-Newtonian corrections even under mildly relativistic conditions [433]. However, this system is chosen as it is an intermediate step to the model in Section 6.3.

6.2.1 Velocity distributions

The statistics of the REL-OCP system are given by the Hamiltonian (6.2) and the ergodic principle applies to the occupation of states in $(\boldsymbol{r}_i, \boldsymbol{p}_i)$-space [10]. In the canonical ensemble, the occupation of a state is proportional to $\exp(-\beta \mathcal{H}_{\text{Rel.}})$ and due to the separability of $\mathcal{H}_{\text{Rel.}}$

[1]The subscript has been dropped for the one-component system investigated.

the momentum distribution is independent of the interaction. To acquire the distribution of normalised velocities, $\beta_i = |\boldsymbol{v}_i|/c$, the following phase space measure must be taken into account: $\boldsymbol{p}_i^2 dp_i = (m_i c)^3 \gamma_i^5 \beta_i^2 d\beta_i$. The resulting velocity distribution function is the Maxwell-Jüttner distribution function [428]

$$f(\beta_i)\, d\beta_i = \frac{\gamma_i^5 \beta_i^2}{\varepsilon \mathrm{K}_2(\varepsilon^{-1})} \exp\left(-\varepsilon^{-1}\gamma_i\right)\, d\beta_i, \tag{6.3}$$

where the appropriate normalisation is given by the modified Bessel function of the second kind $\mathrm{K}_2(x)$. Compared to the classical Maxwell-Boltzmann distribution, the tail of the Maxwell-Jüttner distribution is suppressed, pushing particles into lower velocity states. In the relativistic limit, the kinetic energy (canonical momenta) is unbounded, but velocities are caped. Therefore, an increase in energy is not associated with a substantial increase in spatial translation.

In Figure 6.1, the resulting distribution function obtained from an MD simulation is shown after an equilibration period. The results show that the MD indeed acquires the Maxwell-Jüttner distribution, as previously observed [111, 430–432]. This suggests that the Maxwell-Jüttner distribution is the appropriate equilibrium distribution function and not one of its suggested alternatives, see the discussion by Nakamura [434]. For separable Hamiltonians modelled by MD, the velocity distribution is purely set by the functional form of the kinetic energy and the canonical momentum. This should be contrasted against PIC models, where the collisional module must be made relativistic invariant to acquire the desired distribution function [422].

6.2.2 Mass diffusion

Purely kinematic considerations alter the transport behaviour of relativistic particle systems. An example is mass diffusion, related to particle displacements as described in Section 2.3.3. Random walk estimates for the diffusion coefficient yield a scaling, $D \propto v_{th}^2 \tau$, where v_{th} is the thermal velocity and τ is the time it takes for a particle to change its momentum substantially [435]. These two properties have competing effects as relativistic kinematics

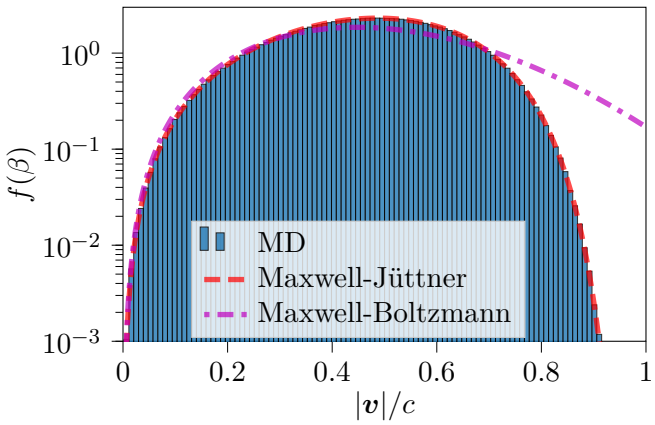

Figure 6.1: Velocity distribution function $f(\beta)$ for normalised velocities $\beta = \boldsymbol{v}/c$, computed in the REL-OCP model (MD) for a system with $\Gamma = 1$ and $\varepsilon = 0.1$. The particles were initialised in a Gaussian distribution in $\boldsymbol{p}$ (non-equilibrium), and are seen to reach the Maxwell-Jüttner distribution after a period of equilibration. The classical Maxwell-Boltzmann distribution ($\varepsilon \to 0$) is shown for comparison.

is introduced. With a finite c, the momentum grows and larger interactions are required to substantially alter the particle trajectories compared to the classical case, increasing τ. However, the particle speed is also capped at c which reduces v_{th} in the relativistic regime.

In Figure 6.2(a) the velocity auto-correlation function is shown within the REL-OCP model at a fixed $\Gamma = 1$. As predicted, the average velocities in units of $\sqrt{k_\mathrm{B}T/m_i}$ are seen to decrease with increasing ε, while the typical decay time for the correlations increases. The linear behaviour on the linear-logarithmic scale in Figure 6.2(a) describes a hydrodynamic behaviour, and the departure from this trend at short times represents the inability of hydrodynamic models to describe the short-time dynamics [204]. In Figure 6.2(b), D is observed to decrease as ε increases and the reduction in v_{th}^2 is larger than the increase in τ. When the relativistic parameter exceeds roughly $\varepsilon \gtrsim 0.05$ the predicted diffusion coefficient is seen to differ from the OCP limit by more than 5%. Corrections on this level are in line with the findings in Paper (E), where a similar system was modelled using a Lennard-Jones interaction. Kremer [436] derived an analytic expression for the relativistic diffusion coefficient within a theory approaching a hard-sphere gas in the classical limit, which was adapted for comparison in Paper (E). The analytical results depend on an unknown cross-section that for comparison was set to match the MD prediction at $\varepsilon = 1$. Kremer's results show qualitative agreement with the

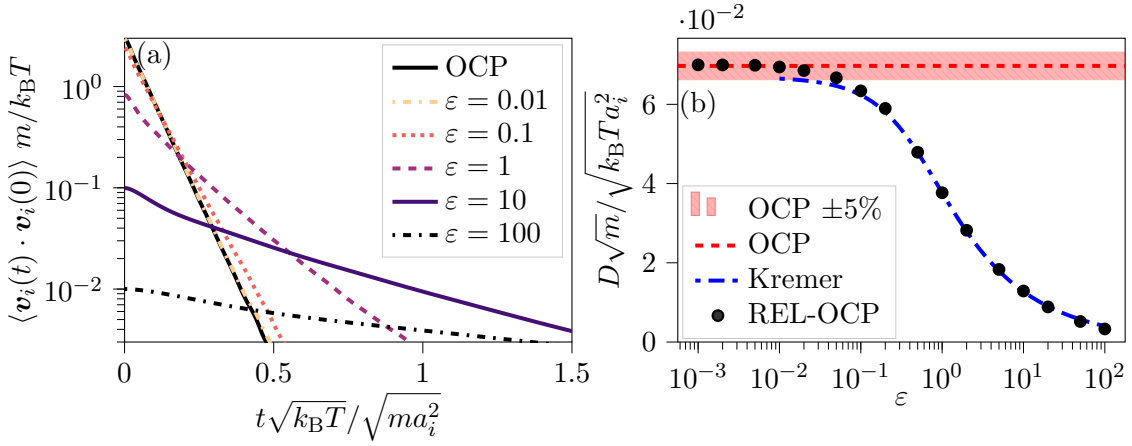

Figure 6.2: (a) Velocity auto-correlation function and (b) diffusion coefficient in REL-OCP model at $\Gamma = 1$ and varying relativistic parameter ε. The models are compared to the OCP limit $\varepsilon \to 0$ and the shaded area shows values within 5% of this limit. Furthermore, the diffusion is compared with the model by Kremer [436] scaled to match the MD predictions at $\varepsilon = 1$. A system of $N = 32000$ particles has been used.

MD predictions and describe the transition from the non-relativistic to the relativistic regime. Only minor changes to the interactions are seen for a wide range of ε.

Before continuing to consider electromagnetic interactions, a comment on relativistic hydrodynamics is warranted, as this is the theory within which the diffusion coefficient would be used. As shown by Kostädt and Liu [437], the diffusion equation (2.13) is incompatible with causality, and several alternative models have been proposed to amend this issue [438–440]. Florkowski *et al.* [441] notes that the breakdown of the classical diffusion equation is primarily on short wavelengths beyond the validity of the hydrodynamic formulation. The classical hydrodynamic formulation is therefore still useful for the description of long-length scales. For a more complete overview of the topic, see Dunkel and Hänggi [442].

6.3 Relativistic interactions

It is well known that the electromagnetic action is Lorentz invariant and Maxwell equations transform appropriately under a Lorentz boost [429]. Electromagnetic interactions adhere to causality constraints and electromagnetic wave propagates at the speed of light. Therefore, the resulting interaction between two particles is retarded, an effect which grows with particle

separation. The particle interactions cannot therefore be described purely in terms of a single separation, and the description in Section 6.2 must be generalised [433]. Furthermore, electromagnetic interaction adds additional degrees of freedom – transverse field modes accounting for radiation – to the description [112, 429].

The electromagnetic action integral is [112, 429]:

$$\mathcal{S}_{\mathrm{EM}} = \int dt \, \left(\mathcal{L}^{\mathrm{P}}_{\mathrm{EM}} + \mathcal{L}^{\mathrm{F}}_{\mathrm{EM}} \right) \tag{6.4}$$

where

$$\mathcal{L}^{\mathrm{P}}_{\mathrm{EM}} = -\sum_{i=1}^{N} m_i c^2 \sqrt{1 - \frac{\boldsymbol{v}_i^2}{c^2}}, \tag{6.5a}$$

and

$$\mathcal{L}^{\mathrm{F}}_{\mathrm{EM}} = \int d^3\boldsymbol{x} \left(\frac{\varepsilon_0}{2} \boldsymbol{E}^2 - \frac{1}{2\mu_0} \boldsymbol{B}^2 + \boldsymbol{j} \cdot \boldsymbol{A} - n\phi \right). \tag{6.5b}$$

The action is defined in terms of positions $\boldsymbol{r}_i$ and velocities $\boldsymbol{v}_i$ of the particles, and the scalar ϕ and vector $\boldsymbol{A}$ potentials of the electromagnetic field. The electric and magnetic fields are $\boldsymbol{E} = -\boldsymbol{\nabla}\phi - \partial_t \boldsymbol{A}$ and $\boldsymbol{B} = \boldsymbol{\nabla} \times \boldsymbol{A}$, respectively. The particles couple to the fields through the charge density

$$n(\boldsymbol{x}) = \sum_{i=1}^{N} q_i S_i(\boldsymbol{x} - \boldsymbol{r}_i) - \frac{1}{V} \sum_{i=1}^{N} q_i, \tag{6.6a}$$

and current density

$$\boldsymbol{j}(\boldsymbol{x}) = \sum_{i=1}^{N} q_i \boldsymbol{v}_i S_i(\boldsymbol{x} - \boldsymbol{r}_i) - \frac{1}{V} \sum_{i=1}^{N} q_i \boldsymbol{v}_i, \tag{6.6b}$$

where q_i is the charge of particle i. The function $S_i(\boldsymbol{x})$ is the density envelope of a particle and relates to microscopic density smearing. In a classical one-component model, particles are treated as points and $S_i(\boldsymbol{x}) = \delta^{(3)}(\boldsymbol{x})$. For the treatment of two-component plasmas, a smearing with quantum origin on the length scale of the de Broglie wavelength Λ_{th} must be incorporated (see Section 1.2.2). In equations (6.6a) and (6.6b), a background subtraction has been included since the simulations discussed will be performed using periodic boundary

conditions [443]. The background must be included for charge and current neutrality, as the current is not proportional to the conserved momentum and will fluctuate in relativistic systems.

From the action integral, the equations of motion for both particles and potentials can be derived [429]. PIC simulations typically solve a similar set of equations [444]. However, in PIC each computational particle represents a large number of physical particles – a *macro particle* – and has an extent in terms of a shape function. The shape function allows for grid computation of the field and is numerical in nature. Formally, this can be seen as a softening of the *numerical collisions* [228] and the effect of microscopic particle collisions is typically added via a Monte Carlo treatment [421, 422]. Therefore, care should be taken when treating microscopic physics in PIC formulations [445].

Alternative routes for evaluating the dynamics in *field-less* formulations are based on the Liénard-Wiechert potentials [446], where the effect of the fields is captured in terms of the history of particle degrees of freedom. The extension of this formulation is the non-instantaneous *action-at-a-distance principles* [194, 447–449] and Fokker's action principle [450], where the action integrals are written in terms of a double integral in time to incorporate the history of the particles. This type of action can be derived by formally solving the equations of motion for the field in terms of particle properties, e.g., $\boldsymbol{A}(\boldsymbol{x},t) = \boldsymbol{A}(\boldsymbol{x};\boldsymbol{r}_1(t),\boldsymbol{v}_1(t),\ldots,\boldsymbol{r}_N(t),\boldsymbol{v}_N(t))$, and inserting the solution into the original Lagrangian [451]. In practice, simulation methods based on non-instantaneous action principles require solving for the historical time point where each pair of particles is causally connected and storing particle histories [115]. Below, a model is discussed that relates to both the field-less and field descriptions on different length scales.

6.3.1 Length-scale separation of electromagnetic interactions

The basic observation is that Maxwell's equations are linear and superpositions of solutions which solve for a subset of the charge and current distributions may be used to form the

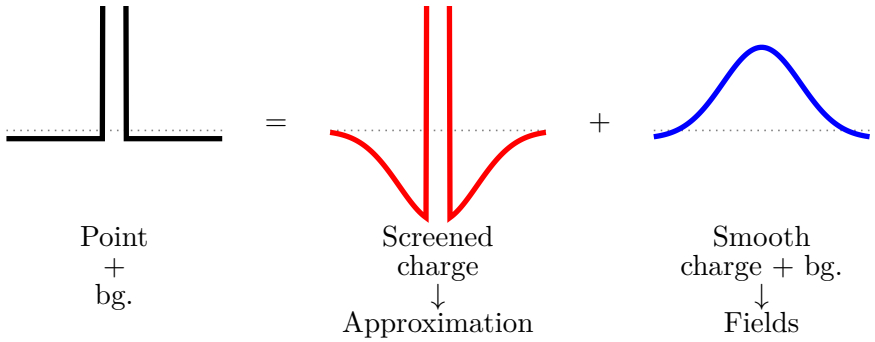

Figure 6.3: Schematic for the separation in equations (6.7) and (6.8). S_i is depicted as a narrow charge (Point) and φ as a Gaussian shape function.

general solution. Therefore, consider the *screened distributions*:

$$n^{(s)}(\boldsymbol{x}) = \sum_{i=0}^{N} \quad q_i \left(S_i(\boldsymbol{x} - \boldsymbol{r}_i) - \sigma^{-3} \varphi\left(\frac{\boldsymbol{x} - \boldsymbol{r}_i}{\sigma} \right) \right), \tag{6.7a}$$

$$\boldsymbol{j}^{(s)}(\boldsymbol{x}) = \sum_{i=0}^{N} q_i \boldsymbol{v}_i \left(S_i(\boldsymbol{x} - \boldsymbol{r}_i) - \sigma^{-3} \varphi\left(\frac{\boldsymbol{x} - \boldsymbol{r}_i}{\sigma} \right) \right), \tag{6.7b}$$

and the *smooth distributions*:

$$n^{(\ell)}(\boldsymbol{x}) = \sum_{i=0}^{N} \quad q_i \sigma^{-3} \varphi\left(\frac{\boldsymbol{x} - \boldsymbol{r}_i}{\sigma} \right) - \frac{1}{V} \sum_{i=1}^{N} q_i, \tag{6.8a}$$

$$\boldsymbol{j}^{(\ell)}(\boldsymbol{x}) = \sum_{i=0}^{N} q_i \boldsymbol{v}_i \sigma^{-3} \varphi\left(\frac{\boldsymbol{x} - \boldsymbol{r}_i}{\sigma} \right) - \frac{1}{V} \sum_{i=1}^{N} q_i \boldsymbol{v}_i, \tag{6.8b}$$

which sum to the original distributions, i.e., $n = n^{(s)} + n^{(\ell)}$ and $\boldsymbol{j} = \boldsymbol{j}^{(s)} + \boldsymbol{j}^{(\ell)}$, and satisfies their own continuity equations. The separation is constructed by adding and subtracting a normalised shape function with scale length σ, analogous to Woodcock and Singer's [224] treatment of the classical Ewald summation. The construction is illustrated in Figure 6.3. The screened charges encapsulate the small length scale density fluctuations, primarily resulting in short-range interactions well suited for MD formulations. Magnetic interactions are not screened in the same way as electric interactions, but the formulation still reduces their range. The smooth charges have a finite extent and are amendable to grid computations where long-range interactions can be handled by a field solver.

The two charge distributions cannot be treated fully separately, as both depend on the same particle positions and velocities. Introduce an offset into the description of the potentials, $\phi = \phi^{(s)} + \phi^{(\ell)}$ and $\boldsymbol{A} = \boldsymbol{A}^{(s)} + \boldsymbol{A}^{(\ell)}$, where $\phi^{(\ell)}$ and $\boldsymbol{A}^{(\ell)}$ are the new dynamic variables and

$$\boldsymbol{\nabla}^2\phi^{(s)} + \frac{\partial}{\partial t}\left(\boldsymbol{\nabla}\cdot\boldsymbol{A}^{(s)}\right) = -n^{(s)}/\varepsilon_0, \tag{6.9a}$$

$$\frac{1}{c^2}\frac{\partial^2\boldsymbol{A}^{(s)}}{\partial t^2} - \boldsymbol{\nabla}^2\boldsymbol{A}^{(s)} + \frac{1}{c^2}\frac{\partial\boldsymbol{\nabla}\phi^{(s)}}{\partial t} = \mu_0\boldsymbol{j}^{(s)}, \tag{6.9b}$$

defines $\phi^{(s)}$ and $\boldsymbol{A}^{(s)}$ which are offsets chosen based on the screened charges. Equation (6.9) is Maxwell's equations with sources $n^{(s)}$ and $\boldsymbol{j}^{(s)}$. By repeated integration by parts and assuming all boundary terms vanish, the action integral in equation (6.4) is rewritten as

$$\mathcal{S}_{\mathrm{EM}} = \int dt\ \left(\mathcal{L}^{\mathrm{P}}_{\mathrm{EM}} + \mathcal{L}^{(\ell)}_{\mathrm{EM}} + \mathcal{L}^{(s)}_{\mathrm{EM}} + \mathcal{L}^{(s-\ell)}_{\mathrm{EM}}\right), \tag{6.10}$$

where

$$\mathcal{L}^{(\ell)}_{\mathrm{EM}} = \int d^3\boldsymbol{x}\left(\frac{\varepsilon_0}{2}\left(\boldsymbol{E}^{(\ell)}\right)^2 - \frac{1}{2\mu_0}\left(\boldsymbol{B}^{(\ell)}\right)^2 + \boldsymbol{j}^{(\ell)}\cdot\boldsymbol{A}^{(\ell)} - n^{(\ell)}\phi^{(\ell)}\right), \tag{6.11a}$$

$$\mathcal{L}^{(s)}_{\mathrm{EM}} = \int d^3\boldsymbol{x}\ \left(\frac{1}{2}\boldsymbol{j}^{(s)}\cdot\boldsymbol{A}^{(s)} - \frac{1}{2}n^{(s)}\phi^{(s)}\right), \tag{6.11b}$$

$$\mathcal{L}^{(s-\ell)}_{\mathrm{EM}} = \int d^3\boldsymbol{x}\ \left(\boldsymbol{j}^{(\ell)}\cdot\boldsymbol{A}^{(s)} - n^{(\ell)}\phi^{(s)}\right). \tag{6.11c}$$

The particle kinetic term $\mathcal{L}^{\mathrm{P}}_{\mathrm{EM}}$ is unchanged and $\mathcal{L}^{(\ell)}_{\mathrm{EM}}$ has the form of a standard electromagnetic field interacting with finite-size particles. The interaction between screened charges are described by $\mathcal{L}^{(s)}_{\mathrm{EM}}$, and the cross term $\mathcal{L}^{(s-\ell)}_{\mathrm{EM}}$ describes an interaction between the screened fields and the smooth charges. Note that this last term does not involve $\phi^{(\ell)}$ or $\boldsymbol{A}^{(\ell)}$, and can be interpreted as a particle-particle interaction with a limited range. The origin of the cross-term $\mathcal{L}^{(s-\ell)}_{\mathrm{EM}}$ can be understood by considering the energy associated with the scalar potential ϕ in

the Coulomb gauge. The energy is quadratic in the density field and proportional to

$$\begin{aligned}\frac{1}{2}\int d^3\boldsymbol{x}_1 \int d^3\boldsymbol{x}_2 \frac{n(\boldsymbol{x}_1)n(\boldsymbol{x}_2)}{|\boldsymbol{x}_1-\boldsymbol{x}_2|} &= \frac{1}{2}\int d^3\boldsymbol{x}_1 n^{(s)}(\boldsymbol{x}_1)\int d^3\boldsymbol{x}_2 \frac{n^{(s)}(\boldsymbol{x}_2)}{|\boldsymbol{x}_1-\boldsymbol{x}_2|} \\ &+ \int d^3\boldsymbol{x}_1 n^{(\ell)}(\boldsymbol{x}_1)\int d^3\boldsymbol{x}_2 \frac{n^{(s)}(\boldsymbol{x}_2)}{|\boldsymbol{x}_1-\boldsymbol{x}_2|} + \frac{1}{2}\int d^3\boldsymbol{x}_1 n^{(\ell)}(\boldsymbol{x}_1)\int d^3\boldsymbol{x}_2 \frac{n^{(\ell)}(\boldsymbol{x}_2)}{|\boldsymbol{x}_1-\boldsymbol{x}_2|},\end{aligned} \tag{6.12}$$

where the first and second term on the right-hand side corresponds to the scalar field contribution in $\mathcal{L}^{(s)}_{\mathrm{EM}}$ and $\mathcal{L}^{(s-\ell)}_{\mathrm{EM}}$, respectively, as the inner integral gives the potential. When comparing the last term and $\mathcal{L}^{(\ell)}_{\mathrm{EM}}$, the field contribution from $\boldsymbol{E}^{(\ell)}$ must be considered.

Formally, equation (6.10) does not pose any simplification to equation (6.4), since equation (6.9) requires solving another system of Maxwell's equations and if $\mathcal{L}^{(s)}_{\mathrm{EM}}$ and $\mathcal{L}^{(s-\ell)}_{\mathrm{EM}}$ are written explicitly they have the form of a Fokker action. However, below it is argued that $\phi^{(s)}$ and $\boldsymbol{A}^{(s)}$ can be more efficiently approximated than the full fields. Another type of split of transverse and longitudinal fields was discussed by Tanaka and Murakami [452].

6.3.2 Short-range interactions

On the atomic scale, the electromagnetic fields are highly fluctuating, especially when considering localised charges. It is therefore challenging to efficiently represent the field on this length scale, both using grid and $\boldsymbol{k}$-space methods. The motivation for the above construction is to isolate the highly fluctuating field components in $\phi^{(s)}$ and $\boldsymbol{A}^{(s)}$. Four treatments of the short-range interactions will be discussed, even if the remainder of the chapter limits itself to considering only the first two approximations. To be explicit, a system of point charges is considered, $S_i(\boldsymbol{x}) = \delta^{(3)}(\boldsymbol{x})$, and the shape function $\varphi(\boldsymbol{x}) = \exp(-\boldsymbol{x}^2/2)/(2\pi)^{3/2}$ is a Gaussian.

Electrostatics

The simplest approximation of $\phi^{(s)}$ and $\boldsymbol{A}^{(s)}$ is the electrostatic one, akin to the Coulomb treatment widely used in MD. This not only neglect retardation and treats interactions as instantaneous, but also magnetic interactions are disregarded. Neglecting retardation is less severe for the screened short-range interaction compared to the equivalent approximation for

the full long-range interaction. In the Coulomb gauge, the potential is

$$\phi^{(s)}(\boldsymbol{x}) = \frac{1}{4\pi\varepsilon_0}\sum_{i=1}^{N} q_i \frac{\operatorname{erfc}\left(|\boldsymbol{x}-\boldsymbol{r}_i|/\sqrt{2\sigma^2}\right)}{|\boldsymbol{x}-\boldsymbol{r}_i|}, \tag{6.13}$$

and $\boldsymbol{A}^{(s)} = 0$. The screened nature of the interaction, $\operatorname{erfc}\left(s/\sqrt{2}\right) \propto \exp\left(-s^2/2\right)$ for $s \gg 1$, makes it suitable for a real space treatment in MD, see Section 2.3.5. Furthermore, the resulting Hamiltonian is separable, which is beneficial for the time-stepping algorithms, see Section 2.3.4.

Darwin approximation

The lowest order correction to the Coulomb interaction is the *Darwin approximation*[2] [453] and is the unique and gauge-invariant correction of order $\mathcal{O}\left(\boldsymbol{v}_i^2/c^2\right)$ [451]. In the quantum mechanical literature, it commonly goes under the name *Breit interaction* [454]. In the Coulomb gauge, the approximation can be derived by neglecting the time dependence of the vector potential [112] and the magnetic interaction is based on instantaneous positions and velocities. However, using other gauge choices, the retardation must be accounted for, see, e.g., Landau and Lifshitz [429].

For the screened charges, the traditional formulation in the Coulomb gauge [112] can be convolved with the charge distribution, resulting in the scalar potential in equation (6.13) and the vector potential

$$\boldsymbol{A}^{(s)}(\boldsymbol{x}) = \frac{1}{4\pi\varepsilon_0}\sum_{i=1}^{N} \frac{q_i}{2c^2|\boldsymbol{x}-\boldsymbol{r}_i|}\mathbf{H}(\boldsymbol{x}-\boldsymbol{r}_i)\boldsymbol{v}_i, \tag{6.14}$$

where

$$\mathbf{H}(\boldsymbol{x}) = \Big(n_1\left(|\boldsymbol{x}|\right) + \boldsymbol{n}_\perp\left(|\boldsymbol{x}|\right)\Big)\mathbf{1} + \Big(n_\parallel\left(|\boldsymbol{x}|\right) - n_\perp\left(|\boldsymbol{x}|\right)\Big)\frac{\boldsymbol{x}\boldsymbol{x}^\mathsf{T}}{|\boldsymbol{x}|^2}, \tag{6.15}$$

and

$$n_1(x) = 1 - x\int \frac{d^3\boldsymbol{y}}{\sigma^3}\frac{\varphi(|\boldsymbol{y}+x\hat{\boldsymbol{z}}|/\sigma)}{|\boldsymbol{y}|} = \operatorname{erfc}\left(x/\sqrt{2\sigma^2}\right), \tag{6.16a}$$

[2]Named after Sir Charles Galton Darwin, grandson to the famous naturalist.

$$n_\perp(x) = -\frac{x}{2}\int \frac{d^3\boldsymbol{y}}{\sigma^3}\frac{\varphi(|\boldsymbol{y}+x\hat{\boldsymbol{z}}|/\sigma)}{|\boldsymbol{y}|}\sin^2\theta, \tag{6.16b}$$

$$n_\parallel(x) = 1 - x\int \frac{d^3\boldsymbol{y}}{\sigma^3}\frac{\varphi(|\boldsymbol{y}+x\hat{\boldsymbol{z}}|/\sigma)}{|\boldsymbol{y}|}\cos^2\theta, \tag{6.16c}$$

given in terms of the angle $\cos\theta = \boldsymbol{y}\cdot\hat{\boldsymbol{z}}/|\boldsymbol{y}|$ and a unit vector $\hat{\boldsymbol{z}}$ in any direction. Note the velocity dependence of $\boldsymbol{A}^{(s)}$ which makes the Lagrangian non-separable and it is non-trivial to invert the canonical momentum, i.e. $\boldsymbol{v}_i = \boldsymbol{v}_i(\boldsymbol{r}_1, \boldsymbol{p}_1, \ldots, \boldsymbol{r}_N, \boldsymbol{p}_N)$, and find the Hamiltonian [455] unless the magnetic interaction is assumed to be a perturbation [429]. This is because the field degrees of freedom are formally "attached" to the particles. For time evolution, the Lagrangian equations of motion are therefore solved and the details of the method are described in Appendix D.2. In many accounts of the Darwin Lagrangian [112, 429], the kinetic term $\mathcal{L}^{\mathrm{P}}_{\mathrm{EM}}$ is expanded in powers of $|\boldsymbol{v}_i|/c$ to match the $\mathcal{O}\left(\boldsymbol{v}_i^2/c^2\right)$ treatment of the interactions. However, here the full relativistic expression is retained, as it results in a marginal computational cost.

Exact Darwin approximation

The approximation some authors have referred to as the *exact Darwin Lagrangian* [456], accounts for some degree of retardation without the need to store particle histories. The approximation can be derived either by assuming the particles travel in straight lines with the current velocities for the purpose of evaluating interactions [456] or by neglecting acceleration and higher order time derivative of the position in an expanded Lagrangian formulation [455]. Straight-line motion and non-accelerated particles do not emit any radiation, which therefore is neglected in this approximation. The benefit compared to a fully retarded solution is the trivial computation to find the causally connected points, and there is no need to store the trajectories.

Full retarded interaction

The full solution of equations (6.9a) and (6.9b) in a field-less manner would be the complete description. The current treatment of short and long-range physics could still be beneficial for this case, as it suppresses the source terms in equation (6.9) on long-length scales and could

reduce the length of the time history needed to be stored for each particle. In the author's view, this would be the way to consistently include radiation originating from the smallest length scales.

6.3.3 Long-range interactions

The Lagrangian for the long-range fields and field-particle interactions, $\mathcal{L}^{(\ell)}_{\mathrm{EM}}$, has the standard form for finite-size particles. This could be treated using grid methods like in PIC simulations. However, the discussion here will be along the lines of an Ewald summation as discussed in Chapters 2 and 3. Working with periodic boundary conditions and the Coulomb gauge, the Lagrangian in Fourier transformed variables is

$$\begin{aligned}\mathcal{L}^{(\ell)}_{\mathrm{EM}} = \frac{1}{V}\sum_{\boldsymbol{k}}\Bigg[&\frac{\varepsilon_0|\boldsymbol{k}|^2}{2}\phi^{(\ell)}_{\boldsymbol{k}}\phi^{(\ell)}_{-\boldsymbol{k}} + \frac{\varepsilon_0}{2}\frac{\partial \boldsymbol{A}^{(\ell)}_{\boldsymbol{k}}}{\partial t}\cdot\frac{\partial \boldsymbol{A}^{(\ell)}_{-\boldsymbol{k}}}{\partial t} - \frac{1}{2\mu_0}\boldsymbol{A}^{(\ell)}_{\boldsymbol{k}}\cdot\boldsymbol{A}^{(\ell)}_{-\boldsymbol{k}} \\ &+ \boldsymbol{j}^{(\ell)}_{-\boldsymbol{k}}\cdot\boldsymbol{A}^{(\ell)}_{\boldsymbol{k}} - n^{(\ell)}_{-\boldsymbol{k}}\phi^{(\ell)}_{\boldsymbol{k}}\Bigg],\end{aligned} \tag{6.17}$$

where $f_{\boldsymbol{k}}$ is the spatial Fourier transform of any field $f(\boldsymbol{x})$, and $\boldsymbol{k}$ is defined as in Section 2.3.6. Given that the fields are real-valued $f_{-\boldsymbol{k}} = f^*_{\boldsymbol{k}}$ and only half of the $\boldsymbol{k}$-vectors need to be explicitly considered. The equations of motion for the field directly follow:

$$|\boldsymbol{k}|^2\phi^{(\ell)}_{\boldsymbol{k}} = \varepsilon_0^{-1}n^{(\ell)}_{\boldsymbol{k}}, \tag{6.18a}$$

$$\frac{\partial \boldsymbol{A}^{(\ell)}_{\boldsymbol{k}}}{\partial t} = \varepsilon_0^{-1}\boldsymbol{\Pi}^{(\ell)}_{-\boldsymbol{k}}, \tag{6.18b}$$

$$\frac{\partial \boldsymbol{\Pi}^{(\ell)}_{\boldsymbol{k}}}{\partial t} = -\frac{|\boldsymbol{k}|^2}{\mu_0}\boldsymbol{A}^{(\ell)}_{-\boldsymbol{k}} + \boldsymbol{j}^{(\ell)}_{-\boldsymbol{k}}, \tag{6.18c}$$

where $\boldsymbol{\Pi}^{(\ell)}_{\boldsymbol{k}}$ is related to the canonical momentum of $\boldsymbol{A}^{(\ell)}_{\boldsymbol{k}}$ and defined via equation (6.18b). In the Coulomb gauge, the scalar potential is set by the current charge distribution, and only the vector potential with two independent polarisations per $\boldsymbol{k}$-mode is time-propagated.

Due to the background contribution in $n^{(\ell)}$ and $\boldsymbol{j}^{(\ell)}$, the source term vanished in equation (6.18) at $\boldsymbol{k} = 0$ and the corresponding field modes are assumed to be zero as well. Furthermore, given the smooth shape function φ, the source terms also vanish when $\sigma|\boldsymbol{k}| \gg 1$ and the field

equations decouple from the particles. This motivates truncating the number of $\boldsymbol{k}$-modes in a numerical evaluation, and without a smooth φ the number of $\boldsymbol{k}$-modes quickly grows unfeasible large [115].

Heat capacity

The introduction of transverse electric and magnetic fields adds additional degrees of freedom to the model, which can store energy. Namely, as given in Appendix D.2, the energy of the transverse electric and magnetic fields per $\boldsymbol{k}$-mode and polarisation $\boldsymbol{\epsilon}^{(i)}$ are

$$E_{\boldsymbol{k}}^{(\mathrm{ele})} = \frac{1}{2\varepsilon_0 V}\left(\boldsymbol{\Pi}_{\boldsymbol{k}}^{(\ell)} \cdot \boldsymbol{\epsilon}^{(i)}\right)\left(\boldsymbol{\Pi}_{-\boldsymbol{k}}^{(\ell)} \cdot \boldsymbol{\epsilon}^{(i)}\right), \tag{6.19a}$$

and

$$E_{\boldsymbol{k}}^{(\mathrm{mag})} = \frac{|\boldsymbol{k}|^2}{2\mu_0 V}\left(\boldsymbol{A}_{\boldsymbol{k}}^{(\ell)} \cdot \boldsymbol{\epsilon}^{(i)}\right)\left(\boldsymbol{A}_{-\boldsymbol{k}}^{(\ell)} \cdot \boldsymbol{\epsilon}^{(i)}\right), \tag{6.19b}$$

respectively. In particular, $\boldsymbol{\Pi}_{\boldsymbol{k}}^{(\ell)}$ has a quadratic energy contribution where equipartition gives an average energy of $\frac{1}{2}k_{\mathrm{B}}T$ per mode and polarisation. There is no fundamental smallest wavelength in the model and the number of $\boldsymbol{k}$-modes is unlimited, despite being truncated in an actual computation. Therefore, the transverse field has a divergent heat capacity, and this is the ultraviolet catastrophe which Planck resolved by quantising the field [457].

For weakly coupled plasmas, fields with wavelengths shorter than the *skin depth* are suppressed, and a further suppression appears for models with finite-size particles. Dawson gives the average magnetic energy as [228]

$$\left\langle E_{\boldsymbol{k}}^{(\mathrm{mag})} \right\rangle_T = \frac{1}{2}\frac{k_{\mathrm{B}}T}{1 + \lambda_{\mathrm{EM}}^2 \boldsymbol{k}^2 e^{\sigma^2 \boldsymbol{k}^2}}, \tag{6.20}$$

where $\lambda_{\mathrm{EM}} = \sqrt{\langle\gamma\rangle_T/\varepsilon}\,\lambda_D$ is the skin depth with the relativistic correction [366, 458]. The average γ-function is given in terms of the generalised Fermi-Dirac integrals in Section 1.2.4 as $\langle\gamma\rangle_T = \tilde{F}_{1/2,2,1/2}(\eta,\varepsilon)/\tilde{F}_{1/2,1,1/2}(\eta,\varepsilon)$ where η is a large negative value in the classical regime. The spectrum in equation (6.20) does not account for any short-range contributions, as the particles are fundamentally considered to have a finite size.

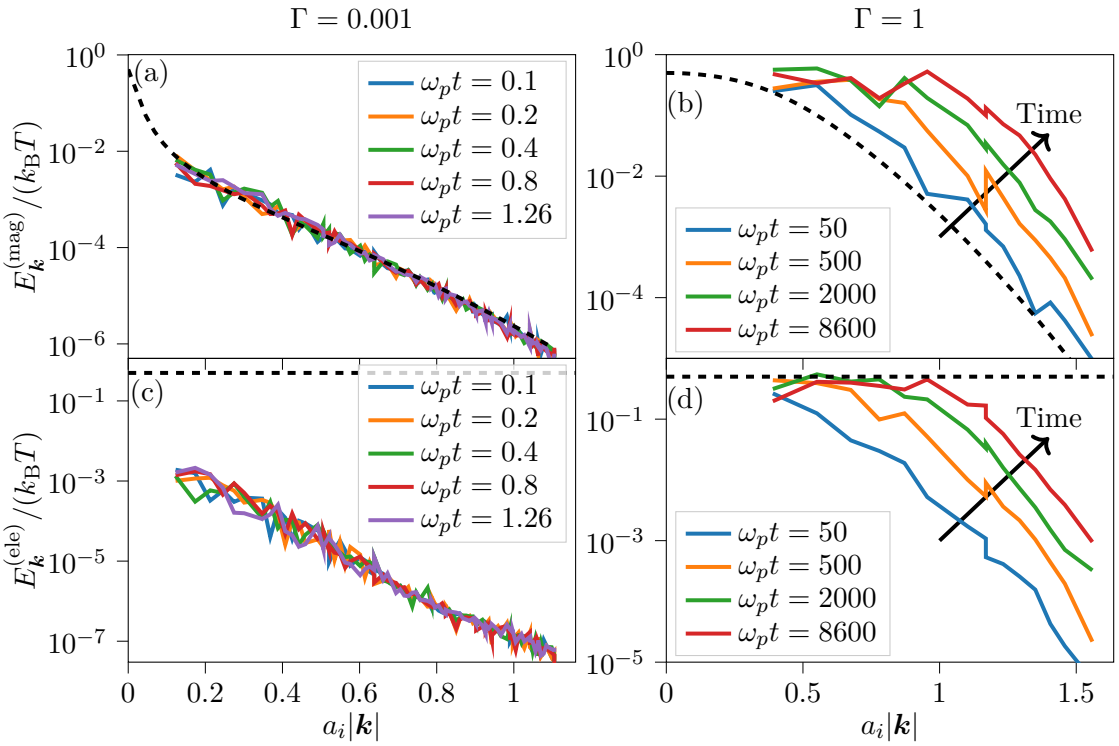

Figure 6.4: Energy stored in transverse electric ((a) and (b)) and magnetic ((c) and (d)) fields for snapshots of two simulations started without any transverse fields. Dashed lines are the spectrum given by equation (6.20) for the magnetic case and equipartition in the electric case. For $\Gamma = 0.001$ ((a) and (c)) and $\Gamma = 1$ ((b) and (d)), system sizes of $N = 32000$ and $N = 1000$ were used, respectively. Both systems have $\sigma = 2a_i$ and $\varepsilon = 0.1$. The simulations used the electrostatic approximation for the short-range fields. Particles were initialised with a Maxwell-Jüttner velocity distribution and a few steps of energy minimisation were performed on the initial random particle positions to avoid overexciting long-wavelength modes [228]. For the strong coupling case, the system was thermostated as described in Section 2.3.7.

The simulation results for the energy content of the transverse field modes in Figure 6.4 show two distinct behaviours in the weak and strong coupling regimes. Equation (6.20) is seen to describe the magnetic energy for the case of $\Gamma = 0.001$ in Figure 6.4(a), and the equilibrium spectrum is reached in less than an inverse plasma frequency and stable after this point. Furthermore, the energy of the electric field, as seen in Figure 6.4(c), is also strongly suppressed. For $\Gamma = 1$, the electric field energy is seen to approach a value close to equipartition with time, but the process is slow when the wavelength of the modes is smaller than the size of the smoothed particles. To maintain a stable temperature, the strong coupling case is thermostated by the method described in Section 2.3.7 as a considerable amount of

energy is transferred from the particles to the field. Therefore, the number of $\boldsymbol{k}$-modes retained in the simulation will impact the average energy of the fields in this case. The interaction time with the particles is long enough that stable measurements of particle properties can be made after a period of thermalisation. This behaviour is expected for a classical treatment of the fields, and Monte Carlo treatments of detailed balance have been used to regularise the high-frequency modes [115].

6.4 Numerical realisation

The formulation in Section 6.3 has been implemented in `LAMMPS`, with short-range interactions given by the electrostatic and Darwin approximations, and field dynamics based on an Ewald-like description. The equations of motion are given in Appendix D.2 for the particles and in equation (6.18) for fields. As described in Section 3.3, `LAMMPS` is structured around a domain decomposition, and each processor treats the particles in a given region. Fourier transformed variables and the field modes are global properties that all processors have access to at each time step. The dominant computational cost is the evaluation of interactions that can be parallelised as the computation of $n_{\boldsymbol{k}}^{(\ell)}$ and $\boldsymbol{j}_{\boldsymbol{k}}^{(\ell)}$ can be calculated for each region and then summed between processors. Evaluation of the force due to field modes (see Appendix D.2) is a local operation if the field degrees of freedom are scattered to all processors. Short-range interactions are tabulated using the method of Wolff and Rudd [459] for the spatial dependence. The velocity-dependent potentials in the Darwin approximation have a polynomial velocity dependence multiplied by a tabulated spatial structure.

The Lagrangian in equation (6.11) is non-separable when using the Darwin approximation and Runge-Kutta methods [213, 214] have been used for time evolution. Multiple explicit *Butcher tableaus* have been tested with similar performance. The results below have been computed using the classical RK4 algorithm given in Section 3.3. The velocity-dependent interaction results in the need to invert a $(3N) \times (3N)$-matrix in each time step, see Appendix D.2. Fortunately, the matrix is sparse if the short-range interactions can be efficiently truncated. The parallel solution of the matrix equation is performed using an iterative Krylov subspace

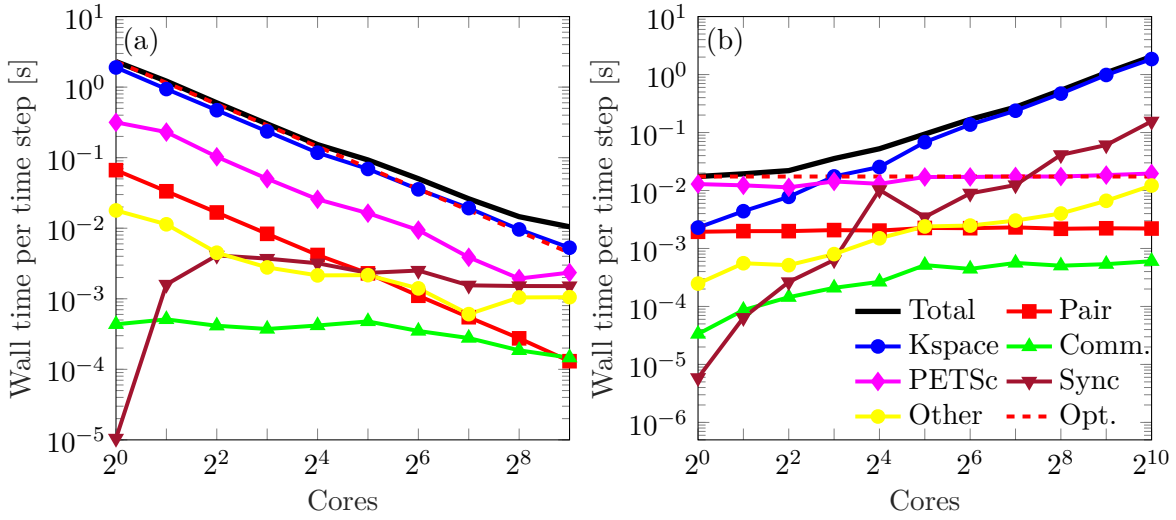

Figure 6.5: Scaling of computational time for relativistic MD implementation at $\Gamma = 0.1$ and $\varepsilon = 0.1$. The length scale of the shape function is $\sigma = 1.5\, a_i$. (a) Strong scaling for $N = 32000$ particles. (b) Weak scaling with $N/\#\text{Cores} = 1000$. Labels are as given in the main text.

method implemented by the `PETSc` library [460–462], which has been incorporated into `LAMMPS`.

The number of $\boldsymbol{k}$-modes used for the computation is given by Kolafa and Perram [223], by noting that the electrostatic interaction from $\phi^{(\ell)}_{\boldsymbol{k}}$ is equivalent to the classical Ewald summation given the Ewald parameter $g = 1/(2\sigma)^3$. This estimate does not consider transverse fields, which should instead be tested by a convergence analysis.

The numerical performance of the implementation is demonstrated in Figure 6.5, where the time spent in different parts of the implementation is shown. In particular, the dominant computational costs are evaluating the short-range interactions (Pair), long-range interaction (Kspace) and inverting the equations of motion (PETSc). The time spent communicating particle properties (Comm.), synchronisation between processors (Sync), time evolution – which includes the communication of field degrees of freedom – and all other aspects of the computation (Other) are typically minor except for the largest systems. Figure 6.5(a) shows the strong scaling for a fixed number of particles $N = 32000$ and $\sigma = 1.5\, a_i$, where the interaction computation demonstrates a close to perfect scaling. The matrix inversion scales well up to a 2^8 cores where the processors primarily communicate rather than perform computations, due

[3]This is not evident from equation (6.13), as the final real-space interaction includes contributions from both $\mathcal{L}^{(s)}_{\text{EM}}$ and $\mathcal{L}^{(s-\ell)}_{\text{EM}}$.

to the small domain treated by each processor.

The weak scaling is shown in Figure 6.5(b) with on average 1000 particles per processor. Both the computation of pair interactions as well as the matrix inversion show close to optimal behaviour up to 2^{10} cores and more than 10^6 particles. The challenging contribution is the long-range interaction in which the algorithm does not scale linearly with particle number N. The classical Ewald summation scale as $\mathcal{O}\left(N^{3/2}\right)$ by allowing the Ewald parameter g to vary. However, the corresponding parameter here σ is tied to the approximations and is preferably kept fixed. With fix σ, the required spatial resolution Δx is constant, while the edge length of the simulation box L scales with the particle number N. Therefore, the number of $\boldsymbol{k}$-modes needed is proportional to N,

$$\#\mathrm{K} \propto \left(\frac{L}{\Delta x}\right)^3 \propto N, \tag{6.21}$$

and as all N particles interact with all $\boldsymbol{k}$-modes the overall computational cost is $\mathcal{O}\left(N^2\right)$. Grid-based algorithms similar to the `PPPM` method [227] could reduce the scaling to $\mathcal{O}\left(N \log N\right)$ and would be desirable for future implementations. For the largest systems, the synchronisation time due to an unbalanced load between processors is substantial. The computational cost associated with each particle in the Ewald summation is $\mathcal{O}\left(N\right)$ and the impact of particle fluctuations therefore grows with size, but this would also be amended by grid-based computations.

6.5 Test and comparison

To test the implementation, the static structure is shown in Figure 6.6 for a system with $\Gamma = 1$ and $\varepsilon = 0.1$. The classical OCP result is shown for comparison, and all the different levels of the relativistic treatment agree well with the classical case. First, consider the separable REL-OCP Hamiltonian. Conversely to the argument regarding the velocity distribution in Section 6.2.1, the static structure is independent of the kinetic term and must agree with the classical limit. Second, a model where the vector potential is neglected, $\boldsymbol{A}(\boldsymbol{x}) = 0$, is shown, equivalent to the REL-OCP model, but computed using the full numerical implementation as if dynamic fields were included. Third, two cases with dynamical transverse fields and varying

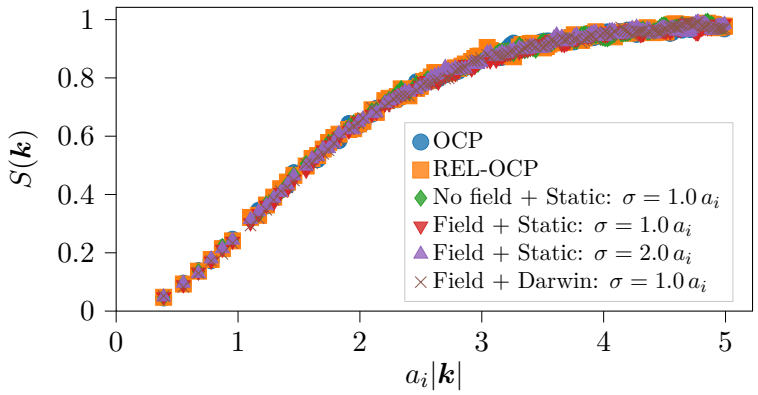

Figure 6.6: Static structure for an OCP system with different levels of relativistic approximations at $\Gamma = 1$ and $\varepsilon = 0.1$. The classical OCP model is compared to models with relativistic kinetic energy, using classical interactions (REL-OCP), computation in the Coulomb gauge neglecting the vector potential $\boldsymbol{A}(\boldsymbol{x})$ (No field + Static), and full electromagnetic computation for long-range fields with electrostatic (Field + Static) and Darwin (Field + Darwin) approximation, respectively, for the short-range interactions.

σ are shown in which the electrostatic approximation for short-range fields is employed. As discussed in Appendix D.2, the static structure is again expected to be the same as for an OCP and demonstrates the independence of the results to σ, which is purely a computational parameter. Last, the Darwin approximation is used for the short-range fields. The Darwin correction is small when the velocities are close to uncorrelated, and this approximation also agrees with the OCP limit within the numerical noise. The Darwin correction would in general be expected to increase in significance if particle velocities are correlated.

6.6 Conclusion

A formulation of relativistic molecular dynamics of charged point-particles is presented which accounts for both the kinetic and interaction terms. The effect of a relativistic formulation for the kinetic energy term was previously investigated in Paper (E) with neutral-neutral particle interactions. This treatment was extended to ionised systems where it is demonstrated that the correct Maxwell-Jüttner velocity distribution is obtained and the diffusion coefficient is seen to be suppressed compared to the non-relativistic limit. The spatial particle transport for strongly coupled plasmas is reduced as velocities are limited to below the speed of light, an

effect that results in corrections larger than 5% to the diffusion coefficient as $k_{\mathrm{B}}T \gtrsim 0.05\, mc^2$.

Treating ionised systems is the more relevant model for thermally relativistic systems, but the long-range Coulomb interactions inevitably lead to a discussion of retarded interactions and electromagnetic effects. To address this issue, a dynamic Ewald summation was developed, where the long-length scale electromagnetic field modes evolve in time based on Maxwell's equations. The number of field modes can be truncated as they couple to the particles via smoothed density and current profiles. The microscopic fields missing in the field formulation are accounted for in a field-less formulation using either the electrostatic or Darwin approximation. The model has been implemented in `LAMMPS` and benchmarked for static structure. The implementation demonstrates good parallel scaling up to 2^9 processors even for moderate-size systems. However, the Ewald summation does not scale linearly with particle number N, something desirable to amend in future implementations using grid-based methods.

The implementation has been used to investigate the energy content of the electromagnetic field modes, where a distinct difference is seen between weakly coupled and strongly coupled plasmas. Collective dynamics and the finite size of the smooth particles suppress short wavelength modes for the weakly coupled case. However, for the strongly coupled system, the field modes acquire an energy close to the equipartition value which suggests an infinite heat capacity of the field unless a quantum truncation of the spectrum is imposed.

Chapter 7
Conclusion and Outlook

7.1 Summary

The main effort in this thesis has been to extend *molecular dynamics* (MD) – which accurately treats strong interactions and many-body correlations – to incorporate various quantum and relativistic effects, and derive dynamic and transport properties from such MD schemes. This has resulted in two separate MD implementations, both built on the scalable open-source code `LAMMPS`. Tailored time integrators, interactions, and particle/field descriptions are provided for the modelling of elongated electron wave packets and relativistic particle-field dynamics, respectively. Both directions taken in this work are motivated by high-energy-density physics, applicable in different parts of phase space, but joined in a common methodology. Unifying the methods would extend the applicable range to model large stellar objects late in their evolution.

Chapter 1 introduces the field of high-energy-density physics with a focus on dimensionless parameters characterising the strength of interaction, quantum degeneracy and relativistic corrections. With this motivation, Chapter 2 discusses atomistic modelling for non-ideal plasmas with a particular emphasis on the technical aspects of MD.

In Chapter 3 an extension of the wave packet formulation using elongated Gaussian states is presented and implemented. The implementation consistently treats long-range Coulomb interactions and approximate exchange properties on a pair-exchange level and has been applied for the modelling of warm dense hydrogen using thousands of particles. The model's ability to resolve electron motion over time scales relevant to the description of ion dynamics is a close to unique feature of wave packet models. This ability is used in Chapters 4 and 5 to investigate the electron *dynamic structure factor* (DSF) on time scales characteristic of electron and ion motion. The electron DSF is directly related to x-ray Thomson scattering and in Chapter 4 it is demonstrated how the method can extract both electron and ion time scale feature from a single computation. Particular attention is given to the inherent quantum characteristics

of the DSF for which a semi-classical formulation is constructed incorporating known limits and constraints. The semi-classical formulation is explicitly tested by the computation of the density response function using the wave packet model. The long wavelength limit of the DSF is explored in Chapter 5, where a comparison between MD results and a two-fluid formulation allows for the extraction of electron transport properties. The extraction is facilitated by Bayesian inference, and the inferred transport properties are in line with a set of reference calculations. The exception is viscosity, which is shown to be markedly lower in the wave packet model compared to classical point particle models.

Chapter 6 addresses relativistic corrections in high-density plasmas based on altered kinematics and electromagnetic interactions. This leads to an MD model where the long-range interactions are treated using dynamically evolving fields, while the short-length scale fields are approximated within a field-less methodology. The particle-field description shares computational similarities with *particle-in-cell* (PIC) simulations, but treats microscopic dynamics and collisions using MD-style pair interactions. In addition to investigating transport properties in the relativistic regime, the model opens the possibility of benchmark collisional models in lower-density applications.

7.2 Outlook: Wave packet molecular dynamics

Wave packet formulations allow for the modelling of electron and ion dynamics on an equal footing. However, this comes at the cost of a reduced description of the electron wave function, generalisations of which are natural extensions. The tests in Chapter 3 suggest that a more flexible functional form which can better describe atomic states while retaining a similar ability to stretch as the elongated Gaussians, would improve ground state properties. In Paper (F), separate descriptions for the bound and free electrons are used, the proportions of which are self-consistently obtained from molecular dynamics. An extension of the scheme is currently being implemented – by Daniel Plummer – where the free electrons are described using the wave packet model from Chapter 3 and would therefore alleviate the requirements of modelling bound states with the same functional form as the free electrons. Furthermore, to extend

the scheme to lower temperatures, a more complete anti-symmetrisation scheme should be employed. Especially, the influence of the metric term on the manifold of anti-symmetric states should be investigated, see Section 3.2.

One of the major unknowns in the wave packet model is the confinement potential, needed to make the state localised and amendable to an MD treatment. The requirements of a confining potential is an artefact of the limited functional form of the wave packets, and further robustness tests with respect to confinement strength are desirable for a larger set of observables and thermodynamic conditions. Full anti-symmetrisation could potentially reduce the need for a confinement potential, especially for highly degenerate matter [296]. In density functional theory computations at warm dense matter conditions, plane waves are commonly used to represent the orbitals, suggesting that a more delocalised structure might be preferable. Wave packet MD using plane waves has only found limited use as they are computationally highly challenging and do not scale linearly with system size [463]. An adaptively splitting wave packet is a potential path forward, retaining some aspects of the traditional wave packet while encoding some delocalisation, but it is not certain such schemes would necessarily converge in the number of subdivisions of each particle and some intricate details appear as particles are subdivided (see the discussion in Paper (G)).

The heat capacity of wave packet models is commonly believed not to be the most accurate [152] due to the way the internal degrees of freedom thermalise. This thermalisation furthermore couples to the confinement potential [305]. However, the heat capacity problem is not specific to wave packet models, but a more general feature of time-dependent mixed quantum and classical simulations [464]. A systematic study of wave packet heat capacity is desirable and would give confidence in applying the model to the highly non-equilibrium and experimentally relevant electron-ion thermalisation process, which in a few instances has already been investigated with wave packet models [152, 166].

7.3 Outlook: Relativistic molecular dynamics

Only a few applications of the relativistic formulation are presented in this thesis, and the possible extensions and applications are numerous. First, further improvements of short-range interactions were listed in Section 6.3.2 where a simulation with fully retarded fields would act as a benchmark for the approximate models and allow for the treatment of ultra-relativistic systems. This would permit the investigation of interaction effects on transport properties throughout the full relativistic regime. Second, a grid-based implementation for the particle-field interactions that scales close to linearly with particle number is highly desirable. Such an implementation would allow for the modelling of weakly coupled systems – which requires the treatment of a larger number of particles – and would open the possibility of comparing the MD formulation to PIC-based simulations. Good initial phenomena for comparison would be a process with a quick time evolution and where collisions play a non-trivial role, e.g., a two-stream or Weibel instability [465].

Relativistic and plasma corrections to Bremsstrahlung emissions were discussed in detail with regard to the solar opacity and the solar neutrinos deficit[1] [466, 467]. Recent work [468], has tested models from Bremsstrahlung emission at high electrostatic coupling. However, it would also be desirable to benchmark the relativistic corrections now possible with the relativistic MD implementation provided.

7.4 Outlook: Relativistic quantum molecular dynamics

A first approximation for a combined quantum and relativistic MD would be to unite the formulations in Chapters 3 and 6, where the density envelope S_i in Chapter 6 would take a finite extent. This would be a generalisation of the formulation used in nuclear physics [416] with dynamical fields. The appropriate action integral should be constructed, where the first step would be a Klein-Gordon or some *scalar electrodynamics* action [469]. However, a proper treatment of fermions requires solutions to the Dirac equation [469].

[1]The solar neutrino problem was resolved instead by an improved understanding of neutrino physics.

Appendix A
Quantum Trajectory Molecular Dynamics

Abstract: Chapter 3 introduced a quantum trajectory method based on the wave packet described by equation (3.8). In the following, additional details of the Pauli interaction and how to acquire ground-state properties are provided.

A.1 Explicit expressions for the Pauli interactions

The evaluation of the overlap integrals and state averages used for the Pauli interactions with the functional form in equation (3.8), only requires standard analytical techniques and the Gaussian mode decomposition described in Section 3.2.2. However, for completeness, the result will be summarised here. First, the overlap integral is

$$\langle q_j|q_i\rangle = \frac{\exp\left(-a_{ij} + \boldsymbol{c}_{ij}^\intercal \mathbf{M}_{ij}^{-1}\boldsymbol{c}_{ij} - \frac{1}{4}\boldsymbol{k}_{ij}^\intercal \mathbf{M}_{ij}^{-1}\boldsymbol{k}_{ij} + \frac{i}{\hbar}\left(\boldsymbol{p}_j^\intercal \boldsymbol{r}_j - \boldsymbol{p}_i^\intercal \boldsymbol{r}_i\right) + i\boldsymbol{\Delta}_{ij}^\intercal \boldsymbol{k}_{ij}\right)}{\sqrt{8\det\left(\mathbf{M}_{ij}\right)}\left(\det\left(\boldsymbol{\Sigma}_i\right)\det\left(\boldsymbol{\Sigma}_j\right)\right)^{1/4}}, \tag{A.1}$$

where

$$\begin{aligned} \boldsymbol{k}_{ij} &= \frac{\boldsymbol{p}_i - \boldsymbol{p}_j}{\hbar}, \\ \mathbf{M}_i &= \frac{1}{4}\boldsymbol{\Sigma}_i^{-1} - \frac{i}{\hbar}\boldsymbol{\Pi}_i,, \\ \mathbf{M}_{ij} &= \mathbf{M}_i + \mathbf{M}_j^*, \end{aligned} \qquad \begin{aligned} \boldsymbol{c}_{ij} &= \mathbf{M}_i\boldsymbol{r}_i + \mathbf{M}_j^*\boldsymbol{r}_j, \\ \boldsymbol{\Delta}_{ij} &= \mathbf{M}_{ij}^{-1}\boldsymbol{c}_{ij}. \end{aligned} \tag{A.2}$$

The total Pauli interaction from summing equation (3.23) over relevant particle pairs is

$$\mathcal{V}_p = \mathcal{V}_{p,\mathrm{kin}} + \mathcal{V}_{p,\mathrm{Coul}} + \mathcal{V}_{p,\mathrm{bg}}, \tag{A.3}$$

where the terms describe the kinetic, interaction and background contribution, respectively. The kinetic contribution is

$$\mathcal{V}_{p,\mathrm{kin}} = -\sum_{i\neq j}(\pm\rho)\left[\frac{\hbar^2}{m_e}\,\mathrm{Tr}\left\{\mathbf{M}_j - \frac{1}{8}\boldsymbol{\Sigma}_j^{-1}\right\} + \frac{2i\hbar}{m_e}\boldsymbol{p}_j^\intercal \mathbf{M}_j \boldsymbol{d}_{ij}\right. \tag{A.4}$$

$$-\frac{2\hbar^2}{m_e}\,\mathrm{Tr}\left\{\mathbf{M}_j\mathbf{M}_j\mathbf{N}_{ij}+\frac{1}{\hbar^2}\mathbf{\Pi}_j\mathbf{\Sigma}_j\mathbf{\Pi}_j\right\}\Bigg]\frac{|\,\langle q_i|q_j\rangle\,|^2}{1\mp|\,\langle q_i|q_j\rangle\,|^2}, \tag{A.5}$$

where the sum is limited to electrons. The upper sign is chosen for pairs i and j interacting through the Pauli potential ($\pm\rho=+1$) and the lower sign is chosen when the correlation potential is employed ($\pm\rho=-\rho$). Furthermore, the vector and matrix properties have been defined:

$$\begin{aligned}\boldsymbol{d}_{ij}&=\frac{\langle q_i|\,(\boldsymbol{x}_i-\boldsymbol{r}_j)\,|q_j\rangle}{\langle q_i|q_j\rangle} &&=\frac{-i}{2}\mathbf{M}_{ij}^{*-1}\boldsymbol{k}_{ij}+\boldsymbol{\Delta}_{ij}^{*}-\boldsymbol{r}_j,\\ \mathbf{N}_{ij}&=\frac{\langle q_i|\,(\boldsymbol{x}_i-\boldsymbol{r}_j)(\boldsymbol{x}_i-\boldsymbol{r}_j)^{\intercal}\,|q_j\rangle}{\langle q_i|q_j\rangle} &&=\frac{1}{2}\mathbf{M}_{ij}^{*-1}+\boldsymbol{d}_{ij}\boldsymbol{d}_{ij}^{\intercal}.\end{aligned} \tag{A.6}$$

An initial step in evaluating the Coulomb contribution is the state average

$$\langle q_iq_j|\,\delta^{(3)}(\boldsymbol{s}-\hat{\boldsymbol{x}}_{12})\,|q_jq_i\rangle=\frac{\exp\left(-2\,\mathrm{Re}\{a_{ij}\}+2\,\mathrm{Re}\left\{\boldsymbol{c}_{ij}^{\intercal}\right\}\mathrm{Re}\{\mathbf{M}_{ij}\}^{-1}\,\mathrm{Re}\{\boldsymbol{c}_{ij}\}-\frac{1}{2}\boldsymbol{s}^{\intercal}\mathcal{M}_{ij}\boldsymbol{s}-\boldsymbol{\kappa}_{ij}^{\intercal}\boldsymbol{s}\right)}{8(2\pi)^{3/2}\sqrt{\det\left(\mathbf{\Sigma}_i\right)\det\left(\mathbf{\Sigma}_j\right)\det\left(\mathrm{Re}\{\mathbf{M}_{ij}\}\right)}}, \tag{A.7}$$

where $\hat{\boldsymbol{x}}_{12}=\hat{\boldsymbol{x}}_1-\hat{\boldsymbol{x}}_2$ and

$$\begin{aligned}\mathcal{M}_{ij}&=\mathrm{Re}\{\mathbf{M}_{ij}\}+\mathrm{Im}\{\mathbf{M}_{ij}\}\,\mathrm{Re}\{\mathbf{M}_{ij}\}^{-1}\,\mathrm{Im}\{\mathbf{M}_{ij}\},\\ \boldsymbol{\kappa}_{ij}&=\boldsymbol{k}_{ij}+2\,\mathrm{Im}\{\boldsymbol{c}_{ij}\}-2\,\mathrm{Im}\{\mathbf{M}_{ij}\}\,\mathrm{Re}\{\mathbf{M}_{ij}\}^{-1}\,\mathrm{Re}\{\boldsymbol{c}_{ij}\}.\end{aligned} \tag{A.8}$$

Using the Gaussian decomposition and equation (A.7), the state average of a Gaussian kernel is

$$\langle q_iq_j|\,e^{-\alpha\hat{\boldsymbol{x}}_{12}^2}\,|q_jq_i\rangle=\frac{\exp\left(-2\,\mathrm{Re}\{a_{ij}\}+2\,\mathrm{Re}\left\{\boldsymbol{c}_{ij}^{\intercal}\right\}\mathrm{Re}\{\mathbf{M}_{ij}\}^{-1}\,\mathrm{Re}\{\boldsymbol{c}_{ij}\}-\frac{1}{2}\boldsymbol{\kappa}_{ij}^{\intercal}\left(\mathcal{M}_{ij}+2\alpha\mathbf{I}\right)^{-1}\boldsymbol{\kappa}_{ij}\right)}{8\sqrt{\det\left(\mathbf{\Sigma}_i\right)\det\left(\mathbf{\Sigma}_j\right)\det\left(\mathrm{Re}\{\mathbf{M}_{ij}\}\left(\mathcal{M}_{ij}+2\alpha\mathbf{I}\right)\right)}}. \tag{A.9}$$

The Coulomb contribution to the Pauli interaction follows as

$$\begin{aligned}\mathcal{V}_{p,\mathrm{Coul}}=-\sum_{i<j}\frac{(\pm\rho)e^2}{4\pi\varepsilon_0}\Bigg[&\sum_{p=1}^{N_p^{(s)}}c_p^{(s)}\frac{\langle q_iq_j|\,e^{-\alpha_p^{(s)}\hat{\boldsymbol{x}}_{12}^2}\,|q_jq_i\rangle-\langle q_iq_j|\,e^{-\alpha_p^{(s)}\hat{\boldsymbol{x}}_{12}^2}\,|q_iq_j\rangle\,|\,\langle q_i|q_j\rangle\,|^2}{1\mp|\,\langle q_i|q_j\rangle\,|^2}\\ &+\sum_{p=1}^{N_p^{(\ell)}}c_p^{(\ell)}\frac{\langle q_iq_j|\,e^{-\alpha_p^{(\ell)}\hat{\boldsymbol{x}}_{12}^2}\,|q_jq_i\rangle-\langle q_iq_j|\,e^{-\alpha_p^{(\ell)}\hat{\boldsymbol{x}}_{12}^2}\,|q_iq_j\rangle\,|\,\langle q_i|q_j\rangle\,|^2}{1\mp|\,\langle q_i|q_j\rangle\,|^2}\Bigg],\end{aligned} \tag{A.10}$$

where $\langle q_i q_j|\, e^{-\alpha_p^{(s)}\hat{\boldsymbol{x}}_{12}^2}\, |q_i q_j\rangle$ is evaluated as in Appendix A in Ono and Ando [307].

The background contribution is split into three terms as described in Section 3.2.3, $\mathcal{V}_{p,\mathrm{bg}} = \mathcal{E}_{\mathrm{bg},r} + \mathcal{E}_{\mathrm{bg},k} + \mathcal{E}_{\mathrm{bg},s}$, which correspond to the real-space, Fourier space, and self-energy terms in an Ewald summation, respectively. The real-space (three-body) term is

$$\mathcal{E}_{\mathrm{bg},r} = -\sum_{i<j}(\pm\rho)\frac{|\,\langle q_i|q_j\rangle\,|^2}{1\mp|\,\langle q_i|q_j\rangle\,|^2}\sum_{\substack{k\\k\neq i,j}}\sum_{p=1}^{N_p^{(s)}}\frac{c_p^{(s)}q_k q_e}{4\pi\varepsilon_0}$$
$$\left(\frac{2\,\mathrm{Re}\Big\{\langle q_j q_k|\, e^{-\alpha_p^{(s)}\hat{\boldsymbol{x}}_{12}^2}\,|q_i q_k\rangle\,\langle q_i|q_j\rangle\Big\}}{|\,\langle q_i|q_j\rangle\,|^2} - \langle q_i q_k|\, e^{-\alpha_p^{(s)}\hat{\boldsymbol{x}}_{12}^2}\,|q_i q_k\rangle - \langle q_j q_k|\, e^{-\alpha_p^{(s)}\hat{\boldsymbol{x}}_{12}^2}\,|q_j q_k\rangle\right), \tag{A.11}$$

where

$$\frac{\mathrm{Re}\Big\{\langle q_j q_k|\, e^{-\alpha\hat{\boldsymbol{x}}_{12}^2}\,|q_i q_k\rangle\,\langle q_i|q_j\rangle\Big\}}{|\,\langle q_i|q_j\rangle\,|^2} = \\ = \frac{\mathrm{Re}\Big\{\exp\Big(-\delta a_{ij,\alpha} + \delta(\boldsymbol{c}\mathbf{M}^{-1}\boldsymbol{c})_{ij,\alpha} - \frac{1}{4}\delta(\boldsymbol{k}\mathbf{M}^{-1}\boldsymbol{k})_{ij,\alpha} + i\delta(\boldsymbol{\Delta k})_{ij,\alpha}\Big)\Big\}}{\sqrt{\det\left(\mathbf{I}+2\alpha\boldsymbol{\Sigma}_k\right)\det\Big(\mathbf{I}+\alpha\mathbf{M}_{ij}^{-1}\left(\mathbf{I}+2\alpha\boldsymbol{\Sigma}_k\right)^{-1}\Big)}}, \tag{A.12}$$

and

$$\begin{aligned}
\delta a_{ij,\alpha} &= a_{ij,\alpha} - a_{ij}, & a_{ij,\alpha} &= a_{ij} + \alpha\boldsymbol{r}_k^{\intercal}\left(\mathbf{I}+2\alpha\boldsymbol{\Sigma}_k\right)^{-1}\boldsymbol{r}_k,\\
\delta(\boldsymbol{c}\mathbf{M}^{-1}\boldsymbol{c})_{ij,\alpha} &= \boldsymbol{c}_{ij,\alpha}^{\intercal}\mathbf{M}_{ij,\alpha}^{-1}\boldsymbol{c}_{ij,\alpha} - \boldsymbol{c}_{ij}^{\intercal}\mathbf{M}_{ij}^{-1}\boldsymbol{c}_{ij}, & \boldsymbol{c}_{ij,\alpha} &= \boldsymbol{c}_{ij} + \alpha\left(\mathbf{I}+2\alpha\boldsymbol{\Sigma}_k\right)^{-1}\boldsymbol{r}_k,\\
\delta(\boldsymbol{k}\mathbf{M}^{-1}\boldsymbol{k})_{ij,\alpha} &= \boldsymbol{k}_{ij}^{\intercal}\mathbf{M}_{ij,\alpha}^{-1}\boldsymbol{k}_{ij} - \boldsymbol{k}_{ij}^{\intercal}\mathbf{M}_{ij}^{-1}\boldsymbol{k}_{ij}, & \mathbf{M}_{ij,\alpha} &= \mathbf{M}_{ij} + \alpha\boldsymbol{r}_k^{\intercal}\left(\mathbf{I}+2\alpha\boldsymbol{\Sigma}_k\right)^{-1},\\
\delta(\boldsymbol{\Delta k})_{ij,\alpha} &= \boldsymbol{\Delta}_{ij,\alpha}^{\intercal}\boldsymbol{k}_{ij} - \boldsymbol{\Delta}_{ij}^{\intercal}\boldsymbol{k}_{ij}, & \boldsymbol{\Delta}_{ij,\alpha} &= \mathbf{M}_{ij,\alpha}^{-1}\boldsymbol{c}_{ij,\alpha}.
\end{aligned} \tag{A.13}$$

The $\boldsymbol{k}$-space evaluation is

$$\mathcal{E}_{\mathrm{bg},k} = \frac{1}{4\pi\varepsilon_0 L^3}\sum_{\boldsymbol{k}\neq\mathbf{0}}\frac{4\pi}{\boldsymbol{k}^2}e^{-\boldsymbol{k}^2/(4g^2)}\rho_{uc}(\boldsymbol{k})\mu(\boldsymbol{k}), \tag{A.14}$$

where

$$\mu(\boldsymbol{k}) = -\sum_{i<j}(\pm\rho)\frac{q_e|\,\langle q_i|q_j\rangle\,|^2}{1\mp|\,\langle q_i|q_j\rangle\,|^2}\left[\mu_{ij}(\boldsymbol{k}) + \mu_{ji}(\boldsymbol{k}) - e^{-\frac{1}{2}\boldsymbol{k}^{\intercal}\boldsymbol{\Sigma}_i\boldsymbol{k} - i\boldsymbol{k}^{\intercal}\boldsymbol{r}_i} - e^{-\frac{1}{2}\boldsymbol{k}^{\intercal}\boldsymbol{\Sigma}_j\boldsymbol{k} - i\boldsymbol{k}^{\intercal}\boldsymbol{r}_j}\right], \tag{A.15}$$

and

$$\mu_{ij}(\boldsymbol{k}) = e^{-\frac{1}{4}\left(\boldsymbol{k}^\intercal \mathbf{M}_{ij}^{-1}\boldsymbol{k} - 2\boldsymbol{k}_{ij}^\intercal \mathbf{M}_{ij}^{-1}\boldsymbol{k}\right)} e^{-i\boldsymbol{\Delta}_{ij}^\intercal \boldsymbol{k}}. \tag{A.16}$$

Lastly, the explicit form for the self interaction is given by

$$\begin{aligned}\mathcal{E}_{\mathrm{bg},s} = &\sum_{i<j}(\pm\rho)\frac{|\langle q_i|q_j\rangle|^2 q_e^2/(4\pi\varepsilon_0)}{1\mp|\langle q_i|q_j\rangle|^2}\sum_{p=1}^{N_p^{(s)}} c_p^{(\ell)} \sum_{k=i,j}\left(\frac{2\,\mathrm{Re}\left\{\langle q_j q_k|\, e^{-\alpha_p^{(\ell)}\hat{\boldsymbol{x}}_{12}^2}\,|q_i q_k\rangle\,\langle q_i|q_j\rangle\right\}}{\sqrt{\det\left(\mathbf{I}+2\alpha_p^{(\ell)}\boldsymbol{\Sigma}_k\right)}\,|\langle q_i|q_j\rangle|^2}\right. \\ &\left. - \frac{1}{\sqrt{\det\left(\mathbf{I}+4\alpha_p^{(\ell)}\boldsymbol{\Sigma}_k\right)}}\right) - 2\frac{\exp\left(-\alpha_p^{(\ell)}\boldsymbol{r}_{ij}^\intercal\left(\mathbf{I}+2\alpha_p^{(\ell)}(\boldsymbol{\Sigma}_i+\boldsymbol{\Sigma}_j)\right)^{-1}\boldsymbol{r}_{ij}\right)}{\sqrt{\det\left(\mathbf{I}+2\alpha_p^{(\ell)}(\boldsymbol{\Sigma}_i+\boldsymbol{\Sigma}_j)\right)}}.\end{aligned} \tag{A.17}$$

This completes the description of the Pauli interactions.

A.2 Generalised friction

To study ground state properties in Section 3.4.1, a friction term is included in the equations of motion. Specifically, the governing equations are modified according to:

$$\frac{d\boldsymbol{p}_i}{dt} = -\frac{\partial\mathcal{H}}{\partial\boldsymbol{r}_i} + \boldsymbol{\Gamma}_i^p, \qquad \text{and} \qquad \frac{d\Pi_{i\alpha\beta}}{dt} = -\tau_{\alpha\beta}\frac{\partial\mathcal{H}}{\partial\Sigma_{i\alpha\beta}} + \left(\boldsymbol{\Gamma}_i^\Pi\right)_{\alpha\beta}, \tag{A.18}$$

where the resulting energy loss,

$$\frac{d}{dt}\mathcal{H} = -\sum_i\left(\frac{\partial\mathcal{H}}{\partial\boldsymbol{p}_i^\intercal}\,\boldsymbol{\Gamma}_i^p + \sum_{\alpha\beta}\tau_{\alpha\beta}\frac{\partial\mathcal{H}}{\partial\Pi_{i\alpha\beta}}\left(\boldsymbol{\Gamma}_i^\Pi\right)_{\beta\alpha}\right), \tag{A.19}$$

can be guaranteed to be monotonic with the choice:

$$\boldsymbol{\Gamma}_i^p = m\gamma_p\,\frac{\partial\mathcal{H}}{\partial\boldsymbol{p}_i} \qquad \left(\boldsymbol{\Gamma}_i^\Pi\right)_{\alpha\beta} = \frac{m}{8}\gamma_\Pi\sum_\gamma\left(\left(\boldsymbol{\Sigma}_i^{-1}\right)_{\alpha\gamma}\tau_{\gamma\beta}\frac{\partial\mathcal{H}}{\partial\Pi_{i\gamma\beta}} + \tau_{\alpha\gamma}\frac{\partial\mathcal{H}}{\partial\Pi_{i\alpha\gamma}}\left(\boldsymbol{\Sigma}_i^{-1}\right)_{\gamma\beta}\right). \tag{A.20}$$

In a description of point particles without velocity-dependent interactions, this choice reduces to the traditional linear drag model.

Appendix B
Dynamic Structure Factors via
Explicit Real Time Electron Dynamics

Abstract: Chapter 4 discussed the computation of the electron dynamic structure factor, where both electron and ion time scale features were resolved and quantum corrections discussed. Some additional details regarding the dependence on the confining potential, the derivation of the equivalent to the f-sum rule for impulse computations, and the numerical details of the impulse computations are provided below.

B.1 Confinement potential for wave packets

The choice of confinement potential is an unknown in the wave packet formulation, and the effect of this regularisation should be tested. Here, the structure factors for two substantially different A_w have been computed to explore this sensitivity. The static ion structure is seen to be rather insensitive to the choice of A_w in Figure B.1(a). Larger variations are seen in the electron subsystem, where a reduced electron screening of ions and weaker electron-electron correlations are observed, two features consistent with larger electron envelopes. Although, overall even the electron dependence on A_w is minor.

Figure B.1(b) shows the classical free-electron dynamic structure factors, where the spectral shapes are seen to be largely independent of A_w. In the collective regime, the less confined wave packets have a narrower plasmon feature, interpreted as a reduced electron-ion collisionality. The reduced collision frequency is consistent with larger extent wave packets, as the distributed packets result in smoother electrostatic fields. Morozov and Valuev [320] have previously observed a dependence in the effective collision frequency on the confinement strength. In conclusion, varying the confinement strength does not alter the qualitative features of the dynamic structure factors, but some smaller variations in screening and collision frequency are seen.

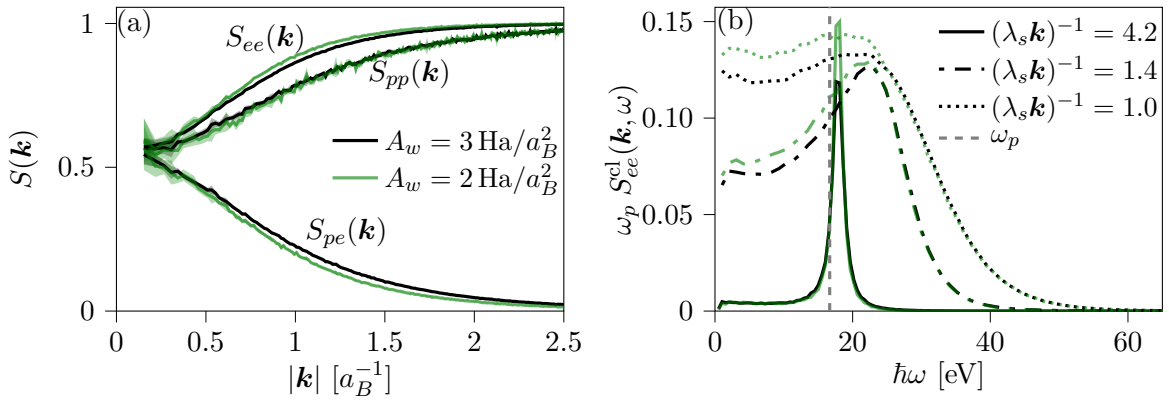

Figure B.1: The dependence on the strength of the confinement potential A_w for two substantively different values. (a) Static structure corresponding to Figure 4.1(a). The ionic structure is insensitive to A_w and only moderate changes are seen in the electron subsystem. (b) Classical free-electron structure factors are to be compared with Figure 4.2(b). The lesser confinement case is seen to experience weaker collisional damping, otherwise yielding similar spectra. The stronger confinement case has been averaged over 70 data runs while the lower confinement case has been averaged over 25, notable in the error estimation (shaded areas). Errors are 95% confidence intervals estimated from the independent runs.

B.2 Details on dynamic structure factor calculations

The smooth interpolation between the appropriate quantum corrections from the collective to single-particle regime, discussed in Section 4.6, is facilitated by a fit including the expected features in the long and short wavelength limit. Specifically, the sum of a GCM [362] – incorporating a diffusive and two propagating modes – and a single particle term is used

$$S^{\mathrm{cl}}(\boldsymbol{k},\omega) = S^{\mathrm{GCM}}(\boldsymbol{k},\omega) + CS^{\mathrm{sp}}(\boldsymbol{k},\omega), \tag{B.1}$$

where

$$\begin{aligned} 2\pi S^{\mathrm{cl}}(\boldsymbol{k},\omega) = 2B_0\frac{\alpha}{\alpha^2+\omega^2} &+ \frac{B_1\gamma}{\gamma^2+(\omega_0+\omega)^2} + \frac{B_1\gamma}{\gamma^2+(\omega_0-\omega)^2} \\ &+ \frac{B_2(\omega_0+\omega)}{\gamma^2+(\omega_0+\omega)^2} + \frac{B_2(\omega_0-\omega)}{\gamma^2+(\omega_0-\omega)^2}, \end{aligned} \tag{B.2}$$

and

$$S^{\mathrm{sp}}(\boldsymbol{k},\omega) = \sqrt{\frac{\beta m_e}{2\pi\boldsymbol{k}^2}}e^{-\frac{\beta m_e}{2\boldsymbol{k}^2}\omega^2}. \tag{B.3}$$

The fitting form is characterised by four fitting coefficients α, ω_0, γ and C, and the remaining parameters are constrained by the three first classical sum-rules in equation (2.20). The explicit constraints are given by:

$$B_0 = \frac{\bar{S}(\boldsymbol{k})(\gamma^2 + \omega_0^2) - \langle\omega^2\rangle_{\mathrm{cl}}^C}{(\alpha-\gamma)^2 + \omega_0^2}, \tag{B.4a}$$

$$B_1 = \frac{\bar{S}(\boldsymbol{k})\alpha(\alpha - 2\gamma) + \langle\omega^2\rangle_{\mathrm{cl}}^C}{(\alpha-\gamma)^2 + \omega_0^2}, \tag{B.4b}$$

$$B_2 = -\frac{\bar{S}(\boldsymbol{k})\alpha(\gamma^2 - \alpha\gamma - \omega_0^2) + \langle\omega^2\rangle_{\mathrm{cl}}^C(\alpha-\gamma)}{\omega_0\left[(\alpha-\gamma)^2 + \omega_0^2\right]}, \tag{B.4c}$$

where $\bar{S}(\boldsymbol{k}) = S(\boldsymbol{k}) - C$ and $\langle\omega^2\rangle_{\mathrm{cl}}^C = (1-C)\boldsymbol{k}^2 k_{\mathrm{B}}T/m_e$. This is an extension of the formulation by Wax and Bryk [362] when incorporating a single particle term. The classical structure factors based on the centre of mass positions were used for the fitting, as incorporating the dynamics of the width was seen to introduce additional modes due to the confinement potential.

The semi-classical correction formula was implemented by shifting the resonance ω_0 according to equation (4.16) (amplitudes in equation (B.4) were re-evaluated) and the two contributions S^{GCM} and S^{sp} are corrected according to equations (4.17) and (4.18), respectively. This automatically satisfies the f-sum rule, directly seen for the single particle term and enforced by equations (B.4) and (4.17) for the collective contribution.

B.3 f-sum rule for density response functions

The fluctuation-dissipation theorem relates $S_{ee}(\boldsymbol{k},\omega)$ and $\mathrm{Im}\{\chi_{ee}\}$, and there is an equivalent f-sum rule for the imaginary part of the response function. Given the fluctuation-dissipation theorem (4.19) and noting that $\mathrm{Im}\{\chi_{ee}\}$ is odd in ω, the f-sum rule reads:

$$\int_{-\infty}^{\infty} d\omega\, \omega\, \mathrm{Im}\{\chi_{\alpha\alpha}(\boldsymbol{k}, -\boldsymbol{k}, \omega)\} = -\frac{2\pi N_\alpha}{\hbar}\omega_R, \tag{B.5}$$

where the $\hbar$ dependence is seen to cancel. Making the connection to the real-time formulation, the causal structure of the response function is accounted for by

$$\chi_{\alpha\alpha}(\boldsymbol{k},-\boldsymbol{k},t)=\Theta(t)\bar{\chi}_{\alpha\alpha}(\boldsymbol{k},-\boldsymbol{k},t), \tag{B.6}$$

where $\Theta(t)$ is the step function and $\bar{\chi}_{\alpha\alpha}(\boldsymbol{k},-\boldsymbol{k},t)$ is an odd function in t. The relation between the time and frequency domain is

$$\bar{\chi}_{\alpha\alpha}(\boldsymbol{k},-\boldsymbol{k},t)=\frac{i}{\pi}\int_{-\infty}^{\infty}d\omega\; e^{-i\omega t}\,\mathrm{Im}\left\{\chi_{\alpha\alpha}(\boldsymbol{k},-\boldsymbol{k},\omega)\right\}, \tag{B.7}$$

and the f-sum rule is

$$\frac{d}{dt}\bar{\chi}_{\alpha\alpha}(\boldsymbol{k},-\boldsymbol{k},t)|_{t=0}=-N_\alpha\frac{\boldsymbol{k}^2}{m_\alpha}. \tag{B.8}$$

The mass m_α is the mass of the particles in question.

Considering the wave packet description and the impulse response calculations in particular. The wave packets are described by classical positions and momenta, and some internal degrees of freedom $\boldsymbol{\sigma}_i$ with associated momentum variables $\boldsymbol{\pi}_i$. The density envelope of a single orbital has a shape ρ_i, i.e.,

$$|\phi_i(\boldsymbol{x})|^2=\rho_i(\boldsymbol{x}-\boldsymbol{r}_i;\boldsymbol{\sigma}_i). \tag{B.9}$$

The external impulse $V_\alpha^{\mathrm{ext}}(\boldsymbol{x})=I_0\delta(t)\exp(i\boldsymbol{k}\cdot\boldsymbol{x})\delta_{\alpha e}$, incurs a change in the momentum variables given by

$$\Delta\boldsymbol{p}_i=-iI_0e^{i\boldsymbol{k}\cdot\boldsymbol{r}_i}\theta_i(\boldsymbol{k})\boldsymbol{k}, \tag{B.10a}$$

$$\Delta\boldsymbol{\pi}_i=-I_0e^{i\boldsymbol{k}\cdot\boldsymbol{r}_i}\frac{\partial\theta_i(\boldsymbol{k})}{\partial\boldsymbol{\sigma}_i}, \tag{B.10b}$$

where the Fourier transform of the density envelope

$$\theta_i(\boldsymbol{k};\boldsymbol{\sigma}_i)=\int d^3\boldsymbol{x}\;\rho_i(\boldsymbol{x};\boldsymbol{\sigma}_i)\,e^{i\boldsymbol{k}\cdot\boldsymbol{x}}, \tag{B.11}$$

accounts for the distributed nature of the state. Assuming the impulse brings upon a small

momentum change, the dynamics shortly after the impulse is

$$\boldsymbol{r}_i^{I_0}(t) = \boldsymbol{r}_i(t) + \frac{\Delta \boldsymbol{p}_i}{m_\alpha} t + \mathcal{O}\left(t^2\right), \tag{B.12a}$$

$$\boldsymbol{\sigma}_i^{I_0}(t) = \boldsymbol{\sigma}_i(t) + \frac{\Delta \boldsymbol{\pi}_i}{m_\alpha} t + \mathcal{O}\left(t^2\right), \tag{B.12b}$$

where $\boldsymbol{r}_i(t)$ and $\boldsymbol{\sigma}_i(t)$ are the unperturbed trajectories. Therefore, the density response to $\mathcal{O}(t)$ is

$$\bar{\chi}_{\alpha\alpha}(\boldsymbol{k}, -\boldsymbol{k}, t) = \frac{\langle \delta n(\boldsymbol{k}, t) \rangle_T}{I_0} = \frac{1}{I_0} \left\langle \sum_i \theta_i(-\boldsymbol{k}; \boldsymbol{\sigma}_i^{I_0}) e^{-i\boldsymbol{k}\cdot\boldsymbol{r}_i^{I_0}} \right\rangle_T, \tag{B.13}$$

and in particular

$$\frac{d}{dt} \bar{\chi}_{\alpha\alpha}(\boldsymbol{k}, -\boldsymbol{k}, t)|_{t=0} = -\frac{N}{m_\alpha} \left(\boldsymbol{k}^2 \left\langle \left|\theta_i(\boldsymbol{k})\right|^2 \right\rangle_T + \left\langle \left| \frac{\partial \theta_i(\boldsymbol{k})}{\partial \boldsymbol{\sigma}_i} \right|^2 \right\rangle_T \right). \tag{B.14}$$

The unperturbed motion has been assumed to be uncorrelated. Equation (B.14) agrees with the f-sum rule for point particles $\theta_i(\boldsymbol{k}) = 1$, but the distributed nature of the particle reduced the strength of the impulse for large $\boldsymbol{k}$, as the functional form of the wave packets prevents density perturbations at length scales much smaller than the wave packet size.

B.4 Impulse simulations

The explicit computations of the density response function by the introduction of an external impulse – as discussed in Section 4.7 – were based on a thermal simulation, snapshots of which were taken 20 fs apart resulting in 24 different starting configurations. The process was repeated for five different initial seeds, resulting in 120 initial configurations. The resulting momentum shifts from the impulse in equation (B.10) were applied to each configuration. For the $\boldsymbol{k}$-vectors considered, three symmetry directions exist and the impulse computation was performed separately in each direction. High-resolution data were also acquired without any impulse, and for varying impulse strengths to confirm the simulation was performed in the linear regime. All impulse simulations are summarised in Table B.1 where a total of 1080 impulse simulations were performed in addition to the thermal simulations.

Table B.1: Summary of impulse simulations shown for the two wavelengths considered. A variety of impulse strengths I_0 has been tested for a subset of the 360 starting configurations to estimate non-linear effects. The required simulation time $t_{\max}$ for the shorter wavelength is reduced.

$\boldsymbol{k}$ $[a_\mathrm{B}^{-1}]$	I_0 $[E_h\,\mathrm{fs}]$	Start config.	Simulations	$t_{\max}$ [fs]
0.31	10^{-4}	30	90	2
	10^{-3}	30	90	2
	10^{-2}	120	360	4
0.61	5×10^{-3}	60	180	4
	10^{-2}	120	360	2

Appendix C

Electron Transport Properties via Explicit Real Time Electron Dynamics

Abstract: Chapter 5 introduced a methodology where the electron dynamic structure factor from a two-fluid model is mapped to the results of atomistic simulations. The focus was particularly on the fast electron dynamics, but for completeness the ion time scale dynamics are given below. Furthermore, some additional details of the inference and reference models used in Chapter 5 are given.

C.1 Ion time scale dynamics

The electron dynamics on ion time scales is obtained by time averaging the hydrodynamic equations over characteristic electron time scales, as described in Section 5.2.1. The electron dynamics on these time scales are given by:

$$\frac{\partial \delta\bar{\rho}_e}{\partial t} = -\rho_{0,e}\boldsymbol{\nabla}\cdot\delta\bar{\boldsymbol{v}}_e, \tag{C.1a}$$

$$\rho_{0,e}\frac{\partial \delta\bar{\boldsymbol{v}}_e}{\partial t} = -\frac{c_{s,e}^2}{\gamma_e}\left(\boldsymbol{\nabla}\delta\bar{\rho}_e + \rho_{0,e}\alpha_{T,e}\boldsymbol{\nabla}\delta\bar{T}_e\right) + \eta_e\boldsymbol{\nabla}^2\delta\bar{\boldsymbol{v}}_e + (\zeta_e + \eta_e/3)\boldsymbol{\nabla}\boldsymbol{\nabla}\cdot\delta\bar{\boldsymbol{v}}_e - \frac{q_e}{m_e}\rho_{0,e}\boldsymbol{\nabla}\delta\bar{\phi} - \boldsymbol{R}_{ei}\left(\rho_{0,e}, \delta\bar{\boldsymbol{v}}_e - \delta\bar{\boldsymbol{v}}_i\right), \tag{C.1b}$$

$$\rho_{0,e}C_{V,e}\frac{\partial \delta\bar{T}_e}{\partial t} = -\rho_{0,e}C_{V,e}\frac{\gamma_e - 1}{\alpha_{T,e}}\boldsymbol{\nabla}\cdot\delta\bar{\boldsymbol{v}}_e + \kappa_e\boldsymbol{\nabla}^2\delta\bar{T}_e - g\left(\delta\bar{T}_e - \delta\bar{T}_i\right), \tag{C.1c}$$

$$\boldsymbol{\nabla}^2\delta\bar{\phi} = -\frac{1}{\varepsilon_0}\left(\frac{q_e}{m_e}\delta\bar{\rho}_e - \frac{q_i}{m_i}\delta\bar{\rho}_i\right). \tag{C.1d}$$

On slow time scales, the inertia and collisional terms are small. Under these assumptions, the electron density is set by the screening of the ions, and in Fourier space the density is

$$\frac{\delta\bar{\rho}^e_{\boldsymbol{k}}}{m_e} = \frac{-q_i/q_e}{1+\lambda_e^2\boldsymbol{k}^2}\frac{\delta\bar{\rho}^i_{\boldsymbol{k}}}{m_i} \equiv |n(\boldsymbol{k})|\frac{\delta\bar{\rho}^i_{\boldsymbol{k}}}{m_i}, \tag{C.2}$$

where $\delta\bar{\boldsymbol{v}}_e \approx 0$ and $\delta\bar{T}_e \approx 0$ have been assumed. The screening length λ_e is defined in Section 5.2.4. The screening cloud form factor $|n(\boldsymbol{k})|$ is equivalent to the long wavelength limit of the corresponding form factor in the Chihara decomposition, discussed in Chapter 4. This screening contribution has been subtracted from the MD electron dynamics structure factors used in Chapter 5 to isolate the free-electron contribution even if this contribution typically falls outside the fitting window in Section 5.5.

Using the adiabatic screening cloud, $|n(\boldsymbol{k})|$, in the linearised hydrodynamic equations for ions, the mean-field electrostatic term becomes akin to a pressure term on length scales much longer than λ_e. Specifically, after performing the same type of transform as in Section 5.2.2, the equations for the ions take the same structure as equation (5.12). The hydrodynamic matrix for the ions is

$$\mathbf{D}_i(\boldsymbol{k}) = \begin{bmatrix} 0 & 1 & 0 \\ -f(\boldsymbol{k})\boldsymbol{k}^2 & \mathfrak{v}_i(\boldsymbol{k}) & -\alpha_{T,i}\frac{c_{s,i}^2\boldsymbol{k}^2}{\gamma_i} \\ 0 & \alpha_{T,i}^{-1}(\gamma_i - 1) & \gamma_i\mathfrak{h}_i(\boldsymbol{k}) \end{bmatrix}, \tag{C.3}$$

where

$$f(\boldsymbol{k}) = \frac{c_{s,\mathrm{IAW}}^2}{\gamma_i} + \left(c_{s,\mathrm{IAW}}^2 - c_{s,i}^2\right)\left(\frac{\gamma_i - 1}{\gamma_i} - \frac{\lambda_e^2\boldsymbol{k}^2}{1+\lambda_e^2\boldsymbol{k}^2}\right), \tag{C.4}$$

and $c_{s,\mathrm{IAW}}^2 = c_{s,i}^2 - \gamma_e^{-1}c_{s,e}^2 q_i m_e/(q_e m_i)$ is the ion acoustic sound speed. On this scale, the collision frequency takes the low-frequency value. The dispersion in case of small dissipative effects, as in Section 5.2.3, is given by:

$$s_0 = -\left(1 + (\gamma_i - 1)\frac{c_{s,\mathrm{IAW}}^2 - c_{s,i}^2}{c_{s,\mathrm{IAW}}^2 - c_{s,i}^2\lambda_e^2\boldsymbol{k}^2}\right)\mathfrak{h}_i(\boldsymbol{k}), \tag{C.5a}$$

$$s_{12} = \pm\, ic_{s,\mathrm{IAW}}|\boldsymbol{k}|\,\Xi(\boldsymbol{k}) - \frac{1}{2}\left((\gamma_i - 1)\frac{(1-\lambda_e^2\boldsymbol{k}^2)c_{s,i}^2}{c_{s,\mathrm{IAW}}^2 - c_{s,i}^2\lambda_e^2\boldsymbol{k}^2}\mathfrak{h}_i(\boldsymbol{k}) + \mathfrak{v}_i(\boldsymbol{k})\right), \tag{C.5b}$$

which describes one entropy mode and two ion-acoustic modes. The latter has a linear

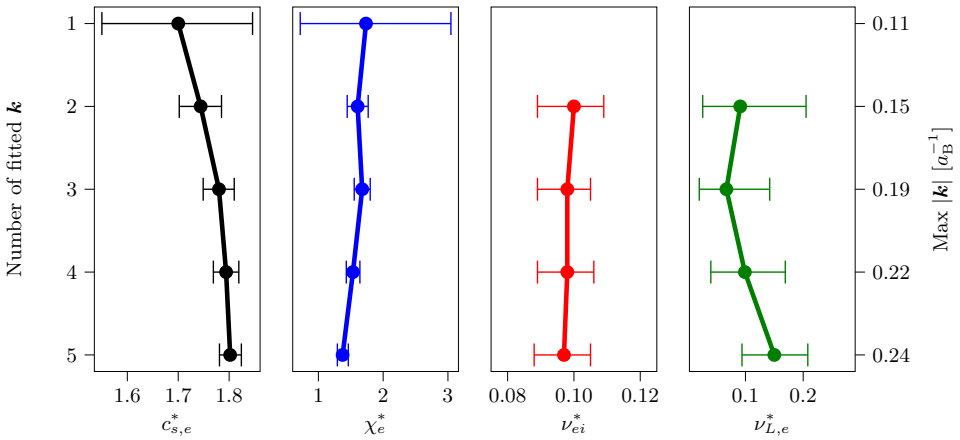

Figure C.1: Dependence of inferred transport coefficients based on the number of spectra used in the fitting procedure. The dependence on each transport coefficient is shown in figures (a)-(e) respectively. Values are the mean and errors are the 16th and 84th percentiles. In figures (d) and (e), the single spectrum fitting is not shown due to complete degeneracy between ν^*_{ei} and $\nu^*_{L,e}$.

dispersion for small $\boldsymbol{k}$ which is flattened for finite $\boldsymbol{k}$ by the factor

$$\Xi(\boldsymbol{k}) = \sqrt{1 - \frac{c^2_{s,\mathrm{IAW}} - c^2_{s,i}}{c^2_{s,\mathrm{IAW}}} \frac{\lambda_e^2 \boldsymbol{k}^2}{1 + \lambda_e^2 \boldsymbol{k}^2}}, \tag{C.6}$$

a feature commonly seen, see, e.g., Mithen *et al.* [110] or Salin [470].

C.2 Extent of hydrodynamic regime of electron liquid

To explore the failure of the hydrodynamic model to fit DSFs at larger $\boldsymbol{k}$, additional spectra were successively added to the MCMC sampling procedure. The resulting parameter estimation is shown in Figure C.1. Most parameters show drifts within the error bars as additional spectra are incorporated, but a distinct change is shown for $\boldsymbol{k} \geq 0.22\, a_\mathrm{B}^{-1}$ in particular for the viscosity estimate. This is the length scale where broadening due to Landau damping is expected to become comparable to the broadening by collisions. The effect of Landau damping, which is not included in the hydrodynamic description, is therefore erroneously attributed to viscosity if too large $\boldsymbol{k}$-vectors are included in the fit. The resulting fits for $\boldsymbol{k} \approx 0.24\, a_\mathrm{B}^{-1}$ are also visually unsatisfactory (not shown).

C.3 Reference transport properties

C.3.1 Ideal treatment

The ideal sound speed is given by the generalised Bohm-Gross dispersion [392] in equation (5.24), but is also related to the ideal equation of state. Namely, the ideal pressure at constant temperature is $p_e = \rho_e \left\langle \boldsymbol{v}_e^2 \right\rangle_T /3$ and relates to the sound speed by [196]

$$c_{s,e}^2 = \gamma_e \frac{\partial p_e}{\partial \rho_e}\bigg|_{T_e} . \tag{C.7}$$

For the two descriptions to coincide, $\gamma_e = 3$ or $\gamma_e = 9/5$ is needed in the high and low-temperature limits, respectively. This differs from the thermodynamics for an ideal system with $\gamma_e = 5/3$ [10], because the adiabatic index must be modelled as time scale dependent for fast electron dynamics [407]. The heat capacity, $C_{V,e}$, within the ideal high-temperature approximation, $k_\mathrm{B}T \gg E_F$, is given by $\rho_{0,e} C_{V,e} = 3k_\mathrm{B}\rho_{e,0}/(2m_e)$.

C.3.2 Stanton and Murillo (2016)

The Stanton and Murillo transport (SMT) model is a classical kinetic treatment in which collision integrals are evaluated based on effective Yukawa interactions [78]. The model was originally developed for ions, but has recently been applied to electron transport properties [87]. Opposite charges are not treated, and electrons are effectively handled as positrons. Therefore, the model does not adhere to the *Barkas effect* [471, 472]. Despite this and limited quantum treatment, the model captures the general trend for a variety of transport properties [61, 87].

The SMT model has been used for the computation of a variety of transport properties. For viscosity and thermal conductivity, the single-component formulation has been used [78], while the presence of ions is still included in the screening. The two-component formulation was employed for the computation of electrical conductivity [87].

C.3.3 One-component plasma

The one-component plasma model is well-studied numerically. Hansen investigated the dispersion relation via a memory function formalism [240] that was later tested by MD [473]. For the dispersion comparison, Hansen's dispersion relation was evaluated using the excess energy from Monte Carlo simulations [241, 242] parameterised by Plummer *et al.* [245].

Scheiner and Baalrud [244] parameterised the thermal conductivity from MD simulations, which in combination with the heat capacity of Hansen [238] and the parameterisation of excess energy [245], has been used to evaluate thermal diffusivity. Similarly, Daligault *et al.* [243] provided a parameterisation of the shear viscosity valid for the gas and fluid regime, which is also taken for comparison.

C.3.4 RPA and first Born approximation

Within the long wavelength limit of the RPA approximation, Thiele *et al.* [348] obtained a correction to the ideal dispersion for moderately degenerate plasmas. Using the notation in Chapter 5, the correction increases the ideal $c_{s,e}$ by a factor

$$\sqrt{1 + 0.088 \frac{\rho_e \Lambda_e^3}{m_e}}, \tag{C.8}$$

where Λ_e is the thermal de Broglie wavelength in equation (1.13).

The model for the dynamic collision frequency in equation (5.37) is compared to the first Born approximation [348] given the ionic structure from Figure 4.1(a). Evaluation of the collision frequency at $\omega = \omega_p$ and $\omega = 0$ provides an estimate of both the collision frequency and the DC conductivity using equation (5.29).

C.3.5 DFT – Molecular dynamics

Hu *et al.* used DFT-MD simulations to parameterise the electron thermal conductivity of deuterium via a dedicated Coulomb logarithm [148]. The simulations were performed at higher densities than those discussed in Chapter 5, where the lowest density considered was $r_s \approx 1.75$.

However, lacking an appropriate heat capacity, the ideal heat capacity is used for comparison, which overestimates the thermal diffusivity.

C.3.6 Conti and Vignale (1999)

Conti and Vignale [395] provided a zero-temperature parameterisation of shear viscosity for a homogeneous quantum Fermi liquid. However, their result is almost three orders of magnitude lower than the classical kinetic results, suggesting that finite temperature effects are dominant at the studied conditions.

Appendix D
Relativistic Molecular Dynamics

Abstract: To supplement the discussion in Chapter 6, additional details are provided regarding the parameterisation of the relativistic one-component plasma, and equations of motion for particles with velocity-dependent pair interactions and particle-field coupling are given explicitly.

D.1 OCP unit systems

Consider a system of relativistic charge particles, all with the same mass $m_i = m$ and charge $q_i = q$. The system can be parameterised by two parameters, namely Γ and ε. This is seen by measuring mass, length, time and charge in units of m, a_i, $\sqrt{ma_i^2/(k_{\mathrm{B}}T)}$, and q, respectively. Explicitly, consider the following normalisation of the physical degrees of freedom:

$$\begin{aligned}
&\boldsymbol{x} = a_i\boldsymbol{\xi}, && n(\boldsymbol{x}) = qa_i^{-3}\mathfrak{n}(\boldsymbol{\xi}), && \boldsymbol{A}(\boldsymbol{x}) = \frac{\sqrt{k_{\mathrm{B}}Tm}}{q}\boldsymbol{\mathcal{A}}(\boldsymbol{\xi}),\\
&\boldsymbol{r}_i = a_i\boldsymbol{x}_i, && \boldsymbol{j}(\boldsymbol{x}) = qa_i^{-3}\sqrt{\frac{k_{\mathrm{B}}T}{m}}\mathfrak{j}(\boldsymbol{\xi}), && \boldsymbol{E}(\boldsymbol{x}) = \frac{k_{\mathrm{B}}T}{qa_i}\boldsymbol{\mathcal{E}}(\boldsymbol{\xi}),\\
&\boldsymbol{v}_i = \sqrt{\frac{k_{\mathrm{B}}T}{m}}\boldsymbol{\eta}_i, && \phi(\boldsymbol{x}) = \frac{k_{\mathrm{B}}T}{q}\Phi(\boldsymbol{\xi}), && \boldsymbol{B}(\boldsymbol{x}) = \frac{\sqrt{k_{\mathrm{B}}Tm}}{qa_i}\boldsymbol{\mathcal{B}}(\boldsymbol{\xi}).
\end{aligned} \tag{D.1}$$

The Lagrangians in equation (6.5) then becomes

$$\begin{aligned}
(k_{\mathrm{B}}T)^{-1}\left(\mathcal{L}^{\mathrm{P}}_{\mathrm{EM}} + \mathcal{L}^{\mathrm{F}}_{\mathrm{EM}} + \mathcal{L}^{\mathrm{I}}_{\mathrm{EM}}\right) = &-\varepsilon^{-1}\sum_{i=1}^{N}\sqrt{1-\varepsilon\boldsymbol{\eta}_i^2}\\
&+\frac{1}{\Gamma}\int d^3\boldsymbol{\xi}\left(\frac{\boldsymbol{\mathcal{E}}^2}{8\pi} - \frac{\boldsymbol{\mathcal{B}}^2}{8\pi\varepsilon}\right) + \int d^3\boldsymbol{\xi}\,\left(\mathfrak{j}\cdot\boldsymbol{\mathcal{A}} - \mathfrak{n}\Phi\right),
\end{aligned} \tag{D.2}$$

which only depend on the parameters Γ and ε. Taking the electrostatic limit, the Lagrangian for the REL-OCP model is obtained in normalised units as

$$(k_{\mathrm{B}}T)^{-1}\mathcal{L}_{\text{REL-OCP}} = -\varepsilon^{-1}\sum_{i=1}^{N}\sqrt{1-\varepsilon\boldsymbol{\eta}_i^2} - \frac{\Gamma}{2}\sum_{i\neq j}\frac{1}{|\boldsymbol{\xi}-\boldsymbol{\xi}_i|}. \tag{D.3}$$

It is clear from the above Lagrangian that Γ scales the interaction, while ε only appears in the kinetic term when magnetic contributions have been neglected. By subtracting the rest mass contribution and taking the limit $\varepsilon \to 0$, the classical OCP Lagrangian is obtained in normalised units.

D.2 Lagrangian time evolution

Based on an arbitrary Lagrangian $\mathcal{L} = \mathcal{L}(q_\mu, \dot{q}_\mu)$ without explicit time dependence and independent on particle histories, the Euler-Lagrange equations (2.7) yields the following equations of motion:

$$\frac{\partial^2 \mathcal{L}}{\partial \dot{q}_\mu \partial \dot{q}_\nu} \ddot{q}_\nu + \frac{\partial^2 \mathcal{L}}{\partial \dot{q}_\mu \partial q_\nu} \dot{q}_\nu = \frac{\partial \mathcal{L}}{\partial q_\mu}. \tag{D.4}$$

The first term corresponds to a mass matrix and the last term is the force $F_\mu = -\partial \mathcal{H}/\partial q_\mu|_{p_\mu} = \partial \mathcal{L}/\partial q_\mu|_{\dot{q}_\mu}$. The remaining term vanishes for a separable Lagrangian, but the magnetic interaction between particles can be captured by this term.

Assume the degrees of freedom are particle positions and field components, namely $q_\mu = \left[\boldsymbol{r}_1^\intercal, \ldots, \boldsymbol{r}_N^\intercal, \phi_{\boldsymbol{k}_1}^{(\ell)}, \boldsymbol{A}_{\boldsymbol{k}_1}^{(\ell)\intercal}, \ldots\right]^\intercal$ and $\dot{q}_\mu = \left[\boldsymbol{v}_1^\intercal, \ldots, \boldsymbol{v}_N^\intercal, \dot{\phi}_{\boldsymbol{k}_1}^{(\ell)}, \dot{\boldsymbol{A}}_{\boldsymbol{k}_1}^{(\ell)\intercal}, \ldots\right]^\intercal$, and the Lagrangian have the form

$$\mathcal{L} = \sum_{i=1}^{N} \mathcal{L}_{\text{Kin}}(\boldsymbol{v}_i) - \frac{1}{2} \sum_{i \neq j} V\left(\boldsymbol{r}_i, \boldsymbol{v}_i, \boldsymbol{r}_j, \boldsymbol{v}_j\right) + \mathcal{L}_{\text{EM}}^{(\ell)}\left(\left\{\boldsymbol{r}_i, \boldsymbol{v}_i\right\}_{i=1}^{N}, \left\{\phi_{\boldsymbol{k}}^{(\ell)}, \boldsymbol{A}_{\boldsymbol{k}}^{(\ell)}, \dot{\boldsymbol{A}}_{\boldsymbol{k}}^{(\ell)}\right\}_{\boldsymbol{k}}\right), \tag{D.5}$$

which is a reformulation of the Lagrangian in equation (6.10). The kinetic term $\mathcal{L}_{\text{Kin}}$ is related to $\mathcal{L}_{\text{EM}}^{\text{P}}$, $V(\cdots)$ represents particle-particle interactions that may be velocity dependent and originate from $\mathcal{L}_{\text{EM}}^{(s)}$ and $\mathcal{L}_{\text{EM}}^{(s-\ell)}$, and $\mathcal{L}_{\text{EM}}^{(\ell)}$ describe long-range interactions and field dynamics. The equations of motion for the particles follow from equation (D.4) and is given by

$$\sum_{j=1}^{N} \mathbf{M}_{ij} \dot{\boldsymbol{v}}_j = \boldsymbol{F}_i^{(\text{micro})} + \boldsymbol{\Phi}_i + \boldsymbol{F}_i^{(\text{field})}, \tag{D.6}$$

where

$$\mathbf{M}_{ii} = \frac{\partial^2 \mathcal{L}_{\text{Kin}}}{\partial \boldsymbol{v}_i \partial \boldsymbol{v}_i^\intercal} - \sum_{j=1}^{N} \frac{\partial V(\boldsymbol{r}_i, \boldsymbol{v}_i, \boldsymbol{r}_j, \boldsymbol{v}_j)}{\partial \boldsymbol{v}_i \partial \boldsymbol{v}_i^\intercal}, \tag{D.7a}$$

$$\mathbf{M}_{ij} = -\frac{\partial^2 V(\boldsymbol{r}_i, \boldsymbol{v}_i, \boldsymbol{r}_j, \boldsymbol{v}_j)}{\partial \boldsymbol{v}_i \partial \boldsymbol{v}_j^\intercal}, \tag{D.7b}$$

$$\boldsymbol{F}_i^{(\text{micro})} = -\sum_{j=1}^{N} \frac{\partial V(\boldsymbol{r}_i, \boldsymbol{v}_i, \boldsymbol{r}_j, \boldsymbol{v}_j)}{\partial \boldsymbol{r}_i}, \tag{D.7c}$$

$$\boldsymbol{\Phi}_i = \sum_{j=1}^{N} \left[\frac{\partial^2 V(\boldsymbol{r}_i, \boldsymbol{v}_i, \boldsymbol{r}_j, \boldsymbol{v}_j)}{\partial \boldsymbol{v}_i \partial \boldsymbol{r}_i^\intercal} \boldsymbol{v}_i + \frac{\partial^2 V(\boldsymbol{r}_i, \boldsymbol{v}_i, \boldsymbol{r}_j, \boldsymbol{v}_j)}{\partial \boldsymbol{v}_i \partial \boldsymbol{r}_j^\intercal} \boldsymbol{v}_j \right], \tag{D.7d}$$

$$\boldsymbol{F}_i^{(\text{field})} = -\frac{1}{V} \left(\frac{\partial n_{-\boldsymbol{k}}^{(\ell)}}{\partial \boldsymbol{r}_i} \phi_{\boldsymbol{k}}^{(\ell)} + \frac{\partial \boldsymbol{j}_{-\boldsymbol{k}}^{(\ell)\intercal}}{\partial \boldsymbol{v}_i} \frac{\partial \boldsymbol{A}_{\boldsymbol{k}}^{(\ell)}}{\partial t} + \frac{\partial^2 \boldsymbol{j}_{-\boldsymbol{k}}^{(\ell)} \cdot \boldsymbol{A}_{\boldsymbol{k}}^{(\ell)}}{\partial \boldsymbol{v}_i \partial \boldsymbol{r}_i^\intercal} \boldsymbol{v}_i - \frac{\partial \boldsymbol{j}_{-\boldsymbol{k}}^{(\ell)} \cdot \boldsymbol{A}_{\boldsymbol{k}}^{(\ell)}}{\partial \boldsymbol{r}_i} \right) \tag{D.7e}$$

$$= -\frac{1}{V} \sum_{\boldsymbol{k} \neq 0} q_i e^{i\boldsymbol{k}\cdot\boldsymbol{r}_i} e^{-\sigma^2 \boldsymbol{k}^2/2} \left(i\boldsymbol{k} \phi_{\boldsymbol{k}}^{(\ell)} + \varepsilon_0^{-1} \boldsymbol{\Pi}_{-\boldsymbol{k}}^{(\ell)} + i(\boldsymbol{v}_i \cdot \boldsymbol{k}) \boldsymbol{A}_{\boldsymbol{k}}^{(\ell)} - i(\boldsymbol{v}_i \cdot \boldsymbol{A}_{\boldsymbol{k}}^{(\ell)}) \boldsymbol{k} \right). \tag{D.7f}$$

The summations in equation (D.7) do not include the $i = j$ term and in equation (D.7f) the Gaussian shape function in Section 6.3.2 has been used. The velocity-dependent interactions add a coupling between different particles in $\mathbf{M}_{ij}$, which have to be inverted for each time step. The equations of motion for the field are given in equation (6.18).

The canonical momentum in the formulation is

$$\boldsymbol{p}_i = \frac{\partial \mathcal{L}_{\text{Kin}}}{\partial \boldsymbol{v}_i} - \sum_{\substack{j=1 \\ j \neq i}}^{N} \frac{\partial V}{\partial \boldsymbol{v}_i} + \frac{1}{V} \sum_{\boldsymbol{k} \neq 0} \frac{\partial \boldsymbol{j}_{-\boldsymbol{k}}^{(\ell)} \cdot \boldsymbol{A}_{\boldsymbol{k}}^{(\ell)}}{\partial \boldsymbol{v}_i} \equiv \boldsymbol{p}_i^{(\text{kin})} + \boldsymbol{p}_i^{(\text{int})} + \boldsymbol{p}_i^{(\text{field})}, \tag{D.8}$$

which has distinct contributions from the kinetic, interaction and field terms. Based on the canonical momentum, the energy of the system is $E = E_{(\text{kin})} + E_{(\text{pot})}^s + E_{(\text{pot})}^p + E_{(\text{field})}$, where

$$E_{(\text{kin})} = \sum_i \left[\boldsymbol{p}_i^{(\text{kin})} \cdot \boldsymbol{v}_i - \mathcal{L}_{\text{Kin}}(\boldsymbol{v}_i) \right], \tag{D.9a}$$

$$E_{(\text{pot})}^s = \sum_i \boldsymbol{p}_i^{(\text{int})} \cdot \boldsymbol{v}_i, \tag{D.9b}$$

$$E_{(\text{pot})}^p = \frac{1}{2V} \sum_{\boldsymbol{k} \neq 0} n_{-\boldsymbol{k}}^{(\ell)} \phi_{\boldsymbol{k}}^{(\ell)} + \frac{1}{2} \sum_{i \neq j} V(\boldsymbol{r}_i, \boldsymbol{v}_i, \boldsymbol{r}_j, \boldsymbol{v}_j), \tag{D.9c}$$

and

$$E_{(\text{field})} = \frac{1}{V}\sum_{\boldsymbol{k}\neq 0}\left[\frac{1}{2\varepsilon_0}\boldsymbol{\Pi}_{\boldsymbol{k}}^{(\ell)}\cdot\boldsymbol{\Pi}_{-\boldsymbol{k}}^{(\ell)} + \frac{|\boldsymbol{k}|^2}{2\mu_0}\boldsymbol{A}_{\boldsymbol{k}}^{(\ell)}\cdot\boldsymbol{A}_{-\boldsymbol{k}}^{(\ell)}\right]. \tag{D.9d}$$

Note that the contribution from $\boldsymbol{p}_i^{(\text{field})}$ has been cancelled with the current source term, as the magnetic interactions do not have an energy contribution. A non-classical interaction contribution E_{Pot}^s appears due to velocity-dependent interactions, which for potentials $V(\cdots)$ linear in $\boldsymbol{v}_i$ cancels with contributions in $E_{(\text{pot})}^p$, typically the case of simple models for the magnetic interactions.

In the special case where $V(\cdots)$ is independent of velocity, e.g., the electrostatic approximation for short-range fields, the Hamiltonian can be explicitly derived as $\boldsymbol{p}_i^{(\text{int})} = 0$. The Hamiltonian in this case is $\mathcal{H} = \mathcal{H}_{(\text{kin})} + E_{(\text{pot})}^p + E_{(\text{field})}$, where

$$\mathcal{H}_{(\text{kin})} = \sum_{i=1}^{N} m_i c^2 \sqrt{1 + \frac{\left(\boldsymbol{p}_i - \boldsymbol{p}_i^{(\text{field})}\right)^2}{(m_i c)^2}}. \tag{D.10}$$

All the dependence on $\boldsymbol{r_i}$ can be separated into a term independent of velocities and fields. Therefore, the static structure is expected to be the same as in the traditional OCP model.

References

[1] National Research Council, Division on Engineering and Physical Sciences, Board on Physics and Plasma Science Committee and Committee on High Energy Density Plasma Physics, *Frontiers in high energy density physics: The x-games of contemporary science* (National Academies Press, 2003).

[2] M. R. Gallas and G. J. Piermarini, "Bulk modulus and Young's modulus of nanocrystalline γ-alumina", Journal of the American Ceramic Society **77**, 2917–2920 (1994).

[3] R. P. Drake, *High-Energy-Density Physics : Foundation of Inertial Fusion and Experimental Astrophysics*, eng, 2nd ed., Graduate Texts in Physics (Springer International Publishing, Cham, 2018).

[4] M. N. Saha, "LIII. Ionization in the solar chromosphere", The London, Edinburgh, and Dublin Philosophical Magazine and Journal of Science **40**, 472–488 (1920).

[5] G. Ecker and W. Kröll, "Lowering of the ionization energy for a plasma in thermodynamic equilibrium", The Physics of Fluids **6**, 62–69 (1963).

[6] J. C. Stewart and K. D. Pyatt Jr, "Lowering of ionization potentials in plasmas", Astrophysical Journal **144**, 1203 (1966).

[7] B. J. B. Crowley, "Average-atom quantum-statistical cell model for hot plasma in local thermodynamic equilibrium over a wide range of densities", Physical Review A **41**, 2179 (1990).

[8] M. Bonitz and L. Kordts, "Ionization potential depression and fermi barrier in warm dense matter: A first-principles approach", Contributions to Plasma Physics, e70001 (2025).

[9] S. D. Bergeson, S. D. Baalrud, C. L. Ellison, E. Grant, F. R. Graziani, T. C. Killian, M. S. Murillo, J. L. Roberts, and L. G. Stanton, "Exploring the crossover between high-energy-density plasma and ultracold neutral plasma physics", Physics of Plasmas **26**, 100501 (2019).

[10] L. D. Landau and E. M. Lifshitz, *Statistical Physics*, Vol. 5 (Pergamon Press, Oxford, 1980).

[11] F. Perrot and M. Rasolt, "A new listing of the effective r_s values for metals", Journal of Physics: Condensed Matter **6**, 1473 (1994).

[12] V. E. Fortov, "Extreme states of matter on earth and in space", Physics-Uspekhi **52**, 615 (2009).

[13] M. Bonitz, Z. A. Moldabekov, and T. Ramazanov, "Quantum hydrodynamics for plasmas—Quo vadis?", Physics of Plasmas **26**, 090601 (2019).

[14] S. X. Hu, L. A. Collins, T. R. Boehly, Y. H. Ding, P. B. Radha, V. N. Goncharov, V. V. Karasiev, G. W. Collins, S. P. Regan, and E. M. Campbell, "A review on *ab initio* studies of static, transport, and optical properties of polystyrene under extreme conditions for inertial confinement fusion applications", Physics of Plasmas **25**, 056306 (2018).

[15] T. Dornheim, S. Groth, and M. Bonitz, "The uniform electron gas at warm dense matter conditions", Physics Reports **744**, 1–86 (2018).

[16] M. French, A. Becker, W. Lorenzen, N. Nettelmann, M. Bethkenhagen, J. Wicht, and R. Redmer, "*Ab initio* simulations for material properties along the Jupiter adiabat", The Astrophysical Journal Supplement Series **202**, 5 (2012).

[17] M. Preising, M. French, C. Mankovich, F. Soubiran, and R. Redmer, "Material properties of Saturn's interior from *Ab Initio* simulations", The Astrophysical Journal Supplement Series **269**, 47 (2023).

[18] J. Christensen-Dalsgaard, "Solar structure and evolution", Living Reviews in Solar Physics **18**, 2 (2021).

[19] B. Militzer and D. M. Ceperley, "Path integral Monte Carlo calculation of the deuterium Hugoniot", Physical Review Letters **85**, 1890 (2000).

[20] T. Guillot, "Interiors of giant planets inside and outside the solar system", Science **286**, 72–77 (1999).

[21] J. Vorberger, I. Tamblyn, B. Militzer, and S. A. Bonev, "Hydrogen-helium mixtures in the interiors of giant planets", Physical Review B **75**, 024206 (2007).

[22] J. J. Fortney and N. Nettelmann, "The interior structure, composition, and evolution of giant planets", Space Science Reviews **152**, 423–447 (2010).

[23] N. Nettelmann, A. Becker, B. Holst, and R. Redmer, "Jupiter models with improved *ab initio* hydrogen equation of state (H-REOS.2)", The Astrophysical Journal **750**, 52 (2012).

[24] W. Lorenzen, A. Becker, and R. Redmer, "Progress in warm dense matter and planetary physics", in *Frontiers and challenges in warm dense matter*, edited by F. Graziani, M. P. Desjarlais, R. Redmer, and S. B. Trickey (Springer International Publishing, Cham, 2014), pp. 203–234.

[25] C. R. Mankovich and J. J. Fortney, "Evidence for a dichotomy in the interior structures of Jupiter and Saturn from helium phase separation", The Astrophysical Journal **889**, 51 (2020).

[26] B. Militzer, F. González-Cataldo, S. Zhang, K. P. Driver, and F. Soubiran, "First-principles equation of state database for warm dense matter computation", Physical Review E **103**, 013203 (2021).

[27] R. Helled, G. Mazzola, and R. Redmer, "Understanding dense hydrogen at planetary conditions", Nature Reviews Physics **2**, 562–574 (2020).

[28] W. J. Borucki, D. G. Koch, G. Basri, N. Batalha, T. M. Brown, S. T. Bryson, D. Caldwell, J. Christensen-Dalsgaard, W. D. Cochran, E. DeVore, et al., "Characteristics of planetary candidates observed by Kepler. II. Analysis of the first four months of data", The Astrophysical Journal **736**, 19 (2011).

[29] F. W. Wagner, N. Tosi, F. Sohl, H. Rauer, and T. Spohn, "Rocky super-earth interiors-structure and internal dynamics of CoRoT-7b and Kepler-10b", Astronomy & Astrophysics **541**, A103 (2012).

[30] C. Dorn, J. Venturini, A. Khan, K. Heng, Y. Alibert, R. Helled, A. Rivoldini, and W. Benz, "A generalized Bayesian inference method for constraining the interiors of super earths and sub-neptunes", Astronomy & Astrophysics **597**, A37 (2017).

[31] C. Dorn, N. R. Hinkel, and J. Venturini, "Bayesian analysis of interiors of HD 219134b, Kepler-10b, Kepler-93b, CoRoT-7b, 55 Cnc e, and HD 97658b using stellar abundance proxies", Astronomy & Astrophysics **597**, A38 (2017).

[32] R. Kippenhahn, A. Weigert, and A. Weiss, *Stellar Structure and Evolution*, Second ed. (Springer, Heidelberg, 2012).

[33] A. Burrows, W. Hubbard, J. Lunine, and J. Liebert, "The theory of brown dwarfs and extrasolar giant planets", Reviews of Modern Physics **73**, 719 (2001).

[34] D. Saumon, W. B. Hubbard, G. Chabrier, and H. M. Van Horn, "The role of the molecular-metallic transition of hydrogen in the evolution of Jupiter, Saturn, and brown dwarfs", The Astrophysical Journal **391**, 827 (1992).

[35] J. Christensen-Dalsgaard, W. Däppen, S. Ajukov, E. Anderson, H. Antia, S. Basu, V. Baturin, G. Berthomieu, B. Chaboyer, S. Chitre, et al., "The current state of solar modeling", Science **272**, 1286–1292 (1996).

[36] J. Schumacher and K. R. Sreenivasan, "Colloquium: Unusual dynamics of convection in the sun", Reviews of Modern Physics **92**, 041001 (2020).

[37] J. Christensen-Dalsgaard, T. Duvall Jr, D. Gough, J. Harvey, and E. Rhodes Jr, "Speed of sound in the solar interior", Nature **315**, 378–382 (1985).

[38] O. R. Pols, *Stellar Structure and Evolution* (Astronomical Institute Utrecht, New York, NY, 2011).

[39] S. Chandrasekhar, "XLVIII. The density of white dwarf stars", The London, Edinburgh, and Dublin Philosophical Magazine and Journal of Science **11**, 592–596 (1931).

[40] G. Chabrier, "Quantum effects in dense Coulumbic matter - Application to the cooling of white dwarfs", The Astrophysical Journal **414**, 695–700 (1993).

[41] G. Chabrier, P. Brassard, G. Fontaine, and D. Saumon, "Cooling sequences and color-magnitude diagrams for cool white dwarfs with hydrogen atmospheres", The Astrophysical Journal **543**, 216 (2000).

[42] S. Chandrasekhar, "The maximum mass of ideal white dwarfs", Astrophysical Journal **74**, 81 (1931).

[43] E. H. Gudmundsson, C. J. Pethick, and R. I. Epstein, "Structure of neutron star envelopes", Astrophysical Journal **272**, 286–300 (1983).

[44] P. Haensel, A. Y. Potekhin, and D. G. Yakovlev, *Neutron Stars 1: Equation of State and Structure* (Springer, New York, NY, 2007).

[45] J. Daligault and S. Gupta, "Electron–ion scattering in dense multi-component plasmas: Application to the outer crust of an accreting neutron star", The Astrophysical Journal **703**, 994 (2009).

[46] P. Sharma and R. K. Chhajlani, "Jeans self gravitational instability of strongly coupled quantum plasma", Physics of Plasmas **21**, 072104 (2014).

[47] J. Nuckolls, L. Wood, A. Thiessen, and G. Zimmerman, "Laser compression of matter to super-high densities: Thermonuclear (CTR) applications", Nature **239**, 139–142 (1972).

[48] R. Betti and O. A. Hurricane, "Inertial-confinement fusion with lasers", Nature Physics **12**, 435–448 (2016).

[49] O. A. Hurricane, P. K. Patel, R. Betti, D. H. Froula, S. P. Regan, S. A. Slutz, M. R. Gomez, and M. A. Sweeney, "Physics principles of inertial confinement fusion and US program overview", Reviews of Modern Physics **95**, 025005 (2023).

[50] J. D. Lawson, "Some criteria for a power producing thermonuclear reactor", Proceedings of the Physical Society. Section B **70**, 6 (1957).

[51] H. Abu-Shawareb, R. Acree, P. Adams, J. Adams, B. Addis, R. Aden, P. Adrian, B. B. Afeyan, M. Aggleton, L. Aghaian, et al., "Lawson criterion for ignition exceeded in an inertial fusion experiment", Physical Review Letters **129**, 075001 (2022).

[52] R. Betti, A. Christopherson, B. Spears, R. Nora, A. Bose, J. Howard, K. Woo, M. Edwards, and J. Sanz, "Alpha heating and burning plasmas in inertial confinement fusion", Physical Review Letters **114**, 255003 (2015).

[53] L. Rayleigh, "The form of standing waves on the surface of running water", Proceedings of the London Mathematical Society **1**, 69–78 (1883).

[54] G. I. Taylor, "The instability of liquid surfaces when accelerated in a direction perpendicular to their planes. I", Proceedings of the Royal Society of London. Series A. Mathematical and Physical Sciences **201**, 192–196 (1950).

[55] R. D. Richtmyer, "Taylor instability in shock acceleration of compressible fluids", eng, Communications on Pure and Applied Mathematics **13**, 297–319 (1960).

[56] E. E. Meshkov, "Instability of the interface of two gases accelerated by a shock wave", Fluid Dynamics **4**, 101–104 (1969).

[57] M. Tabak, J. Hammer, M. E. Glinsky, W. L. Kruer, S. C. Wilks, J. Woodworth, E. M. Campbell, M. D. Perry, and R. J. Mason, "Ignition and high gain with ultrapowerful lasers", Physics of Plasmas **1**, 1626–1634 (1994).

[58] R. Betti, C. D. Zhou, K. S. Anderson, L. J. Perkins, W. Theobald, and A. A. Solodov, "Shock ignition of thermonuclear fuel with high areal density", Physical Review Letters **98**, 155001 (2007).

[59] J. A. Gaffney, S. X. Hu, P. Arnault, A. Becker, L. X. Benedict, T. R. Boehly, P. M. Celliers, D. M. Ceperley, O. Čertík, J. Clérouin, et al., "A review of equation-of-state models for inertial confinement fusion materials", High Energy Density Physics **28**, 7–24 (2018).

[60] P. E. Grabowski, S. B. Hansen, M. S. Murillo, L. G. Stanton, F. R. Graziani, A. B. Zylstra, S. D. Baalrud, P. Arnault, A. D. Baczewski, L. X. Benedict, et al., "Review of the first charged-particle transport coefficient comparison workshop", High Energy Density Physics **37**, 100905 (2020).

[61] L. J. Stanek, A. Kononov, S. B. Hansen, B. M. Haines, S. X. Hu, P. F. Knapp, M. S. Murillo, L. G. Stanton, H. D. Whitley, S. D. Baalrud, et al., "Review of the second charged-particle transport coefficient code comparison workshop", Physics of Plasmas **31**, 052104 (2024).

[62] S. M. Wahl, W. B. Hubbard, B. Militzer, T. Guillot, Y. Miguel, N. Movshovitz, Y. Kaspi, R. Helled, D. Reese, E. Galanti, et al., "Comparing Jupiter interior structure models to Juno gravity measurements and the role of a dilute core", Geophysical Research Letters **44**, 4649–4659 (2017).

[63] S. X. Hu, V. N. Goncharov, T. R. Boehly, R. L. McCrory, S. Skupsky, L. A. Collins, J. D. Kress, and B. Militzer, "Impact of first-principles properties of deuterium–tritium on inertial confinement fusion target designs", Physics of Plasmas **22**, 056304 (2015).

[64] S. Ichimaru, "Strongly coupled plasmas: High-density classical plasmas and degenerate electron liquids", Reviews of Modern Physics **54**, 1017 (1982).

[65] M. Bonitz, T. Dornheim, Z. A. Moldabekov, S. Zhang, P. Hamann, H. Kählert, A. Filinov, K. Ramakrishna, and J. Vorberger, "*Ab initio* simulation of warm dense matter", Physics of Plasmas **27**, 042710 (2020).

[66] M. Bonitz, J. Vorberger, M. Bethkenhagen, M. Böhme, D. Ceperley, A. Filinov, T. Gawne, F. Graziani, G. Gregori, P. Hamann, S. Hansen, M. Holzmann, S. X. Hu, H. Kählert, V. Karasiev, U. Kleinschmidt, L. Kordts, C. Makait, B. Militzer, Z. Moldabekov, C. Pierleoni, M. Preising, K. Ramakrishna, R. Redmer, S. Schwalbe, P. Svensson, and T. Dornheim, "Toward first principles-based simulations of dense hydrogen", Physics of Plasmas **31**, 110501 (2024).

[67] S. W. de Leeuw, J. W. Perram, and E. R. Smith, "Simulation of electrostatic systems in periodic boundary conditions. I. Lattice sums and dielectric constants", Proceedings of the Royal Society of London. A. Mathematical and Physical Sciences **373**, 27–56 (1980).

[68] F. F. Chen, *Introduction to plasma physics and controlled fusion*, eng, Third edition (Springer International Publishing, Cham, 2018).

[69] E. L. Pollock and J.-P. Hansen, "Statistical mechanics of dense ionized matter. II. Equilibrium properties and melting transition of the crystallized one-component plasma", Physical Review A **8**, 3110 (1973).

[70] S. Hamaguchi, R. T. Farouki, and D. H. E. Dubin, "Triple point of Yukawa systems", Physical Review E **56**, 4671 (1997).

[71] D. H. E. Dubin and T. M. O'neil, "Trapped nonneutral plasmas, liquids, and crystals (the thermal equilibrium states)", Reviews of Modern Physics **71**, 87 (1999).

[72] M. I. McMahon and R. J. Nelmes, "High-pressure structures and phase transformations in elemental metals", Chemical Society Reviews **35**, 943–963 (2006).

[73] X. Dong, A. R. Oganov, A. F. Goncharov, E. Stavrou, S. Lobanov, G. Saleh, G.-R. Qian, Q. Zhu, C. Gatti, V. L. Deringer, et al., "A stable compound of helium and sodium at high pressure", Nature Chemistry **9**, 440–445 (2017).

[74] D. N. Polsin, A. Lazicki, X. Gong, S. J. Burns, F. Coppari, L. E. Hansen, B. J. Henderson, M. F. Huff, M. I. McMahon, M. Millot, et al., "Structural complexity in ramp-compressed sodium to 480 GPa", Nature communications **13**, 2534 (2022).

[75] H. Fujihisa, Y. Nakamoto, M. Sakata, K. Shimizu, T. Matsuoka, Y. Ohishi, H. Yamawaki, S. Takeya, and Y. Gotoh, "Ca-VII: A chain ordered host-guest structure of calcium above 210 GPa", Physical Review Letters **110**, 235501 (2013).

[76] A. P. Drozdov, P. P. Kong, V. S. Minkov, S. P. Besedin, M. A. Kuzovnikov, S. Mozaffari, L. Balicas, F. F. Balakirev, D. E. Graf, V. B. Prakapenka, et al., "Superconductivity at 250 K in lanthanum hydride under high pressures", Nature **569**, 528–531 (2019).

[77] P. Debye and E. Hückel, "Zur Theorie der Elektrolyte: I. Gefrierpunktserniedrigung und verwandte Erscheinungen (on the theory of electrolytes: I. Lowering of the freezing point and related phenomena)", Physikalische Zeitschrift **24**, 185 (1923).

[78] L. G. Stanton and M. S. Murillo, "Ionic transport in high-energy-density matter", Physical Review E **93**, 043203 (2016).

[79] C. Paquette, C. Pelletier, G. Fontaine, and G. Michaud, "Diffusion coefficients for stellar plasmas", Astrophysical Journal Supplement Series **61**, 177 (1986).

[80] D. O. Gericke, M. S. Murillo, and M. Schlanges, "Dense plasma temperature equilibration in the binary collision approximation", Physical Review E **65**, 036418 (2002).

[81] A. S. Richardson, *2019 NRL Plasma Formulary* (Naval Research Laboratory, Washington, DC, 2019).

[82] R. S. Cohen, L. Spitzer Jr, and P. M. R. Routly, "The electrical conductivity of an ionized gas", Physical Review **80**, 230 (1950).

[83] L. Spitzer Jr and R. Härm, "Transport phenomena in a completely ionized gas", Physical Review **89**, 977 (1953).

[84] Y. T. Lee and R. M. More, "An electron conductivity model for dense plasmas", The Physics of Fluids **27**, 1273–1286 (1984).

[85] S. Ichimaru and S. Tanaka, "Theory of interparticle correlations in dense, high-temperature plasmas. V. Electric and thermal conductivities", Physical Review A **32**, 1790 (1985).

[86] G. Gregori and D. O. Gericke, "A reduced coupled-mode description for the electron-ion energy relaxation in dense matter", Europhysics Letters **83**, 15002 (2008).

[87] L. G. Stanton and M. S. Murillo, "Efficient model for electronic transport in high energy-density matter", Physics of Plasmas **28**, 082301 (2021).

[88] Z. A. Moldabekov, T. Dornheim, and M. Bonitz, "Screening of a test charge in a free-electron gas at warm dense matter and dense non-ideal plasma conditions", Contributions to Plasma Physics **62**, e202000176 (2022).

[89] A. Selchow, G. Röpke, A. Wierling, H. Reinholz, T. Pschiwul, and G. Zwicknagel, "Dynamic structure factor for a two-component model plasma", Physical Review E **64**, 056410 (2001).

[90] J. P. Hansen and I. R. McDonald, "Thermal relaxation in a strongly coupled two-temperature plasma", Physics Letters A **97**, 42–44 (1983).

[91] V. Golubnychiy, M. Bonitz, D. Kremp, and M. Schlanges, "Dynamical properties and plasmon dispersion of a weakly degenerate correlated one-component plasma", Physical Review E **64**, 016409 (2001).

[92] V. Golubnychiy, M. Bonitz, D. Kremp, and M. Schlanges, "Plasmon dispersion of a weakly degenerate nonideal one-component plasma", Contributions to Plasma Physics **42**, 37–41 (2002).

[93] G. Zwicknagel and T. Pschiwul, "Dynamic response of two-component model plasmas", Contributions to Plasma Physics **43**, 393–397 (2003).

[94] J. N. Glosli, F. R. Graziani, R. M. More, M. S. Murillo, F. H. Streitz, M. P. Surh, L. X. Benedict, S. Hau-Riege, A. B. Langdon, and R. A. London, "Molecular dynamics

simulations of temperature equilibration in dense hydrogen", Physical Review E **78**, 025401(R) (2008).

[95] G. Kelbg, "Theorie des Quanten-Plasmas", Annalen der Physik **467**, 219–224 (1963).

[96] C. Deutsch, M. M. Gombert, and H. Minoo, "Classical modelization of symmetry effects in the dense high-temperature electron gas", Physics Letters A **66**, 381–382 (1978).

[97] H. Minoo, M. M. Gombert, and C. Deutsch, "Temperature-dependent Coulomb interactions in hydrogenic systems", Physical Review A **23**, 924 (1981).

[98] A. V. Filinov, V. O. Golubnychiy, M. Bonitz, W. Ebeling, and J. W. Dufty, "Temperature-dependent quantum pair potentials and their application to dense partially ionized hydrogen plasmas", Physical Review E **70**, 046411 (2004).

[99] R. E. Wyatt, *Quantum Dynamics with Trajectories: Introduction to Quantum Hydrodynamics*, Vol. 28 (Springer Science & Business Media, New York, NY, 2005).

[100] D. Bohm, "A suggested interpretation of the quantum theory in terms of "hidden" variables. I", Physical Review **85**, 166 (1952).

[101] D. Michta, F. Graziani, and M. Bonitz, "Quantum hydrodynamics for plasmas–a Thomas-Fermi theory perspective", Contributions to Plasma Physics **55**, 437–443 (2015).

[102] Z. A. Moldabekov, M. Bonitz, and T. S. Ramazanov, "Theoretical foundations of quantum hydrodynamics for plasmas", Physics of Plasmas **25**, 031903 (2018).

[103] D. Michta, "Quantum hydrodynamics: Theory and computation with applications to charged particle stopping in warm dense matter", PhD thesis (Princeton University, 2020).

[104] D. Kremp, M. Schlanges, and W.-D. Kraeft, *Quantum Statistics of Nonideal Plasmas*, Vol. 25 (Springer Science & Business Media, Berlin, 2005).

[105] E. Daniel and S. H. Vosko, "Momentum distribution of an interacting electron gas", Physical Review **120**, 2041 (1960).

[106] J. Hofmann, M. Barth, and W. Zwerger, "Short-distance properties of Coulomb systems", Physical Review B **87**, 235125 (2013).

[107] H. Reinholz, "Dielectric and optical properties of dense plasmas", in Annales de Physique, Vol. 30 (Masson, Paris, 2005).

[108] J. Chihara, "Difference in x-ray scattering between metallic and non-metallic liquids due to conduction electrons", Journal of Physics F: Metal Physics **17**, 295 (1987).

[109] J. Chihara, "Interaction of photons with plasmas and liquid metals-photoabsorption and scattering", Journal of Physics: Condensed Matter **12**, 231 (2000).

[110] J. P. Mithen, J. Daligault, and G. Gregori, "Extent of validity of the hydrodynamic description of ions in dense plasmas", Physical Review E **83**, 015401 (2011).

[111] D. M. Testa, P. Svensson, J. Jackson, T. Campbell, and G. Gregori, "Self-diffusion of a relativistic lennard-jones gas via semirelativistic molecular dynamics", Physical Review E **107**, 054138 (2023).

[112] J. D. Jackson, *Classical Electrodynamics*, 2nd ed. (Wiley, New York, NY, 1975).

[113] G. Chabrier and A. Y. Potekhin, "Equation of state of fully ionized electron-ion plasmas", Physical Review E **58**, 4941 (1998).

[114] W. G. Vincenti and B. S. Baldwin, "Effect of thermal radiation on the propagation of plane acoustic waves", Journal of Fluid Mechanics **12**, 449–477 (1962).

[115] R. More, F. Graziani, J. Glosli, and M. Surh, "Radiation in particle simulations", High Energy Density Physics **6**, 29–38 (2010).

[116] K. Falk, "Experimental methods for warm dense matter research", High Power Laser Science and Engineering **6**, e59 (2018).

[117] C. E. Weir, E. R. Lippincott, A. Van Valkenburg, and E. N. Bunting, "Infrared studies in the 1-to 15-micron region to 30,000 atmospheres", Journal of Research of the National Bureau of Standards **63**, 55–62 (1959).

[118] S. Deemyad and I. F. Silvera, "Melting line of hydrogen at high pressures", Physical Review Letters **100**, 155701 (2008).

[119] Z. Konôpková, R. S. McWilliams, N. Gómez-Pérez, and A. F. Goncharov, "Direct measurement of thermal conductivity in solid iron at planetary core conditions", Nature **534**, 99–101 (2016).

[120] S. Tateno, K. Hirose, Y. Ohishi, and Y. Tatsumi, "The structure of iron in Earth's inner core", Science **330**, 359–361 (2010).

[121] N. Holmes, M. Ross, and W. Nellis, "Temperature measurements and dissociation of shock-compressed liquid deuterium and hydrogen", Physical Review B **52**, 15835 (1995).

[122] G. V. Boriskov, A. I. Bykov, R. I. Il'Kaev, V. D. Selemir, G. V. Simakov, R. F. Trunin, V. D. Urlin, A. N. Shuikin, and W. J. Nellis, "Shock compression of liquid deuterium up to 109 GPa", Physical Review B **71**, 092104 (2005).

[123] Y. B. Zel'Dovich and Y. P. Raizer, *Physics of Shock Waves and High-Temperature Hydrodynamic Phenomena* (Dover Publications, INC, Mineola, NY, 2002).

[124] D. G. Hicks, T. R. Boehly, P. M. Celliers, J. H. Eggert, S. J. Moon, D. D. Meyerhofer, and G. W. Collins, "Laser-driven single shock compression of fluid deuterium from 45 to 220 GPa", Physical Review B **79**, 014112 (2009).

[125] M. D. Knudson and M. P. Desjarlais, "High-precision shock wave measurements of deuterium: Evaluation of exchange-correlation functionals at the molecular-to-atomic transition", Physical Review Letters **118**, 035501 (2017).

[126] P. M. Celliers, G. W. Collins, D. G. Hicks, M. Koenig, E. Henry, A. Benuzzi-Mounaix, D. Batani, D. K. Bradley, L. B. Da Silva, R. J. Wallace, et al., "Electronic conduction in shock-compressed water", Physics of Plasmas **11**, L41–L44 (2004).

[127] R. F. Smith, J. H. Eggert, R. Jeanloz, T. S. Duffy, D. G. Braun, J. R. Patterson, R. E. Rudd, J. Biener, A. E. Lazicki, A. V. Hamza, et al., "Ramp compression of diamond to five terapascals", Nature **511**, 330–333 (2014).

[128] R. F. Smith, D. E. Fratanduono, D. G. Braun, T. S. Duffy, J. K. Wicks, P. M. Celliers, S. J. Ali, A. Fernandez-Pañella, R. G. Kraus, D. C. Swift, et al., "Equation of state of iron under core conditions of large rocky exoplanets", Nature Astronomy **2**, 452–458 (2018).

[129] P. Loubeyre, P. Celliers, D. Hicks, E. Henry, A. Dewaele, J. Pasley, J. Eggert, M. Koenig, F. Occelli, K. Lee, et al., "Coupling static and dynamic compressions: First measurements in dense hydrogen", High Pressure Research **24**, 25–31 (2004).

[130] P. Loubeyre, S. Brygoo, J. Eggert, P. M. Celliers, D. K. Spaulding, J. R. Rygg, T. R. Boehly, G. W. Collins, and R. Jeanloz, "Extended data set for the equation of state of warm dense hydrogen isotopes", Physical Review B **86**, 144115 (2012).

[131] D. H. H. Hoffmann, A. Blazevic, P. Ni, O. Rosmej, M. Roth, N. A. Tahir, A. Tauschwitz, S. Udrea, D. Varentsov, K. Weyrich, et al., "Present and future perspectives for high energy density physics with intense heavy ion and laser beams", Laser and Particle beams **23**, 47–53 (2005).

[132] S. H. Glenzer, G. Gregori, R. W. Lee, F. J. Rogers, S. W. Pollaine, and O. L. Landen, "Demonstration of spectrally resolved x-ray scattering in dense plasmas", Physical Review Letters **90**, 175002 (2003).

[133] S. H. Glenzer, O. L. Landen, P. Neumayer, R. W. Lee, K. Widmann, S. W. Pollaine, R. J. Wallace, G. Gregori, A. Höll, T. Bornath, R. Thiele, V. Schwarz, W.-D. Kraeft, and R. Redmer, "Observations of plasmons in warm dense matter", Physical Review Letters **98**, 065002 (2007).

[134] G. Gregori, S. Glenzer, K. B. Fournier, K. M. Campbell, E. L. Dewald, O. S. Jones, J. H. Hammer, S. B. Hansen, R. J. Wallace, and O. L. Landen, "X-ray scattering measurements of radiative heating and cooling dynamics", Physical Review Letters **101**, 045003 (2008).

[135] R. R. Fäustlin, T. Bornath, T. Döppner, S. Düsterer, E. Foerster, C. Fortmann, S. Glenzer, S. Göde, G. Gregori, R. Irsig, et al., "Observation of ultrafast nonequilibrium collective dynamics in warm dense hydrogen", Physical Review Letters **104**, 125002 (2010).

[136] O. Ciricosta, S. M. Vinko, H.-K. Chung, B.-I. Cho, C. R. D. Brown, T. Burian, J. Chalupský, K. Engelhorn, R. W. Falcone, C. Graves, et al., "Direct measurements of the ionization potential depression in a dense plasma", Physical Review Letters **109**, 065002 (2012).

[137] A. Levy, P. Audebert, R. Shepherd, J. Dunn, M. Cammarata, O. Ciricosta, F. Deneuville, F. Dorchies, M. Fajardo, C. Fourment, et al., "The creation of large-volume, gradient-free warm dense matter with an x-ray free-electron laser", Physics of Plasmas **22**, 030703 (2015).

[138] S. M. Vinko, O. Ciricosta, T. R. Preston, D. S. Rackstraw, C. R. D. Brown, T. Burian, J. Chalupský, B. I. Cho, H.-K. Chung, K. Engelhorn, et al., "Investigation of femtosecond collisional ionization rates in a solid-density aluminium plasma", Nature Communications **6**, 6397 (2015).

[139] P. K. Patel, A. J. Mackinnon, M. H. Key, T. E. Cowan, M. E. Foord, M. Allen, D. F. Price, H. Ruhl, P. T. Springer, and R. Stephens, "Isochoric heating of solid-density matter with an ultrafast proton beam", Physical Review Letters **91**, 125004 (2003).

[140] T. G. White, J. Vorberger, C. R. D. Brown, B. J. B. Crowley, P. Davis, S. H. Glenzer, J. W. O. Harris, D. C. Hochhaus, S. Le Pape, T. Ma, et al., "Observation of inhibited electron-ion coupling in strongly heated graphite", Scientific Reports **2**, 889 (2012).

[141] S. B. Hansen, A. Y. Faenov, T. A. Pikuz, K. B. Fournier, R. Shepherd, H. Chen, K. Widmann, S. C. Wilks, Y. Ping, H. K. Chung, et al., "Temperature determination using K α spectra from M-shell Ti ions", Physical Review E **72**, 036408 (2005).

[142] D. Durante, M. Parisi, D. Serra, M. Zannoni, V. Notaro, P. Racioppa, D. R. Buccino, G. Lari, L. Gomez Casajus, L. Iess, et al., "Jupiter's gravity field halfway through the Juno mission", Geophysical Research Letters **47**, e2019GL086572 (2020).

[143] A. P. Ingersoll, "Cassini exploration of the planet Saturn: A comprehensive review", Space Science Reviews **216**, 122 (2020).

[144] N. Nettelmann, B. Holst, A. Kietzmann, M. French, R. Redmer, and D. Blaschke, "*Ab initio* equation of state data for hydrogen, helium, and water and the internal structure of Jupiter", The Astrophysical Journal **683**, 1217 (2008).

[145] B. Militzer, W. B. Hubbard, S. Wahl, J. I. Lunine, E. Galanti, Y. Kaspi, Y. Miguel, T. Guillot, K. M. Moore, M. Parisi, et al., "Juno spacecraft measurements of Jupiter's gravity imply a dilute core", The Planetary Science Journal **3**, 185 (2022).

[146] D. J. Stevenson, "Thermodynamics and phase separation of dense fully ionized hydrogen-helium fluid mixtures", Physical Review B **12**, 3999 (1975).

[147] S. X. Hu, B. Militzer, V. N. Goncharov, S. Skupsky, et al., "First-principles equation-of-state table of deuterium for inertial confinement fusion applications", Physical Review B **84**, 224109 (2011).

[148] S. X. Hu, L. A. Collins, T. R. Boehly, J. D. Kress, V. N. Goncharov, and S. Skupsky, "First-principles thermal conductivity of warm-dense deuterium plasmas for inertial confinement fusion applications", Physical Review E **89**, 043105 (2014).

[149] P. Mabey, S. Richardson, T. G. White, L. B. Fletcher, S. H. Glenzer, N. J. Hartley, J. Vorberger, D. O. Gericke, and G. Gregori, "A strong diffusive ion mode in dense ionized matter predicted by Langevin dynamics", Nature Communications **8**, 14125 (2017).

[150] R. A. Davis, W. A. Angermeier, R. K. T. Hermsmeier, and T. G. White, "Ion modes in dense ionized plasmas through nonadiabatic molecular dynamics", Physical Review Research **2**, 043139 (2020).

[151] Y. Yao, Q. Zeng, K. Chen, D. Kang, Y. Hou, Q. Ma, and J. Dai, "Reduced ionic diffusion by the dynamic electron–ion collisions in warm dense hydrogen", Physics of Plasmas **28**, 012704 (2021).

[152] W. A. Angermeier, B. S. Scheiner, N. R. Shaffer, and T. G. White, "Disentangling the effects of non-adiabatic interactions upon ion self-diffusion within warm dense hydrogen", Philosophical Transactions of the Royal Society A **381**, 20230034 (2023).

[153] A. Kononov, T. W. Hentschel, S. B. Hansen, and A. D. Baczewski, "Trajectory sampling and finite-size effects in first-principles stopping power calculations", npj Computational Materials **9**, 205 (2023).

[154] C. Makait, F. B. Fajardo, and M. Bonitz, "Time-dependent charged particle stopping in quantum plasmas: Testing the G1–G2 scheme for quasi-one-dimensional systems", Contributions to Plasma Physics **63**, e202300008 (2023).

[155] Y.-F. Shi, S. Ren, H.-K. Chung, J. S. Wark, and S. M. Vinko, "Exploring relaxation dynamics in warm dense plasmas by tailoring non-thermal electron distributions with a free electron laser", Physics of Plasmas **31**, 082305 (2024).

[156] D. Michta, F. Graziani, T. Luu, and J. Pruet, "Effects of nonequilibrium particle distributions in deuterium-tritium burning", Physics of Plasmas **17**, 012707 (2010).

[157] A. Ng, P. Celliers, G. Xu, and A. Forsman, "Electron-ion equilibration in a strongly coupled plasma", Physical Review E **52**, 4299 (1995).

[158] T. E. Foster, H. Fetsch, and N. J. Fisch, "Fast correlation heating in moderately coupled electron–ion plasmas", Journal of Plasma Physics **89**, 905890506 (2023).

[159] L. Spitzer, *Physics of Fully Ionized Gases*, eng, 2d rev. ed, Interscience tracts on physics and astronomy ; 3 (Interscience Publishers, New York, NY, 1962).

[160] H. Brysk, "Electron-ion equilibration in a partially degenerate plasma", Plasma Physics **16**, 927 (1974).

[161] P. Celliers, A. Ng, G. Xu, and A. Forsman, "Thermal equilibration in a shock wave", Physical Review Letters **68**, 2305 (1992).

[162] Z. Chen, B. Holst, S. E. Kirkwood, V. Sametoglu, M. Reid, Y. Y. Tsui, V. Recoules, and A. Ng, "Evolution of ac conductivity in nonequilibrium warm dense gold", Physical Review Letters **110**, 135001 (2013).

[163] L. B. Fletcher, J. Vorberger, W. Schumaker, C. Ruyer, S. Goede, E. Galtier, U. Zastrau, E. P. Alves, S. D. Baalrud, R. A. Baggott, et al., "Electron-ion temperature relaxation in warm dense hydrogen observed with picosecond resolved x-ray scattering", Frontiers in Physics **10**, 838524 (2022).

[164] M. W. C. Dharma-Wardana and F. Perrot, "Energy relaxation and the quasiequation of state of a dense two-temperature nonequilibrium plasma", Physical Review E **58**, 3705 (1998).

[165] S. Rightley and S. D. Baalrud, "Kinetic model for electron-ion transport in warm dense matter", Physical Review E **103**, 063206 (2021).

[166] Q. Ma, J. Dai, D. Kang, M. S. Murillo, Y. Hou, Z. Zhao, and J. Yuan, "Extremely low electron-ion temperature relaxation rates in warm dense hydrogen: Interplay between quantum electrons and coupled ions", Physical Review Letters **122**, 015001 (2019).

[167] Y. S. Lavrinenko, I. V. Morozov, and I. A. Valuev, "Electron–ion temperature relaxation in nonideal plasmas: High accuracy classical molecular dynamics simulations", Contributions to Plasma Physics **64**, e202300158 (2024).

[168] S. H. Glenzer and R. Redmer, "X-ray Thomson scattering in high energy density plasmas", Reviews of Modern Physics **81**, 1625 (2009).

[169] J. Vorberger, T. R. Preston, N. Medvedev, M. P. Böhme, Z. A. Moldabekov, D. Kraus, and T. Dornheim, "Revealing non-equilibrium and relaxation in laser heated matter", Physics Letters A **499**, 129362 (2024).

[170] C. Fortmann, R. Thiele, R. R. Fäustlin, T. Bornath, B. Holst, W.-D. Kraeft, V. Schwarz, S. Toleikis, T. Tschentscher, and R. Redmer, "Thomson scattering in dense plasmas with density and temperature gradients", High Energy Density Physics **5**, 208–211 (2009).

[171] P. M. Kozlowski, B. J. B. Crowley, D. O. Gericke, S. P. Regan, and G. Gregori, "Theory of Thomson scattering in inhomogeneous media", Scientific Reports **6**, 24283 (2016).

[172] A. D. Baczewski, L. Shulenburger, M. P. Desjarlais, S. B. Hansen, and R. J. Magyar, "X-ray Thomson scattering in warm dense matter without the Chihara decomposition", Physical Review Letters **116**, 115004 (2016).

[173] T. Dornheim, Z. Moldabekov, J. Vorberger, H. Kählert, and M. Bonitz, "Electronic pair alignment and roton feature in the warm dense electron gas", Communications Physics **5**, 304 (2022).

[174] M. Schörner, M. Bethkenhagen, T. Döppner, D. Kraus, L. B. Fletcher, S. H. Glenzer, and R. Redmer, "X-ray Thomson scattering spectra from density functional theory molecular dynamics simulations based on a modified Chihara formula", Physical Review E **107**, 065207 (2023).

[175] J.-P. Hansen and I. R. McDonald, *Theory of Simple Liquids*, 2nd ed. (Academic Press, London, 1986).

[176] S. Tanaka and S. Ichimaru, "Thermodynamics and correlational properties of finite-temperature electron liquids in the Singwi-Tosi-Land-Sjölander approximation", Journal of the Physical Society of Japan **55**, 2278–2289 (1986).

[177] S.-H. Chen and M. Kotlarchyk, *Interactions of Photons and Neutrons with Matter* (World Scientific Publishing Co. Pte. Ltd., Singapore, 2007).

[178] D. Landau and K. Binder, *A guide to Monte Carlo Simulations in Statistical Physics*, 5th ed. (Cambridge University Press, Cambridge, 2021).

[179] S. Weinzierl, *Introduction to Monte Carlo methods*, 2000.

[180] N. Metropolis, A. W. Rosenbluth, M. N. Rosenbluth, A. H. Teller, and E. Teller, "Equation of state calculations by fast computing machines", The Journal of Chemical Physics **21**, 1087–1092 (1953).

[181] W. K. Hastings, "Monte Carlo sampling methods using Markov chains and their applications", Biometrika **57**, 97–109 (1970).

[182] J. Goodman and J. Weare, "Ensemble samplers with affine invariance", Communications in Applied Mathematics and Computational Science **5**, 65–80 (2010).

[183] L. A. Zepeda-Ruiz, A. Stukowski, T. Oppelstrup, and V. V. Bulatov, "Probing the limits of metal plasticity with molecular dynamics simulations", Nature **550**, 492–495 (2017).

[184] M. Karplus and G. A. Petsko, "Molecular dynamics simulations in biology", Nature **347**, 631–639 (1990).

[185] D. C. Rapaport, *The Art of Molecular Dynamics Simulation* (Cambridge University Press, Cambridge, 2004).

[186] L. Boltzmann, *Vorlesungen über Gastheorie: 2. Teil*, Vol. 2 (JA Barth, Leipzig, 1898).

[187] B. Leimkuhler and S. Reich, *Simulating Hamiltonian Dynamics*, Cambridge Monographs on Applied and Computational Mathematics 14 (Cambridge University Press, Cambridge, 2004).

[188] R. W. Hall and B. J. Berne, "Nonergodicity in path integral molecular dynamics", The Journal of Chemical Physics **81**, 3641–3643 (1984).

[189] M. E. Tuckerman, B. J. Berne, G. J. Martyna, and M. L. Klein, "Efficient molecular dynamics and hybrid Monte Carlo algorithms for path integrals", The Journal of Chemical Physics **99**, 2796–2808 (1993).

[190] J. R. Ray and H. Zhang, "Correct microcanonical ensemble in molecular dynamics", Physical Review E **59**, 4781 (1999).

[191] J. White, F. Román, A. González, and S. Velasco, "Periodic boundary conditions and the correct molecular-dynamics ensemble", Physica A: Statistical Mechanics and its Applications **387**, 6705–6711 (2008).

[192] A. K. Kerman and S. E. Koonin, "Hamiltonian formulation of time-dependent variational principles for the many-body system", Annals of Physics **100**, 332–358 (1976).

[193] H. W. Woodcock and P. Havas, "Approximately relativistic Lagrangians for classical interacting point particles", Physical Review D **6**, 3422 (1972).

[194] R. Marnelius, "Lagrangian and Hamiltonian formulation of relativistic particle mechanics", Physical Review D **10**, 2535 (1974).

[195] S. Ichimaru, S. Mitake, S. Tanaka, and X.-Z. Yan, "Theory of interparticle correlations in dense, high-temperature plasmas. I. General formalism", Physical Review A **32**, 1768 (1985).

[196] J. P. Boon and S. Yip, *Molecular Hydrodynamics* (Dover Publications, New York, NY, 1991).

[197] I. G. Currie, *Fundamental Mechanics of Fluids*, 2nd ed. (McGraw-Hill, New York, NY, 1993).

[198] Z. Donkó and P. Hartmann, "Thermal conductivity of strongly coupled Yukawa liquids", Physical Review E **69**, 016405 (2004).

[199] Z. Donkó and P. Hartmann, "Shear viscosity of strongly coupled Yukawa liquids", Physical Review E **78**, 026408 (2008).

[200] R. Kubo, "The fluctuation-dissipation theorem", Reports on Progress in Physics **29**, 255 (1966).

[201] T. Scopigno, G. Ruocco, and F. Sette, "Microscopic dynamics in liquid metals: The experimental point of view", Reviews of Modern Physics **77**, 881 (2005).

[202] H. Kählert, "Thermodynamic and transport coefficients from the dynamic structure factor of Yukawa liquids", Physical Review Research **2**, 033287 (2020).

[203] M. Schörner, H. R. Rüter, M. French, and R. Redmer, "Extending *ab initio* simulations for the ion-ion structure factor of warm dense aluminum to the hydrodynamic limit using neural network potentials", Physical Review B **105**, 174310 (2022).

[204] J. P. Mithen, J. Daligault, and G. Gregori, "Molecular dynamics simulations for the shear viscosity of the one-component plasma", Contributions to Plasma Physics **52**, 58–61 (2012).

[205] Z. A. Moldabekov, S. Groth, T. Dornheim, H. Kählert, M. Bonitz, and T. S. Ramazanov, "Structural characteristics of strongly coupled ions in a dense quantum plasma", Physical Review E **98**, 023207 (2018).

[206] K. Sturm, "Dynamic structure factor: An introduction", Zeitschrift für Naturforschung A **48**, 233–242 (1993).

[207] T. Dornheim, J. Vorberger, S. Groth, N. Hoffmann, Z. A. Moldabekov, and M. Bonitz, "The static local field correction of the warm dense electron gas: An *ab initio* path integral Monte Carlo study and machine learning representation", The Journal of Chemical Physics **151**, 194104 (2019).

[208] E. M. Lifshitz and L. P. Pitaevskii, *Course of Theoretical Physics: Physical Kinetics*, trans. by J. B. Sykes and R. N. Franklin, Vol. 10 (Elsevier, Oxford, 2008).

[209] K. Singwi, A. Sjölander, M. Tosi, and R. Land, "Electron correlations at metallic densities. IV", Physical Review B **1**, 1044 (1970).

[210] P. Vashishta and K. S. Singwi, "Electron correlations at metallic densities. V", Physical Review B **6**, 875 (1972).

[211] S. Tanaka, "Correlational and thermodynamic properties of finite-temperature electron liquids in the hypernetted-chain approximation", The Journal of Chemical Physics **145**, 214104 (2016).

[212] D. Levesque and L. Verlet, "Molecular dynamics and time reversibility", Journal of Statistical Physics **72**, 519–537 (1993).

[213] C. Runge, "Über die numerische auflösung von Differentialgleichungen", Mathematische Annalen **46**, 167–178 (1895).

[214] W. Kutta, "Beitrag zur Naherungsweisen Integration Totaler Differentialgleichungen", Zeitschrift für Mathematik und Physik **46**, 435–453 (1901).

[215] A. Ralston, "Runge-Kutta methods with minimum error bounds", Mathematics of Computation **16**, 431–437 (1962).

[216] J. C. Butcher, "A history of Runge-Kutta methods", Applied Numerical Mathematics **20**, 247–260 (1996).

[217] M. Tao, "Explicit symplectic approximation of nonseparable Hamiltonians: Algorithm and long time performance", Physical Review E **94**, 043303 (2016).

[218] R. Zhang, H. Qin, Y. Tang, J. Liu, Y. He, and J. Xiao, "Explicit symplectic algorithms based on generating functions for charged particle dynamics", Physical Review E **94**, 013205 (2016).

[219] R. Zhang, Y. Wang, Y. He, J. Xiao, J. Liu, H. Qin, and Y. Tang, "Explicit symplectic algorithms based on generating functions for relativistic charged particle dynamics in time-dependent electromagnetic field", Physics of Plasmas **25**, 022117 (2018).

[220] S. Plimpton, "Fast parallel algorithms for short-range molecular dynamics", Journal of Computational Physics **117**, 1–19 (1995).

[221] P. P. Ewald, "Die Berechnung optischer und elektrostatischer Gitterpotentiale", Annalen der Physik **369**, 253–287 (1921).

[222] M. Deserno and C. Holm, "How to mesh up Ewald sums. I. A theoretical and numerical comparison of various particle mesh routines", The Journal of Chemical Physics **109**, 7678–7693 (1998).

[223] J. Kolafa and J. W. Perram, "Cutoff errors in the Ewald summation formulae for point charge systems", Molecular Simulation **9**, 351–368 (1992).

[224] L. V. Woodcock and K. Singer, "Thermodynamic and structural properties of liquid ionic salts obtained by Monte Carlo computation. Part 1. - Potassium chloride", Transactions of the Faraday Society **67**, 12–30 (1971).

[225] J. W. Perram, H. G. Petersen, and S. W. De Leeuw, "An algorithm for the simulation of condensed matter which grows as the 3/2 power of the number of particles", Molecular Physics **65**, 875–893 (1988).

[226] T. Darden, D. York, and L. Pedersen, "Particle mesh Ewald: An N log(N) method for Ewald sums in large systems", The Journal of Chemical Physics **98**, 10089 (1993).

[227] R. W. Hockney and J. W. Eastwood, *Computer Simulation using Particles*, First ed. (Taylor & Francis Group, New York, NY, 1988).

[228] J. M. Dawson, "Particle simulation of plasmas", Reviews of Modern Physics **55**, 403 (1983).

[229] S. Jin, L. Li, Z. Xu, and Y. Zhao, "A random batch Ewald method for particle systems with coulomb interactions", SIAM Journal on Scientific Computing **43**, B937–B960 (2021).

[230] S. Jin and L. Li, "Random batch methods for classical and quantum interacting particle systems and statistical samplings", in *Active particles, volume 3: Advances in theory, models, and applications* (Springer, Cham, 2021), pp. 153–200.

[231] S. Nosé, "A molecular dynamics method for simulations in the canonical ensemble", Molecular Physics **52**, 255–268 (1984).

[232] W. G. Hoover, "Canonical dynamics: Equilibrium phase-space distributions", Physical Review A **31**, 1695 (1985).

[233] S. Nosé and M. L. Klein, "Constant pressure molecular dynamics for molecular systems", Molecular Physics **50**, 1055–1076 (1983).

[234] G. J. Martyna, M. L. Klein, and M. Tuckerman, "Nosé–Hoover chains: The canonical ensemble via continuous dynamics", The Journal of Chemical Physics **97**, 2635–2643 (1992).

[235] B. Larder, D. O. Gericke, S. Richardson, P. Mabey, T. G. White, and G. Gregori, "Fast nonadiabatic dynamics of many-body quantum systems", Science Advances **5**, eaaw1634 (2019).

[236] T. Schneider and E. Stoll, "Molecular-dynamics study of a three-dimensional one-component model for distortive phase transitions", Physical Review B **17**, 1302 (1978).

[237] S. Brush, H. Sahlin, and E. Teller, "Monte Carlo study of a one-component plasma. I", The Journal of Chemical Physics **45**, 2102–2118 (1966).

[238] J. P. Hansen, "Statistical mechanics of dense ionized matter. I. Equilibrium properties of the classical one-component plasma", Physical Review A **8**, 3096 (1973).

[239] P. Vieillefosse and J. P. Hansen, "Statistical mechanics of dense ionized matter. V. Hydrodynamic limit and transport coefficients of the classical one-component plasma", Physical Review A **12**, 1106 (1975).

[240] J. P. Hansen, "Plasmon dispersion of the strongly coupled one component plasma in two and three dimensions", Journal de Physique Lettres **42**, 397–400 (1981).

[241] J. Caillol, "Thermodynamic limit of the excess internal energy of the fluid phase of a one-component plasma: A Monte Carlo study", The Journal of Chemical Physics **111**, 6538–6547 (1999).

[242] J.-M. Caillol and D. Gilles, "An accurate equation of state for the one-component plasma in the low coupling regime", Journal of Physics A: Mathematical and Theoretical **43**, 105501 (2010).

[243] J. Daligault, K. O. Rasmussen, and S. D. Baalrud, "Determination of the shear viscosity of the one-component plasma", Physical Review E **90**, 033105 (2014).

[244] B. Scheiner and S. D. Baalrud, "Testing thermal conductivity models with equilibrium molecular dynamics simulations of the one-component plasma", Physical Review E **100**, 043206 (2019).

[245] D. Plummer, P. Svensson, D. O. Gericke, P. Hollebon, S. M. Vinko, and G. Gregori, "Ionization calculations using classical molecular dynamics", Physical Review E **111**, 015204 (2024).

[246] M. Baus and J.-P. Hansen, "Statistical mechanics of simple Coulomb systems", Physics Reports **59**, 1–94 (1980).

[247] A. Wierling, "Dynamic local field corrections for two-component plasmas at intermediate coupling", Journal of Physics A: Mathematical and Theoretical **42**, 214051 (2009).

[248] C. Fortmann, A. Wierling, and G. Röpke, "Influence of local-field corrections on Thomson scattering in collision-dominated two-component plasmas", Physical Review E **81**, 026405 (2010).

[249] B. Farid, V. Heine, G. E. Engel, and I. J. Robertson, "Extremal properties of the Harris-Foulkes functional and an improved screening calculation for the electron gas", Physical Review B **48**, 11602 (1993).

[250] S. Moroni, D. M. Ceperley, and G. Senatore, "Static response and local field factor of the electron gas", Physical Review Letters **75**, 689 (1995).

[251] T. Dornheim, S. Groth, J. Vorberger, and M. Bonitz, "*Ab initio* path integral Monte Carlo results for the dynamic structure factor of correlated electrons: From the electron liquid to warm dense matter", Physical Review Letters **121**, 255001 (2018).

[252] S. K. Kodanova, T. S. Ramazanov, and M. K. Issanova, "Impact of the local field correction on transport and dynamic properties of warm dense matter", Matter and Radiation at Extremes **10**, 037601 (2025).

[253] T. Ott, M. Bonitz, L. G. Stanton, and M. S. Murillo, "Coupling strength in coulomb and Yukawa one-component plasmas", Physics of Plasmas **21**, 113704 (2014).

[254] S. Hamaguchi and R. T. Farouki, "Thermodynamics of strongly-coupled Yukawa systems near the one-component-plasma limit. I. Derivation of the excess energy", The Journal of Chemical Physics **101**, 9876–9884 (1994).

[255] R. T. Farouki and S. Hamaguchi, "Thermodynamics of strongly-coupled Yukawa systems near the one-component-plasma limit. II. Molecular dynamics simulations", The Journal of Chemical Physics **101**, 9885–9893 (1994).

[256] J. Caillol and D. Gilles, "Monte Carlo simulations of the Yukawa one-component plasma", Journal of Statistical Physics **100**, 933–947 (2000).

[257] T. Ott, M. Bonitz, and Z. Donko, "Effect of correlations on heat transport in a magnetized strongly coupled plasma", Physical Review E **92**, 063105 (2015).

[258] M. S. Murillo, "Viscosity estimates of liquid metals and warm dense matter using the Yukawa reference system", High Energy Density Physics **4**, 49–57 (2008).

[259] D. M. Ceperley, "Path integrals in the theory of condensed helium", Reviews of Modern Physics **67**, 279 (1995).

[260] T. Dornheim, "Fermion sign problem in path integral Monte Carlo simulations: Quantum dots, ultracold atoms, and warm dense matter", Physical Review E **100**, 023307 (2019).

[261] M. Troyer and U. J. Wiese, "Computational complexity and fundamental limitations to fermionic quantum Monte Carlo simulations", Physical Review Letters **94**, 170201 (2005).

[262] D. M. Ceperley, "Fermion nodes", Journal of Statistical Physics **63**, 1237–1267 (1991).

[263] T. Dornheim, S. Schwalbe, P. Tolias, M. P. Böhme, Z. A. Moldabekov, and J. Vorberger, "*Ab initio* density response and local field factor of warm dense hydrogen", Matter and Radiation at Extremes **9**, 057401 (2024).

[264] D. Chandler and P. G. Wolynes, "Exploiting the isomorphism between quantum theory and classical statistical mechanics of polyatomic fluids", The Journal of Chemical Physics **74**, 4078–4095 (1981).

[265] I. R. Craig and D. E. Manolopoulos, "Quantum statistics and classical mechanics: Real time correlation functions from ring polymer molecular dynamics", The Journal of Chemical Physics **121**, 3368–3373 (2004).

[266] P. Hohenberg and W. Kohn, "Inhomogeneous electron gas", Physical Review **136**, B864 (1964).

[267] N. D. Mermin, "Thermal properties of the inhomogeneous electron gas", Physical Review **137**, A1441 (1965).

[268] W. Kohn and L. J. Sham, "Self-consistent equations including exchange and correlation effects", Physical Review **140**, A1133 (1965).

[269] J. P. Perdew and A. Zunger, "Self-interaction correction to density-functional approximations for many-electron systems", Physical Review B **23**, 5048 (1981).

[270] V. V. Karasiev, T. Sjostrom, J. Dufty, and S. Trickey, "Accurate homogeneous electron gas exchange-correlation free energy for local spin-density calculations", Physical Review Letters **112**, 076403 (2014).

[271] M. F. Kasim and S. M. Vinko, "Learning the exchange-correlation functional from nature with fully differentiable density functional theory", Physical Review Letters **127**, 126403 (2021).

[272] F. Lambert, J. Clérouin, S. Mazevet, and D. Gilles, "Properties of hot dense plasmas by orbital-free molecular dynamics", Contributions to Plasma Physics **47**, 272–280 (2007).

[273] T. G. White, S. Richardson, B. J. B. Crowley, L. K. Pattison, J. W. O. Harris, and G. Gregori, "Orbital-free density-functional theory simulations of the dynamic structure factor of warm dense aluminum", Physical Review Letters **111**, 175002 (2013).

[274] L. Collins, I. Kwon, J. Kress, N. Troullier, and D. Lynch, "Quantum molecular dynamics simulations of hot, dense hydrogen", Physical Review E **52**, 6202 (1995).

[275] H. R. Rüter and R. Redmer, "*Ab initio* simulations for the ion-ion structure factor of warm dense aluminum", Physical Review Letters **112**, 145007 (2014).

[276] M. French, G. Röpke, M. Schörner, M. Bethkenhagen, M. P. Desjarlais, and R. Redmer, "Electronic transport coefficients from density functional theory across the plasma plane", Physical Review E **105**, 065204 (2022).

[277] R. M. Wentzcovitch, J. L. Martins, and P. B. Allen, "Energy versus free-energy conservation in first-principles molecular dynamics", Physical Review B **45**, 11372(R) (1992).

[278] R. J. Magyar, L. Shulenburger, and A. D. Baczewski, *Stopping of deuterium in warm dense deuterium from Ehrenfest time-dependent density functional theory*, 2016.

[279] K. Ramakrishna and J. Vorberger, "*Ab initio* dielectric response function of diamond and other relevant high pressure phases of carbon", Journal of Physics: Condensed Matter **32**, 095401 (2020).

[280] K. Ramakrishna, A. Cangi, T. Dornheim, A. Baczewski, and J. Vorberger, "First-principles modeling of plasmons in aluminum under ambient and extreme conditions", Physical Review B **103**, 125118 (2021).

[281] Z. A. Moldabekov, M. Pavanello, M. P. Böhme, J. Vorberger, and T. Dornheim, "Linear-response time-dependent density functional theory approach to warm dense matter with adiabatic exchange-correlation kernels", Physical Review Research **5**, 023089 (2023).

[282] F. R. Graziani, J. D. Bauer, and M. S. Murillo, "Kinetic theory molecular dynamics and hot dense matter: Theoretical foundations", Physical Review E **90**, 033104 (2014).

[283] D. Michta, M. Surh, and F. Graziani, "Kinetic theory molecular dynamics: Numerical considerations", High Energy Density Physics **9**, 696–701 (2013).

[284] D. B. Boercker and J. W. Dufty, "Degenerate quantum gases in the binary collision approximation", Annals of Physics **119**, 43–70 (1979).

[285] M. Bonitz, *Quantum Kinetic Theory*, Second edition (Springer, Cham, 2016).

[286] S. Frydrych, J. Vorberger, N. J. Hartley, A. K. Schuster, K. Ramakrishna, A. M. Saunders, T. van Driel, R. W. Falcone, L. B. Fletcher, E. Galtier, et al., "Demonstration of x-ray Thomson scattering as diagnostics for miscibility in warm dense matter", Nature Communications **11**, 2620 (2020).

[287] Z. Moldabekov, T. Dornheim, G. Gregori, F. Graziani, M. Bonitz, and A. Cangi, "Towards a quantum fluid theory of correlated many-fermion systems from first principles", SciPost Physics **12**, 062 (2022).

[288] F. Haas, *Quantum Plasmas: An Hydrodynamic Approach*, Atomic, optical, and plasma physics 65 (Springer Science & Business Media, New York, NY, 2011).

[289] H. Feldmeier and J. Schnack, "Molecular dynamics for fermions", Reviews of Modern Physics **72**, 655 (2000).

[290] P. E. Grabowski, "A review of wave packet molecular dynamics", in Frontiers and challenges in warm dense matter, edited by F. Graziani, M. P. Desjarlais, R. Redmer, and S. B. Trickey (2014), pp. 265–282.

[291] E. J. Heller, "Time-dependent approach to semiclassical dynamics", The Journal of Chemical Physics **62**, 1544–1555 (1975).

[292] N. Corbin and K. Singer, "Semiclassical molecular dynamics of wave packets", Molecular Physics **46**, 671–677 (1982).

[293] C. Lasser and C. Su, "Various variational approximations of quantum dynamics", Journal of Mathematical Physics **63**, 072107 (2022).

[294] J. Broeckhove, L. Lathouwers, and P. Van Leuven, "Time-dependent variational principles and conservation laws in wavepacket dynamics", Journal of Physics A: Mathematical and General **22**, 4395 (1989).

[295] M. Knaup, P. Reinhard, C. Toepffer, and G. Zwicknagel, "Wave packet molecular dynamics simulations of warm dense hydrogen", Journal of Physics A: Mathematical and General **36**, 6165 (2003).

[296] B. Jakob, P.-G. Reinhard, C. Toepffer, and G. Zwicknagel, "Wave packet simulation of dense hydrogen", Physical Review E **76**, 036406 (2007).

[297] B. Jakob, P.-G. Reinhard, C. Toepffer, and G. Zwicknagel, "Wave packet simulations for the insulator–metal transition in dense hydrogen", Journal of Physics A: Mathematical and Theoretical **42**, 214055 (2009).

[298] D. Klakow, C. Toepffer, and P.-G. Reinhard, "Hydrogen under extreme conditions", Physics Letters A **192**, 55–59 (1994).

[299] D. Klakow, C. Toepffer, and P.-G. Reinhard, "Semiclassical molecular dynamics for strongly coupled Coulomb systems", The Journal of Chemical Physics **101**, 10766–10774 (1994).

[300] M. S. Murillo and E. Timmermans, "Self-similar wavepackets for describing warm dense matter", Contributions to Plasma Physics **43**, 333–337 (2003).

[301] A. Lenglet and G. Maynard, "Wave packet molecular dynamics to study atom electrons in strong fields", Nuclear Instruments and Methods in Physics Research Section A **577**, 343–348 (2007).

[302] I. V. Morozov and I. A. Valuev, "Improvement of wave packet molecular dynamics using packet splitting", Contributions to Plasma Physics **52**, 140–144 (2012).

[303] P. E. Grabowski, A. Markmann, I. V. Morozov, I. A. Valuev, C. A. Fichtl, D. F. Richards, V. S. Batista, F. R. Graziani, and M. S. Murillo, "Wave packet spreading and localization in electron-nuclear scattering", Physical Review E **87**, 063104 (2013).

[304] W. A. Angermeier and T. G. White, "An investigation into the approximations used in wave packet molecular dynamics for the study of warm dense matter", Plasma **4**, 294–308 (2021).

[305] W. Ebeling and B. Militzer, "Quantum molecular dynamics of partially ionized plasmas", Physics Letters A **226**, 298–304 (1997).

[306] W. Ebeling, A. Filinov, M. Bonitz, V. Filinov, and T. Pohl, "The method of effective potentials in the quantum-statistical theory of plasmas", Journal of Physics A: Mathematical and General **39**, 4309 (2006).

[307] J. Ono and K. Ando, "Semiquantal molecular dynamics simulations of hydrogen-bond dynamics in liquid water using multi-dimensional Gaussian wave packets", The Journal of Chemical Physics **137**, 174503 (2012).

[308] M. Knaup, P.-G. Reinhard, and C. Toepffer, "Wave packet molecular dynamics simulations of hydrogen near the transition to a metallic fluid", Contributions to Plasma Physics **39**, 57–60 (1999).

[309] V. Buch, "Exploration of multidimensional variational Gaussian wave packets as a simulation tool", The Journal of Chemical Physics **117**, 4738–4750 (2002).

[310] P. A. Frantsuzov and V. A. Mandelshtam, "Quantum statistical mechanics with Gaussians: Equilibrium properties of van der Waals clusters", The Journal of Chemical Physics **121**, 9247–9256 (2004).

[311] Y. Shigeta, T. Inui, T. Baba, K. Okuno, H. Kuwabara, R. Kishi, and M. Nakano, "Quantal cumulant mechanics and dynamics for multidimensional quantum many-body clusters", International Journal of Quantum Chemistry **113**, 348–355 (2013).

[312] J. C. Lagarias, J. A. Reeds, M. H. Wright, and P. E. Wright, "Convergence properties of the Nelder–Mead simplex method in low dimensions", SIAM Journal on Optimization **9**, 112–147 (1998).

[313] J. T. Su and W. A. Goddard III, "Excited electron dynamics modeling of warm dense matter", Physical Review Letters **99**, 185003 (2007).

[314] J. T. Su and W. A. Goddard III, "The dynamics of highly excited electronic systems: Applications of the electron force field", The Journal of Chemical Physics **131**, 244501 (2009).

[315] A. Jaramillo-Botero, J. Su, A. Qi, and W. A. Goddard III, "Large-scale, long-term nonadiabatic electron molecular dynamics for describing material properties and phenomena in extreme environments", Journal of Computational Chemistry **32**, 497–512 (2011).

[316] H. Kim, J. T. Su, and W. A. Goddard, "High-temperature high-pressure phases of lithium from electron force field (eFF) quantum electron dynamics simulations", Proceedings of the National Academy of Sciences **108**, 15101–15105 (2011).

[317] H. Xiao, A. Jaramillo-Botero, P. L. Theofanis, and W. A. Goddard III, "Non-adiabatic dynamics modeling framework for materials in extreme conditions", Mechanics of Materials **90**, 243–252 (2015).

[318] Y. Liu, X. Liu, S. Zhang, H. Liu, C. Mo, Z. Fu, and J. Dai, "Molecular dynamics investigation of the stopping power of warm dense hydrogen for electrons", Physical Review E **103**, 063215 (2021).

[319] M. Knaup, P.-G. Reinhard, and C. Toepffer, "Wave packet molecular dynamics simulations of deuterium in the region of laser shock-wave experiments", Contributions to Plasma Physics **41**, 159–162 (2001).

[320] I. V. Morozov and I. A. Valuev, "Localization constraints in Gaussian wave packet molecular dynamics of nonideal plasmas", Journal of Physics A: Mathematical and Theoretical **42**, 214044 (2009).

[321] Y. S. Lavrinenko, I. V. Morozov, and I. A. Valuev, "Reflecting boundary conditions for classical and quantum molecular dynamics simulations of nonideal plasmas", Contributions to Plasma Physics **56**, 448–458 (2016).

[322] E. Gabriel, G. E. Fagg, G. Bosilca, T. Angskun, J. J. Dongarra, J. M. Squyres, V. Sahay, P. Kambadur, B. Barrett, A. Lumsdaine, R. H. Castain, D. J. Daniel, R. L. Graham, and T. S. Woodall, "Open MPI: Goals, concept, and design of a next generation MPI implementation", in Proceedings, 11th European PVM/MPI users' group meeting (Sept. 2004), pp. 97–104.

[323] W. C. Swope, H. C. Andersen, P. H. Berens, and K. R. Wilson, "A computer simulation method for the calculation of equilibrium constants for the formation of physical clusters

of molecules: Application to small water clusters", The Journal of Chemical Physics **76**, 637–649 (1982).

[324] M. D. Feit, J. A. Fleck Jr, and A. Steiger, "Solution of the Schrödinger equation by a spectral method", Journal of Computational Physics **47**, 412–433 (1982).

[325] A. Markmann, F. Graziani, and V. S. Batista, "Kepler predictor–corrector algorithm: Scattering dynamics with one-over-r singular potentials", Journal of Chemical Theory and Computation **8**, 24–35 (2012).

[326] S. M. Greene and V. S. Batista, "Tensor-train split-operator fourier transform (TT-SOFT) method: Multidimensional nonadiabatic quantum dynamics", Journal of Chemical Theory and Computation **13**, 4034–4042 (2017).

[327] P. Vashishta, R. K. Kalia, A. Nakano, and J. P. Rino, "Interaction potentials for alumina and molecular dynamics simulations of amorphous and liquid alumina", Journal of Applied Physics **103**, 083504 (2008).

[328] B. J. B. Crowley and G. Gregori, "X-ray scattering by many-particle systems", New Journal of Physics **15**, 015014 (2013).

[329] B. J. B. Crowley and G. Gregori, "Quantum theory of Thomson scattering", High Energy Density Physics **13**, 55–83 (2014).

[330] J. J. Sakurai, *Advanced Quantum Mechanics* (Addison Wesley Publ. Co., Reading, MA, 1967).

[331] J. J. Sakurai and J. Napolitano, *Modern Quantum Mechanics*, eng, Second edition. (Cambridge University Press, Cambridge, 2017).

[332] T. Döppner, O. L. Landen, H. J. Lee, P. Neumayer, S. P. Regan, and S. H. Glenzer, "Temperature measurement through detailed balance in x-ray Thomson scattering", High Energy Density Physics **5**, 182–186 (2009).

[333] A. Descamps, B. K. Ofori-Okai, K. Appel, V. Cerantola, A. Comley, J. H. Eggert, L. B. Fletcher, D. O. Gericke, S. Göde, O. Humphries, et al., "An approach for the measurement of the bulk temperature of single crystal diamond using an x-ray free electron laser", Scientific Reports **10**, 14564 (2020).

[334] T. Dornheim, M. Böhme, D. Kraus, T. Döppner, T. R. Preston, Z. A. Moldabekov, and J. Vorberger, "Accurate temperature diagnostics for matter under extreme conditions", Nature Communications **13**, 7911 (2022).

[335] T. Dornheim, M. P. Böhme, D. A. Chapman, D. Kraus, T. R. Preston, Z. A. Moldabekov, N. Schlünzen, A. Cangi, T. Döppner, and J. Vorberger, "Imaginary-time correlation function thermometry: A new, high-accuracy and model-free temperature analysis technique for x-ray Thomson scattering data", Physics of Plasmas **30**, 042707 (2023).

[336] H. J. Lee, P. Neumayer, J. Castor, T. Döppner, R. W. Falcone, C. Fortmann, B. A. Hammel, A. L. Kritcher, O. L. Landen, R. W. Lee, D. D. Meyerhofer, D. H. Munro, R. Redmer, S. P. Regan, S. Weber, and S. H. Glenzer, "X-ray Thomson-scattering measurements of density and temperature in shock-compressed beryllium", Physical Review Letters **102**, 115001 (2009).

[337] T. Ma, T. Döppner, R. W. Falcone, L. Fletcher, C. Fortmann, D. O. Gericke, O. L. Landen, H. J. Lee, A. Pak, J. Vorberger, et al., "X-ray scattering measurements of

strong ion-ion correlations in shock-compressed aluminum", Physical Review Letters **110**, 065001 (2013).

[338] M. F. Kasim, T. P. Galligan, J. Topp-Mugglestone, G. Gregori, and S. M. Vinko, "Inverse problem instabilities in large-scale modeling of matter in extreme conditions", Physics of Plasmas **26**, 112706 (2019).

[339] T. Gawne, T. Campbell, A. Forte, P. Hollebon, G. Perez-Callejo, O. S. Humphries, O. Karnbach, M. F. Kasim, T. R. Preston, H. J. Lee, A. Miscampbell, Q. Y. van den Berg, B. Nagler, S. Ren, R. B. Royle, J. S. Wark, and S. M. Vinko, "Investigating mechanisms of state localization in highly ionized dense plasmas", Physical Review E **108**, 035210 (2023).

[340] G. Gregori, A. Ravasio, A. Höll, S. H. Glenzer, and S. J. Rose, "Derivation of the static structure factor in strongly coupled non-equilibrium plasmas for x-ray scattering studies", High Energy Density Physics **3**, 99–108 (2007).

[341] T. Dornheim, P. Tolias, Z. A. Moldabekov, A. Cangi, and J. Vorberger, "Effective electronic forces and potentials from *ab initio* path integral Monte Carlo simulations", The Journal of Chemical Physics **156**, 244113 (2022).

[342] T. Dornheim, Z. A. Moldabekov, K. Ramakrishna, P. Tolias, A. D. Baczewski, D. Kraus, T. R. Preston, D. A. Chapman, M. P. Böhme, T. Döppner, F. Graziani, M. Bonitz, A. Cangi, and J. Vorberger, "Electronic density response of warm dense matter", Physics of Plasmas **30**, 032705 (2023).

[343] T. Dornheim, Z. A. Moldabekov, P. Tolias, M. Böhme, and J. Vorberger, "Physical insights from imaginary-time density–density correlation functions", Matter and Radiation at Extremes **8**, 056601 (2023).

[344] A. V. Filinov, J. Ara, and I. M. Tkachenko, "Dynamical response in strongly coupled uniform electron liquids: Observation of plasmon-roton coexistence using nine sum rules, Shannon information entropy, and path-integral Monte Carlo simulations", Physical Review B **107**, 195143 (2023).

[345] K.-U. Plagemann, H. R. Rüter, T. Bornath, M. Shihab, M. P. Desjarlais, C. Fortmann, S. H. Glenzer, and R. Redmer, "*Ab initio* calculation of the ion feature in x-ray Thomson scattering", Physical Review E **92**, 013103 (2015).

[346] G. Röpke, A. Selchow, A. Wierling, and H. Reinholz, "Lindhard dielectric function in the relaxation-time approximation and generalized linear response theory", Physics Letters A **260**, 365–369 (1999).

[347] A. Höll, T. Bornath, L. Cao, T. Döppner, S. Düsterer, E. Förster, C. Fortmann, S. H. Glenzer, G. Gregori, T. Laarmann, et al., "Thomson scattering from near-solid density plasmas using soft x-ray free electron lasers", High Energy Density Physics **3**, 120–130 (2007).

[348] R. Thiele, T. Bornath, C. Fortmann, A. Höll, R. Redmer, H. Reinholz, G. Röpke, A. Wierling, S. H. Glenzer, and G. Gregori, "Plasmon resonance in warm dense matter", Physical Review E **78**, 026411 (2008).

[349] K.-U. Plagemann, P. Sperling, R. Thiele, M. P. Desjarlais, C. Fortmann, T. Döppner, H. J. Lee, S. H. Glenzer, and R. Redmer, "Dynamic structure factor in warm dense beryllium", New Journal of Physics **14**, 055020 (2012).

[350] J. Vorberger and D. O. Gericke, "*Ab initio* approach to model x-ray diffraction in warm dense matter", Physical Review E **91**, 033112 (2015).

[351] S. Groth, T. Dornheim, and J. Vorberger, "*Ab Initio* path integral Monte Carlo approach to the static and dynamic density response of the uniform electron gas", Physical Review B **99**, 235122 (2019).

[352] P. Hamann, T. Dornheim, J. Vorberger, Z. A. Moldabekov, and M. Bonitz, "Dynamic properties of the warm dense electron gas based on *ab initio* path integral Monte Carlo simulations", Physical Review B **102**, 125150 (2020).

[353] G. Gregori, S. H. Glenzer, W. Rozmus, R. W. Lee, and O. L. Landen, "Theoretical model of x-ray scattering as a dense matter probe", Physical Review E **67**, 026412 (2003).

[354] M. Schumacher, F. Smend, and I. Borchert, "Incoherent scattering of gamma rays by inner-shell electrons", Journal of Physics B: Atomic and Molecular Physics **8**, 1428 (1975).

[355] B. A. Mattern and G. T. Seidler, "Theoretical treatments of the bound-free contribution and experimental best practice in x-ray Thomson scattering from warm dense matter", Physics of Plasmas **20**, 022706 (2013).

[356] J. Ortner, F. Schautz, and W. Ebeling, "Quasiclassical molecular-dynamics simulations of the electron gas: Dynamic properties", Physical Review E **56**, 4665 (1997).

[357] W. Ebeling and J. Ortner, "Quasiclassical theory and simulations of strongly coupled plasmas", Physica Scripta **1998**, 93 (1998).

[358] G. Zwicknagel and T. Pschiwul, "WPMD simulations of a two-component plasma", Journal of Physics A: Mathematical and General **39**, 4359 (2006).

[359] T. K. et al., "CP2K: An electronic structure and molecular dynamics software package - Quickstep: Efficient and accurate electronic structure calculations", The Journal of Chemical Physics **152**, 194103 (2020).

[360] J. VandeVondele and J. Hutter, "Gaussian basis sets for accurate calculations on molecular systems in gas and condensed phases", Journal of Chemical Physics **127**, 114105 (2007).

[361] S. Goedecker, M. Teter, and J. Hutter, "Separable dual-space Gaussian pseudopotentials", Physical Review B **54**, 1703 (1996).

[362] J. F. Wax and T. Bryk, "An effective fitting scheme for the dynamic structure of pure liquids", Journal of Physics: Condensed Matter **25**, 325104 (2013).

[363] G. Giuliani and G. Vignale, *Quantum Theory of the Electron Liquid* (Cambridge University Press, Cambridge, UK, 2008).

[364] D. Pines and P. Nozières, *Theory of Quantum Liquids: Normal Fermi liquids* (CRC Press, Boca Raton, FL, 2018).

[365] H.-P. Breuer, B. Kappler, and F. Petruccione, "Stochastic wave-function approach to the calculation of multitime correlation functions of open quantum systems", Physical Review A **56**, 2334 (1997).

[366] D. B. Melrose, *Quantum Plasmadynamics: Unmagnetized Plasmas*, Vol. 735 (Springer, Berlin, 2008).

[367] D. B. Melrose and A. Mushtaq, "Dispersion in a thermal plasma including arbitrary degeneracy and quantum recoil", Physical Review E **82**, 056402 (2010).

[368] A. Q. R. Baron, *Introduction to high-resolution inelastic x-ray scattering*, 2020.

[369] G. Gregori and D. O. Gericke, "Low frequency structural dynamics of warm dense matter", Physics of Plasmas **16**, 056306 (2009).

[370] S. W. Lovesey, *Theory of neutron scattering from condensed matter*, Oxford science publications (Clarendon Press, Oxford, 1984).

[371] V. V. Belyi, "Thomson scattering in inhomogeneous plasmas: The role of the fluctuation-dissipation theorem", Scientific Reports **8**, 7946 (2018).

[372] V. V. Belyi, "Theory of Thomson scattering in inhomogeneous plasmas", Physical Review E **97**, 053204 (2018).

[373] T.-N. Beuermann, R. Redmer, and T. Bornath, "Thomson scattering from dense inhomogeneous plasmas", Physical Review E **99**, 053205 (2019).

[374] A. Sakko, A. Rubio, M. Hakala, and K. Hämäläinen, "Time-dependent density functional approach for the calculation of inelastic x-ray scattering spectra of molecules", The Journal of Chemical Physics **133**, 174111 (2010).

[375] P. Hamann, L. Kordts, A. Filinov, M. Bonitz, T. Dornheim, and J. Vorberger, "Prediction of a roton-type feature in warm dense hydrogen", Physical Review Research **5**, 033039 (2023).

[376] A. L. Kritcher, P. Neumayer, J. Castor, T. Döppner, R. W. Falcone, O. L. Landen, H. J. Lee, R. W. Lee, E. C. Morse, A. Ng, et al., "Ultrafast x-ray Thomson scattering of shock-compressed matter", Science **322**, 69–71 (2008).

[377] K. Falk, E. J. Gamboa, G. Kagan, D. S. Montgomery, B. Srinivasan, P. Tzeferacos, and J. F. Benage, "Equation of state measurements of warm dense carbon using laser-driven shock and release technique", Physical Review Letters **112**, 155003 (2014).

[378] L. B. Fletcher, H. J. Lee, T. Döppner, E. Galtier, B. Nagler, P. Heimann, C. Fortmann, S. LePape, T. Ma, M. Millot, et al., "Ultrabright X-ray laser scattering for dynamic warm dense matter physics", Nature Photonics **9**, 274–279 (2015).

[379] C. R. Weber, D. S. Clark, A. W. Cook, L. E. Busby, and H. F. Robey, "Inhibition of turbulence in inertial-confinement-fusion hot spots by viscous dissipation", Physical Review E **89**, 053106 (2014).

[380] E. L. Vold, R. M. Rauenzahn, C. Aldrich, K. Molvig, A. N. Simakov, and B. M. Haines, "Plasma transport in an Eulerian AMR code", Physics of Plasmas **24**, 042702 (2017).

[381] S. P. Lyon and J. D. Johnson, "SESAME: The Los Alamos National Laboratory equation of state database", in *Technical report No. LA-UR-92-3407* (Los Alamos National Laboratory, Los Alamos, 1995).

[382] U. von Toussaint, "Bayesian inference in physics", Reviews of Modern Physics **83**, 943 (2011).

[383] R. Schmidt, B. J. B. Crowley, J. Mithen, and G. Gregori, "Quantum hydrodynamics of strongly coupled electron fluids", Physical Review E **85**, 046408 (2012).

[384] S. I. Anisimov, B. L. Kapeliovich, T. L. Perelman, et al., "Electron emission from metal surfaces exposed to ultrashort laser pulses", Journal of Experimental and Theoretical Physics **66**, 375–377 (1974).

[385] D. S. Ivanov and L. V. Zhigilei, "Combined atomistic-continuum modeling of short-pulse laser melting and disintegration of metal films", Physical Review B **68**, 064114 (2003).

[386] L. Jiang and H.-L. Tsai, "A plasma model combined with an improved two-temperature equation for ultrafast laser ablation of dielectrics", Journal of Applied Physics **104**, 093101 (2008).

[387] T. Q. Qiu and C. L. Tien, "Heat transfer mechanisms during short-pulse laser heating of metals", Journal of Heat Transfer **115**, 835–841 (1993).

[388] A. F. A. Bott and G. Gregori, "Thomson scattering cross section in a magnetized, high-density plasma", Physical Review E **99**, 063204 (2019).

[389] V. E. Zakharov, "Collapse of Langmuir waves", Soviet Physics JETP **35**, 908–914 (1972).

[390] T. Mondal and G. Gregori, "Quantum effects on dynamic structure factors in dense magnetized plasmas", Physical Review Research **6**, 013089 (2024).

[391] R. Schmidt, "On the theory of Thomson scattering in the warm dense matter regime", PhD thesis (Universität Rostock, Rostock, Sept. 2012).

[392] N. R. Arista and W. Brandt, "Dielectric response of quantum plasmas in thermal equilibrium", Physical Review A **29**, 1471 (1984).

[393] P. Neumayer, C. Fortmann, T. Döppner, P. Davis, R. W. Falcone, A. L. Kritcher, O. L. Landen, H. J. Lee, R. W. Lee, C. Niemann, et al., "Plasmons in strongly coupled shock-compressed matter", Physical Review Letters **105**, 075003 (2010).

[394] R. Nifosi, S. Conti, and M. P. Tosi, "Dynamic exchange-correlation potentials for the electron gas in dimensionality D=3 and D=2", Physical Review B **58**, 12758 (1998).

[395] S. Conti and G. Vignale, "Elasticity of an electron liquid", Physical Review B **60**, 7966 (1999).

[396] R. Cauble and W. Rozmus, "Transport properties of the two-component strongly coupled plasma", Journal of Plasma Physics **37**, 405–421 (1987).

[397] S. A. Khan and M. Bonitz, "Quantum hydrodynamics", in *Complex plasmas: scientific challenges and technological opportunities*, edited by M. Bonitz, J. Lopez, K. Becker, and H. Thomsen (Springer International Publishing, Cham, 2014), pp. 103–152.

[398] J.-R. Zhou and D. K. Ferry, "2-D simulation of quantum effects in small semiconductor devices using quantum hydrodynamic equations", VLSI Design **3**, 159–177 (1995).

[399] P. Mabey, "A study on dense plasmas using molecular dynamics and X-ray scattering techniques", PhD thesis (University of Oxford, 2016).

[400] T. G. White, H. Poole, E. E. McBride, M. Oliver, A. Descamps, L. B. Fletcher, W. A. Angermeier, C. H. Allen, K. Appel, F. P. Condamine, et al., "Speed of sound in methane under conditions of planetary interiors", Physical Review Research **6**, L022029 (2024).

[401] J. Clérouin, N. Desbiens, V. Dubois, and P. Arnault, "Bayesian inference of x-ray diffraction spectra from warm dense matter with the one-component-plasma model", Physical Review E **94**, 061202(R) (2016).

[402] H. Poole, D. Cao, R. Epstein, I. Golovkin, T. Walton, S. X. Hu, M. Kasim, S. M. Vinko, J. R. Rygg, V. N. Goncharov, et al., "A case study of using x-ray Thomson scattering to diagnose the in-flight plasma conditions of DT cryogenic implosions", Physics of Plasmas **29**, 072703 (2022).

[403] H. Poole, M. K. Ginnane, M. Millot, H. M. Bellenbaum, G. W. Collins, S. X. Hu, D. Polsin, R. Saha, J. Topp-Mugglestone, T. G. White, et al., "Multimessenger measurements of the static structure of shock-compressed liquid silicon at 100 GPa", Physical Review Research **6**, 023144 (2024).

[404] K. M. M. Prabhu, *Window Functions and their Applications in Signal Processing* (CRC press, Boca Raton, FL, 2014).

[405] L. Malagò and G. Pistone, "Information geometry of the Gaussian distribution in view of stochastic optimization", in Proceedings of the 2015 ACM conference on foundations of genetic algorithms xiii (2015), pp. 150–162.

[406] D. Foreman-Mackey, D. W. Hogg, D. Lang, and J. Goodman, "emcee: The MCMC hammer", Publications of the Astronomical Society of the Pacific **125**, 306 (2013).

[407] J. P. Palastro, E. A. Williams, D. E. Hinkel, L. Divol, and D. J. Strozzi, "Kinetic dispersion of Langmuir waves. I. The Langmuir decay instability", Physics of Plasmas **16**, 092304 (2009).

[408] D. Foreman-Mackey, "corner.py: Scatterplot matrices in Python", The Journal of Open Source Software **1**, 24 (2016).

[409] T. W. Hentschel, A. Kononov, A. D. Baczewski, and S. B. Hansen, "Statistical inference of collision frequencies from x-ray Thomson scattering spectra", **32**, 013906 (2024).

[410] K. Wille, *The Physics of Particle Accelerators: An Introduction* (Clarendon Press, Oxford, 2000).

[411] J. Rosenzweig, C. Pellegrini, L. Serafini, C. Ternieden, and G. Travish, "Space-charge oscillations in a self-modulated electron beam in multi-undulator free-electron lasers", Nuclear Instruments and Methods in Physics Research Section A **393**, 376–379 (1997).

[412] D. Umstadter, "Relativistic laser–plasma interactions", Journal of Physics D **36**, R151 (2003).

[413] B. N. Breizman, P. Aleynikov, E. M. Hollmann, and M. Lehnen, "Physics of runaway electrons in tokamaks", Nuclear Fusion **59**, 083001 (2019).

[414] R. Blandford, D. Meier, and A. Readhead, "Relativistic jets from active galactic nuclei", Annual Review of Astronomy and Astrophysics **57**, 467–509 (2019).

[415] P. Blasi, "The origin of galactic cosmic rays", The Astronomy and Astrophysics Review **21**, 70 (2013).

[416] S. A. Bass, M. Belkacem, M. Bleicher, M. Brandstetter, L. Bravina, C. Ernst, L. Gerland, M. Hofmann, S. Hofmann, J. Konopka, et al., "Microscopic models for ultrarelativistic heavy ion collisions", Progress in Particle and Nuclear Physics **41**, 255–369 (1998).

[417] H. Sorge, H. Stöcker, and W. Greiner, "Poincaré invariant Hamiltonian dynamics: Modelling multi-hadronic interactions in a phase space approach", Annals of Physics **192**, 266–306 (1989).

[418] E. Lehmann, R. Puri, A. Faessler, T. Maruyama, G. Li, N. Ohtsuka, S. Huang, D. Khoa, and M. Matin, "Relativistic versus nonrelativistic quantum molecular dynamics", Progress in Particle and Nuclear Physics **30**, 219–228 (1993).

[419] M. Bleicher, E. Zabrodin, C. Spieles, S. A. Bass, C. Ernst, S. Soff, L. Bravina, M. Belkacem, H. Weber, H. Stöcker, et al., "Relativistic hadron-hadron collisions in the ultra-relativistic quantum molecular dynamics model", Journal of Physics G **25**, 1859 (1999).

[420] J. Weil, V. Steinberg, J. Staudenmaier, L. Pang, D. Oliinychenko, J. Mohs, M. Kretz, T. Kehrenberg, A. Goldschmidt, B. Bäuchle, et al., "Particle production and equilibrium properties within a new hadron transport approach for heavy-ion collisions", Physical Review C **94**, 054905 (2016).

[421] T. Takizuka and H. Abe, "A binary collision model for plasma simulation with a particle code", Journal of Computational physics **25**, 205–219 (1977).

[422] F. Peano, M. Marti, L. O. Silva, and G. Coppa, "Statistical kinetic treatment of relativistic binary collisions", Physical Review E **79**, 025701(R) (2009).

[423] E. P. Alves, W. B. Mori, and F. Fiuza, "Numerical heating in particle-in-cell simulations with Monte Carlo binary collisions", Physical Review E **103**, 013306 (2021).

[424] M. Fiore, F. Fiúza, M. Marti, R. A. Fonseca, and L. O. Silva, "Relativistic effects on the collisionless–collisional transition of the filamentation instability in fast ignition", Journal of Plasma Physics **76**, 813–832 (2010).

[425] T. S. Komatsu, S. Matsumoto, T. Shimada, and N. Ito, "A glimpse of fluid turbulence from the molecular scale", International Journal of Modern Physics C **25**, 1450034 (2014).

[426] J. L. Barber, K. Kadau, T. C. Germann, P. Lomdahl, B. Holian, and B. Alder, "Atomistic simulation of the Rayleigh-Taylor instability", in Journal of Physics: Conference series, Vol. 46, 1 (IOP Publishing, 2006), p. 58.

[427] P. Tzeferacos, A. Rigby, A. F. A. Bott, A. R. Bell, R. Bingham, A. Casner, F. Cattaneo, E. M. Churazov, J. Emig, F. Fiuza, et al., "Laboratory evidence of dynamo amplification of magnetic fields in a turbulent plasma", Nature Communications **9**, 591 (2018).

[428] F. Jüttner, "Das Maxwellsche gesetz der Geschwindigkeitsverteilung in der Relativtheorie", Annalen der Physik **339**, 856–882 (1911).

[429] L. D. Landau and E. M. Lifshitz, *The Classical Theory of Fields*, 3rd rev. English ed., Course of Theoretical Physics (Pergamon Press, Oxford, 1971).

[430] A. Aliano, L. Rondoni, and G. Morriss, "Maxwell-Jüttner distributions in relativistic molecular dynamics", The European Physical Journal B **50**, 361–365 (2006).

[431] M. Ghodrat and A. Montakhab, "Molecular dynamics simulation of a relativistic gas: Thermostatistical properties", Computer Physics Communications **182**, 1909–1913 (2011).

[432] N. Kubli and H. J. Herrmann, "Thermostat for a relativistic gas", Physica A: Statistical Mechanics and its Applications **561**, 125261 (2021).

[433] W. N. Herman and P. Havas, "Approximately relativistic Lagrangians for classical interacting point particles. III", Physical Review D **17**, 1985 (1978).

[434] T. K. Nakamura, "Relativistic equilibrium distribution by relative entropy maximization", Europhysics Letters **88**, 40009 (2009).

[435] P. Helander and D. J. Sigmar, *Collisional Transport in Magnetized Plasmas*, Vol. 4 (Cambridge university press, Cambridge, 2005).

[436] G. M. Kremer, "Diffusion of relativistic gas mixtures in gravitational fields", Physica A **393**, 76–85 (2014).

[437] P. Kostädt and M. Liu, "Causality and stability of the relativistic diffusion equation", Physical Review D **62**, 023003 (2000).

[438] J. Masoliver and G. H. Weiss, "Finite-velocity diffusion", European Journal of Physics **17**, 190 (1996).

[439] T. Koide, "Microscopic derivation of causal diffusion equation using the projection operator method", Physical Review E **72**, 026135 (2005).

[440] T. Koide, "Microscopic formula for transport coefficients of causal hydrodynamics", Physical Review E **75**, 060103(R) (2007).

[441] W. Florkowski, M. P. Heller, and M. Spaliński, "New theories of relativistic hydrodynamics in the LHC era", Reports on Progress in Physics **81**, 046001 (2018).

[442] J. Dunkel and P. Hänggi, "Relativistic brownian motion", Physics Reports **471**, 1–73 (2009).

[443] R. Lee and M. Lampe, "Electromagnetic instabilities, filamentation, and focusing of relativistic electron beams", Physical Review Letters **31**, 1390 (1973).

[444] M. Touati, R. Codur, F. Tsung, V. K. Decyk, W. B. Mori, and L. O. Silva, "Kinetic theory of particle-in-cell simulation plasma and the ensemble averaging technique", Plasma Physics and Controlled Fusion **64**, 115014 (2022).

[445] M. D. Acciarri, C. Moore, L. P. Beving, and S. D. Baalrud, "When should PIC simulations be applied to atmospheric pressure plasmas? Impact of correlation heating", Plasma Sources Science and Technology **33**, 035009 (2024).

[446] E. Wiechert, "Elektrodynamische elementargesetze", Annalen der Physik **309**, 667–689 (1901).

[447] R. Hakim, "Remarks on relativistic statistical mechanics. I", Journal of Mathematical Physics **8**, 1315–1344 (1967).

[448] A. F. Kracklauer, "A theory of the electromagnetic two-body interaction", Journal of Mathematical Physics **19**, 808–811 (1978).

[449] W. N. Herman, "Formulation of Noether's theorem for Fokker-type variational principles", Journal of Mathematical Physics **26**, 2769–2776 (1985).

[450] A. D. Fokker, "Ein invarianter Variationssatz für die Bewegung mehrerer elektrischer Massenteilchen", Zeitschrift für Physik **58**, 386–393 (1929).

[451] J. L. Anderson and S. Schiminovich, "Relations between field-plus source and Fokker-type action principles", Journal of Mathematical Physics **8**, 255–264 (1967).

[452] M. Tanaka and M. Murakami, "Relativistic and electromagnetic molecular dynamics simulations for a carbon–gold nanotube accelerator", Computer Physics Communications **241**, 56–63 (2019).

[453] C. G. Darwin, "LI. The dynamical motions of charged particles", The London, Edinburgh, and Dublin Philosophical Magazine and Journal of Science **39**, 537–551 (1920).

[454] G. Breit, "The effect of retardation on the interaction of two electrons", Physical Review **34**, 553 (1929).

[455] B. Trubnikov and V. Kosachev, "Relativistic generalization of the Darwin Lagrangian", Zh. Eksp. Teor. Fiz **66**, 1311–1315 (1974).

[456] H. Essén, "The exact Darwin Lagrangian", Europhysics Letters **79**, 60002 (2007).

[457] M. Planck, "On the theory of the energy distribution law of the normal spectrum", Verh. Deut. Phys. Ges **2**, 237–245 (1900).

[458] E. V. Stenson, J. Horn-Stanja, M. R. Stoneking, and T. S. Pedersen, "Debye length and plasma skin depth: Two length scales of interest in the creation and diagnosis of laboratory pair plasmas", Journal of Plasma Physics **83**, 595830106 (2017).

[459] D. Wolff and W. Rudd, "Tabulated potentials in molecular dynamics simulations", Computer Physics Communications **120**, 20–32 (1999).

[460] S. Balay, S. Abhyankar, M. F. Adams, S. Benson, J. Brown, P. Brune, K. Buschelman, E. M. Constantinescu, L. Dalcin, A. Dener, V. Eijkhout, J. Faibussowitsch, W. D. Gropp, V. Hapla, T. Isaac, P. Jolivet, D. Karpeev, D. Kaushik, M. G. Knepley, F. Kong, S. Kruger, D. A. May, L. C. McInnes, R. T. Mills, L. Mitchell, T. Munson, J. E. Roman, K. Rupp, P. Sanan, J. Sarich, B. F. Smith, S. Zampini, H. Zhang, H. Zhang, and J. Zhang, *PETSc Web page*, `https://petsc.org/`, 2024.

[461] S. Balay, S. Abhyankar, M. F. Adams, S. Benson, J. Brown, P. Brune, K. Buschelman, E. Constantinescu, L. Dalcin, A. Dener, V. Eijkhout, J. Faibussowitsch, W. D. Gropp, V. Hapla, T. Isaac, P. Jolivet, D. Karpeev, D. Kaushik, M. G. Knepley, F. Kong, S. Kruger, D. A. May, L. C. McInnes, R. T. Mills, L. Mitchell, T. Munson, J. E. Roman, K. Rupp, P. Sanan, J. Sarich, B. F. Smith, H. Suh, S. Zampini, H. Zhang, H. Zhang, and J. Zhang, *PETSc/TAO users manual*, tech. rep. ANL-21/39 - Revision 3.22 (Argonne National Laboratory, 2024).

[462] S. Balay, W. D. Gropp, L. C. McInnes, and B. F. Smith, "Efficient management of parallelism in object oriented numerical software libraries", in Modern software tools in scientific computing, edited by E. Arge, A. M. Bruaset, and H. P. Langtangen (1997), pp. 163–202.

[463] P. E. Grabowski, M. S. Murillo, V. S. Batista, L. X. Benedict, M. P. Desjarlais, F. R. Granziani, A. Markmann, D. F. Richards, M. P. Surh, and H. D. Whitley, *Simulating quantum high energy density plasmas: Approximations according to the time-dependent variational principle*, tech. rep. (Los Alamos National Laboratory (LANL), Los Alamos, NM (United States), 2012).

[464] P. V. Parandekar and J. C. Tully, "Detailed balance in Ehrenfest mixed quantum-classical dynamics", Journal of Chemical Theory and Computation **2**, 229–235 (2006).

[465] M. Honda, J. Meyer-ter-Vehn, and A. Pukhov, "Collective stopping and ion heating in relativistic-electron-beam transport for fast ignition", Physical Review Letters **85**, 2128 (2000).

[466] V. N. Tsytovich, R. Bingham, U. de Angelis, and A. Forlani, "Collective plasma processes in the solar interior and the problem of the solar neutrinos deficit", Physics-Uspekhi **39**, 103 (1996).

[467] V. N. Tsytovich, R. Bingham, U. De Angelis, and A. Forlani, "Relativistic corrections to collective photon scattering in plasmas", Journal of Quantitative Spectroscopy and Radiative Transfer **55**, 797–807 (1996).

[468] J. Kinney, H. LeFevre, C. Kuranz, and S. Baalrud, "Mean force emission theory for classical bremsstrahlung in strongly coupled plasmas", Physics of Plasmas **31**, 053302 (2024).

[469] M. E. Peskin and D. V. Schroeder, *An Introduction to Quantum Field Theory* (CRC press, Boca Raton, FL, 2018).

[470] G. Salin, "Hydrodynamic limit of the Yukawa one-component plasma", Physics of Plasmas **14**, 082316 (2007).

[471] F. M. Smith, W. Birnbaum, and W. H. Barkas, "Measurements of meson masses and related quantities", Physical Review **91**, 765 (1953).

[472] W. H. Barkas, W. Birnbaum, and F. M. Smith, "Mass-ratio method applied to the measurement of L-meson masses and the energy balance in pion decay", Physical Review **101**, 778 (1956).

[473] J. P. Mithen, J. Daligault, and G. Gregori, "Onset of negative dispersion in the one-component plasma", in AIP Conference proceedings, Vol. 1421 (American Institute of Physics, 2012), pp. 68–72.